Spinning the Higgs

Spin and parity measurement of the discovered Higgs-like boson in the $H \to WW \to \ell\nu\ell\nu$ decay mode

Rosemarie Aben

CERN-THESIS-2015-034
17/06/2015

Cover photo: Martin Moos/Lonely Planet Images/Getty Images
Merry-go-round spinning on Place de l'Hôtel-de-Ville, Paris
Typeset: LaTeX
Printed by: Gildeprint

Spinning the Higgs

Spin and parity measurement of the discovered Higgs-like boson in the $H \to WW \to \ell\nu\ell\nu$ decay mode

ACADEMISCH PROEFSCHRIFT

ter verkrijging van de graad van doctor
aan de Universiteit van Amsterdam
op gezag van de Rector Magnificus
prof. dr. D.C. van den Boom
ten overstaan van een door het college voor promoties
ingestelde commissie,
in het openbaar te verdedigen in de Agnietenkapel
op woensdag 17 juni 2015, te 10:00 uur

door

Rosemarie Zoë Aben

geboren te Amsterdam

Promotiecommissie:

Promotor:	prof. dr. S.C.M. Bentvelsen
Copromotor:	dr. ir. P.M. Kluit
Overige Leden:	dr. M.P. Decowski
	prof. dr. E.L.M.P. Laenen
	prof. dr. F.L. Linde
	prof. dr. ir. E.N. Koffeman
	prof. dr. M.H.M. Merk
	dr. S. Caron

Faculteit der Natuurwetenschappen, Wiskunde en Informatica

This work is part of the research program of the Stichting voor Fundamenteel onderzoek der Materie (FOM), which is part of the Nederlandse organisatie voor Wetenschappelijk Onderzoek (NWO). It was carried out at the Nationaal Instituut voor Subatomaire Fysica (Nikhef) in Amsterdam, the Netherlands.

Contents

Introduction

The known elementary particles are gathered in the Standard Model (SM) of Particle Physics. This is a quantum field theory, that describes the particles and their interactions through the electromagnetic, weak and strong force. The existence of every elementary particle in the model has experimentally been proven. There is however one problem: according to the model the elementary particles are massless, while from experiments and everyday life it is clear that particles do have a mass. An explanation with experimental foundation for this discrepancy is needed in order to justify the Standard Model. In 1964, the Higgs mechanism, named after one of its inventors, has been developed and incorporated in the SM for this purpose [1–6].

The Higgs mechanism explains how elementary particles can acquire a mass through interaction with a Higgs field. To proof this mechanism experimentally, a manifestation of the field, the Higgs boson, has to be found. Although the mechanism predicts all of the properties of this boson - except for its mass - it is very hard to detect due to its small production rate.

The search for the Higgs boson has been one of the primary motivations for the construction of the Large Hadron Collider (LHC) at CERN, the European Organisation for Nuclear Research. In this circular particle accelerator bunches of protons collide with record breaking energies of up to 8 TeV in 2012. Around the collider different types of detectors are positioned to measure the particles that emerge from the proton collisions. Two of the detectors, ATLAS and CMS, have had as objective to discover the Higgs boson; both succeeded in doing so.

On the 4th of July 2012, the discovery of a Higgs-like boson was announced. Both the ATLAS and CMS experiments claimed the discovery of a new particle with a mass of around 125 GeV, with a local significance of around five standard deviations [7,8]. This means that the probability for the observed excess in data, while there is actually no Higgs-like boson and the observed excess is a random fluctuation, is one in 3.5 million.

The new particle is consistent with a Higgs-like boson, in the sense that its measured properties match with these predicted for a Higgs boson: its mass falls in the allowed range, its production rate in the various decay modes is as expected, and from its decay into pairs of vector bosons, the particle can be identified as a neutral boson. However, this does not yet prove that the particle is the SM Higgs boson. Only when all of its properties have been measured and found to agree with the predictions of the Standard Model, it can be excluded that the observed signal is not that of a Higgs boson look-alike with slightly different properties.

Two important quantum numbers that can be measured are the spin and parity of the new boson. All elementary particles have a non-zero spin, but the Higgs boson is predicted to have no spin. This property is inherent to a quantum field that generates mass for elementary particles. Consequently, if the new particle turns out to have a non-zero spin it cannot be a manifestation of the Higgs field. The SM Higgs boson is predicted to have even parity. There are however extensions of the Standard Model that predict more than one Higgs particle, where one of the additional Higgs bosons has odd parity. Thus, the measurement of the spin and parity of the Higgs-like boson will already give a clear indication of its true nature.

In the analysis that is presented in this thesis the compatibility of the observed signal with different hypotheses for the new boson will be studied. The null hypothesis yields the agreement with the SM Higgs boson: $J^P = 0^+$, while the alternative hypotheses include bosons with different spin and parity configurations: $J^P = 0^-, 1^+, 1^-$ and 2^+. In this way four tests can be conducted, where in each test the compatibility of the observed signal with the null hypothesis and one of the alternative hypotheses is evaluated. This allows to make a statement about the probability that the signal is that of the SM Higgs boson or of the alternative boson.

The spin and parity are measured, using the kinematical properties of the particles into which the Higgs boson decays, since the Higgs boson itself has too small a lifetime to be detected. The SM Higgs boson has various decay modes, the three most sensitive channels for a Higgs boson with a mass of ~ 125 GeV include $H \to ZZ^*$, $H \to \gamma\gamma$ and $H \to WW^*$. In this thesis the spin and parity are evaluated for the decay channel $H \to W^+W^- \to \ell^+\nu\ell^-\bar{\nu}$. The advantage of this channel is its relatively high production rate and good possibilities to reduce the backgrounds, allowing for a sensitive analysis on the basis of the accumulated data in 2012. Its final state can however not be fully reconstructed due to the non-detectable neutrinos. This makes the analysis nevertheless challenging.

This analysis is not the only one performed to characterise the new Higgs-like boson. At CERN many analyses are carried out to unravel the properties of the Higgs-like boson: precise measurements of its mass and couplings to the other SM particles are ongoing, and preparations for measurements of other properties are made. For this, not only the decay of the Higgs boson into pairs of W-bosons, but also decays into other bosons as well as into fermions are evaluated. Eventually the results of the different channels and measurements are combined to allow for a complete statement about the nature of the observed Higgs-like boson.

In this thesis, first the theoretical background of the Standard Model and the Higgs mechanism is described in chapter 1. Then the LHC and the ATLAS detector are presented in chapter 2. I have carried out several muon detector related tasks, of which being an expert-on-call for the muon detector system was the primary occupation, hence chapter 3 give a concise overview of the Muon detector control and data acquisition systems. In chapter 4 the phenomenology, simulation and reconstruction of the events that are used in the analysis are explained.

As said, the final state of the decay channel under study cannot be fully reconstructed, nevertheless, we have developed a method to reconstruct events in the rest frame of the Higgs boson. First this method has been used to improve the Higgs mass resolution, however after the discovery we optimised the method to allow for the construction of new spin and parity sensitive variables. This is the subject of chapter 5. Initially, in 2010, I started working on the rate measurement of the Higgs boson in the WW channel, both contributing to the analyses of the Higgs production through vector boson fusion and gluon gluon fusion. Since the discovery of the Higgs-like

boson in 2012, I shifted to the spin and parity analysis, which is presented in two parts. First, the preparations for the spin and parity measurement are given in chapter 6, then the actual measurement and results are presented in chapter 7. It is a fully analytical analysis, such that every step of the properties measurement can be calculated and evaluated. This distinguishes the analysis from the official ATLAS multivariate analysis [9]. Finally, the conclusions and outlook are presented.

Chapter 1

Theoretical overview

In the fifth century B.C. Greek philosophers formulated a theory, called Atomism, that described the fundamental building blocks of matter. It stated that all matter is built of unchangeable and eternal particles - the atoms - and of empty space in which atoms can scatter and pack into different orientations. The first steps towards a description of nature using particles were taken.

The quest for the correct description of particle physics continued ever since and today we have a single mathematical model describing the known elementary particles and the way they interact through the strong, the electromagnetic and the weak force. This model is called the Standard Model of Particle Physics. The foundations for this model were laid in the 1960s, when physicists tried to categorise the already observed elementary particles and fundamental forces. The resulting model predicted additional - not yet observed - particles. When in 1983 the existence of the predicted W- and Z-bosons was experimentally verified, including measurements of their masses that corresponded to the predicted values, the power of the model became exceptionally clear. With the discovery of a Higgs-like boson in 2012, experimental evidence for every particle predicted by the Standard Model has been obtained. Given that the Higgs boson is the particle of which the discovery completes the Standard Model, a thorough experimental research of the discovered boson is essential: every predicted property will have to be verified experimentally.

The justification of the Standard Model and the measurement of the properties of the Higgs-like boson include numerous experimental challenges. A good understanding of the theoretical framework of particle physics is indispensable in order to fully appreciate the complex strategies that are developed to overcome these experimental challenges. Therefore, in this chapter a concise overview of theoretical particle physics is given. First, the physics leading to the necessity of the Higgs mechanism is elucidated in section 1.1; this includes the particle content of the Standard Model, the mathematical ingredients and finally the electroweak theory. Then spontaneous symmetry breaking will be introduced in section 1.2, which is the mechanism that predicts the Higgs boson and its properties. Subsequently the focus is shifted to the evaluation of the spin and parity of the Higgs boson. Section 1.3 gives a concise overview of these two quantum numbers, and in section 1.4 alternative spin and parity hypotheses for the observed signal are formulated.

1.1 The Standard Model of Particle Physics

Concisely stated, the Standard Model (SM) is a quantum field theory that describes elementary particles as excitations of quantum fields. The dynamics of the particles is summarised in a single equation called the SM Lagrangian. The Lagrangian is constrained by demanding invariance under local symmetries. Initially, the required invariance prevents elementary particles to have a mass. However, when the concept of spontaneous symmetry breaking is introduced, massive particles may be generated. This so-called Higgs mechanism completes the description of the current understanding of elementary particle physics. Many advanced physics concepts are introduced in these few sentences. They will be elucidated in the following sections. Refs. [10–12] are used as guideline to discuss the theoretical framework. Additionally, Refs. [13–16] are used to clarify the principles of the Higgs mechanism.

1.1.1 Particles and forces

The particles described in the Standard Model are referred to as elementary particles, because they do not possess any substructure within the current experimental resolution. They represent the fundamental building blocks of nature. An elementary

particle is uniquely defined by its quantum numbers and mass. Furthermore, each particle has a corresponding antiparticle with the same mass but opposite additive quantum numbers (colour, electric charge and helicity). The elementary particles may be categorised according to their spin, which results in two types of particles: bosons and fermions.

Bosons

Particles with integer spin are called bosons and obey Bose-Einstein statistics. The vector bosons (spin value of one) function as mediators of the fundamental forces. An elementary particle is said to experience a fundamental force when it couples to the corresponding vector boson. The quantum numbers of the particle define in which interactions it can take part.

The massless photon mediates the electromagnetic force. It is the only vector boson that cannot couple to itself as it does not carry the quantum number corresponding to the force it mediates, in this case electric charge. The strong force is mediated by eight types of massless gluons, and the massive $W^{\pm}$ and Z^0 bosons mediate the weak force. As the weak bosons do have a mass, the weak force has a relatively short range with respect to the electromagnetic and the strong interactions. Gravity is the fourth fundamental force, mediated by a hypothetical graviton of spin-2, however, this force is not incorporated in the SM, as it is too weak to play a role in fundamental particle physics. According to the electroweak theory the electromagnetic and weak interactions do not appear as unrelated phenomena, but rather as two different manifestations of a single fundamental force. This will be the subject of section 1.1.5. The strong interaction will not be further discussed as a thorough understanding of this type of interactions is not necessary to understand the experimental research that is the subject of this thesis.

There is yet one more boson included in the Standard Model: the Higgs boson. The Higgs boson arises in the model when the elementary particle acquire a mass through spontaneous symmetry breaking. Unlike any other elementary particle it has zero spin, it is a so-called scalar boson. The Higgs boson can hardly be classified as a force carrier nor as a matter particle: an outsider, though crucial to complete the SM. Why

the inclusion of the Higgs mechanism results in a particle with unique properties will be explained in section 1.2.

Fermions

Particles with half-integer spin are called fermions and comply with Fermi-Dirac statistics. Fermions are often referred to as the matter particles and interact through the exchange of vector bosons. All fermions are subject to the electroweak force, because they have non-zero electroweak quantum numbers: they carry weak hypercharge and some also have a weak isospin. The fermions may further be divided into quarks and leptons. Quarks are the fermions subject to the strong force, since they carry colour charge, the quantum number defining the strong interaction. Furthermore, the division into quarks and leptons is a convenient structure for the description of electroweak theory, as it allows particles to be ordered in multiplets.

The fermions are additionally classified into three generations of four particles each, two quarks and two leptons, as shown in figure 1.1. This choice of classification is driven by the fact that the only difference between the generations is the mass of its particles. Each generation consists of an up-type quark (up, charm and top), a down-type quark (down, strange, bottom), a charged lepton (electron, muon, tau) and a neutral lepton (electron-neutrino, muon-neutrino, tau-neutrino). Elementary particles decay into lighter particles, unless they are prevented from doing so by conservation laws. As a consequence stable matter is exclusively built from particles of the first generation: the up- and down-quarks form protons and neutrons that together with electrons build up atoms.

While leptons exist as free particles, quarks are always confined within hadrons, forming a bound state of either two quarks, the mesons, or three quarks, the baryons. This is a result of the strong coupling between the quarks that increases as their distance increases, which makes it impossible for a quark to escape the bound state. All fermions have a mass; the values are given in figure 1.1. The values of the quark masses have large uncertainties as confinement makes measurement of individual quark masses impossible and therefore model-dependent. Although experiments have shown that neutrinos also have mass [19], the Standard Model still treats them as massless. Since

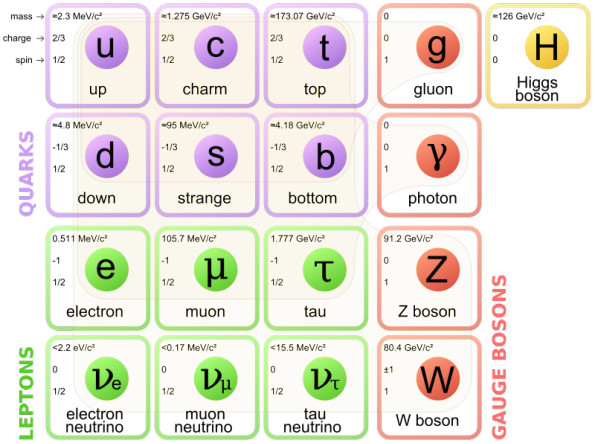

Figure 1.1: *The particle content of the Standard Model of Particle Physics [17]. Masses are taken from Ref. [18].*

the mass of the neutrinos is relatively close to zero, this approximation does hardly affect the precision of Standard Model predictions.

1.1.2 Mathematical formulation

The regime of elementary particle physics is recognised by high velocities and small distances. A scale at which a classical description does not suffice. In the following the mathematical concepts that are used to formulate the Standard Model are described.

Lorentz invariant theory

Elementary particles travel with velocities close or equal to the speed of light. At these velocities observations depend on the frame of reference in which they are measured. Constructing the SM in a Lorentz invariant way assures that these measurements do not depend on a specific frame of reference.

Quantum field theory

Particle interactions take place at a scale at which the Planck constant, $\hbar$, cannot be neglected. Therefore the SM should be formulated using quantum mechanics. Moreover, in the regime of relativistic quantum mechanics, particles as well as forces

are described as quantum fields[1] and hence the Standard Model is formulated as a quantum field theory (QFT).

Renormalisable theory

The Standard Model should not contain infinities, as infinities are not physical. However, initially infinities do appear in the calculations of the amplitudes of scattering processes of elementary particles. A scattering process has an infinite number of intermediate states and therefore the amplitude is calculated using perturbation theory. This approximation principle causes infinities when higher order diagrams are included. Nevertheless, allowing the infinities to be absorbed into a finite number of physical quantities solves this problem. This process is called renormalisation and can be applied to the SM without introducing new infinities.

The formulation of the SM as a renormalisable QFT is summarised in a Lagrangian[2]. A Lagrangian is defined as the difference between the kinetic energy and potential energy of a dynamical system, per density volume and has units of energy per density volume. The equations of motions of a dynamical system are determined by substitution of the Lagrangian into the Euler-Lagrange equation:

$$\partial_\mu \left[\frac{\partial \mathcal{L}}{\partial(\partial_\mu \phi_i)} \right] = \frac{\partial \mathcal{L}}{\partial \phi_i} \tag{1.1}$$

or differently stated by minimising the action: $S = \int d^4x \mathcal{L}$. To describe a Lorentz invariant theory the Lagrangian has to be a Lorentz scalar and as such has four dimensions. Thus, each term allowed in the Lagrangian of the SM has to have exactly four dimensions.

1.1.3 Symmetries

Symmetries are an essential element of physics and should be discussed before constructing the SM Lagrangian. In general, a symmetry is an operation that, when it

[1] Particles are, strictly speaking, excitations of the ground states of to the particle corresponding fields, nevertheless, identifying the particles directly with the fields will suffice in the context of this thesis.

[2] With 'Lagrangian' actually the Lagrangian density is meant. The relation between the Lagrangian (L) and its density ($\mathcal{L}$) is: $L = \int \mathcal{L} dx dy dz$.

acts upon a system, leaves it invariant, i.e. that carries the system into a configuration indistinguishable from the original one. Symmetries play an important role in nature, ranging from the structure of a snowflake, to the interactions of elementary particles. The importance of symmetries is expressed in Noether's theorem: every symmetry in physics yields a conservation law and vice versa. As an example, the laws of physics are symmetric under translations in time, yielding conservation of energy. The theorem implies that if a certain symmetry would not be respected, the corresponding conservation law would not hold and moreover, the related conserved quantity would not be conserved. Thus, the SM Lagrangian should be constructed in such a way that it reflects the symmetries governed by the strong, weak and electromagnetic interactions.

The symmetries constraining the Standard Model stem from a powerful principle called gauge invariance. Gauge symmetries are represented by continuous mathematical groups that, when acting upon the Lagrangian in the form of a gauge transformation, leave it invariant. If a gauge symmetry is constant over space-time it is referred to as a global symmetry and a transformation from one field configuration to another - that both describe the same physical system - will yield a simple phase transformation. The Standard Model should govern global gauge invariance as substantiated by Noether's theorem: the conservation laws should be obeyed. Although not initiated by theoretical foundations, a global symmetry may be promoted into a local symmetry, by demanding the symmetry operation to depend on space-time coordinates. This happens to be an elegant way to describe elementary particle interactions.

The product group that reflects the gauge symmetry of the Standard Model is given by: $SU(3)_C \otimes SU(2)_L \otimes U(1)_Y$. Here $SU(3)_C$ represents the symmetry governed by the strong interactions: it affects fields possessing colour charge. The second and third group are inextricably linked as they together describe the structure of the electroweak interactions, where $SU(2)_L$ only affects left-handed particles and $U(1)_Y$ particles possessing weak hypercharge.

Before constructing the SM Lagrangian using gauge invariance, the method for this

is best explained by imposing local gauge invariance on pure electromagnetic interactions, as quantum electrodynamics (QED) is an Abelian[3] gauge theory and hence less complex.

1.1.4 Quantum electrodynamics as stepping stone

The QED Lagrangian will be deduced for a Dirac fermion with mass m that is not subjected to a potential. This could for example be a free electron. In QFT, fermions are represented by spinor fields, denoted as ψ. The adjoint field is defined as $\bar{\psi} = \psi^\dagger \gamma^0$, where γ^0 is one of the Dirac γ-matrices (γ^μ). The Lagrangian may be derived starting from the Lagrangian for a free Dirac fermion:

$$\mathcal{L}_{\text{Dirac}} = i\bar{\psi}\gamma^\mu \partial_\mu \psi - m\bar{\psi}\psi \tag{1.2}$$

where the first term represents the kinetic energy of the fermion and the second term its mass. $\mathcal{L}_{\text{Dirac}}$ is constructed such that substitution into the Euler-Lagrange equation (1.1) leads to the corresponding equation of motion, which is the Dirac equation:

$$(i\gamma^\mu \partial_\mu - m)\psi = 0 \tag{1.3}$$

QED is symmetric under the $U(1)_{EM}$ symmetry group, with the electric charge as the generator of the group and hence also the conserved quantity of the symmetry. This corresponds to symmetry transformations under an arbitrary real phase constant α:

$$\psi(x) \to \psi'(x) = e^{i\alpha}\psi(x) \tag{1.4}$$

When $\psi(x)$ is replaced by $\psi'(x)$ in Eq. 1.2, the Lagrangian is indistinguishable from the original one and thus invariant under global $U(1)_{EM}$ gauge transformations.

[3] A gauge theory is Abelian if the group that reflects its symmetry is commutative, which implies that the result of applying the group operator to two group elements does not depend on the order of the elements.

The Lagrangian in Eq. 1.2 describes a QFT without particle interactions. To obtain an interacting QFT the phase constant α should be allowed to vary as a function of space-time coordinates: $\alpha = \alpha(x)$. The Lagrangian is not invariant under this *local* gauge transformation, as $\partial_\mu(e^{i\alpha(x)}\psi) \neq e^{i\alpha(x)}(\partial_\mu\psi)$ Hence, a method has to be developed to restore the invariance of $\mathcal{L}_{\text{Dirac}}$ on a local level. For this purpose a new vector field, $A_\mu(x)$, is introduced. It transforms as:

$$A_\mu(x) \rightarrow A'_\mu(x) = A_\mu(x) + \frac{1}{e}\partial_\mu a(x) \tag{1.5}$$

where e is the electric charge of the Dirac fermion. Additionally, the partial derivative is replaced by a covariant derivative[4] that transforms like the vector field:

$$\partial_\mu \rightarrow D_\mu = \partial_\mu - ieA_\mu(x) \tag{1.6}$$

Substitution of Eqs. 1.5 and 1.6 in the Lagrangian given by Eq. 1.2 leaves it invariant as $D_\mu(e^{i\alpha(x)}\psi) = e^{i\alpha(x)}(D_\mu\psi)$. Consequently, a local gauge invariant Lagrangian is obtained and as an immediate consequence it describes an interaction between a fermion and a vector field as represented by the last term in the Lagrangian:

$$\begin{aligned}\mathcal{L} &= i\bar{\psi}\gamma^\mu D_\mu\psi - m\bar{\psi}\psi \\ &= \mathcal{L}_{\text{Dirac}} - eA_\mu(x)\bar{\psi}(x)\gamma^\mu\psi(x)\end{aligned} \tag{1.7}$$

Moreover, the electric charge is also conserved by the local gauge symmetry as e remains unconstrained. To be able to identify the gauge field, $A_\mu(x)$, with a physical field a kinetic term representing the propagation of the field through space-time needs to be added to the Lagrangian. This is allowed provided that the expression is gauge invariant. The kinetic term is given by:

[4] In general, a covariant derivative ensures that a mathematical formulation will be independent of the coordinate system in which the physical system is defined, i.e. it ensures that the space-time symmetries, like energy and momentum, are conserved.

$$\mathcal{L}_{kin} = -\frac{1}{4} F_{\mu\nu}(x) F^{\mu\nu}(x) \tag{1.8}$$

where $F_{\mu\nu} = \partial_\mu A_\nu - \partial_\nu A_\mu$ is the field strength tensor. With the addition of the kinetic the gauge field, $A_\mu(x)$, can be recognised as the (massless) photon field.

In summary, identifying the symmetry of the electromagnetic interaction and demanding local gauge invariance of the Lagrangian under this symmetry, and additionally requiring the introduced gauge field to be physical, gives rise to the Lagrangian representing electromagnetic interactions:

$$\mathcal{L}_{QED} = \underbrace{i\bar{\psi}\gamma^\mu\partial_\mu\psi}_{E_{\text{kin}} \text{ of fermion}} - \underbrace{m\bar{\psi}\psi}_{\text{mass of fermion}} - \underbrace{eA_\mu(x)\bar{\psi}(x)\gamma^\mu\psi(x)}_{\text{interaction}} - \underbrace{\frac{1}{4}F_{\mu\nu}(x)F^{\mu\nu}(x)}_{E_{\text{kin}} \text{ of photon}} \tag{1.9}$$

This method is not uniquely reserved for QED, it may be used to acquire all interaction terms required in the SM Lagrangian. Hence, it is one of the key ingredients in the formulation of the Standard Model.

1.1.5 Electroweak theory

Inspired by Einstein's attempt to unify gravity and electrodynamics and within the spheres of Bludmann's suggestion that neutral weak interactions might exist [21], Glashow formulated a unified description of the electromagnetic and weak interactions [22]. He published the theory in 1961 accompanied by the advise not to take it too seriously as the theory was not renormalisable. However, in 1967 Salam and Weinberg brought the model to a next level and formulated it as a spontaneously broken theory [23, 24]. When in 1971 't Hooft showed this model to be renormalisable [25, 26], it was surely taken seriously and in 1999 't Hooft and his thesis advisor Veltman were awarded for this achievement with the Nobel Prize.

The electroweak theory is based upon the $SU(2)_L \otimes U(1)_Y$ symmetry group. Gauge invariance under local $U(1)$ gauge transformations is already explored in the previous section and will be used as guideline to acquire local gauge invariance under the

$SU(2)$ symmetry group. This is a more complex process as $SU(2)$ is a non-Abelian symmetry group. Subsequently, the two formulations will be combined in the product group to obtain the electroweak Lagrangian.

Local gauge invariance under $SU(2)$

The Lagrangian for the $SU(2)$ symmetry group is derived starting with the Dirac Lagrangian given in Eq. 1.2, that is adjusted such that it describes a system consisting of singlets and doublets of fermions rather than a single fermion. Furthermore, the fermions are assumed to be massless for now:

$$\mathcal{L}_{\text{Dirac}} = i \sum_{f=1}^{3} \bar{\Psi} \gamma^{\mu} \partial_{\mu} \Psi \tag{1.10}$$

The transformations under $SU(2)_L$ are represented by $[2 \times 2]$ matrices, rather than by a simple phase, explaining the non-Abelian character of this symmetry operation:

$$\Psi(x) \rightarrow \Psi'(x) = e^{i\alpha^a(x)T_a} \Psi(x) \text{ , a=1,2,3} \tag{1.11}$$

where $T_a = \frac{1}{2}\sigma_a$, with σ_a representing the Pauli matrices. The $SU(2)_L$ group has three generators represented by the isospin operators, T_a. Consequently, also *three* phases $\alpha^a(x)$ have to be included that, because they are required to depend on space-time coordinates, result in the violation of local gauge invariance. To restore the local symmetry three gauge fields W_{μ}^{a} are introduced. They transform as:

$$W_{\mu}^{a}(x) \rightarrow W_{\mu}'^{a}(x) = W_{\mu}^{a}(x) + \frac{1}{g}\partial_{\mu}\alpha^{a}(x) + \epsilon_{abc} W_{\mu}^{b} \alpha^{c}(x) \text{ , a=1,2,3} \tag{1.12}$$

where g is the coupling constant that represents the strength of the coupling to the gauge fields, and ϵ_{abc} is the Levi-Civita symbol. The first part of the transformation is similar to the transformation of A_{μ} given by Eq. 1.5, while the third term results from the non-Abelian character of $SU(2)$. Furthermore, the covariant derivative is defined as:

$$\partial_\mu \rightarrow D_\mu = \partial_\mu - igT_a W_\mu^a(x) \tag{1.13}$$

Finally, to be able to identify the three gauge fields, W_μ^a, with dynamical fields, associated kinematic terms need to be added:

$$\mathcal{L}_{\text{kin}} = -\frac{1}{4} W_{\mu\nu}^a W_a^{\mu\nu} \tag{1.14}$$

where $W_{\mu\nu}^a = \partial_\mu W_\nu^a - \partial_\nu W_\mu^a + g\epsilon_{abc} W_\mu^b W_\nu^c$ is the field strength tensor for a non-Abelian QFT. Since the field strength tensor contains a term quadratic in the fields, the kinetic term gives rise to cubic and quartic self-interactions amongst the gauge fields. Yet another consequence of the non-Abelian character of the $SU(2)$ operations.

Electroweak unification

All fermions are subject to the electroweak force. However, experimental observations[5] have shown that the electroweak force distinguishes between left-handed and right-handed fermions. This is a result of the difference in the values of their electroweak quantum numbers; the weak isospin and weak hypercharge. The weak hypercharge and the third component of the weak isospin are related to the electric charge, as established in the Gell-Mann - Nishijima formula:

$$Q = T_3 + \frac{Y}{2} \tag{1.15}$$

In the unified description of electromagnetic and weak interactions the generator of the $U(1)$ group is represented by the weak hypercharge instead of the electric charge. All fermions possess weak hypercharge and transform therefore uniformly under $U(1)_Y$. The generator of the $SU(2)_L$ group is presented by the weak isospin.

[5]The experiment that first showed the distinction in behaviour of left- and right-handed fermions was conducted by Chien-Shiung Wu in 1957, who studied the conservation of parity in Beta-decay [27].

While left-handed fermions possess weak isospin, right-handed fermions do not. Consequently, left-handed fermions transform as doublets under $SU(2)_L$ gauge transformations, while right-handed fermions transform as singlets:

$$\begin{pmatrix}\nu_i\\ \ell_i\end{pmatrix}_L \ , \ \begin{pmatrix}u_i\\ d_i\end{pmatrix}_L \ , \ (\ell_i)_R \ , \ (u_i)_R \ , \ (d_i)_R \ ; \ \text{i=1,2,3} \tag{1.16}$$

Therefore, the electroweak force treats fermions differently depending on their chirality. In the construction of the electroweak Lagrangian this difference is taken into account by the use of left-handed and right-handed projections $\psi_{L,R}$ of the fermion fields ψ_f: $\psi_{L,R} = \frac{1}{2}(1 \mp \gamma^5)\psi$, with $\psi_f = \psi_L + \psi_R$.

From the descriptions of the electromagnetic and weak interactions follows that the electroweak Lagrangian should include a total of four fields: a triplet of gauge fields W^a_μ that transform as in Eq. 1.12 with three associated generators T_a, and a singlet field B_μ that transforms in analogy with the QED gauge field A_μ as given by Eq. 1.5, with associated generator Y. The covariant derivative that includes these four gauge fields and distinguishes between left- and right-handed fermions is given by:

$$D^{L,R}_\mu = \partial_\mu - igI^{L,R}_a W^a_\mu - i\frac{g'}{2}YB_\mu, \text{ with } I^L_a = \frac{1}{2}\sigma_a = T_a \ , \ I^R_a = 0 \tag{1.17}$$

Substitution of the covariant derivative in the Lagrangian, as given by Eq. 1.10, and subsequently adding the kinetic terms for the gauge fields as given by Eqs. 1.8 and 1.14, results in the local gauge invariant electroweak Lagrangian including all fermions and vector bosons:

$$\mathcal{L}_{EW} = \underbrace{\sum_j i\bar{\psi}^j_L\gamma^\mu D^L_\mu\psi^j_L + \sum_{j,\sigma} i\bar{\psi}^j_{R\sigma}\gamma^\mu D^R_\mu\psi^j_{R\sigma}}_{E_{\text{kin}}\text{ fermions + int. gauge fields-fermions}} \underbrace{-\frac{1}{4}W^a_{\mu\nu}W^{\mu\nu}_a - \frac{1}{4}B_{\mu\nu}B^{\mu\nu}}_{E_{\text{kin}}\text{ gauge fields + gauge field self-int.}} \tag{1.18}$$

where j runs over the three generations of the Standard Model and σ can either be positive or negative, denoting up-type fermions and down-type fermions respectively.

Thus, a renormalisable Lagrangian including all Standard Model particles is obtained. However, the particles cannot yet be identified with the physical particles, as $\mathcal{L}_{EW}$ does not contain mass terms for the particles. Explicit mass terms for the gauge fields, $\frac{1}{2}m^2 W^a_\mu W^{a,\mu}$, have been avoided as they will break gauge invariance. This is a problem as three of the four gauge fields should represent *massive* gauge bosons. Also fermion masses cause difficulties. A general fermion mass term is of the form: $m\bar{\psi}\psi = m(\bar{\psi}_L\psi_R + \bar{\psi}_R\psi_L)$ and since left-handed fermion fields transform as doublets, while right-handed fermion fields transform as singlets this term is not gauge invariant under $SU(2)_L \otimes U(1)_Y$ rotations and would lead to mixing of the left- and right-handed fields, which describes no known physical phenomenon. Nevertheless, experimental observations show that fermions do have a mass. Thus, a method to include gauge invariant mass terms for bosons and fermions in the electroweak Lagrangian has to be found.

1.2 The Higgs mechanism

The Lagrangian as given by Eq. 1.18 does not give an adequate description of the electroweak theory as it involves only massless fermions and bosons. Adding mass terms by hand violates gauge invariance, so another procedure has to be followed. The proposed method is called the Higgs mechanism, which will retain the symmetry of the Lagrangian, while the symmetry of the ground state is broken through spontaneous symmetry breaking, giving rise to gauge invariant mass terms. The mechanism is named after Peter Higgs, who developed this model in 1964, practically at the same time as Robert Brout and François Englert. The Higgs mechanism can account for the masses of bosons as well as fermions. To give a clear description of the mechanism, it will first be applied to a renormalised local $U(1)$ gauge invariant theory, like QED, which will give rise to a massive gauge boson. Of course, the gauge boson in QED, being the photon, should be massless; it is merely an example to show that it is possible to generate a massive boson in a Lorentz invariant way. The transition to spontaneous symmetry breaking of the electroweak theory will be made afterwards, and finally also the generation of masses for the fermions will be explained.

1.2.1 The Higgs mechanism in $U(1)$

The first step is to introduce a new field, ϕ, that is defined as a complex scalar field. In this way two degrees of freedom will be added to Lagrangian that can be used in the subsequent steps of the Higgs mechanism. One is free to add an expression including new fields to the Lagrangian of a renormalised theory as long as the expression fits the dimensions of the Lagrangian and the field retains the symmetries of the described physical system. The new field is defined as:

$$\phi = \frac{1}{\sqrt{2}}(\phi_1 + i\phi_2) \tag{1.19}$$

The local $U(1)$ gauge invariant Lagrangian for the introduced scalar field, including an interaction with the massless gauge boson A_μ is given by:

$$\mathcal{L}_{\text{scalar}} = (D^\mu\phi)^\dagger(D_\mu\phi) - \frac{1}{4}F^{\mu\nu}F_{\mu\nu} - V(\phi) \tag{1.20}$$

with D_μ as defined in Eq. 1.6 and the corresponding transformation of A_μ given by Eq. 1.5.

The next step is to find out which particles may appear in the presence of the new scalar field. For this purpose, perturbations around the vacuum of the described system are studied. In general, the vacuum is defined as the minimum of the potential of a system. A suitable potential to study the perturbations around the vacuum yields:

$$V(\phi) = \mu^2(\phi^\dagger\phi) + \lambda(\phi^\dagger\phi)^2, \text{ with } \lambda > 0 \ , \ \mu^2 < 0 \tag{1.21}$$

The value of λ is chosen to be positive to ensure stability against unbounded oscillations, and higher powers in ϕ are omitted to ensure that the theory is renormalisable. The value of μ^2 can be chosen positive in order to give rise to a potential with a single vacuum state, however, this merely generates two massive scalar particles with common mass and does not lead to the desired massive gauge boson. Choosing μ^2 to be negative, on the other hand, results in a potential with an infinite number of vacua that lie on a circle with radius $\sqrt{\frac{-\mu^2}{2\lambda}}$. This is depicted in figure 1.2.

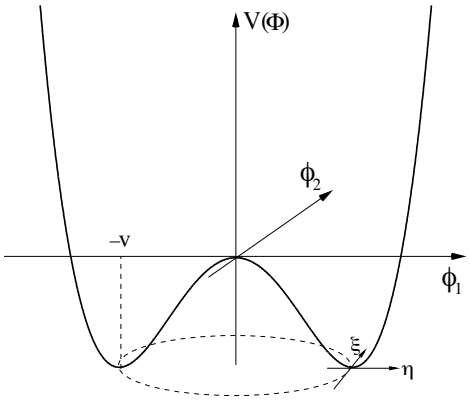

Figure 1.2: *Two-dimensional illustration of the Higgs potential $V(\phi)$ as defined in Eq. 1.21 with parameters $\lambda > 0$ and $\mu^2 < 0$. The dashed circle with radius v indicates the infinite set of vacuum states. (ξ, η) are the fields shifted with respect to (ϕ_1, ϕ_2) [13].*

A physical system can however only have one ground state, therefore, a single vacuum state has to be chosen. This immediately leads to a situation in which the symmetry of the Lagrangian is no longer respected by the vacuum. This is known as spontaneous symmetry breaking and turns out to have vital consequences as will become clear in the following. Which vacuum state is chosen is arbitrary and does not affect the ensuing physical consequences. Nevertheless, it is convenient to choose it such that in the subsequent results one can recognise physical fields and interactions. An appropriate choice is:

$$\phi_{1,\text{vac}} = \sqrt{\frac{-\mu^2}{2\lambda}} \equiv \frac{v}{\sqrt{2}} \ , \ \phi_{2,\text{vac}} = 0 \tag{1.22}$$

where v is called the vacuum expectation value. One can check that the $U(1)_{EM}$ phase transformation, $\phi(x) \rightarrow \phi'(x) = e^{i\alpha(x)}\phi(x)$, does not leave the vacuum invariant, while the Lagrangian is still symmetric under the $U(1)_{EM}$ symmetry group and hence describes the true physical system.

Having constructed a suitable potential, perturbations around the chosen vacuum can be studied. It is convenient to express these perturbations in terms of the shifted real

fields η and ξ, as defined in figure 1.2, with $\eta/\sqrt{2} \equiv \phi_1 - v/\sqrt{2}$ and $\xi/\sqrt{2} \equiv \phi_2$. Consequently, the scalar field, ϕ, expressed in terms of the shifted fields is defined as:

$$\phi = \frac{1}{\sqrt{2}}(\eta + v + i\xi) \tag{1.23}$$

In terms of the perturbed scalar field the Lagrangian, given by Eq. 1.20, becomes:

$$\mathcal{L}(\eta,\xi) = \frac{1}{2}(\partial^\mu\eta)^2 + \mu^2\eta^2 + (\partial^\mu\xi)^2 - \frac{1}{4}F^{\mu\nu}F_{\mu\nu} + \frac{1}{2}e^2v^2A^\mu A_\mu - evA_\mu(\partial^\mu\xi) + \text{int. terms} \tag{1.24}$$

where $|\partial^\mu\phi|^2 = (\partial^\mu\phi)(\partial_\mu\phi)$. The Lagrangian now describes, besides a gauge boson, two scalar particles: a massive η-particle, of mass $\sqrt{-\mu^2}$ and a massless ξ-particle. The ξ-particle is a so-called Goldstone boson. According to Goldstone's theorem such a massless scalar particle appears for every broken generator of the original symmetry and as the $U(1)$ group has only one generator, spontaneously breaking this symmetry gives rise to one Goldstone boson [28]. The η-particle arises as a 'side-effect' of spontaneous symmetry breaking and is better known as the Higgs boson.

Moreover, whereas previously the QED Lagrangian, given by Eq. 1.9, described a massless gauge boson, now a term proportional to $A^\mu A_\mu$ appears in the Lagrangian. This term may be identified as the general expression for the mass of a gauge boson, V: $\frac{1}{2}M_V^2V^\mu V_\mu$. Hence, a *massive* gauge boson, with a mass equal to ev has been generated. However, not to rejoice too soon: this massive gauge boson still has only two (transverse) polarisation states, alike a massless particle. To obtain a physical massive gauge boson an additional degree of freedom should be used to add a third (longitudinal) polarisation state.

Figure 1.3: *Illustration of the non-physical coupling between the gauge field, A, and the Goldstone boson ξ.*

Amongst the desired trilinear and quartic interaction terms in the Lagrangian the expression $evA_\mu(\partial^\mu\xi)$, that reflects the interaction as depicted in figure 1.3, stands out, since it has no physical interpretation whatsoever. The gauge freedom of A_μ, which is explained in the following, may be exploited to remove this term, or differently stated, to have the non-physical ξ-particle absorbed by the gauge boson as its third polarisation state. Eq. 1.5 shows that A_μ is only fixed up to a term $\partial_\mu\alpha$ and therefore A_μ can be redefined as:

$$A_\mu \to A'_\mu = A_\mu - \frac{1}{ev}(\partial_\mu\xi) \tag{1.25}$$

which is referred to as gauge freedom. When the Lagrangian in Eq. 1.24 is rewritten in terms of A'_μ a single expression for A'_μ remains: $\frac{1}{2}e^2v^2A'_\mu A'^\mu$, and the non-physical ξ-particle has disappeared. The chosen gauge, i.e. setting the phase of rotation α to $-\xi/v$, is called the unitary gauge. The local phase transformation that accompanies this gauge leads to a real scalar field that is also independent of ξ:

$$\phi \to \phi' = e^{-i\xi(x)/v}\phi = (v+\eta)/\sqrt{2} \tag{1.26}$$

Rewriting the Lagrangian in terms of the perturbed scalar field as redefined in Eq. 1.26 results in the final Lagrangian for the spontaneously broken $U(1)_{EM}$ gauge invariant theory:

$$\begin{aligned}\mathcal{L} = &\underbrace{\frac{1}{2}(\partial^\mu\eta)^2 + \mu^2\eta^2}_{E_{\text{kin}}\text{ \& mass of Higgs}} \underbrace{-\frac{1}{4}F^{\mu\nu}F_{\mu\nu} + \frac{1}{2}e^2v^2A_\mu A^\mu}_{E_{\text{kin}}\text{ \& mass of gauge field}} + \underbrace{e^2vA_\mu A^\mu\eta + \frac{1}{2}e^2\eta^2A_\mu A^\mu}_{\text{interactions Higgs and gauge field}} \\ &- \underbrace{\lambda v\eta^3 - \frac{1}{4}\lambda\eta^4}_{\text{Higgs self-couplings}}\end{aligned} \tag{1.27}$$

In summary, the introduction of a complex scalar field, the *Higgs field*, that is subject to a potential that leads to spontaneous symmetry breaking, gives rise to a mass term for the gauge boson. Initially the gauge boson only has two polarisation states,

while three are required for massive particles. However, by a convenient choice of gauge, the Goldstone boson that appears in the Lagrangian may be absorbed by the gauge boson that in this way acquires a third polarisation state and becomes a true massive gauge boson. Finally, also a massive scalar boson appears in the Lagrangian as a consequence of spontaneous symmetry breaking and this boson is known as the Higgs boson. The Higgs boson manifests itself in couplings with the gauge boson as well as in self-couplings, as indicated in Eq. 1.27. Thus, in the end, the two degrees of freedom that were added through the introduced scalar field appear as the longitudinal polarisation of the gauge boson and as a massive scalar Higgs boson.

1.2.2 The Higgs mechanism in $SU(2)_L \otimes U(1)_Y$

The application of the Higgs mechanism to the electroweak theory that has been described in section 1.1.5 involves the generation of mass for three gauge bosons, W^+, W^+ and Z^0, while one gauge boson, the photon, should remain massless. The masses of the fermions are addressed later. Three degrees of freedom are needed to account for the longitudinal polarisation states of the massive bosons and hence a scalar field with sufficient degrees of freedom should be introduced into the theory. As the $SU(2)_L \otimes U(1)_Y$ symmetry of the electroweak Lagrangian needs to be reflected by the new field, it may either be defined as an isospin doublet or as a singlet. Since a singlet does not add sufficient degrees of freedom, the scalar field is chosen to be a doublet with weak isospin $I = \frac{1}{2}$ and hypercharge $Y = 1$:

$$\phi = \begin{pmatrix} \phi^+ \\ \phi^0 \end{pmatrix} = \frac{1}{\sqrt{2}} \begin{pmatrix} \phi_1 + i\phi_2 \\ \phi_3 + i\phi_4 \end{pmatrix} \tag{1.28}$$

The weak quantum numbers are chosen in a way that, according to the Gell-Mann - Nishijima formula, given by Eq. 1.15, the value of the electric charge, Q, is zero. A non-trivial value as will be readily apparent. The local gauge invariant Lagrangian for the new scalar field, including interactions with the four gauge fields that have been described in section 1.1.5, $W_\mu^{1,2,3}$ and B_μ, is given by:

$$\mathcal{L}_{\text{scalar}} = (D^\mu \phi)^\dagger (D_\mu \phi) - V(\phi) \tag{1.29}$$

with D_μ as defined as D_μ^L in Eq. 1.17. The expression for the potential $V(\phi)$ is yet again described by Eq. 1.21. However, it should be noted that as the scalar field represents an isospin doublet, the potential is now established in four-dimensional space and can no longer be visualised. Nevertheless, the potential still yields an infinite number of vacuum states with common vacuum expectation value $v = \sqrt{-\mu^2/\lambda}$. A convenient choice for the physical vacuum state is: $\phi_1 = \phi_2 = \phi_3 = 0$ and $\phi_3 = v/\sqrt{2}$. Thus the expression for the vacuum becomes:

$$\langle\phi\rangle_0 = \begin{pmatrix} 0 \\ v/\sqrt{2} \end{pmatrix} \tag{1.30}$$

The selection of one vacuum state breaks both the $U(1)_Y$ and $SU(2)_L$ symmetries of the vacuum, reflected by the fact that the local gauge transformations given by Eqs. 1.4 and 1.11 no longer leave the vacuum invariant.

To explore which new particles appear by the incorporation of the new scalar field, oscillations around the vacuum are performed. As this is now in four-dimensional space the perturbations are to be parametrised by four real fields: ξ^i with $i = 1, 2, 3$ and η . The subsequent perturbed scalar field is given by:

$$\phi = e^{\frac{i\xi^i\tau_i}{2v}} \begin{pmatrix} 0 \\ (v+\eta)/\sqrt{2} \end{pmatrix} \tag{1.31}$$

Thus, introducing the scalar field and perturbing it around the vacuum leads to the appearance of three ξ-particles and one η-particle. Yet again the ξ-particles result in non-physical interactions in the Lagrangian. Therefore, they are rotated away by expressing the theory in the unitary gauge, which yields the phase transformation:

$$\phi \to \phi' = e^{\frac{-i\xi^i\tau_i}{2v}}\phi = \frac{1}{\sqrt{2}} \begin{pmatrix} 0 \\ v+\eta \end{pmatrix} \tag{1.32}$$

The Lagrangian that is obtained by substitution of the perturbed field, ϕ', as given by Eq. 1.32 into Eq. 1.29 does not yet correspond to the physical situation. The Lagrangian involves bilinear terms in the gauge fields that do not have a physical interpretation and moreover, the gauge fields do not have quantum numbers that reflect the properties that the physical fields should have.

Physical interpretation

The theory is expressed in a basis of generators given by T_i and Y. This results in the mathematical gauge fields, W_μ^i and B_μ, which do not reflect the physical situation. For example, $W^{1,2,3}$ are indistinguishable while $W^\pm$ and Z^0 clearly differ in, for example, charge. As a consequence, these fields would not act upon an isospin doublet of quarks or leptons in the way one would expect.

Furthermore, looking closer at the breaking of the vacuum, it also becomes apparent that all four generators break the vacuum, which according to Goldstone's theorem results in four Goldstone bosons, while only three are needed. Nevertheless, one is free to rotate the basis of generators in such a way that a basis is obtained that includes one generator that leaves the vacuum invariant and leads to physical fields.

Without focusing on the basis of generators, one may find that physical fields are obtained by eliminating the bilinear terms in the Lagrangian. This can be done by diagonalising the matrix: $[\tau_1 W_\mu^1 + \tau_2 W_\mu^2 + \tau_3 W_\mu^3 + Y B_\mu]$. From this follows that a linear combination of W^1 and W^2 result in W^+ and W^-:

$$W^\pm = \frac{1}{\sqrt{2}}(W^1 \mp iW^2) \tag{1.33}$$

and mixing of W^3 and B^μ leads to the neutral gauge bosons Z_μ and the photon A_μ:

$$Z_\mu = \cos(\theta_W) W_\mu^3 - \sin(\theta_W) B_\mu \tag{1.34}$$

$$A_\mu = \sin(\theta_W) W_\mu^3 + \cos(\theta_W) B_\mu \tag{1.35}$$

where θ_W is the weak mixing angle, or Weinberg angle.

A different set of generators is associated with these physical fields. The basis is spanned by two linear combinations of $[\tau_1, \tau_2]$ and two linear combinations of $[\tau_3, Y]$. To make sure that the field A_μ should remain massless one linear combination has to leave the vacuum invariant. In general, a generator G leaves the vacuum invariant if:

$$e^{i\alpha G}\langle\phi\rangle_0 \simeq (1 + i\alpha G)\langle\phi\rangle_0 = \langle\phi\rangle_0 \tag{1.36}$$

This means that if $G\langle\phi\rangle_0 = 0$, the generator G does leave the vacuum invariant. It turns out that the linear combination of the generators τ_3 and Y has this property: $\frac{1}{2}(\tau_3 + Y)\langle\phi\rangle_0 = 0$ and according to the Gell-Mann - Nishijima formula this linear combination is equal to the electric charge. Consequently, $U(1)_{EM}$ is still a symmetry of the vacuum as Q is the generator of this group and hence, the photon remains massless.

When the Lagrangian as given by Eq. 1.29 is expressed in terms of the physical fields and the perturbed field ϕ' as given by Eq. 1.32, the final electroweak Lagrangian after symmetry breaking is obtained:

$$\mathcal{L}_H = \frac{1}{2}(\partial_\mu\eta)(\partial^\mu\eta) + (v+\eta)^2\left(\frac{g^2}{4}W_\mu^\dagger W^\mu + \frac{1}{8}(g^2+g'^2)Z_\mu Z^\mu\right) - \lambda v^2\eta^2 - \lambda v\eta^3 - \frac{1}{4}\eta^4 \tag{1.37}$$

In this representation of the electroweak theory the terms proportional to $V_\mu V^\mu$ can be recognised as mass terms for the gauge bosons, where $M_{W^+} = M_{W^-} = \frac{1}{2}vg$ and $M_{Z^0} = \frac{1}{2}v\sqrt{g^2+g'^2}$. Moreover, no such term is present for the A_μ field, indicating that the photon indeed remains massless. The massive gauge bosons acquired a third polarisation state when the theory was defined in the unitary gauge and hence the Goldstone bosons are absorbed by the gauge bosons.

As g and g' are free parameters the values of the masses of the gauge bosons are not predicted by the SM. Nevertheless, the ratio of $M_{W^\pm}$ and M_{Z^0} can be determined. Knowing that the photon couples to the electric charge e, the electroweak couplings can be related by: $e = g\sin(\theta_W) = g'\cos(\theta_W)$ and hence $\cos\theta_W = M_W/M_Z$. This ratio has been confirmed by the measurements of θ_W, M_Z and M_W [18].

Finally, one more particle, represented by η, appeared in the Lagrangian, which is the Higgs boson, appearing as a consequence of spontaneous symmetry breaking. Also for the Higgs boson a mass term is present, from which follows that the mass of the Higgs boson is: $M_{H^0} = \sqrt{2\lambda v^2}$. λ is another free parameter in the SM and therefore the value of the mass of the Higgs boson is not predicted.

In summary, with the introduction of a Higgs field with four degrees of freedom, along with a potential that induced spontaneous symmetry breaking a theory is obtained that involves three massive gauge bosons, the $W^{\pm}$ and Z^0 bosons, a massless photon and additionally a massive scalar Higgs boson with quadratic and quartic self-couplings. Also couplings between the gauge bosons and the Higgs boson are obtained. The Lagrangian that comprises all of this is a gauge invariant renormalisable Lorentz scalar, hence it represents a physical theory. The last step in the description of electroweak theory is the generation of mass for the fermions.

1.2.3 Fermion masses

The Higgs mechanism has initially been developed to generate massive gauge bosons, however, the method turned out to also be suitable to acquire massive fermions. Thus, as long as there is no experimental evidence for a fermiophobic Higgs boson, i.e. a Higgs boson that does not couple to quarks and leptons, it is assumed that the same mechanism is responsible for the generation of both boson and fermion masses.

The general expression for a fermion mass term, defined as $m\bar{\psi}\psi$, is not gauge invariant as the left-handed fermion fields transform as doublets while the right-handed fields transform as singlets. Therefore a rotation under $SU(2)_L \otimes U(1)_Y$ will break gauge invariance of the Lagrangian. However, if the mass term can be constructed such that it is a singlet under $U(1)$ as well as $SU(2)$ rotations, then mixing of left- and right-handed states will not occur and the expression for the mass term will be gauge invariant. It turns out that the mass term does have this property if it is redefined such that it contains a complex Higgs doublet. Hence, the gauge invariant fermion mass terms are of the form: $G_f \bar{\psi}_L \Phi \psi_R$ with G_f the so-called Yukawa coupling, $\bar{\psi}_L$ the left-handed fermion doublet, ψ_R the right-handed fermion singlet and with the Higgs field as defined in Eq. 1.28. The Lagrangian, involving such mass terms for both the leptons and quarks, yields:

$$\mathcal{L}_{\text{Yukawa}} = -G_l^{ij} \bar{L}_L^i \phi l_R^j - G_d^{ij} \bar{Q}_L^i \phi d_R^j - G_u^{ij} \bar{Q}_L^i \phi_C u_R^j + \text{hermitian conjugate} \quad (1.38)$$

where $\bar{L}_L^i$ and $\bar{Q}_L^i$ are the lepton and quark isospin doublets and l_R^j,d_R^j,u_R^j denote the isospin singlets for the charged leptons, the up-type quarks and the down-type quarks. For the leptons there is only one term, while there are two terms for the quarks, because it is assumed that there are no right-handed neutrinos and hence no neutrino singlets. The Yukawa couplings, G_f^{ij}, are matrices that define the coupling constants as well as the mixing between the three generations of quarks. The third term involves the charge-conjugate Higgs doublet, $\phi_C = i\sigma_2\phi^*$, in order to be able to acquire mass for the up-type quarks. The hermitian conjugate terms represent the expressions for the antiquarks and antileptons.

The Lagrangian, given in Eq. 1.38 appears to describe only *interactions* between the Higgs field and the fermions, while also mass terms should become apparent. This can once more be achieved by defining a potential that initiates spontaneous symmetry breaking. The same potential and gauge as in the previous section may be chosen, resulting in the same perturbed Higgs field, which is given in Eq. 1.32. When this field is substituted in the Lagrangian given by Eq. 1.38, terms that can be recognised as mass terms appear. Consequently, the Lagrangian for electrons and electron-neutrinos yields:

$$\begin{aligned}\mathcal{L}_{\text{electron}} &= -G_e\frac{1}{\sqrt{2}}\left[(\bar{\nu},\bar{e})_L\begin{pmatrix}0\\v+\eta\end{pmatrix}e_R + \bar{e}_R(0,v+\eta)\begin{pmatrix}\nu\\e\end{pmatrix}_L\right]\\ &= -\frac{G_e}{\sqrt{2}}v(\bar{e}_Le_R+\bar{e}_Re_L) - \frac{G_e}{\sqrt{2}}(\bar{e}_Le_R+\bar{e}_Re_L)\eta\\ &= -m_e\bar{e}e - \frac{m_e}{v}\bar{e}e\eta\end{aligned} \tag{1.39}$$

where the electron mass is equal to: $m_e = \frac{G_e v}{\sqrt{2}}$. The form of the Higgs doublet, which has been chosen in the context of generating mass for the vector bosons, also results in the neutrino remaining massless, as should be the case in the SM. The coupling between the Higgs boson and the electron is proportional to the electron mass, since the coupling strength is equal to $\frac{m_e}{v}$. This means that the lighter the fermion the weaker the interaction with the Higgs boson. The Lagrangian for the quarks is generated in the same way and yields similar mass and interaction terms. Like the gauge boson masses, also the fermion masses are not predicted, since the Yukawa couplings, G_f, yield free parameters.

The final and complete Lagrangian for the electroweak theory may be defined as:

$$\mathcal{L} = \mathcal{L}_{EW} + \mathcal{L}_{H} + \mathcal{L}_{\text{Yukawa}} \tag{1.40}$$

where the massless electroweak Lagrangian, the scalar Lagrangian and the Yukawa Lagrangian are given by Eqs. 1.18, 1.37 and 1.38 respectively. To acquire the complete SM Lagrangian one would need to add a term to the Lagrangian resembling the strong interaction, $\mathcal{L}_{QCD}$. The derivation of the Lagrangian for strong interaction may be found in e.g. Ref. [14].

1.3 The spin and parity of the SM Higgs boson

The Standard Model that has been formulated in the previous sections, gives predictions for all properties and quantum numbers of the the SM Higgs boson, except for its mass: the SM Higgs boson is an electrical neutral, positive parity, massive, elementary particle of spin-0, and its coupling to other particles, self coupling, cross section and decay width as a function of its mass are fixed. The two quantum numbers that are evaluated in this thesis are the spin and parity of the discovered Higgs-like boson. In this section, these quantum numbers and their effect on the experimental signature of the Higgs boson decay are discussed.

The spin of an elementary particle is identified with the quantum angular momentum that cannot be accounted for with orbital angular momentum, where the latter is the quantum mechanical equivalent of classical angular momentum. Spin is a fundamental property of the elementary particles, where all fermions have spin-$\frac{1}{2}$ and the vector bosons have spin-1. The hypothetical graviton is predicted to have spin-2. The projection of spin onto the direction of motion of a particle is called helicity. The helicity, S_i, determined along the i-axis ($i = x, y, z$), is quantised and can take values: $S_i \in \{-s, -(s-1), ..., s-1, s\}$, with s the spin of the particle. Thus fermions can be in helicity state $\pm\frac{1}{2}$ and the vector bosons can be in helicity states -1, 0 or $+1$.

From the SM Lagrangian follows that the SM Higgs boson must have zero spin. This can also be conceptually understood in the context of mass being a Lorentz

invariant property of elementary particles. If the Higgs boson would have spin it would transform as a vector or tensor when going from one reference frame to another, resulting in mass not being generated in a uniform way. Consequently, the mass of a particle would depend on the reference frame in which it is measured. Therefore, the only allowed spin for a Higgs boson is spin-0.

The parity of a particle reflects the effect of spatial inversion of the wave function of a particle and can either be positive or negative. Positive parity indicates that the wave function is invariant under a spatial inversion, while negative parity indicates that the wave function changes sign under spatial inversion. Parity is often linked to charge conjugation in the context of CP violation. CP symmetry states that the laws of physics are invariant under consecutively applying a charge conjugation transformation and a parity transformation. However, CP violation occurs, for example in the mixing of quarks through an imaginary phase that appears in the CKM matrix. In the context of the SM Higgs boson the notions of parity and CP are often used interchangeably since the SM Higgs boson is electrically neutral and as such a charge conjugation transformation does leave the Higgs boson invariant. There are plausible extensions of the SM in the form of two Higgs doublet models that predict the existence of a CP-odd Higgs boson aside from a CP-even Higgs boson [29]. Therefore the measurement of the parity of the observed signal is an important test of these extended models.

The spin and parity of the discovered Higgs-like boson can be evaluated by means of the signature of the final state. The final state of the SM Higgs decay under study consists of two oppositely charged leptons and two neutrinos, that emanate from two W-bosons of opposite charge. In order to conserve the angular momentum in the event, the W-bosons and therefore also the final state particles have a certain configuration. The helicity of the W-bosons, being spin-1 particles, can take three different values: -1, 0 and +1. Given the spin-0 nature of the Higgs boson, there are three possible helicity combinations for the two W-bosons that conserve the angular momentum: (+1,+1), (-1,-1) and (0,0). Additionally, the V-A structure of the weak interaction, which is responsible for the decay of the W-bosons into the leptons and neutrinos, imposes that the neutrinos occur only as left handed particles, i.e. in a negative helicity state, and antineutrinos in a positive helicity state. This results in the two leptons in the final state mostly being emitted in the same direction, as

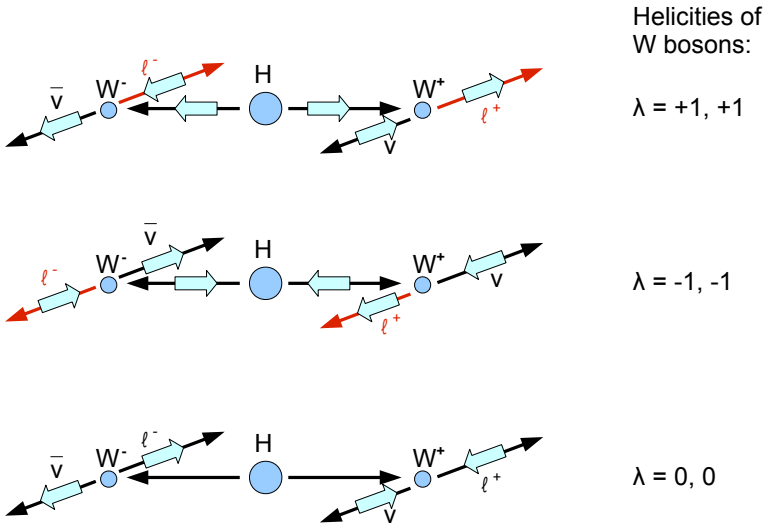

Figure 1.4: *Schematic diagrams of the allowed SM Higgs boson decays into two leptonically decaying W-bosons in the Higgs rest frame. Three combinations of the helicity states of the W-bosons are possible: both positive (upper diagram), both negative (middle diagram) and both zero (lower diagram). This affects the configuration of the final state particles. The bold blue arrows indicate the helicity of the particles and the black long arrows the direction of motion of the particles. [30].*

shown in figure 1.4. Only when both W-bosons are in a zero helicity state, there is no preferential direction for the leptons as a result of conservation of angular momentum.

This specific configuration of the leptons is only present when the original particle is a scalar. Would the original particle be a particle with spin-1 or spin-2, then the configuration of the final state particles would be different. In a more subtle way also the parity of the Higgs-like boson affects the kinematical properties of the final state particles. Thus, the spin and parity of the observed signal can be evaluated by means of the observables of the two leptons. The observable that is most sensitive to the spin of the Higgs-like boson is the angle in the transverse plane between the leptons, referred to as $\Delta\phi_{\ell\ell}$, which tends to be small for Higgs boson decays. This leads also to smaller values of the invariant mass of the dilepton pair, $M_{\ell\ell}$, which is therefore also a spin sensitive observable, and defined as:

$$\begin{aligned} M_{\ell\ell} &= \sqrt{(E_{l1}+E_{l2})^2+(\vec{p}_{l1}+\vec{p}_{l2})^2} \\ &= E_{l1}^2-\vec{p}_{l1}^{\,2}+E_{l2}^2-\vec{p}_{l2}^{\,2}+2E_{l1}E_{l2}-2|\vec{p}_{l1}||\vec{p}_{l2}|\cos(\Delta\psi_{\ell\ell}) \\ &\simeq 2E_{l1}E_{l2}(1-\cos(\Delta\psi_{\ell\ell})) \end{aligned} \tag{1.41}$$

The latter equality holds for $m_{l_{1,2}} << E_{l_{1,2}}$, which is the case for the events under study. The angle $\Delta\psi_{\ell\ell}$ is the three-dimensional opening angle between the leptons. Hence, if the observed signal is that of a spin-0 boson, $M_{\ell\ell}$ tends to be smaller. The $\Delta\phi_{\ell\ell}$ and $M_{\ell\ell}$ observables will play an important role in the analysis of the spin and parity of the Higgs-like boson.

1.4 Alternative hypotheses for the observed signal

In the previous sections it has been shown that the Standard Model is a renormalisable and complete field theory that is in principle valid up to any energy scale. The Standard Model can however be expanded by introduction of new particles, for example in terms of an extended Higgs sector. It is even possible to formulate an extended complete theory that is again renormalisable, like the minimal supersymmetric extension of the SM. However, if one just wants to test how a new particle would behave in the context of the SM, it is also possible to use an effective field theory (EFT). This is a theory that is valid up to a certain energy scale Λ, where it is assumed that no other new particles than the introduced one are present below this cutoff scale. Possible new physics above Λ is disregarded and as such an EFT is not a complete theory. It is however a perfect tool to study alternative hypotheses for the observed signal, without the necessity to develop a complete and consistent field theory.

The Higgs characterisation model [95] is a model that is developed to study and model alternative hypotheses for the observed signal, following an EFT approach. The effective Lagrangian is represented by the SM Lagrangian, excluding the Higgs boson itself, plus a new bosonic state with a mass of 125 GeV that can couple to the SM particles via interactions of the lowest possible dimensions. The beyond the Standard Model (BSM) couplings and parameters introduced in the effective

Lagrangian can be adapted such that the preferred alternative bosons and associated couplings are obtained. If the parameters are set in accordance with a CP-even scalar with SM couplings, and all the BSM parameters are set to zero, the SM Lagrangian is retrieved. For the analysis presented in this chapter the cutoff scale is set to 1 TeV, which is in line with the experimental results of the LHC and other colliders that show no evidence for new physics at a lower energy scale.

There are many hypotheses possible for the observed signal, and even within fixed spin and CP hypotheses different models for the alternative bosons are conceivable. Therefore, for each spin and CP hypothesis, a choice for a specific model has to be made, where the most general or substantiated model is preferred. Only the bosons with $J_{CP} = 0^-, 1^+, 1^-, 2^+$ are considered, since these are the most likely alternative hypotheses. If these fixed hypotheses are excluded, more subtle models with different couplings and properties, may be studied. In the following, the effective Lagrangians and associated couplings that represent the relevant alternative hypotheses are described. For more information about the formulation of these Lagrangians, see Refs. [95, 96].

1.4.1 Spin-0

There are several BSM theories that consider the existence of an additional CP-odd Higgs boson and possible mixing between the CP-even and CP-odd Higgs bosons. This mixing would imply CP violation in the Higgs sector that is large enough to account for the imbalance of matter and antimatter in the universe. The two Higgs-doublet models (2HDM) [29] and the minimal supersymmetric Standard Model (MSSM) [97] are examples of theories that include both a CP-even and a CP-odd Higgs-like boson.

The Lagrangian that is formulated to describe a spin-0 Higgs-like boson is formulated such that when the SM couplings are inserted and a CP-even state is assumed, the SM Higgs boson is retrieved. BSM effects are introduced in the most general way: the CP-odd boson couples to the SM particles in the same way as the SM Higgs boson does, while additional BSM effects are included by means of interactions with SM particles via higher-dimensional operators. The coupling of the spin-0 boson, X_0, with two W-bosons, as well as the interaction with fermions is taken into account. The coupling with fermions has to be included, given that the production of the X_0-boson

through gluon gluon fusion goes via a top quark loop. The $q\bar{q}$ production process is not considered, as its contribution is negligible compared to ggF. The effective Lagrangian that describes the coupling of a spin-0 boson to W-bosons is given by:

$$\begin{aligned}\mathcal{L}_0^W =&\{c_\alpha \kappa_{\mathrm{SM}} g_{\mathrm{HWW}} W_\mu^+ W^{-\mu} \\ &- \frac{1}{2}\frac{1}{\Lambda}[c_\alpha \kappa_{\mathrm{HWW}} W_{\mu\nu}^+ W^{-\mu\nu} + s_\alpha \kappa_{\mathrm{AWW}} W_{\mu\nu}^+ W^{-\mu\nu}] \\ &- \frac{1}{\Lambda} c_\alpha \kappa_{\mathrm{H}\partial\mathrm{W}} (W_\nu^+ \partial_\mu W^{-\mu\nu} + h.c.)\} X_0\end{aligned} \tag{1.42}$$

where $W_{\mu\nu} = \partial_\mu W_\nu - \partial_\nu W_\mu$ and $\tilde{W}_{\mu\nu} = \frac{1}{2}\epsilon_{\mu\nu\rho\sigma} W^{\rho\sigma}$. The dimensionless real coupling parameters κ_i are used to introduce BSM effects. The κ_{SM} may be set to a value other than 1 to introduce deviations in the SM coupling of the Higgs boson to W-bosons, g_{HWW}. The κ_{HWW} and κ_{AWW} appear in the higher dimensional terms and are the CP-even and CP-odd BSM coupling parameters. The $\kappa_{\mathrm{H}\partial\mathrm{W}}$ is a derivative operator that is related to contact operators that are discussed in Refs. [98, 99]. The contributions of the CP-even and CP-odd terms are set with $c_\alpha \equiv \cos(\alpha)$ and $s_\alpha \equiv \sin(\alpha)$ respectively, where α denotes the CP mixing angle.

The effective Lagrangian that describes the interaction of a spin-0 boson with the third generation of fermions is given by:

$$\mathcal{L}_0^f = \sum_{f=t,b,\tau} \psi_f^\dagger (\kappa_{\mathrm{SM}} g_{\mathrm{SM}} + c_\alpha \kappa_{\mathrm{H}ff} g_{\mathrm{H}ff} + i s_\alpha \kappa_{\mathrm{A}ff} g_{\mathrm{A}ff} \gamma_5) \psi_f X_0 \tag{1.43}$$

where $\kappa_{\mathrm{H}ff}$ and $\kappa_{\mathrm{A}ff}$ denote the BSM coupling parameters and $g_{\mathrm{H}ff}$ and $g_{\mathrm{A}ff}$ the BSM couplings, of respectively a CP-even and a CP-odd boson in the SM model. Table 1.1 lists the settings of the parameters used to obtain the SM CP-even and BSM CP-odd spin-0 bosons.

1.4.2 Spin-1

The Higgs-like signal is also observed in the $H \to \gamma\gamma$ decay channel and since the Yang-Landau theorem [100, 101] states that a massive spin-1 particle cannot couple

$\mathbf{J^{CP}}$	**Coupling parameters**		
0^+	$\kappa_{\mathrm{SM}} = 1, \kappa_{\mathrm{HWW}} = 0, \kappa_{\mathrm{AWW}} = 0$	$c_\alpha = 1,\ s_\alpha = 0$	$\kappa_{\mathrm{H}ff} = \kappa_{\mathrm{A}ff} = 0$
0^-	$\kappa_{\mathrm{SM}} = 1, \kappa_{\mathrm{HWW}} = 0, \kappa_{\mathrm{AWW}} = 1$	$c_\alpha = 0,\ s_\alpha = 1$	$\kappa_{\mathrm{H}ff} = 0, \kappa_{\mathrm{A}ff} = 1$

Table 1.1: *The settings used to model a SM CP-even and BSM CP-odd spin-0 boson. An explanation of the used notation is given in the text.*

to two massless spin-1 particles, this suggests that the observed signal cannot be of a spin-1 particle. Nevertheless, the case that the observed signal comes from two resonances with similar masses, where one of these gives rise to the events with two photons in the final state cannot be excluded a priori. Therefore the hypothesis of a spin-1 boson is still considered. There are several interpretations of such a spin-1 boson possible, for example in the context of BSM theories that predict the existence of additional Z prime bosons. However there is no well-substantiated model that is awaiting the discovery of a vector boson with a mass of around 125 GeV.

The effective Lagrangian for a spin-1 boson, X_1, with positive or negative parity, is constructed by taking into account the most general interactions of a neutral spin-1 boson, like the Z-boson, with the SM particles, where only those with the lowest canonical dimensions are considered. Furthermore, only production through $q\bar{q}$ annihilation is taken into account, as the Yang-Landau theorem excludes also production of an X_1-boson through ggF. The interaction of a spin-1 boson with two W-bosons is described in analogy with the coupling of a Z-boson to W-bosons. The following effective Lagrangian is obtained:

$$\begin{aligned}\mathcal{L}_1^W =& i\kappa_{\mathrm{W1}} g_{\mathrm{WWZ}} (W^+_{\mu\nu} W^{-\mu} - W^-_{\mu\nu} W^{+\mu}) X_1^\nu + i\kappa_{\mathrm{W2}} g_{\mathrm{WWZ}} W^+_\mu W^-_\nu X_1^{\mu\nu} \\ & - \kappa_{\mathrm{W3}} W^+_\mu W^-_\nu (\partial^\mu X_1^\nu + \partial^\nu X_1^\mu) \\ & + i\kappa_{\mathrm{W4}} W^+_\mu W^-_\nu \tilde{X}^{\mu\nu} - \kappa_{\mathrm{W5}} \epsilon_{\mu\nu\rho\sigma} [W^{+\mu} (\partial^\rho W^{-\nu}) - (\partial^\rho W^{+\mu}) W^{-\nu}] X_1^\sigma\end{aligned} \tag{1.44}$$

where $g_{\mathrm{WWZ}} = -e \cot\theta_W$ is the coupling constant of the interaction of two W-bosons with the spin-1 boson. The coupling parameters κ_{W1} to κ_{W5} are used to fix the strength of the various BSM couplings. The Lagrangian that describes the coupling to fermions is given by:

J^{CP}	Coupling parameters		
1^+	$\kappa_{f_a,f_b} \neq 0$	$\kappa_{\mathrm{W}1} = \kappa_{\mathrm{W}2} = \kappa_{\mathrm{W}4} = \kappa_{\mathrm{W}5} = 0$	$\kappa_{\mathrm{W}3} = 1$
1^-	$\kappa_{f_a,f_b} \neq 0$	$\kappa_{\mathrm{W}1} = \kappa_{\mathrm{W}2} = \kappa_{\mathrm{W}3} = \kappa_{\mathrm{W}4} = 0$	$\kappa_{\mathrm{W}5} = 1$

Table 1.2: *The settings of the coupling parameters with which a CP-even and CP-odd spin-1 boson can be described.*

$$\mathcal{L}_1^f = \sum_{f=l,q} \bar{\psi}_f \gamma_\mu (\kappa_{f_a} a_f - \kappa_{f_b} b_f \gamma_5) \psi_f X_1^\mu \tag{1.45}$$

with a_f and b_f the SM vector and axial vector couplings, as defined in [95]. Table 1.2 lists the settings of the parameters to obtain a CP-even and a CP-odd spin-1 boson.

1.4.3 Spin-2

There exist a large number of possible models for a spin-2 boson. The chosen model describes a graviton-like tensor [102] that is minimally coupled to SM particles, since it is expected that exclusion of such a spin-2 boson automatically also excludes spin-2 bosons with stronger couplings to the SM particles. The alternative hypothesis of a CP-odd spin-2 boson is not considered as this hypothesis has even less theoretical foundation than its CP-even equivalent. The effective Lagrangian for a minimally coupled CP-even spin-2 boson, $X_2^{\mu\nu}$, to fermions and bosons is given by:

$$\mathcal{L}_2^p = \sum_{p=V,f} -\frac{1}{\Lambda} \kappa_p T_{\mu\nu}^p X_2^{\mu\nu} \tag{1.46}$$

with $T_{\mu\nu}^p$ the energy-momentum tensor. The production of a spin-2 boson can go via gluon gluon fusion or $q\bar{q}$ annihilation, but, when higher order QCD corrections are included, there is no prediction for the ratio between these two production mechanisms. Therefore various fractions of the two production processes are explored by testing different settings of the parameters κ_g and κ_q.

At LO the $q\bar{q}$ and ggF processes are independent, but at NLO, processes with contributions of both κ_g and κ_q enter the model, which gives rise to a term proportional to $(\kappa_q - \kappa_g)^2$ that grows with $\sqrt{s}^2$ of the hard process as $s^3/m^4\Lambda^2$. This would lead

$\mathbf{J^{CP}}$	Coupling parameters		$\mathbf{p_T^H}$ cutoff
2^+	$\kappa_g = 1$	$\kappa_q = 1$	
2^+	$\kappa_g = 1$	$\kappa_q = 0$	$p_T^H < 125$ GeV
2^+	$\kappa_g = 1$	$\kappa_q = 0$	$p_T^H < 300$ GeV
2^+	$\kappa_g = 0.5$	$\kappa_q = 1$	$p_T^H < 125$ GeV
2^+	$\kappa_g = 0.5$	$\kappa_q = 1$	$p_T^H < 300$ GeV

Table 1.3: *The different settings of the coupling parameters, used to model a CP-even spin-2 boson via different ratios of the two production mechanisms.*

to unitarity violation if no cutoff scale Λ would be introduced. Moreover, in the 1-jet channel this effect leads to a large tail at high values of the Higgs p_T spectrum, which affects some of the spin sensitive variables. According to the definition of an EFT, at a scale Λ new physics appears that would correct the unitarity violation behaviour below Λ, which would therefore also correct the Higgs p_T spectrum. It is however unknown at which p_T scale the EFT would be corrected by new physics. This means that it is not known up to which value the calculations of the Higgs p_T spectrum are valid. Therefore, the spin-2 model is evaluated at two different cutoffs of the Higgs p_T spectrum that are both below Λ. The first one is set to $p_T^H = 300$ GeV, since no events with a p_T^H over this value would normally be expected. The second tested cutoff is set to 125 GeV, since this is the lowest possible value of Λ and thus the lowest value up to which the EFT could possibly be valid.

A total of five different models are tested for the spin-2 hypothesis, consisting of different settings for κ_g, κ_q and the Higgs p_T cutoff. The parameters set for the different hypotheses are listed in table 1.3. The hypothesis with $\kappa_g = \kappa_q = 1$, also referred to as the universal couplings model, corresponds to production fractions of 96% ggF and 4% $q\bar{q}$. It is the hypothesis that does not suffer from the unitarity violating behaviour and as such does not require a p_T cutoff. The other hypotheses, with non universal couplings, are tested for the two p_T^H cutoffs. The case where $\kappa_g = 1$ and $\kappa_q = 0$ corresponds to 100% ggF. It would be logical to consider additionally the case where $\kappa_g = 0$ and $\kappa_q = 1$, however, there are problems with the modelling of the Higgs p_T distribution for this hypothesis, as is shown in Ref. [103]. Therefore, the hypothesis with $\kappa_g = 0.5$ and $\kappa_q = 1$ is tested instead, which corresponds to 14% ggF and 86% $q\bar{q}$. When in the remainder of this thesis the spin-2 signal is discussed, this

is done for the signal generated with $\kappa_g = \kappa_q = 1$. The final results are nevertheless generated for all models.

To test the predictions given by the Standard Model, as well as by the models corresponding to the effective Lagrangians, events will be simulated according to these theoretical predictions and subsequently compared to real collision data. In this way experimental foundation for the theory may be obtained. First, the experimental setup that is used to acquire data is described in the next chapter.

Chapter 2

The Large Hadron Collider and the ATLAS detector

The discovery and study of heavy particles, like the Higgs boson, requires highly energetic particle collisions of which the final state particles can be measured with high precision. For this purpose the Large Hadron Collider and the ATLAS detector have been built. In this chapter, this experimental setup and its performance are presented.

2.1 The Large Hadron Collider

The Large Hadron Collider (LHC) is today's largest and most powerful particle accelerator [31]. It is a 27 km long circular collider that is designed to collide beams of protons with a centre-of-mass energy of 14 TeV. The LHC is located at CERN, the laboratory of the European Organisation for Nuclear Research, and placed approximately 100 m underground in the tunnel that previously harboured the Large Electron Proton collider. The concept of the LHC was officially approved in 1984. Ten years later its construction was given green light, which ensued from 1998 to 2009. The LHC has had successful operations from 2010 to 2012 at centre-of-mass energies

of 7 and 8 TeV. In 2013 and 2014 the LHC has been closed to allow for upgrades that will enable operations at design energy. The experimental program of the LHC continues from 2015 onwards.

2.1.1 Objectives

The primary objective to build the LHC is to search for physics processes with small cross sections and high mass. This requires high luminosity beams as well as a high centre-of-mass energy of the collisions, as these parameters determine the production rate of a physics process. The production rate, R, of a process with cross section σ is described by: $R = L\sigma(\sqrt{s})$, with L the instantaneous luminosity and σ depending on the centre-of-mass energy $\sqrt{s}$, as well as on the specific process.

The centre-of-mass energy is equal to the sum of the energies of the proton beams. The design value is $\sqrt{s} = 14$ TeV, which is much larger than the $\sqrt{s} = 1.96$ TeV at which Tevatron, being the previous largest accelerator, operated up to 2012. The centre-of-mass energy depends on the energy of the protons and requires an accelerator capable of accelerating the protons to near the speed of light, while keeping the proton beams within their trajectories.

The instantaneous luminosity depends on the beam parameters and can be written as:

$$L = \frac{f_{\text{rev}}\, N_b\, n_p^2}{4\pi\, \sigma_T^2} \tag{2.1}$$

where f_{rev} is the revolution frequency, N_b is the number of bunches per beam, n_p is the number of protons per bunch and σ_T is the transverse beam size at the interaction point. In order to allow for high instantaneous luminosity, both the design of the LHC and its operations have been focussed on optimising the beam parameters. In table 2.1 the design values of the primary beam parameters are given, as well as the values used during the three years of operations. Ultimately, the LHC will operate with $L = 10^{34}$ cm^{-2}s^{-1}.

Beam parameter	**2010**	**2011**	**2012**	**Design**
Centre-of-mass energy [TeV]	7	7	8	14
Instant. luminosity [$\mathrm{cm}^{-2}\mathrm{s}^{-1}$]	2.07×10^{32}	3.65×10^{33}	7.73×10^{33}	10^{34}
Protons per bunch ($\times 10^{11}$)	$0.1 - 1.2$	$0.6 - 1.2$	$1.6 - 1.7$	1.15
Number of bunches	$1 - 348$	$200 - 1380$	1380	2808
Bunch spacing [ns]	≥ 150	75/50	50	25
Av. collisions per bunch crossing	≤ 3	9.1	20.7	22

Table 2.1: *Overview of the beam parameters used during the first three years of LHC operations and compared to the design values at which the LHC will ultimately operate [32].*

These unprecedented values for the luminosity and energy require an accelerator with excellent performance in bending, accelerating and focussing of the proton beams. This largely directs the design of the LHC.

2.1.2 Design

In figure 2.1 a schematic overview of the accelerator complex is shown. The protons, obtained by ionising hydrogen atoms, are first accelerated to an energy of 450 GeV by a chain of pre-accelerators: first to an energy of 50 MeV by the Linear Accelerator (LINAC), then to 1.14 GeV in the Proton Synchrotron Booster (PSB); to 26 GeV in the Proton Synchrotron (PS); and finally to 450 GeV in the Super Proton Synchrotron (SPS). Subsequently, bunches of protons are injected in the LHC at set time intervals to acquire two proton beams with opposite directions, that consist of a fixed number of bunches with set bunch spacing.

In the LHC the proton beams travel in opposite directions through two separate vacuum beam pipes that are situated within the same iron yoke. The iron yoke also holds the multipoles that provide the magnetic fields that are used to focus and bend the proton beams. More than 1200 superconductive dipole magnets, providing a magnetic field of 8.3 T, are used to bend the protons along the LHC ring, while quadrupole magnets focus the beams. Yet higher multipoles are used to make corrections to the paths of the beams. To allow for the high magnetic field strength, the magnets are superconducting and cooled with helium to a temperature as low as 1.9 K.

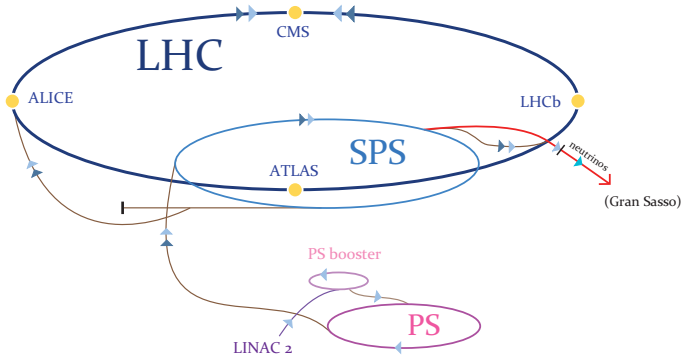

Figure 2.1: *The accelerator complex at CERN, consisting of pre-accelerators and the LHC. The four main detectors are indicated [33].*

The protons are accelerated to their required energy by superconductive radio frequency (RF) cavities that are situated at one point along the LHC ring. These electromagnetic resonators effectuate an accelerating field of 5 MV/m. A total of eight cavities per beam are used to accelerate the protons from the injection energy of 450 GeV to the ultimate design energy of 7 TeV. Once the beams are ramped to the required energy, the cavities guarantee a constant energy, and a fixed bunch structure within the proton beams. The process from injection to obtaining stable beams takes approximately 15 minutes.

At four points along the LHC the two beam pipes intersect to allow for collisions. At these interaction points the major experiments are located. These involve two general purpose detectors, ATLAS and CMS, that are designed to study a large variety of physics processes. There are specifically two general purpose detectors in order to have independent cross checks of physics results. Additionally, there are two detectors that are dedicated to measure more specific physics processes: LHCb focusses primarily on the study of B-mesons and on CP violation in hadron decays, while ALICE is devoted to the study of the quark-gluon plasma, to which end also periods of lead-ion collisions are included in the LHC program.

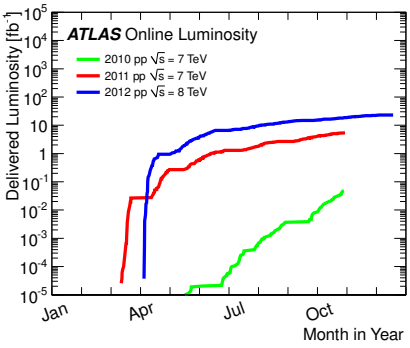

Figure 2.2: *The total luminosity delivered by the LHC to ATLAS in 2010, 2011 and 2012. The y-axis has a logarithmic scale [35].*

2.1.3 Operations and performance

Thus far, the LHC has had three years of operations, referred to as Run I, in 2010 and 2011 at $\sqrt{s} = 7$ TeV and in 2012 at $\sqrt{s} = 8$ TeV [32, 34]. The first year was mainly devoted to commissioning, gaining understanding of the machine and establishing confidence in the performance of the protection system. In 2011 beam parameters, like the bunch spacing, were explored and pushed to higher levels, allowing for an increase of instantaneous luminosity. Essentially, 2012 had as main objective to accumulate data. The beam parameters used in the three years of operations are listed in table 2.1. In 2012 yet 36% of the total time scheduled for physics was spent in stable beams, which is encouraging given that this was only the third year of operations.

The performance of the LHC is reflected in the amount of accumulated data, which is defined as the instantaneous luminosity integrated over time: $L = \int \mathcal{L} dt$. The integrated luminosity is expressed in units of inverse barns, where 1 barn $= 1 \times 10^{-28}$ m^2. Figure 2.2 shows the luminosity delivered by the LHC in 2010, 2011 and 2012, which yields 48.1 pb^{-1}, 5.46 fb^{-1} and 22.8 fb^{-1} respectively. Considering that the total integrated luminosity delivered by the LHC has been sufficient to discover a Higgs-like boson, the first three years of LHC operations have been very successful.

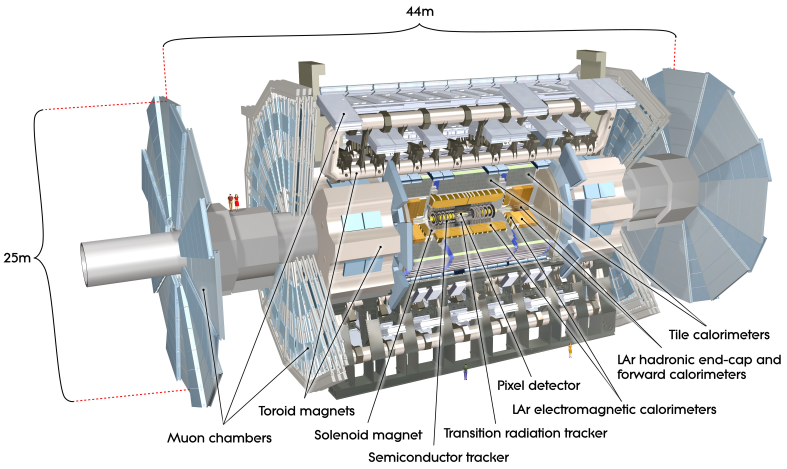

Figure 2.3: *Cut-away view of the ATLAS detector. The dimensions of the detector are 25 m in height and 44 m in length. The weight of the detector is approximately 7000 tonnes.*

2.2 The ATLAS detector

The energy and luminosity of the pp collisions that the LHC will ultimately deliver, require a detector able to cope with high interaction rates, radiation doses, and particle multiplicities and energies. Furthermore, the physics objectives of the ATLAS detector, being precision measurements of known processes and searches for new physics, require sensitivity to a wide variety of final state signatures. These requirements dictate the design of the ATLAS (A Toroidal LHC AparatuS) detector.

The ATLAS detector is forward-backward symmetric with respect to the interaction point, and its geometry is defined by four different detector systems and two magnet systems [36, 37]. The design aims for almost hermetic coverage to avoid that particles escape detection. Figure 2.2 shows a cut-away view of the ATLAS detector. From inside out the main subdetectors are: the inner detector, the electromagnetic calorimeter, the hadronic calorimeter and the muon spectrometer.

The inner detector allows for the tracking of charged particles and vertex reconstruction, while the calorimeters and the muon spectrometer are used for particle identification and high precision momentum and energy measurements. In this way,

electrons, muons, photons, jets and transverse missing energy can be reconstructed. The two magnet systems allow for momentum measurements of charged particles. To deal with the high particle flux, the subdetectors are of high granularity and have fast read-out systems. Furthermore, the high interaction rate requires a fast and efficient trigger on interesting events, in order to reduce the incoming data rates to an acceptable level.

After an explanation of the ATLAS coordinate system, the subdetectors and trigger system are discussed in more detail. This chapter is completed with an overview of ATLAS operations.

Coordinate system

To describe the detector and objects within the detector, a right-handed coordinate system is used, as shown in figure 2.4, with the nominal interaction point of ATLAS at its origin. The z-axis is defined along the beam line, with the positive z-axis pointing in the anticlockwise direction. The x-y plane, or transverse plane, is the plane perpendicular to the z-axis; with the x-axis pointing horizontally towards the centre of the LHC, and the y-axis pointing upwards, being perpendicular to the x- and z-axis. Sometimes also the r-axis is used, which is defined in the transverse plane as: $r = \sqrt{x^2 + y^2}$.

Two angles are used to describe directions in the detector. The azimuthal angle ϕ is measured as the angle with the positive x-axis in the x-y plane, going from 0 to π for $y > 0$ and from 0 to $-\pi$ for $y < 0$. The polar angle θ measures the angle with the positive z-axis in the r-z plane, and ascends from 0 to π.

More often than θ the pseudorapidity, η, is used, which is defined as: $\eta = -\ln[\tan(\frac{\theta}{2})]$. The pseudorapidity is the preferred measure to define positions in the detector, since particle production is approximately constant in units of η. In terms of the pseudorapidity, the detector can be divided in several regions. The central region is called the barrel and extends up to $|\eta| \simeq 1.4$. The barrel is extended on both sides with two end-caps that approximately cover the regions $1.6 < |\eta| < 2.7$. Furthermore, there are two forward regions that extend up to $|\eta| \simeq 4.9$.

Finally, the opening radius between two objects is defined as: $\Delta R = \sqrt{\Delta\phi^2 + \Delta\eta^2}$.

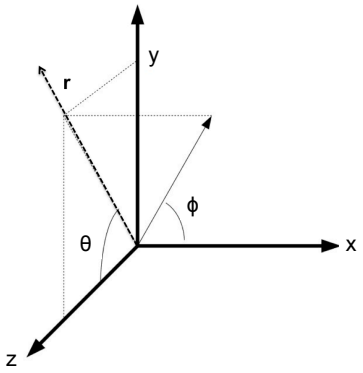

Figure 2.4: *Definition of the right-handed coordinate systems used to define positions and directions in the ATLAS detector. The z-axis points along the beam pipe in the anti-clockwise direction and the x-axis points towards the centre of the LHC. The azimuthal angle, ϕ, is defined in the x-y plane and, and the polar angle, θ, in the r-z plane.*

2.2.1 The inner detector

The inner detector is closest to the beam axis and provides information on particles with $|\eta| < 2.5$ and $p_T > 100$ MeV. Its objective is the reconstruction of the tracks of charged particles, to enable momentum, charge and direction measurements, and to identify the vertices of an event. The curvature of the tracks is provided by a 2 T magnetic field that is generated by the superconducting solenoid magnet system surrounding the inner detector.

The design resolution of momentum measurements with the inner detector is $\sigma_{p_T}/p_T = 0.05\%\ p_T \oplus 1\%$, with p_T in GeV. To achieve this high resolution, very fine detector granularity is required in order to obtain sufficient measurement points; while the amount of material should be kept to a minimal, in order to prevent energy loss and scattering of particles. Furthermore, due to its position, the inner detector has to deal with high radiation rates: around 1000 particles cross the inner detector every 25 ns. To meet the requirements, the inner detector consists of three separate detection systems: a pixel detector, a silicon strip Semi Conductor Tracker (SCT) and a Transition Radiation Tracker (TRT), as is depicted in figure 2.5.

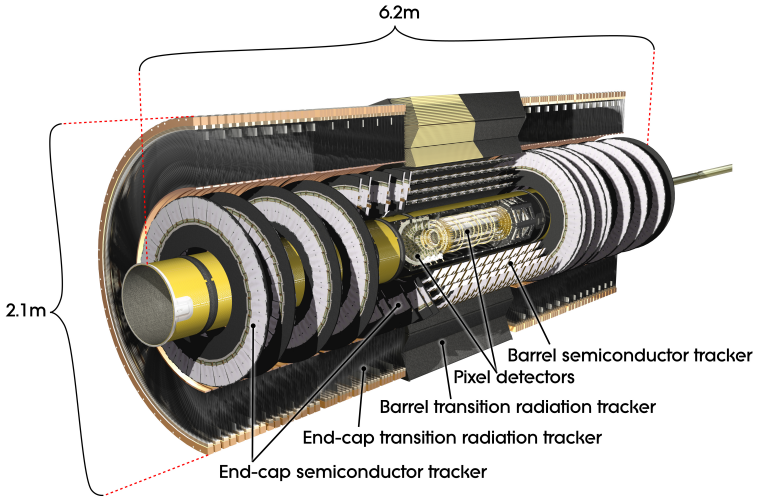

Figure 2.5: *Cut-away view of the inner detector. The subdetectors are indicated.*

The pixel detector

The pixel detector is made of silicon based pixel sensors, as this material is resistant to the high radiation rates. The barrel consists of three concentric layers around the beam line at radii of approximately 5, 9 and 12 cm, while the end-caps are formed by three discs. This construction provides three measurements in three-dimensions. The 1744 pixel sensors, being $50 \times 400\,\mu\text{m}^2$ in size, are operated as follows: a voltage of 150 V ensures that the silicon is depleted of electrons, such that particles traversing the depleted region induce a current that can be measured by the read-out electronics. To cope with the high particle multiplicities and allow for vertex reconstruction, each sensor has a spatial resolution of $10\,\mu$m in $(r - \phi)$ and $115\,\mu$m in z.

The SCT

The SCT surrounds the pixel detector and, being silicon based, relies on a a similar technology as the pixel detector. The SCT consists of four layers, both in the barrel and in the end-caps. The 4088 modules that form the SCT are composed of up to four silicon strip sensors of 6×6 cm each. Every sensor provides a two-dimensional measurement and by placing two sensors on top of each other under an angle of 40

mrad, three-dimensional space points are obtained. This construction results in an average of eight hits per track, or four space points, with a spatial resolution of 17 μm in $(r - \phi)$ and 580 μm in z.

The TRT

The TRT occupies the outermost layer of the inner detector, between radii of 55 and 108 cm. It consists of gaseous drift straw tubes that cover the region up to $|\eta| = 2.0$. The straws used in the barrel region are 144 cm long and positioned in 73 layers. The straws used in the end-caps are 37 cm long and arranged radially in 160 layers. If a charged particle traverses a straw, the gas in the straw is ionised along the particle's trajectory, resulting in electrons that drift towards a wire that spans the centre of the tube. The resultant drift time is used to calculate the radial distance with respect to the wire. Thus, the straws provide a 2-dimensional measurement in $(r - \phi)$ with an intrinsic resolution of 17 μm. The construction of the TRT allows for the collection of an average of 36 hits per track, which is needed to measure the bending of the track and contributes to a high momentum resolution.

2.2.2 The calorimeters

The calorimeters surround the inner detector and solenoid magnet system and are designed to trigger on and provide energy measurements of both charged and neutral particles. Only purely weakly interacting particles, like neutrinos, pass the calorimeters undetected. Furthermore, the calorimeters are used for particle identification and to reconstruct the missing transverse energy (E_T^{miss}) of an event. The calorimetry system covers the barrel and end-cap regions and additionally includes forward calorimeters to provide coverage up to $|\eta| = 4.9$. A cut-away view of the calorimeter system is shown in figure 2.6.

The used calorimeters are sampling devices. This means that they are built of two types of layers: an active medium that allows reconstruction of the depth and width of particle showers emanating from particles entering the calorimeter, and an absorber material that optimally absorbs the energy of particles in order to limit the depth of

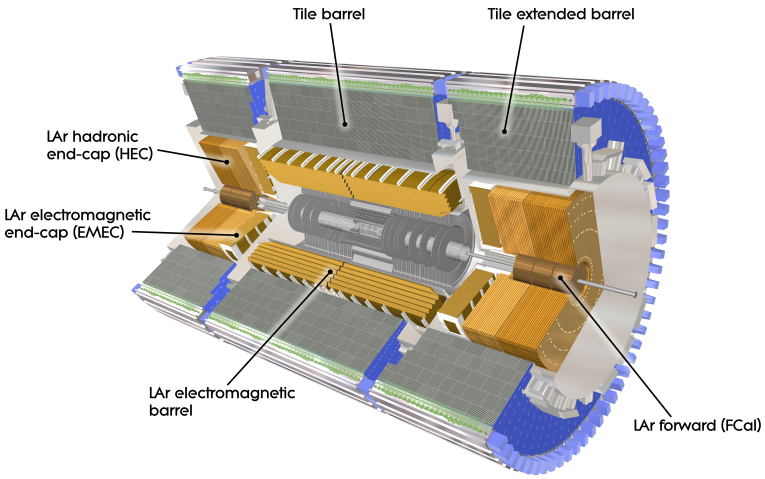

Figure 2.6: *Cut-away view of the electromagnetic and hadronic calorimeters. The calorimeters are based on liquid argon (LAr) and tile techniques.*

the particle showers. The calorimeter system consist of two types: the liquid argon (LAr) calorimeters [38] and the tile calorimeters [39].

Since electromagnetic showers penetrate through less material than hadronic showers, the calorimeter system consist of an inner electromagnetic calorimeter (ECAL) that is optimised for detection of photons and electrons, and an outer hadronic calorimeter (HCAL) that has a stronger absorbing power, such that the hadronic showers are stopped and measured within the calorimeter volume and punch throughs into the muons spectrometer are kept to a minimum. To allow for high energy resolutions, the radii of both calorimeters are chosen such that the electromagnetic and hadronic showers are stopped within the respective volumes. The ECAL has a thickness, measured in radiation lengths[1] (X0), of $X0 = 22$ in the barrel and $X0 = 24$ in the end-caps, and the HCAL extends up to 11 interaction lengths[2] (λ). Furthermore, the forward calorimeters (FCAL) provide measurements of both electromagnetic and hadronic showers in the most forward regions.

[1]The radiation length is defined as the mean length traveled by an electron until it has $1/e$ of its original energy left, with $e = 2.72$.

[2]The interaction length is defined as the mean path length travelled by a hadron until it has $1/e$ of its original energy left.

In the ECAL, both in the barrel and end-caps, liquid argon is used as active medium and lead plates function as absorbers. To guarantee full $r - \phi$ coverage any gaps between the different detector units are removed by using accordion shaped absorber plates. The intrinsic energy resolution of the ECAL is $\sigma_E/E = 10\% \sqrt{E} \oplus 0.7\%$ (E in GeV) with a typical granularity of $\Delta\eta \times \Delta\phi = 0.025 \times 0.025$.

In the barrel HCAL scintillator tiles are used as active medium and steel functions as absorber. For the end-cap HCALs has been chosen to use liquid argon as active medium and copper as absorber material. The intrinsic energy resolution of the HCAL is $\sigma_E/E = 50\% \sqrt{E} \oplus 3\%$ (E in GeV).

To provide hermetic coverage, which is essential for good E_T^{miss} resolution, the calorimeter system includes two forward calorimeters in the range of $3.1 < |\eta| < 4.9$. The FCALs stretch over 10 interaction lengths and consist of three modules each, where the inner module is optimised for electromagnetic measurements, and the outer two are employed for hadronic measurements. Liquid argon is employed as active medium and the absorber material consists of copper for the electromagnetic module and tungsten for the hadronic modules. The intrinsic energy resolution of the FCALs yields $\sigma_E/E = 100\% \sqrt{E} \oplus 10\%$ (E in GeV).

2.2.3 The muon spectrometer

The outermost and largest part of ATLAS is covered by the muon spectrometer [40]. It extends up to a radius of ~ 10 m and stretches on both sides of the interaction point up to $z \simeq 21.5$ m. A cut-away view of the muon spectrometer is shown in figure 2.7. The muon spectrometer has two main functions: to provide an independent muon trigger and to reconstruct muons within its own volume (standalone reconstruction). To correctly determine the momentum of highly energetic muons, long muons tracks are required; this explains the large volume of the spectrometer. Furthermore, having momentum measurements of muons in the muon spectrometer, in addition to measurements in the inner detector, improves the momentum resolution and also allows for muon detection outside the acceptance of the inner detector.

An independent momentum measurement requires measurement of a track at - at least - three different locations. Therefore, in the barrel region the muon stations are

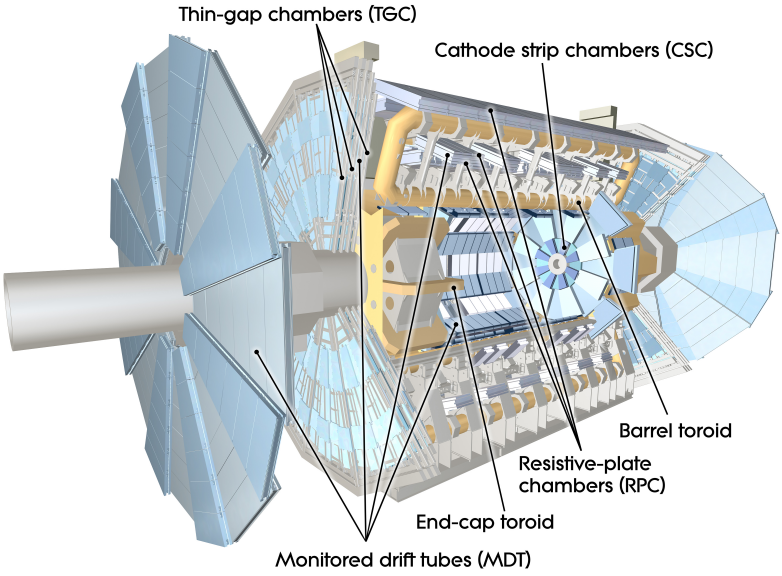

Figure 2.7: *Cut-away view of the muon system. The precision and trigger chambers, as well as the magnet system are indicated.*

positioned in three concentric layers around the beam axis, at radii of approximately 5, 8 and 10 m. Also in the end-caps measurements at three different locations are provided by three wheels of muon stations. In the transition region between the barrel and end-cap an additional layer of muon stations is placed to assure also three measurements for muons traversing this region.

The muon stations that form the muon spectrometer consist of different types of trigger and precision tracking chambers, depending on the position of a muon station within the spectrometer. A toroidal magnet system provides the magnetic field needed for momentum measurements.

Standalone muon measurements are possible for muons with momenta between 3 GeV and 3 TeV. Muons with smaller momenta are solely measured by the inner detector as they will not have sufficient energy to traverse the calorimeters. The muon spectrometer is designed to have a momentum resolution of 10% for muons with a transverse momentum of 1 TeV. This design resolution is taken into account in the design of the magnet system, the detector geometry and the muon chambers.

Magnet system

The magnet system is used to bend the trajectories of the muons, such that their momenta can be deduced from the curvature. The magnet system consists of three sections: a barrel toroid inducing a magnetic field of approximately 0.5 T and extending up to $|\eta| = 1.4$, and two smaller end-cap toroids, providing magnetic fields of approximately 1 T, that are inserted in the barrel toroid and cover the regions $1.6 < |\eta| < 2.7$. Each toroid is built up of eight superconducting coils. This configuration leads to a magnetic field that is on average orthogonal to the muon trajectories and minimises degradation of the momentum resolution due to multiple scattering.

Precision chambers

The precision tracking in the muon spectrometer is mainly performed with monitored drift tube (MDT) chambers. Only in the inner layer of the end-caps, Cathode Strip Chambers (CSCs) are used, as MDTs cannot keep up with the high data rates in the forward region. The function of the chambers is measuring muon momentum with high precision.

The MDT chambers consist of aluminium tubes with a diameter of 30 mm. The tubes are filled with a gas mixture that ionises when a muon traverses the tubes. This results in an electrical signal that is induced by the drift of the freed electrons to a wire located in the centre of the tube. This gives a two-dimensional measurement with a spatial resolution of 80 μm per tube. There is no measurement of the position in the direction along the tube.

Within a chamber, the MDTs are grouped into two multilayers that each consist of three or four layers of up to 72 MDTs. A measurement with an MDT chamber gives the angle and position of a track in the plane perpendicular to the tubes. The intrinsic spatial resolution of such a measurement is 35 μm per chamber.

The CSCs are multi-wire proportional chambers. These chambers are used in the forward region, as they can handle counting rates up to 1000 Hz/cm^2. A CSC consists of multiple anode wires and two layers of cathode strips with a gas mixture in between. Again, when a muon traverses a CSC, the gas along the trajectory ionises, resulting

in an electrical signal. The two layers of strips are placed under an angle of 90 degrees to acquire a three-dimensional position measurement with an intrinsic resolution of 40 μm in the direction of the bending plane and of 5 mm perpendicular to this plane.

Trigger chambers

The muon spectrometer trigger chambers - the Resistive Plate Chambers (RPCs) in the barrel and the Thin Gap Chambers (TGCs) in the end-caps - are used for muon identification in the level-1 trigger of the trigger system that is discussed in section 2.2.4. Furthermore, the trigger chambers provide the coordinate and direction of a track in the direction along the MDTs, since these are not measured by the MDT chambers themselves. The trigger chambers are designed to have good time resolution, which is necessary for triggering, and good granularity in order to provide a sharp cut-off on the muon momenta.

The RPCs consist of two resistive plates that are separated by a 2 mm gap that is filled with a gas mixture. Traversing particles ionise the gas and the freed electrons are subsequently detected by readout strips that are placed on the anode side of the plates. Each RPC station consists of two layers of RPCs, where one layer provides the η coordinate and the other the ϕ coordinate of the tracks. The RPCs are designed to have a spatial resolution of ~ 10 mm and a time resolution of 1.5 ns.

The TGCs are multi-wire proportional chambers, like the CSCs. Yet the distance between two wires is smaller to ensure that the drift time is smaller than the nominal bunch spacing of 25 ns. A three-dimensional measurement is obtained with a spatial resolution of $2 - 7$ mm and a time resolution of 4 ns.

2.2.4 Trigger and data acquisition

The interaction rate of the LHC, operating at nominal luminosity and with bunch crossings every 25 ns, will be 40 MHz. This implies a data rate of $50 - 60$ TB/s, which is too large to store, let alone analyse. However, the bulk of the data is coming from soft collisions that are of no interest to the physics goals of ATLAS. Therefore, ATLAS has a trigger system that reduces the data rate and selects the most interesting

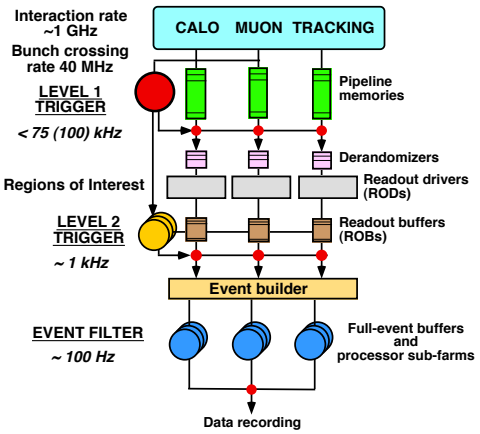

Figure 2.8: *Block diagram of the combined ATLAS trigger and DAQ system that provides event rate reduction and storage of interesting events. Data come in at the top of the diagram and are evaluated and selected or rejected at three different levels. The process ends with recording of the selected events [36].*

events [41]. Triggering is performed at three stages: a hardware implemented level 1 trigger (LVL1), a software based level 2 (LVL2) trigger and an Event Filter (EF); the latter two are jointly referred to as the High-level Trigger (HLT). The trigger system is complemented with a data acquisition (DAQ) system that is responsible for (temporary) data storage. A schematic representation of the combined trigger and DAQ system (TDAQ) is shown in figure 2.8.

The LVL1 trigger reduces the event rate to $\sim$ 75 kHz. The time for decision making is less than 2.5 μs. In this limited amount of time it is only possible to use information from a subset of detectors: the calorimeter operating at reduced granularity and the muon spectrometer trigger chambers. Based on this information, regions of interest (RoIs) that include signatures of high-pT photons, electrons or muons, jets or large missing transverse energy are defined. The RoIs are passed to the HLT if the preset p_T or energy threshold is exceeded, isolation requirements are fulfilled and the event is matched with one of the predefined signatures.

The LVL2 trigger is designed to reduce in approximately 40 ms the event rate to 3.5 kHz. This is enough time to analyse the RoIs using the full detector granularity within the RoIs. At this stage fast object reconstruction is used to better determine

the object properties. If the objects meet the stricter selections of the LVL2 trigger, the event is passed to the EF.

The EF uses information of the entire detector at full granularity to perform event reconstruction, which takes approximately 4 s per event, and subsequently select interesting events. At this stage the event rate is reduced to a final 200 Hz, which is low enough to store the data for further analysis.

The exact thresholds and selections used at each stage of the trigger system are variable and adopted to the instantaneous luminosity of the LHC, in order to keep a constant output rate. Events passing the HLT are allocated to various data streams, depending on their primary objects. There are three physics streams: the Muon, Egamma and JetTauEtmiss streams. Additionally, there is a minimum bias (MinBias) stream that contains a random set of events that can be used for e.g. performance studies. Events can be allocated to more than one stream if there are triggers for different objects within the event.

Additionally, various so-called trigger chains that use specific selection criteria are used simultaneously to trigger on different physics processes. One trigger chain may for example require simultaneous detection of two high-p_T muons, while another chain triggers on one tightly isolated electron. The collection of simultaneously used chains is called a trigger menu. During 2012 data taking up to 1000 chains were exploited within one trigger menu.

At each stage of triggering the data are temporarily stored and eventually recorded using a complex data acquisition system. Before the LVL1 decision is made the data are held in pipeline memories, as depicted in figure 2.8. Data that are subsequently accepted by the LVL1 trigger are stored in read-out buffers (ROBs), until they are processed by the LVL2 trigger. Data accepted by the LVL2 trigger are passed onto the event builder (EB). After EF acceptation the events are written to a mass storage that is accessible for offline physics analysis. Storage of 200 events per second comes down to recording approximately 3200 Tbytes of raw data per year.

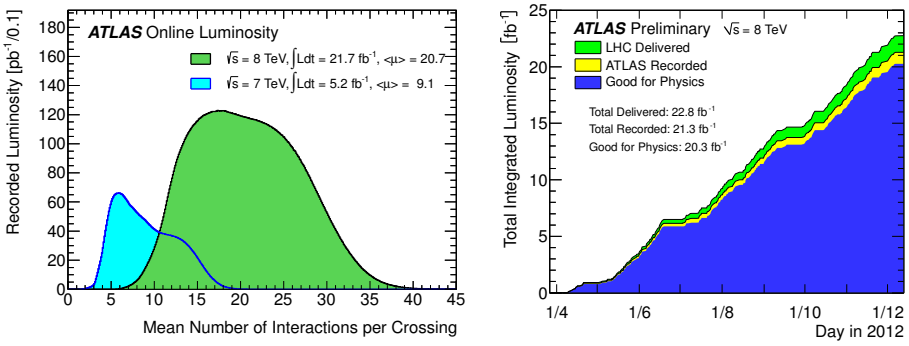

(a) (b)

Figure 2.9: *(a) Average number of collisions per bunch crossing, weighted with the recorded luminosity, for the 2011 and 2012 datasets. (b) The total integrated luminosity delivered by the LHC, recorded by ATLAS, and qualified as good for physics, in 2012 [35].*

2.2.5 Operations and performance

The ATLAS detector has been taking data since 2008. Before the LHC was delivering data, the detector was taking cosmic data. These were used to commission and get to understand the detector. Additionally, the modelling of the magnetic field has been optimised during this time. Thus, at the start up of the LHC in 2010, ATLAS could start taking well calibrated data right-away.

As the beam intensity increased over time, the conditions for data taking changed. One of the main challenges has been to adjust the experiment to the increasing number of collisions per bunch crossing, referred to as in-time pile-up (μ). The pile-up has been increasing from one collision per bunch crossing in 2010 to an average of $\mu = 20.7$ in 2012. Figure 2.9a shows the luminosity weighted distributions of the pile-up for the 2011 and 2012 datasets. The reason to run with increased pile-up is to gather more data, but this comes at a cost. As more interesting events fire the trigger, while the data output rate should not increase, tighter trigger selections are required. Additionally, the number of tracks in the inner detector and the energy deposits in the calorimeters increase due to the pile-up. This makes event reconstruction more challenging. Nevertheless, due to good primary vertex reconstruction and tracking, running with higher pile-up is possible and advantageous.

Subdetector	Number of channels	Operational fraction
Pixels	80 M	95.0 %
SCT Silicon Strips	6.3 M	99.3 %
TRT Transition Radiation Tracker	350 k	97.5 %
LAr EM calorimeter	170 k	99.9 %
Tile calorimeter	9800	98.3 %
Hadronic end-cap LAr calorimeter	5600	99.6 %
Forward LAr calorimeter	3500	99.8 %
LVL1 calo trigger	7160	100 %
LVL1 muon RPC trigger	370 k	100 %
LVL1 muon TGC trigger	320 k	100 %
MDT Monitored Drift Tubes	350 k	99.7 %
CSC Cathode Strip Chambers	31 k	96.0 %
RPC barrel muon chambers	370 k	97.1 %
TGC end-cap muon chambers	320 k	98.2 %

Table 2.2: *The operational status of the subdetectors of ATLAS on 19 October 2014 [42].*

During the three years of operations, ATLAS has been recording data with an average efficiency of 93.2%. Figure 2.9b shows the luminosity that has been delivered by the LHC and subsequently recorded by ATLAS in 2012. The efficiency is not 100 % as a result of for example the necessity to temporarily stop the trigger to restart a failing subsystem. Figure 2.9b also indicates the amount of the recorded data that can be used for physics analyses, which yields 20.3 fb^{-1} for the 2012 dataset. Data are qualified as good for physics if there are no detector failures or if failures do not lead to a significant set of events that cannot be reconstructed.

The operations of the individual subsystems of ATLAS have been outstanding: averaged over the years of operations, every subdetector has recorded data more than 99% of the time that was spent in stable beams. Table 2.2 shows a snapshot of the operational status of the detector in October 2012.

The performance of ATLAS will be further discussed in section 4.4, where the performance of event and object reconstruction is detailed.

Finally, operations would not have been so successful without an optimal performing detector control system (DCS). With the DCS the detector can be monitored and

controlled from the control room of ATLAS. This ensures fast recovery of a failing subsystem, either automatically by the DCS itself or by a manual action from the shifter or subsystem expert. The DCS is a complex system with specific features for each subdetector. In the next chapter the DCS, as well as the DAQ system, will be discussed for the MDT chambers.

Chapter 3

DAQ and DCS for the muon MDT chambers

Although it often receives little attention, streamlined data acquisition, detector operations, and data quality monitoring are essential to acquire good physics results. The heart of the management and control of these processes is the ATLAS control room. During data taking periods the control room is occupied with so-called shifters, who take care of smooth operation of the detector, and monitor the data quality, trigger and data acquisition, and detector hardware. A considerable part of the detector operations is automatised, but for certain tasks and also when unexpected or severe problems occur, manual intervention is needed. Each subdetector has its own shifters and experts that are responsible to keep the detector running in good state.

The primary expert-on-call for the MDTs and CSCs is the first responsible in line in case of problems with the data acquisition (DAQ) system, the detector control system (DCS) or data quality (DQ) monitoring of these chambers, as well as for the common muon system processes. Problems that cannot be solved by the shifter are handled by the expert-on-call. This requires knowledge of both the hardware and software architecture of the various systems. As not all of this can be covered in this thesis, only a concise overview of the architecture of the DAQ system and the DCS of the

MDTs is given. Additionally, the operations and performance of these systems during the first three years of running will be discussed.

3.1 MDT electronics and DAQ system

Data acquisition is the term used for the signal processing that starts with a muon leaving a hit in one of the MDTs and via a route through several electrical devices ends with delivery of the information about the incoming muon to the read-out system (ROS), where event reconstruction starts. Since event reconstruction demands high precision in time and position it is essential that the read-out electronics preserves the inherent measurement resolution of the MDTs (80 μm) and additionally copes with the high hit rates [43]. The system consists of on-chamber read-out electronics that is radiation hard and resistant to the magnetic field, and electronics that is located outside the experimental cavern and is used for further data acquisition.

Figure 3.1 depicts the architecture of the on-chamber MDT electronics. On one side of an MDT chamber the MDTs are connected to the high voltage (HV). The HV is distributed over the tubes by means of a HV hedgehog card that is mounted on the chamber. The read-out of the MDTs takes place on the other side of the chamber. The signals of eight tubes are processed (amplified, shaped and discriminated) by an ASD chip. The ASD chip measures the deposited charge and passes the signal if the charge exceeds a predefined threshold. The output of three ASDs is led to one time-to-digital converter (TDC) chip, where the arrival times of both the leading and trailing edges of signals are stored. This information is crucial for track reconstruction. To ensure that the time information is compatible with timing in other detector parts, it is measured in units of the Timing, Trigger and Control (TTC) clock, which is synchronised with the bunch crossing of the LHC [44]. The ASDs and TDC are implemented on a printed circuit board, called a mezzanine card. Since the maximum number of MDTs per chamber is 432 and one mezzanine card serves twenty-four drift tubes, the number of mezzanine cards per MDT chamber can add up to eighteen.

The mezzanine cards of one chamber are controlled by a single processor, called the Chamber Service Module (CSM). The CSM is a multiplexer that collects the data of the chamber into one output data stream and sends it via an optical link to the

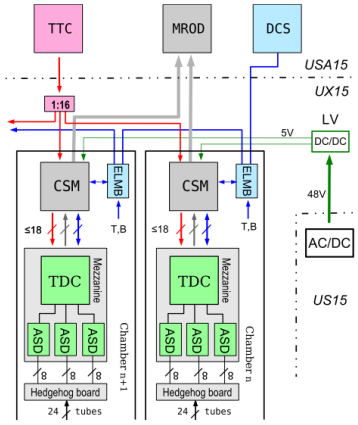

Figure 3.1: *Diagram of the MDT read-out electronics. Each chamber has up to 18 mezzanine cards that are controlled by one CSM, and up to six CSMs are connected to one ROD. Each CSM is also connected to an MDM, indicated as 'ELMB', to enable communication with the DCS project [43].*

DAQ system. The CSM is also responsible for transmission of TTC signals to the mezzanine cards. Furthermore, the CSM is linked to the MDT DCS module (MDM), to allow for communication with the DCS for monitoring and electronics initialisation. The MDM, of which the ELMB is the active module, will be discussed as part of the DCS in the next section.

The output data stream of the CSM leaves the front-end electronics and is routed through an optical fibre to the off-chamber electronics that is situated in the counting room. The data streams of up to six CSMs enter through an MDT read-out driver (MROD). The MRODs, a total of 204 for the whole ATLAS MDT system, are situated in sixteen crates that each have their own crate controller, to which one can connect from remote. A primary function of the MRODs is to use the data output of the CSMs to form basic fragments of muon tracks by grouping hits from fired MDTs. Subsequently, the data are sent to the read-out buffer (ROB), where the data are stored until the LVL1 trigger decision is made. Accepted events are sent to the read-out system (ROS), where the data of the complete muon spectrometer are collected. The ROS provides an interface between the data kept in the ROB and the LVL2 processing farm, and event building systems, and is the last device in the muon read-out and data acquisition chain [45].

3.2 Detector Control System

The detector control system (DCS) provides an architecture with which the detector can be safely and efficiently operated. The DCS of the muon system has as main tasks:

- Operate and monitor the thousands of HV and LV channels of the power system;
- Configure and (re)initialise the front-end electronics;
- Monitor the optical alignment system, the gas system, the voltage and temperatures of the front-end electronics, and environmental conditions, like the magnetic field and temperature;
- Archive all these non-event based parameters for usage in physics analysis and to trace problems;
- Respond to changes and anomalies in the environmental and detector conditions;
- Control the actions allowed under specific running conditions to prevent configurations that are harmful for the detector;
- Adjust working point parameters, like voltage and front-end thresholds, to guarantee synchronised operation with the LHC.

To be able to perform these actions the DCS consists of numerous software protocols, databases and user interfaces. In the following, the DCS architecture and software will be described, as well as the three sets of hardware that are directly handled by the DCS [46, 47].

3.2.1 Architecture and software

The muon DCS is part of the central ATLAS DCS, which is organised following a hierarchical structure to allow for transparent and efficient management of all subsystems in the ATLAS detector. ATLAS as a whole is represented by a global control station (GCS) - the top level of the hierarchy - followed by a layer of subdetector

control stations (SCS). The SCSs provide access for user interfaces, and each of the four types of muon chambers has its own SCS. At the lowest level there are the local control stations (LCS) that connect computer nodes with the hardware. For example, every single HV and LV channel has its own LCS.

The detector has a huge amount of output parameters, from environmental conditions to trigger rates, that make the number of states in which ATLAS can be close to infinite. This stands in the way of transparent detector operations. The introduction of a finite state machine (FSM) solves this by translating the large number of detector states into a small set of predefined states, that are denoted as: READY, STANDBY, TRANSITION, SHUTDOWN and NOT-READY. A snapshot of the muon FSM is shown in figure 3.2. The states can be adopted by the control stations and depend on the readiness of the specific station and the running phase of ATLAS. If for example the beams are to be injected in the LHC, ATLAS needs to be put in the safe STANDBY state, which means for the MDTs that the HV of part of the chambers has to be lowered from 3080 V to 2500 V. If all parameters of the MDT chambers are between the boundaries that are set for injection, then the state of the MDT DCS will be STANDBY. Only if all LCSs are in this state, the state of ATLAS as a whole will be STANDBY and the injection permit is given to the LHC. If there is a problem that withholds the permit, the cause of this can be figured out by navigating down the FSM, following the control stations that are NOT-READY and show a warning status, until the parameter that is out of boundaries is reached.

The software that is used to create the FSM environment is called PVSS [48]. It is a supervisory control and data acquisition (SCADA) tool. PVSS works with the concept of data-points: all output parameters of the detector are processed by the DCS as data-points and ordered in a tree structure. Processes, called managers, can be designed to act on these data-points. The managers are the heart of controlling the detector. As long as data-points do not change significantly, i.e. when the system is stable, there is no need for managers to act. However, when data-points change managers will automatically come into action. For example, the request of the LHC to ATLAS to get into the correct state for beam injection, results in changing data-point. These changes alert the managers that act upon the data-points corresponding to the HV channels of the MDTs as to guarantee that the MDTs will get into the safe STANDBY state. In this way the detector is largely managed by preprogrammed

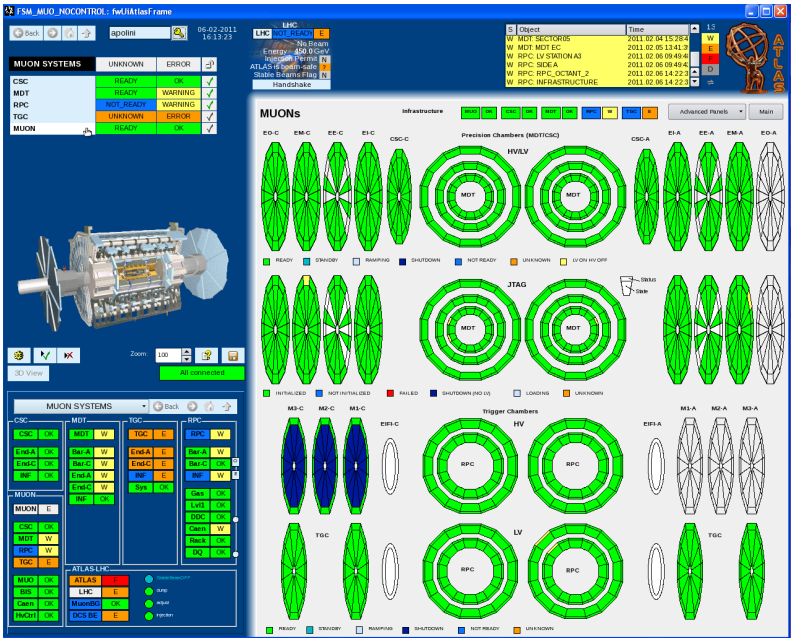

Figure 3.2: *FSM user interface of the muon system. This panel is the overview panel, used to navigate through the different layers of the muon system and to perform action to specific stations or the muon system as a whole. The FSM indicates the state of the various control stations and additionally shows their status (*OK, WARNING, ERROR *or* FATAL*).*

processes that act when alerted by changing data-points. The data-point concept also allows for visualisation of detector processes: panels can be built to do parametrisations on data-points, such as alarm handling, archiving and sorting. These panels are subsequently ran on the computers in the control room and used for detector operations by shifters and experts.

3.2.2 The power supply system

The MDT power system, consisting of the LV and HV power supplies, is operated by the DCS and common to the MDTs and CSCs. The commercial EASY system from CAEN, that is used for the power supplies, works with a master-slave architecture, as shown in figure 3.3. Starting at the lowest level of the power system, the HV and LV channels connect the MDTs with the power boards. These boards are situated in

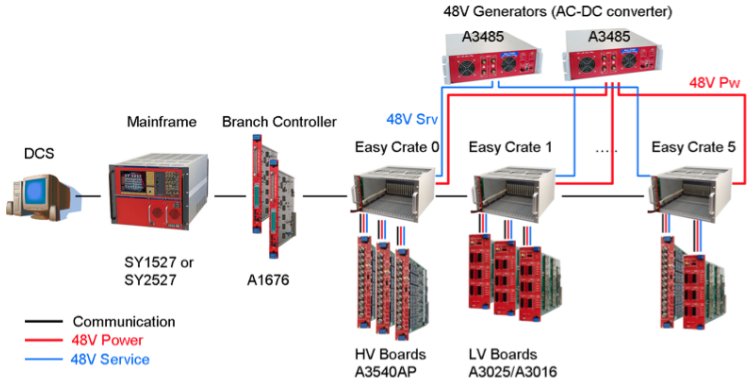

Figure 3.3: *The MDT power system architecture. In total, there are two mainframes that are shared by the MDT and CSC chambers. From the mainframes the control splits into higher granularity.*

crates in the experimental cavern. Each set of six crates is controlled with a branch controller. This is a master board to which can be connected from remote, in order to manage the lower layers of power electronics. Finally, there are two mainframes that both manage around sixteen branch controllers and that are each connected to a power generator. In this way around 6000 HV and 2000 LV channels are configurable [49]. To allow for data exchange between the power system and the software, the mainframes are connected to the DCS via an interface called OPC, which stand for Object Linking and Embedding (OLE) for Process Control.

In the FSM the power system can be monitored and controlled at each level, from the individual channels to the mainframes. Most processes are however conducted fully automatically by PVSS managers to keep the power operations safe. Manual actions are sometimes required and involve for example power-cycling of the mainframes after a power cut.

3.2.3 The front-end electronics monitoring and control

The second set of hardware managed by the DCS are the already mentioned MDT DCS Modules (MDMs), that are situated on every MDT chamber. A picture of an MDM is shown in figure 3.4. The active module of an MDM is the Embedded Local Monitor Board (ELMB). ELMBs are general-purpose plug-on modules that have been

accustomed for usage in ATLAS. On the one hand, the MDMs are used to initialise and control the front-end electronics: configuration parameters are retrieved from a database and sent from DCS via JTAG to the MDM. JTAG is the protocol used for communication between the MDMs and the DCS.

On the other hand, the MDMs are used for monitoring of the environmental conditions. This involves the read-out of $\sim$ 140.000 temperature sensors and 1650 magnetic field probes, as well as monitoring of the 50.000 voltage and temperature values of the front-end electronics. The outputs of the sensors are processed as data-points and sent to the conditions database for later use during off-line track reconstruction and suchlike. All of this is performed using the CAN-bus protocol that provides distributed control and monitoring, i.e. communication between the different electrical components within the system [50].

Figure 3.4: *Picture of an MDM. The input for monitoring of the front-end electronics is indicated as CSM-ADC. The inputs for environmental conditions monitoring, communication via JTAG, and for the CAN-bus connection are indicated as well.*

3.2.4 Optical alignment system

The optical alignment system of the MDT chambers is the third hardware system managed by the DCS. The alignment of the MDT chambers is continuously monitored, since the smallest deviations of the chambers from their nominal positions affect the muon track reconstruction. It is not feasible to correct the physical chamber positions, considering that it is impossible to keep the alignment stable at the scale of the intrinsic resolutions of the chambers of 35μm. However, with archived information on the positions of the chambers, the muon tracks themselves can be corrected during off-line reconstruction.

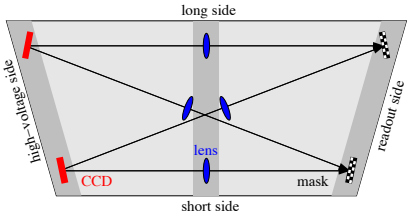

Figure 3.5: *Schematic representation of the RASNIK optical alignment system, used to monitor the alignment within an MDT chamber. The masks, lenses and CCDs form optical lines, and their relative displacement is measured [51].*

The optical alignment is primarily performed with a setup called RASNIK [52]. The RASNIK system forms a set of optical paths that each consist of three elements as depicted in figure 3.5: a led projects an image of a coded mask via a lens onto an optical sensor. The system measures the relative displacements of the three elements of one optical path. In this way the positions and deformations of chambers can be measured with a resolution of 30 μm [53]. There are optical paths within chambers, both along the sides and the diagonals, as also shown in the figure, and optical paths between the three layers of muon stations.

In order to use this information in track reconstruction the images of the coded masks are archived into a database by DCS. Also the information of the optical alignment system that is additionally used in the end-caps, called BCAM [54], is stored in this database.

3.3 Operational performance

The DAQ and DCS form a very well tuned system. After four years of experience in data taking, both cosmics and collisions, the architecture of the DCS has been commissioned and tuned such that in general only little intervention is needed and most DCS and DAQ actions are automised. Reoccurring issues have been traced and resolved. Operations started with one shifter for every muon subdetector, but as of 2011 a single shifter can monitor the whole muon spectrometer.

Expert intervention involved problems ranging from ambiguous DCS alarms and broken LV/HV boards to non-responding parts of the detector, communication lost with large fractions of the detector, and recovery of power cuts or cooling failures. Most problems could be resolved from the control room or remote and did not require access to the experimental cavern.

The DAQ system has been very stable. The rate at which broken electronics, like broken mezzanine cards, had to be replaced has been lower than expected. Problems occurring during operations had mostly to do with MDT chambers or MRODs dropping out of data taking. Clear procedures to resolve this have been set up to decide upon the correct action, depending on the running state and the number of affected muon chambers. Additionally, automatic recovery of dropped mezzanines and chambers has been established, such that only after four failing recoveries manual intervention is required. Furthermore, to allow for automatic recovery or stopless removal of MRODs that encounter problems, an additional mechanism has been implemented, such that loss of data or a hangup of a larger part of the MDT chambers is prevented.

The PVSS architecture has shown to work very well for detector operations. It has the flexibility to adjust the DCS architecture according to the needs that emerge during data taking. For example, to allow for the muon operations to be handled by a single shifter, the user interfaces of the four different muon subdetectors could gradually be unified. And to further facilitate operations, an additional node, indicated as MUON, has been added aside from the four subdetector nodes, as visible in figure 3.2. This node allows to perform - in one go - actions that are common for the subdetectors, and is the perfect place to accommodate devices that are common to the muon subdetectors.

As operations advanced, more PVSS managers that handle processes automatically have been implemented. For example, initially bringing the muon system from STANDBY into READY state when stable beams were reached, required a manual operation on the HV channels, but this is has been changed into an automatic action triggered by the LHC stable beams flag.

The experience with the CAEN power system has been good. The power board failure rate is much less than the imputed 10 % and involves mostly only individual channels.

Several problems that have been encountered during operations have been solved. To name a few issues:

- Loss of communication with individual LV/HV boards occurred occasionally after a power cut. This initially required access to the ATLAS cavern to manually reset the affected boards. In 2011 the Muon CAEN Reset Network has been implemented, allowing for remote resets of boards;
- During ramping of the HV channels to nominal voltage, the large amount of data updates frequently overloaded the OPC server, leading to crashes and subsequent data loss. This could be solved by tuning the OPC group configuration and optimising the refresh intervals;
- Reoccurring but rare cases of losing all communication with the power system have been occurring. To guarantee immediate action, a set of alerting mechanisms has been implemented.

Also the MDMs perform very well, with only two out of the more than 2500 ELMBs, that are used for the whole muon system, failing. Initialisation of the MDT front-end electronics with the MDMs via JTAG works efficiently: in less than 2.5 minutes the full MDT system can be reinitialised. Improvements to reduce this time even further are ongoing.

Concerning the MDT chambers, all across Run I more than 99.5% of the elements were fully operational. Only rarely the MDT system caused a significant loss of data. This was however never due to a broken element, but a result of some data corruption. Concerning the CSCs, there were at the end four broken HV layers, out of a total of 128 HV layers. It can be concluded that operations of the MDT chambers and the CSCs, and the muon spectrometer in general, have been very successful. During the 2013-2014 shutdown the DCS and DAQ systems have been further optimised to resolve outstanding issues and allow for smooth operations at higher energies.

In this and the previous chapter the experimental setup used to acquire data has been described and it has been shown that its performance is excellent. In the next chapter the phenomenology, simulation and reconstruction of the events that are generated and processed with the LHC and ATLAS are discussed.

Chapter 4

Events in ATLAS

The analysis presented in this thesis is based on the events that are produced in the proton-proton (pp) collisions of the LHC and recorded with the ATLAS detector. In this chapter, the most important information about these events is gathered. The phenomenology of pp collisions is described in section 4.1. Additionally, the production and decay of Higgs bosons is detailed in section 4.2. Subsequently, the simulation of events, using Monte Carlo (MC) generators, will be addressed in section 4.3. These MC simulations shall later on be used to interpret the collision data. The last step preceding the actual data analysis is the reconstruction of 'physics objects' is events. This event reconstruction is applied to both data and MC simulations. The algorithms used for the event reconstruction and their performance are the subject of section 4.4, which provides also an overview of the actual performance of the ATLAS detector.

4.1 Phenomenology of proton-proton collisions

It has been chosen to collide protons in the LHC, since this allows for centre-of-mass energies of up to 14 TeV, because protons suffer of less synchrotron radiation than electrons, and a higher beam intensity is possible compared to anti-protons. Consequently, it is possible to reach a design energy that is much higher than that of

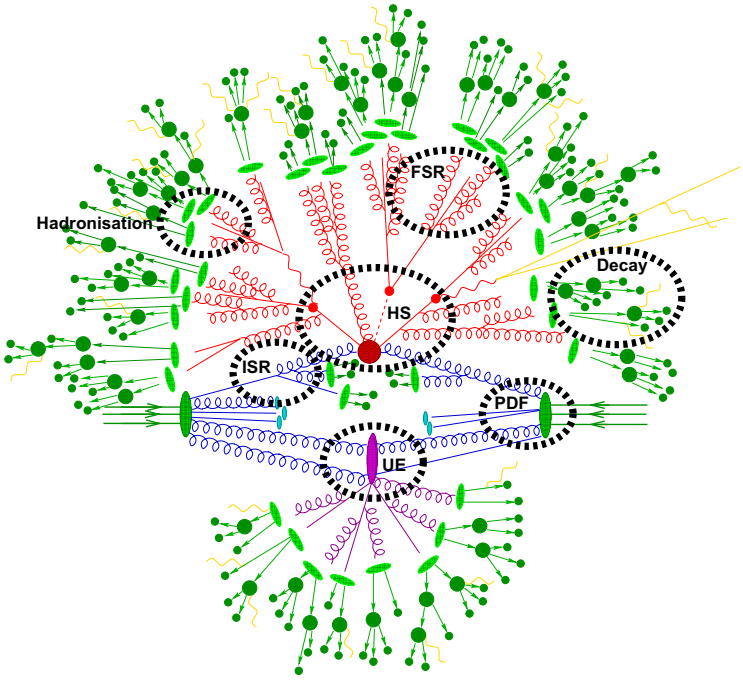

Figure 4.1: *Illustration of a pp collision, including a hard interaction. The various processes that take place in the collision are indicated: the hard scattering (HS) between two incoming partons, the subsequent decay, the initial and final state radiation (ISR, FSR), the hadronisation, and the activity amongst the partons that do not take part in the hard scatter, denoted as the underlying event (UE). The figure is taken from Ref. [55], with modifications by [56].*

the large electron positron collider (LEP), which was the previous collider at CERN, and the Tevatron collider at Fermilab that collided protons with anti-protons. Yet, also the use of protons brings along a challenge as they are composite objects. This implies that the actual collision takes place between its constituents, the quarks and gluons, that have an unknown energy fraction and flavour. This complicates the description of pp interactions. Aside of protons, also ions are collided in the LHC. These collisions are used to study the quark-gluon plasma and are less suited to study elementary interactions, since there is too much activity to extract a hard scattering.

4.1.1 Signature of proton-proton collisions

Protons are baryons composed of two up quarks and one down quark, and a *sea* formed by virtual quark-antiquark pairs and gluons. In pp collisions the actual interaction takes place between these constituents, also called partons. Several processes take place within a pp collision, as illustrated in figure 4.1:

- **The hard scatter** (HS) between two partons - one of each proton - is characterised with large momentum transfer, which may result in the production of a heavy particle that subsequently decays and can be detected by means of its final state particles. Hence, this is the interesting part of the collision;
- The partons are colour charged and therefore radiate gluons. In case that the partons are quarks, also photons are radiated. When this happens before the hard scatter, it is called **initial state radiation** (ISR), while emission after the hard scatter is called **final state radiation** (FSR);
- The quarks and gluons emanating from ISR, FSR and the hard scatter, as well as the partons that did not take part in the hard interaction will split further into quark-antiquark pairs or gluon pairs and as such loose energy through this process of **parton showering**;
- Confinement requires that only colourless particles exist in nature, therefore the gluons and quarks that emanate from the parton showering will form colourless hadrons in a process called **hadronisation**. These hadrons will subsequently decay into other particles, resulting in showers of particles called jets;
- All the activity that does not belong to the hard interaction, but to the interaction, hadronisation and decay of the other partons in the protons is referred to as the **underlying event** (UE).

Since it is not possible to identify which partons interact in the hard scatter, nor what fraction of the total proton energies they carry, the cross section of an individual hard interaction cannot be established. The total centre-of-mass energy of the pp collisions is however given by the collider. Therefore, the total hadronic cross section, constituted by all aforementioned processes, and including the partonic cross section summed over all possible parton interactions and energies, is used.

4.1.2 The hadronic cross section

To be able to define the hadronic cross section, the processes that take place in a pp collision are divided into two: the hard interaction(s), characterised with large momentum transfer, and the soft processes, with small momentum transfer. The underlying theory for both hard and soft processes is quantum chromodynamics (QCD), but the approach of how to describe the two is very different [57].

The reason for this is that the strong coupling constant, α_s, depends on the momentum transfer, Q^2: $\alpha_s(Q^2)$ decreases with increasing Q^2. Consequently, processes with high momentum transfer can be described with a series expansion, as the higher order terms grow increasingly small, allowing to disregard these terms. Processes with low momentum transfer, on the other hand, cannot be expanded in series as higher order terms grow increasingly large. For this reason, only the hard scatter can be described with perturbation theory, while the soft processes can only be described with phenomenological models and are therefore less understood.

Fortunately, the principle of factorisation allows to describe the hard and soft processes that constitute the hadronic cross section, using different formulations. In this way the interaction between two protons can be calculated as the convolution of functions describing the hard interactions, i.e. the partonic cross sections, and functions that recount non perturbative soft processes, called parton distribution functions (PDFs). The factorisation scale μ_F, specifies the separation between the soft and hard processes. Consequently, the total hadronic cross section can be factorised in terms of the two partons that take part in the hard interaction, $q_a q_b \to X$:

$$\sigma_{pp\to X+c} = \sum_{a,b} \int dx_1 dx_2 f_a(x_1, \mu_F^2) f_b(x_2, \mu_F^2) \hat{\sigma}_{q_a q_b \to X}(x_1, x_2, \alpha_s(\mu_R^2), \mu_F^2) + \mathcal{O}\left(\frac{\Lambda_{\text{QCD}}^2}{Q^2}\right) \tag{4.1}$$

where $x_{1,2}$ are the so-called Bjorken fractions of the proton momenta carried by the incoming partons; $f(x, \mu_F^2)$ are the PDFs, and μ_R is the renormalisation scale. The latter two will be discussed hereafter. The last term in Eq 4.1 corresponds to the neglected lowest soft terms that can also not be described with PDFs, as they are

of the order of the energy scale of QCD, Λ_{QCD}. It implies that the precision of the hadronic cross section increases with increasing momentum transfer, Q^2.

The PDFs, $f_a(x_1, \mu_F^2)$, give the probability to find a parton of type a - a gluon or one of the quarks - with a Bjorken fraction x_1 of the total proton momentum, inside the proton. The momentum fractions of all partons constituting one proton sum up to one. As PDFs describe non-perturbative processes, they cannot be analytically determined. Nevertheless, as they do not depend on the specific process that one wants to describe, the PDFs can be derived using precision measurements of well-understood processes. There are several experiments that measure PDFs. In this thesis, various PDF sets are used in the modelling of the different background and signal processes, as will be addressed in section 6.3. As an example, figure 4.2 shows the PDFs, parametrised by MSTW [58], as a function of the momentum fraction x, for each type of parton, evaluated at $Q^2 = 10$ GeV^2 and $Q^2 = 10^4$ GeV^2. The two figures indicate that the parton density depends on the energy scale Q^2 of the process: for higher Q^2, the density of particles with low momentum fractions increases, implying that an increasing number of sea quarks are visible at higher momentum transfer.

The partonic cross section is calculated by expansion in power series of the strong coupling constant. The lowest or leading order in the expansion series represents the tree level Feynman diagrams. Inclusion of higher order contributions, i.e. Feynman diagrams with additional vertices, makes the cross section prediction more precise, however, the calculations are also more complicated. Therefore, the partonic cross sections are determined up to a certain fixed order, where the associated energy scale is called the renormalisation scale μ_R. Since not all orders are included, non-physical scales have to be fixed and are mostly set equal to the typical momentum scale of the hard scattering: $\mu_R = \mu_F = Q^2$.

With a method to determine the hadronic cross section at hand, the expected production cross sections of interesting physics processes in pp collisions can be determined. Figure 4.5 shows the cross sections of several SM processes as a function of the centre-of-mass energy ($\sqrt{s}$). The nominal $\sqrt{s}$ of the Tevatron and the LHC are indicated. The Higgs production cross section is also included and predicted to be ten to eleven orders of magnitude smaller than the total pp cross section. This explains the necessity of high luminosity for the Higgs searches.

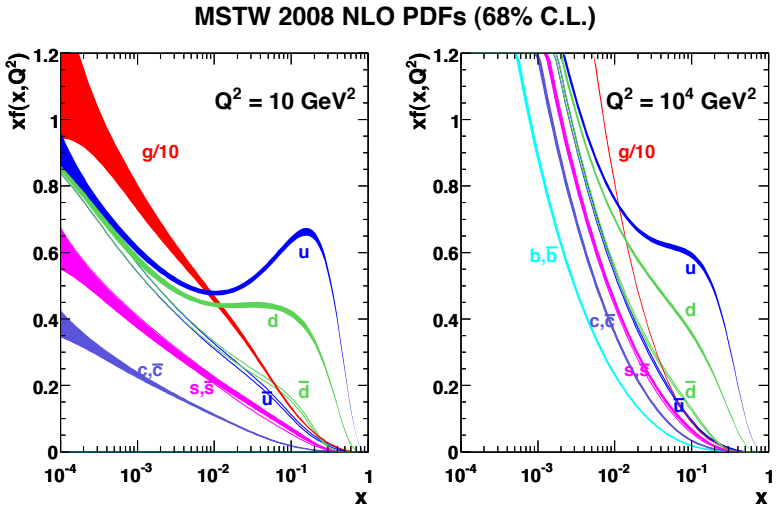

Figure 4.2: *The parton distribution functions, $f(x, Q^2)$, for the quarks and the gluon, given as a function of the momentum fraction x. The PDFs are parameterised by MSTW08 and given for momentum transfer scales of $Q^2 = 10$ GeV^2 on the left and $Q^2 = 10^4$ GeV^2 on the right. The bands denote the 68% confidence level uncertainties [58].*

4.2 Higgs events in ATLAS

The search for the Higgs boson and the study of its properties is one of the main goals of the ATLAS and CMS experiments. There are various production and decay modes in which the SM Higgs boson can be analysed. The primary production and decay modes, in the context of the LHC pp collisions, are discussed in this section.

The production cross sections as well as the decay branching fractions depend on the mass of the involved particles, because the Higgs boson couples to massive fermions, f, and massive bosons, V, according to:

$$g_{Hf\bar{f}} = \frac{m_f}{v}\,, \quad g_{HVV} = \frac{2m_V^2}{v} \tag{4.2}$$

where $v = 246$ GeV is the vacuum expectation value [18]. This implies that the primary mechanisms for both Higgs boson production and decay involve the coupling to W and Z bosons, and to the third generation of quarks and leptons. Coupling to

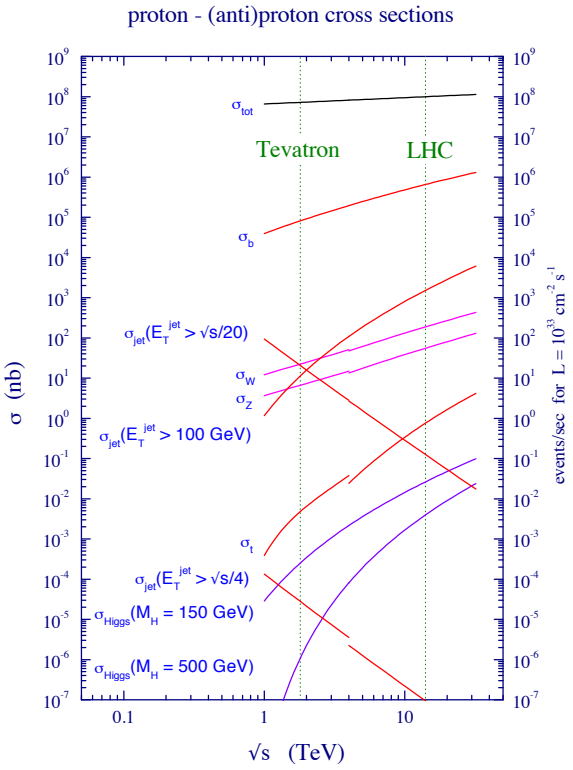

Figure 4.3: *The predicted SM cross sections of several benchmark processes as a function of the centre-of-mass energy $\sqrt{s}$. The design energy of the LHC, being $\sqrt{s} = 14$ TeV, is indicated [57].*

massless particles is induced via a loop in which the Higgs boson couples either to a virtual $t\bar{t}$ pair or to a virtual W^+W^- pair.

4.2.1 Production mechanisms

The Higgs boson can be produced through different mechanisms. The four main mechanisms include:

- **Gluon gluon fusion** (ggF), denoted as $gg \to H$, is mediated by a top quark loop, as shown in figure 4.4a. Lighter quark contributions are in principle possible, but suppressed proportional to m_q^2. Gluon gluon fusion is the dominant

production mode at the LHC, mainly because of the large Higgs coupling to the heavy top quark. What also contributes is the fact that the dynamics is dictated by the strong interaction, where at leading order the cross section is proportional to α_s^2. The ggF mechanism is the primary mechanism considered in the Higgs boson searches with leptonic final states.

- **Vector boson fusion** (VBF), denoted as $qq \to q'q'H$, is directed by the electroweak interaction and has the second largest cross section. The Higgs boson is produced via the scattering of two quarks, which is mediated by the exchange of a W or Z boson, where the Higgs boson is radiated off the vector boson propagator, as shown in figure 4.4b. The scattered quarks give rise to two hard jets in the forward and backward region of the detector, resulting in a clear signature that can be used to distinguish the Higgs signal from background events.

- **Associated production with a vector boson** (VH), denoted as $q\bar{q}' \to WH$ or ZH, is also called Higgs strahlung since the Higgs boson radiates off a vector boson, as shown in figure 4.4c. This mechanism has a substantial lower cross section since this process is kinematically suppressed due to the higher energy required to create a vector boson aside from a Higgs boson.

- **Associated production with a $t\bar{t}$ pair** (ttH), denoted as $gg \to t\bar{t}H$, is shown in figure 4.4d. This process also requires gluons with high momenta in order to allow for production of two top quarks and a Higgs boson, hence the low cross section.

The cross sections of the production mechanisms as a function of the Higgs boson mass are given in figure 4.5, where the cross sections are determined for pp collisions at a centre-of-mass energy of 8 TeV. The order up to which the cross sections are determined differs and is specified in the figure. All production cross sections are determined including at least next-to-leading-order (NLO) QCD corrections. This is important, as for example the gluon-gluon fusion cross section increases with approximately 80% by including this correction. Additionally, mostly also NLO electroweak (EW) corrections are included. Further corrections include next-to-next-to-leading-order (NNLO) and nex-to-next-to-leading-log (NNLL) QCD corrections. The calculation of the Feynman diagrams constituting these higher order corrections is highly comprehensive, which explains why no orders higher than NNLO are so far included.

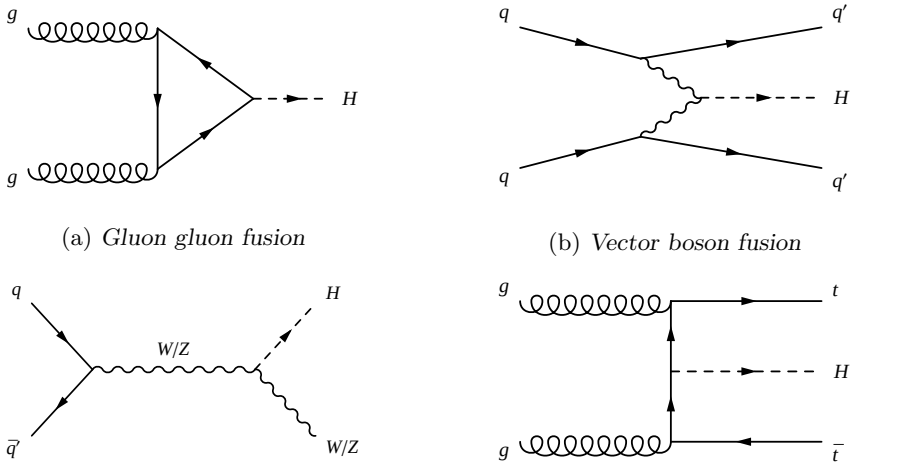

(a) *Gluon gluon fusion*

(b) *Vector boson fusion*

(c) *Higgs strahlung*

(d) *Associated production with top quarks*

Figure 4.4: *Leading order Feynman diagrams of the four main SM Higgs production mechanisms at the LHC.*

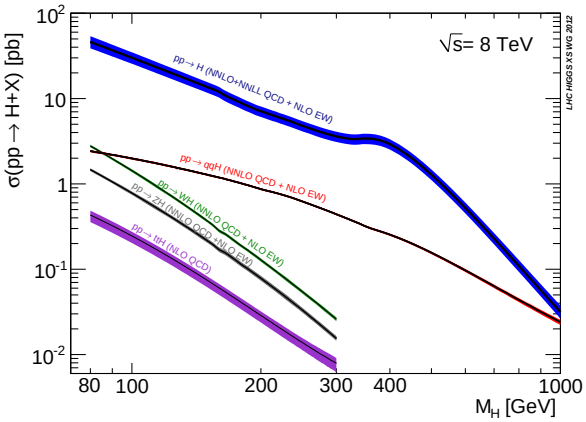

Figure 4.5: *Production cross sections for the SM Higgs boson as a function of its mass, produced in pp collisions at a centre-of-mass energy of 8 TeV. The bands include the theoretical uncertainties [59].*

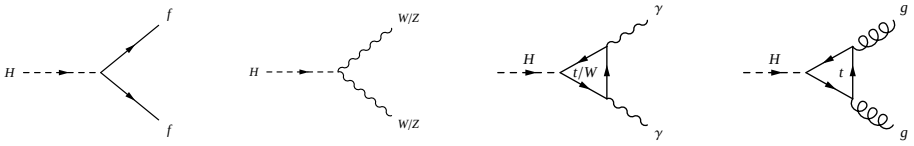

(a) (b) (c) (d)

Figure 4.6: *Feynman diagrams of the Higgs boson decay modes, including couplings to massive fermions (a) and bosons (b), and loop induced couplings to photons (c) and gluons (d).*

4.2.2 Decay channels

The Higgs boson can decay into any kinematically allowed pair of massive fermions or bosons, or indirectly into massless particles via a quark or weak boson loop. Figure 4.6 shows the Feynman diagrams of the different Higgs boson decay modes.

Aside of the coupling strengths, the decay branching fractions depend also on the Higgs mass itself, as for lower Higgs masses, decays into heavier particles are kinematically suppressed. Figure 4.7a shows the branching fractions as a function of the Higgs mass for the dominant decay channels. Once the Higgs mass is established, its branching fractions are uniquely defined.

The total decay width of the Higgs boson depends on its mass as well. Figure 4.7b shows the Higgs decay width, Γ_H, as a function of the Higgs boson mass. In the low mass range the Higgs resonance is very narrow, with $\Gamma_H < 10$ MeV, but the width increases rapidly with the mass and at large masses the width is even larger than the Higgs mass itself. For $M_H = 125$ GeV the decay width yields $\Gamma_H = 4.1$ MeV, which corresponds to a life time of only 6.8×10^{-22} s. This explains why only the decay products of the Higgs boson can be experimentally detected.

The sensitivity for observing the Higgs boson in a specific decay channel does not only depend on its branching fraction, also the preceding production mode, the reconstructed mass resolution, the signal selection efficiency and the amount of background in the final state have to be taken into account. For example, around $M_H = 125$ GeV the dominant decay mode is $H \to b\bar{b}$, however, as its final state has to be extracted from hadronic collision data, which involve a lot of QCD activity, it is hard to distinguish this signal from the background. Therefore this decay mode has to be studied

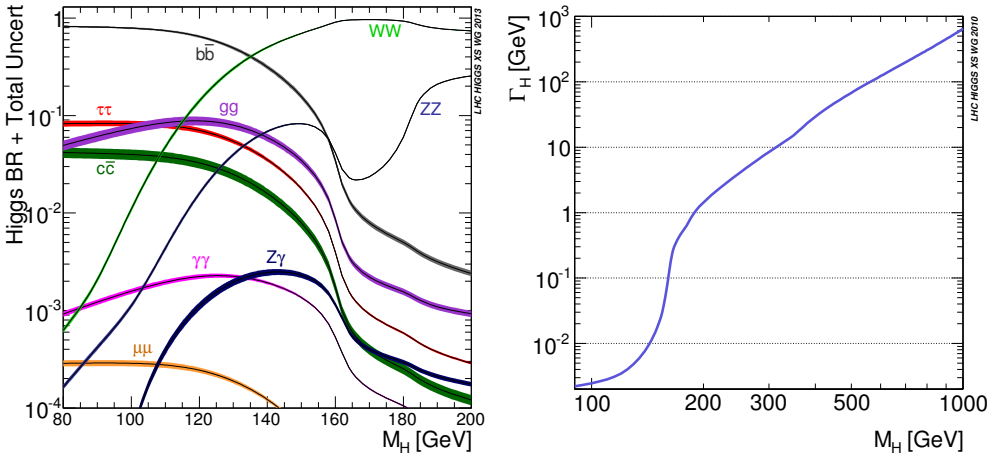

(a) (b)

Figure 4.7: *(a) Decay branching fractions of the SM Higgs boson as a function of its mass. The bands indicate the theoretical uncertainties. (b) Total decay width, (Γ_H), of the Higgs boson as a function of its mass. [59]*

in combination with production through VBF, resulting in a lower total cross section of this process.

The most sensitive search channels are the ones with bosons and leptons in the final state, as these yield a clear signature against the background. For $M_H = 125$ GeV, highest sensitivity is obtained for the $H \to \gamma\gamma$, $H \to ZZ^* \to 4\ell$ and $H \to WW^* \to \ell\nu\ell\nu$ channels, produced through ggF. Since $2M_{W,Z} > M_H$, one of the weak bosons in the two latter decays must be virtual. The $\gamma\gamma$ and ZZ^* decay modes are particularly interesting for the Higgs mass measurement, because the final states can be fully reconstructed. The ZZ^* channel has an exceptionally clean signature, facilitating background reduction. The $\gamma\gamma$ channel deals with much more background, but as it falls off smoothly a mass peak can be distinguished. The WW^* channel has poor mass resolution due to the undetectable neutrinos in the final state, however, its branching ratio is large, allowing for a high statistics Higgs discovery.

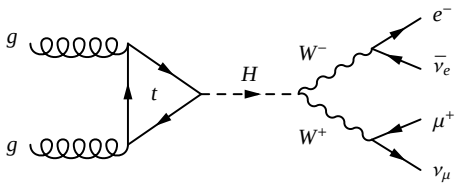

Figure 4.8: *Leading order Feynman diagram of the $gg \to H \to W^+W^- \to \ell^+\nu\ell^-\bar{\nu}$ Higgs signal.*

4.2.3 $H \to W^+W^-$ decay channel

The WW^* channel has a branching fraction of 21.5% for a 125 GeV Higgs mass. This includes all possible final state. As a W-boson can decay both leptonically and hadronically, these final states involve $\ell\nu\ell\nu$, $\ell\nu qq$ and $qqqq$. Given the large QCD background, the most sensitive final state is the fully leptonic decay.

Due to the neutrinos in the final state the Higgs boson mass cannot be precisely determined. Therefore the search for the Higgs boson is limited to a counting experiment of the events in broad bins of the reconstructed Higgs mass. In the rate and properties analyses, events with two leptons of opposite charge and with substantial missing energy are selected, where additionally up to two jets are considered. To increase the signal selection efficiency the analyses are performed in mutually exclusive categories that are determined on the basis of the lepton flavour combination and the number of jets in the final state. Different backgrounds are dominant within the different categories, as will be detailed in section 6.4.2. The relevant categories for the analysis presented in this thesis are the 0-jet and 1-jet channel, that refer to the presence of either no or one jet in the final state.

In principle, all production mechanisms are considered in this channel, however, given the total statistics of the Run I dataset, only the ggF production mode allows for a discovery and is considered in the Higgs properties measurements. Figure 4.8 shows the LO Feynman diagram of production through ggF and decay into the fully leptonic final state, where the $e\nu\mu\nu$ final state is depicted. This is the signal studied in this thesis. Only electrons and muons are considered in the final state. τ-leptons are not explicitly considered. In the hadronic τ decay the signal is difficult to distinguish from the background, and is mostly removed by cuts that are used to reduce the

background. The leptonic τ decays give rise to a an electron or a muon and two neutrinos, which results in a final state similar to the one considered. However, due to the larger total missing energy, also these events are mostly removed by the event selections.

4.3 Event simulation

The Higgs signal processes as well as the SM background processes are simulated, as to be able to compare the real collision data with the theoretical predictions. Additionally, simulations have been used to get to understand the ATLAS experiment and to test its performance. The event simulation comprises four steps:

- **Event generation**: in the first step, the pp collisions and event structures are simulated. To do so, event generators are used that produce large samples of simulated events;
- **Detector simulation**: the propagation of the simulated final state particles through the detector and their interactions with its material are subsequently simulated to allow for comparison of simulated events with collision data that are detected in ATLAS;
- **Digitisation**: the propagation of particles through the detector results in energy deposits that give rise to electrical signals that are processed by the read-out electronics. The detector signals obtained from the energy deposits are simulated during the digitisation;
- **Even reconstruction**: like collision data, the simulated events are run through the trigger system and event reconstruction algorithms to define the physics objects produced in an event.

The event reconstruction used for both collision data and simulated data is the subject of section 4.4. In this section the event generation and detector simulation are further discussed. The specific simulation of the physics processes of interest for the analysis presented in this thesis is discussed in section 6.3.

4.3.1 Event generation

Given the quantum mechanical nature of particle physics, only the probability of the occurrence of a certain final state can be determined. Precise determination of this probability, as well as accurate comparison of data and simulations, requires large event samples. To acquire large samples of simulated data, event generators are used. The generators use random number Monte Carlo (MC) techniques to generate the interactions between the incoming partons, according to the cross section of the process under study. In this way the probabilities of the occurrence of different physics processes can be determined.

To simulate the complex event structure following from the initial pp interaction, the simulation process is split into several stages: the hard scatter, parton showering, hadronisation and the underlying event [56].

Hard scatter

The simulation of the hard scatter includes the determination of the matrix element, which is done perturbatively as discussed in section 4.1.2. Event generators that simulate the complete event structure, thus also including the parton showering, hadronisation and underlying event, calculate the matrix element up to leading order, with a fixed number of particles in the final state. Dedicated generators calculate the matrix element at NLO or even with NNLO corrections, but need interfacing with other generators to obtain the full event structure. Some physics processes are difficult to generate at NLO, in these cases, LO events are weighted with a so-called k-factor to obtain the NLO contribution, where the k-factor is the ratio of the cross sections of the LO and NLO processes. The largest uncertainties in the simulation of the hard scatter arise due to the uncertainties of the PDFs that are used to determine the momenta of the incoming partons, and the unaccounted for higher order diagrams.

Parton showers

The branching of the initial quarks and gluons is simulated in the process of parton showering. It includes the simulation of ISR and FSR. The branching of the quarks

and gluons ends when the particles reach energies in the order of 1 GeV. The result is a shower of partons emanating from the initial partons. Since the showering typically involves low momentum transfers, this process cannot be described perturbatively. Instead the parton shower models are tuned to data distributions as to precisely describe the data.

The branching of the particles implies the inclusion of higher order effects. This results in diagrams that are identical to the ones obtained by including higher order matrix elements in the hard interaction. To avoid double counting of these diagrams, a matching scheme is used to define if either the hard scatter or the parton showering is used to generate a specific event, where hard and large angle parton emissions are assigned to the hard scatter and soft and collinear emissions to the parton showering. The scheme that is used for the relevant processes described in this thesis is the MLM scheme [60].

Hadronisation

Hadronisation ensures that the colour charged particles emanating from parton showers form colour neutral particles, as required by confinement. Again, the involved processes are too soft to be described with perturbation theory, therefore the simulation of the hadronisation is performed using approximations derived from phenomenological models.

Underlying event and pile-up

The underlying event represents the additional activity in the event that is not associated to the partons that took part in the hard scatter. This can also include another interaction of two incoming partons, resulting in so called multiple interactions. The processes occurring as part of the underlying event involve mostly low momentum transfer and are therefore simulated on the basis of phenomenological models. Pile-up is taken into account by adding separately generated events.

4.3.2 Event generators

Event generation is independent from the detector simulation, offering the possibility to use a variety of independent event generators that are used by various experiments. Most event generators are capable of both generating SM processes and beyond the Standard Model processes. The generators used in the analysis presented in this thesis are briefly described below.

There are three all-round generators that simulate both the hard interaction at leading order, and the underlying event, and provide the parton showering, hadronisation and decay. These generators are called PYTHIA [61,62], HERWIG [63] and SHERPA [64]. The basic principles of these generators are the same, but the approach of the colour flow and parton showering differs slightly. The calculation of the hard interaction includes the matrix elements of $2 \to 2$ and $2 \to 1$ processes only.

There are also matrix element generators that do calculate $2 \to n$ processes, however, these generators require interfacing with one of the aforementioned generators to establish the parton showering and hadronisation. The $2 \to n$ generators include ALPGEN [65] and MADGRAPH [66, 67] .

Finally, there are also matrix element generators that calculate the matrix element including NLO QCD corrections, but also these need interfacing with all-round generators. The used NLO generators are MC@NLO [68] and POWHEG [69].

4.3.3 Detector modelling

The output of the event generation is a sample of simulated events, each with a complete list of the properties of the final state particles in the event. To allow for comparison of the simulated events with the collision data, the next step is to model the propagation of the final state particles through the ATLAS detector. To simulate the geometry of the ATLAS detector as well as the propagation of the particles through the detector, a package, called GEANT4 [70], is used.

The tracking of the particles through the detector involves the simulation of particle interactions with the detector material and possible decay processes. Furthermore, the detector response to a particle that passes through active detector material is

simulated. This includes the simulation of the energy measurements and subsequent response of the read-out electronics. Subsequently, the digitisation into detector signals takes place. The result is an event format that is equal to that of real collision data.

Although the detector geometry is simulated in great detail, there is a limit to the precision with which this is possible. It is not feasible to take into account every single cable. Moreover, the time needed to simulate an event has to be kept within limits. This results in small differences between data and simulation that should be taken into account in the physics analyses. An additional uncertainty arises due to the finite precision with which the positions of detector parts within ATLAS are known. Inevitable misalignments of detector parts in ATLAS result in poorer resolution of the simulation. Nevertheless, as the understanding of the ATLAS detector improves, differences can be reduced by introduction of for example scale factors and momentum smearing in the data analyses.

The full event simulation, including the detector modelling, requires several CPU minutes for an average event. This length is the result of the extensive physics models needed to describe the interaction with the detector, notably with the calorimeters, in combination with the detailed detector description. To allow for faster simulations, also simulations including a simplified detector description are performed, called ATLFAST II simulations [71]. These simulation include the tracking in full detail, but instead of simulating energy deposits in the calorimeters also in full detail, parametrisations of the particles showers are used. The resulting samples are validated by comparing them to the full reconstruction samples and can subsequently be used to complement the statistics acquired with full detector simulations. By using the fast reconstruction, the simulation time is reduced by a factor of 10 to 20.

After the event simulation an detector modelling the simulated events are reconstructed. This event reconstruction is applied both to simulated events and events from collision data.

4.4 Event and object reconstruction

Most interesting particles created in hard interactions decay before they can be detected, therefore only the decay products are measured with the ATLAS detector. By identifying these final state particles, an event can be reconstructed and the original particle created during the hard scatter can be recovered. The final state particles are detected and measured on the basis of the trace of electrical signals they leave in the detector. To use this information in physics analyses the traces have to be identified with the original objects. The physics objects include electrons, muons, taus, photons and jets. Neutrinos can be indirectly detected by studying the momentum balance in the transverse plane, which leads to the reconstruction of missing transverse energy that can be associated to neutrinos. Each physics object has a dedicated reconstruction algorithm with which the particles are identified and their properties reconstructed. Inner detector tracks are used to reconstruct the primary and secondary vertices of an event and as such the physics objects are combined into a reconstructed event. In this chapter the reconstruction of tracks, electrons, muons, jets and missing transverse energy is discussed, as these objects play an important role in the analysis presented in this thesis. As τ-leptons are not directly considered in the analysis and neutrinos are evaluated as missing transverse energy, in the following the notion of leptons refers to electrons and muons only.

4.4.1 Track and vertices

The reconstruction of charged particles involves the reconstruction of tracks in the inner detector that may subsequently be combined with measurements in the calorimeters and muon spectrometer to define e.g. muons and electrons. The track reconstruction algorithm, called NEWT [72], has been developed as to be robust against the high track multiplicities.

The tracking starts with the conversion of the raw data from the pixel, SCT and TRT into space-points and clusters. Then track finding is performed, using inside-out tracking. Firstly, track seeds are formed on the basis of the space-points in the pixel detector and the first layer of the SCT. Then these seeds are extended with hits in the other layers of the SCT to obtain track candidates. In this process hits that

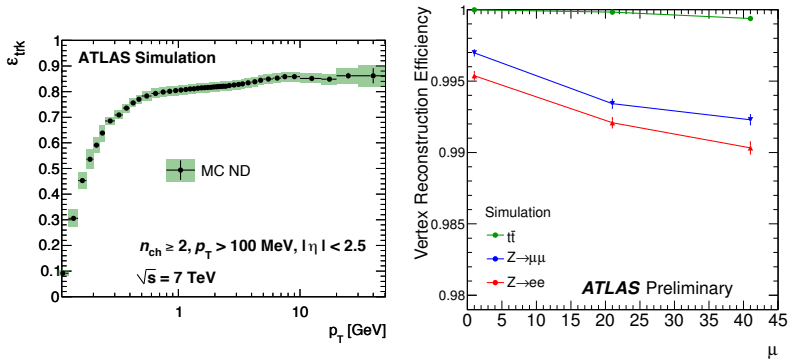

(a) *Track reconstruction efficiency* (b) *Vertex reconstruction efficiency*

Figure 4.9: *(a) The track reconstruction efficiency as a function of p_T, derived from non-diffractive MC, simulated at $\sqrt{s} = 7$ TeV. Statistical uncertainties are represented by the black lines, and the systematic uncertainties are shown as green bands [73]. (b) The vertex reconstruction efficiency as a function of the average number of pp interactions per bunch crossing for simulations of three physics signatures. The points are calculated before any event selection is applied [74].*

lay outside the expected track are called outliers, while so-called holes correspond to the absence of expected hits. Quality cuts are defined on the basis of good hits, holes and outliers and applied to the track candidates. Finally, the track candidates are extended to the TRT. Only tracks of $p_T > 100$ MeV and with at least nine hits and no holes in the pixel detector are considered as to reduce the number of fake tracks. Figure 4.9a shows the track reconstruction efficiency for simulated pions as a function of p_T. The efficiency increases with the p_T of the particles and reaches close to 90% for high p_T tracks.

The tracks are subsequently used to define the vertices of an event [75]. These can be primary vertices, indicating the interaction points of the incoming partons, and secondary vertices that mark particle decays. The vertex reconstruction consist of two steps: firstly, the vertex finding algorithm is run to associate tracks to vertices, and secondly the vertex fitting algorithm determines the position and other parameters of the vertex. This process is iterated several times. In the first iteration exactly one vertex is fitted, after which the tracks that are incompatible with this vertex with more than 7σ are used as seeds for new vertices. This process continues until no new vertices with at least two tracks van be found.

If there is more than one vertex in the event, the one with the highest sum of the p_T^2 of the associated tracks is selected as the one corresponding to the hard scatter and is referred to as the primary vertex. The vertex reconstruction efficiency is shown in figure 4.9b as a function of the average number of interactions per bunch crossing, determined for MC simulations of $t\bar{t}$, $Z \to \mu^+\mu^-$ and $Z \to e^+e^-$ events. The efficiency decreases slightly with increasing pile-up due to an increase of fake tracks and merging of vertices of nearby interactions. Nevertheless, over the full range the vertex reconstruction efficiency is higher than 99%.

4.4.2 Muons

High precision tracking of muons is performed using the inner detector (ID) and muon spectrometer (MS). To a lesser extend also information from the calorimeters is used. The combination of ID and MS information results in high purity muon identification and good momentum resolution for muons ranging from the GeV up to the TeV scale. Using the available information of the sub-detectors four different types of muons are identified [76]:

- **Stand-alone (SA) muons** are reconstructed using only information of the MS. This is possible, since three layers of muon chambers enable the measurement of the curvature of the tracks and hence the determination of the muon momentum. To obtain the required parameters of the muon track at the interaction point, the SA track is extrapolated back to the point of closest approach to the beam line, whereby the estimated energy loss of the muons in the calorimeters is taken into account. SA muons are mostly used to cover the range $2.5 < |\eta| < 2.7$, which is not covered by CB muons, due to the absence of ID tracks in this region;
- **Combined (CB) muons** are reconstructed by matching ID and MS tracks. The matching of tracks is performed by a statistical combination of the track parameters of the SA and ID tracks. CB muons are most frequently used in physics analyses, as the combined tracks have the best momentum resolution and the sample has minimal contamination of muons originating from secondary interactions and decays of long-lived particles. CB muons cover the range $|\eta| < 2.5$;

- **Segment tagged (ST) muons** are formed from ID tracks that are extrapolated to the MS and associated with at least one muon track segment in an MDT or CSC chamber. These ST muons are mostly used to increase the acceptance of muons that cross only one layer of MS chambers, which may be due to the low p_T of the muon or because it traverses a region with reduced MS acceptance ($1.1 < |\eta| < 1.3$), and as such fall outside the selection criteria of SA and CB muons;
- **Calorimeter-tagged (CaloTag) muons** are identified with an ID track that is matched to an energy deposit in the calorimeter that is compatible with a minimum ionising particle. This type of muon has low purity, but it recovers the acceptance in the gap region of the MS of $|\eta| < 0.1$, where CB muons have reduced efficiency.

There are two reconstruction algorithms for muons, denoted as chain 1 [77] and chain 2 [78]. Both reconstruct these different muon types. The algorithms have similar performance and have been merged into a unified chain that will be used from 2015 onwards. The analysis presented in this thesis still uses the muons reconstructed with chain 1, and considers CB and ST muons.

The reconstruction efficiency of the CB muons is a combination of the ID and MS reconstruction efficiencies and the matching efficiency. To determine the reconstruction efficiency, a tag-and-probe method [79] is applied to both data and simulations of $Z \to \mu\mu$ events that are selected by requiring two oppositely charged isolated muons, with an invariant mass close to the Z boson mass.. Additionally data and MC samples of J/Ψ events are used to cover the low p_T range. In the tag-and-probe method, one muon is required to be a CB muon. This is the tag muon. The other muon, which is the probe, is required to be a CaloTag muon. Then the efficiency is determined as the fraction of the probe muons that are reconstructed as CB muons. The reconstruction efficiency of the other muon types is also determined using tag-and-probe methods.

Figure 4.10a shows the reconstruction efficiencies of the various muon types as a function of the pseudorapidity. The CB+ST muons have an efficiency of ~ 0.98 over the full η range, except for the region $|\eta| < 0.1$, which could be compensated with the inclusion of CaloTag muons. Furthermore, by comparing the CB and CB+ST results one can see that the ST muons nicely compensate for the reduced efficiency of CB

muons in the transition regions. The efficiencies determined for data and simulations agree within 0.5%, except for the region $1.5 < \eta < 2.2$. This is due to the fact that some non-operational pixel modules in this region were included in the simulations.

Figure 4.10b shows the reconstruction efficiency of CB+ST muons as a function of p_T. The efficiency is expected to be independent of the transverse momentum of the muons, which is confirmed by these experimental results. Finally, the reconstruction efficiency is also studied as a function of the average number of interactions per bunch-crossing. Figure 4.10c shows the reconstruction efficiency as a function of pile-up and indicates good stability. Only at values of $\langle\mu\rangle > 35$ a drop in efficiency of 2% is observed, which can be explained by the reduced ID reconstruction efficiency under these high pile-up conditions. The small difference between data and simulations is the result of an additional selection requirement of one hit in the inner pixel detector layer that has a different efficiency for data and simulations.

To ensure similar reconstruction efficiencies between data and MC, which is necessary to make precise comparisons in the physics analyses, so called scale factors (SF) are applied to the MC events. A SF is calculated as the ratio of the Data and MC efficiencies: $SF \equiv \epsilon^{Data}/\epsilon^{MC}$, and determined for every efficiency discrepancy between data and MC. Scale factors for the efficiency and momentum of muons are typically in the order of a per mille.

4.4.3 Electrons

Electrons created in a collision, traverse the inner detector, 'leaving' a track, and are stopped in the electromagnetic calorimeter. The reconstruction of an electron involves identification of clusters of energy deposits in the calorimeter, refitting of tracks reconstructed in the inner detector and finally matching the two to obtain an electron candidate.

The energy clusters are seeded from energy deposits with $E_T > 2.5$ GeV, using a sliding window algorithm [80] with a fixed window of 3×5 in units of 0.025×0.025 in (η, ϕ) space. The identified seed clusters are subsequently matched with tracks.

The track reconstruction described in section 4.4.1 is initially used to reconstruct all tracks, but is inefficient for electron tracks as energy loss due to bremsstrahlung, which

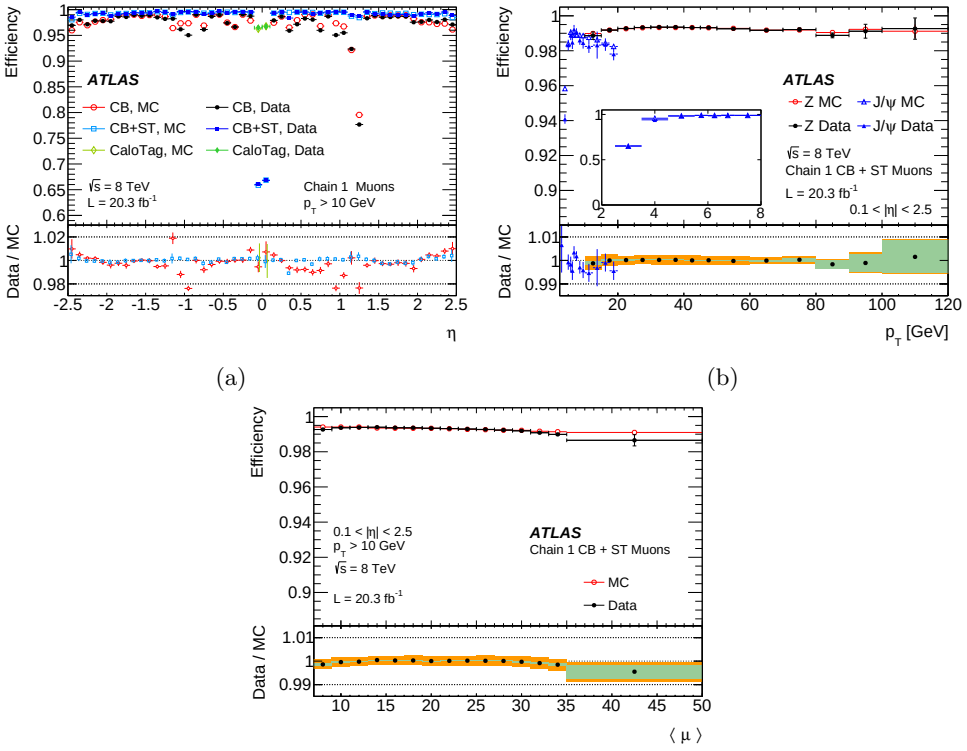

Figure 4.10: *The muon reconstruction efficiencies as a function of $|\eta|$ (a), p_T (b) and $\langle\mu\rangle$ (c), measured in $Z \to \mu\mu$ events. The insert in (b) details the efficiency in the low p_T region, measured in $J/\Psi \to \mu\mu$ events. The error bars indicate the statistical uncertainty. The lower panels in the plots show the ratio between the measured and predicted efficiencies. The error bars on this ratio in (a) are the combination of statistical and systematic uncertainties. In (b) and (c), the green areas depict the pure statistical uncertainty, while the orange areas reflect the systematic uncertainties [76].*

is significant for electrons, is not taken into account. Therefore, as of 2012, electron track candidates are refitted with the Gaussian Sum Filter (GSF) algorithm [81]. The GSF algorithm models the energy loss as a weighted sum of Gaussian components, instead of modelling it as a single Gaussian, and as such takes into account alterations in the curvature of the trajectory due to bremsstrahlung. This leads to a significant improvement in the reconstruction efficiency, as will be shown.

Having the clusters and refitted tracks defined, tracks with $p_T > 0.5$ GeV are extrapolated from their last measurement point to the middle layer of the EM calorimeter. The tracks are matched to a cluster seed if the η and ϕ coordinates of the track and cluster seed match within $|\eta| < 0.05$ and $|\phi| < 0.1$.

Finally, the four-momentum of the electron candidate is determined. The (η, ϕ) coordinates are taken from the track, unless the track has less than four silicon hits, in which case the η coordinate is taken from the EM cluster. The energy of the electron candidate is determined by enlarging the cluster size to 3×7 and comprises four contributions [82]: the estimated energy deposit in the material in front of the EM calorimeter, the measured energy deposit in the cluster, the estimated energy deposit outside the cluster and the estimated energy deposit beyond the EM calorimeter.

At this stage, also electrons emanating from photon conversions and jets, as well as jets that are misidentified as electrons are amongst the electron candidates. Therefore quality cuts are applied to the electron candidates. There are three sets of selections, called *loose*, *medium* and *tight*, that provide increasing background rejection. The cuts are optimised in bins of η and E_T, as to take into account the detector structure and provide good separation between signal electrons and background electrons. In the analysis presented in this thesis *tight++* electrons are used, where the ++ indicates that the criteria have been optimised for the higher pile-up conditions. The quality cuts include for example specific cuts on the number of hits and holes of inner detector tracks; the exact cuts used in the three sets are listed in e.g. [80].

The reconstruction efficiency is determined using a tag-and-probe method on $Z \to ee$ events, where the tag electron should be a tight electron. The efficiency is defined as the number of times the probe electron is reconstructed as a tight electron as well. Figure 4.11 shows the reconstruction efficiency in data and MC as a function of η and E_T, both for the full 2011 dataset and the early 2012 dataset. The use of the GSF algorithm explains the increase in efficiency for the 2012 data.

Figure 4.12 shows the identification efficiency as a function of the number of reconstructed primary vertices in the event for the three different sets of selection criteria. The tight selection has a lower efficiency, but the purity of the signal is larger. The flatness of the distributions indicates that the reconstruction and identification is robust against pile-up.

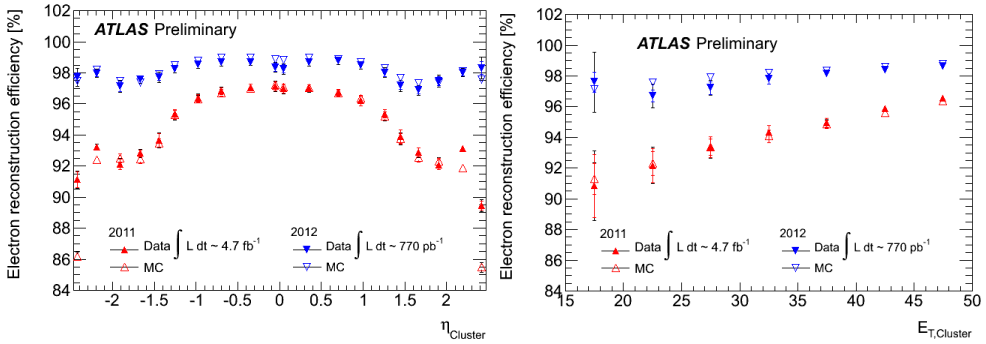

(a) (b)

Figure 4.11: *The electron reconstruction efficiency in data and MC as a function of the η of the EM cluster (a) and E_T (b) for the full 2011 dataset and the early 2012 dataset [83].*

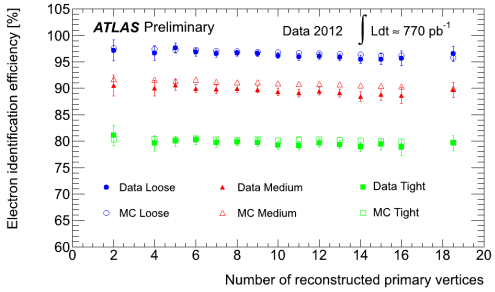

Figure 4.12: *The electron identification efficiency as a function of the number of reconstructed primary vertices, given for the three sets of selection criteria [83].*

The differences in the efficiencies between data and MC are corrected for by scale factors that are applied to the MC events.

4.4.4 Missing transverse energy

Missing transverse energy, E_T^{miss}, is defined as the magnitude of the momentum imbalance in the transverse plane. In this plane momentum balance is expected, as the incoming particles have mostly negligible transverse momentum. A net transverse momentum may therefore signify that undetectable particles, like neutrinos or weakly interacting supersymmetric particles, were produced in the collision. The E_T^{miss} variable is of utmost importance in the analysis of the $H \to WW$ signal, as

it gives information about the transverse component of the neutrinos present in the final state.

The missing transverse energy, defined as $E_T^{\text{miss}} = \sqrt{(E_x^{\text{miss}})^2 + (E_y^{\text{miss}})^2}$, is the magnitude of the missing transverse momentum, $\vec{E}_T^{\text{miss}}$. The $\vec{E}_T^{\text{miss}}$ is reconstructed from the negative vector sum in the transverse plane of all particles detected in the pp collision [84]. The E_T^{miss} reconstruction is complicated, since the momentum balance is affected by detectable particles escaping the detector due to the non-hermetic detector coverage, misreconstruction of objects, calorimeter noise, pile-up events, cosmic rays and more. These contributions lead to fake E_T^{miss} and as such to a reduced resolution. Nevertheless, the reconstruction is optimised to reduce the effect of these contributions as much as possible. To compare the reconstructed E_T^{miss} to the actual missing transverse energy due to neutrinos, the so-called true missing transverse energy, $E_{T,\text{true}}^{\text{miss}}$, is used, which is derived from MC simulations as the sum of the transverse energy from all generated non-interacting particles in the event.

The E_T^{miss} is reconstructed on the basis of energy deposits in the calorimeters and muon spectrometer tracks. Therefore, the x and y components of E_T^{miss} can be calculated as:

$$E_{x(y)}^{\text{miss}} = E_{x(y)}^{\text{miss, calo}} + E_{x(y)}^{\text{miss},\mu} \tag{4.3}$$

where low-p_T tracks that do not reach up to the calorimeter, as well as inner detector muon tracks that are not matched to a muon spectrometer track, are also taken into account. The two terms in Eq 4.3 are referred to as the calorimeter and muon terms, and described below.

Calorimeter term

Rather than from the generic calorimeter cels with energy deposits, the calorimeter term is calculated from the clusters that are associated to reconstructed physics objects. This allows for calibration of the clusters according to the objects they belong to. The objects include: electrons, photons, hadronically decaying τ-leptons, jets and muons. Cells with energy deposits that are not associated with any of these

high-p_T objects, as well as low p_T tracks that did not enter the calorimeter, are also accounted for and assembled in the $E_T^{\text{miss, SoftTerm}}$ term [85]. The calorimeter term can be calculated as follows:

$$E_{x(y)}^{\text{miss, calo}} = E_{x(y)}^{\text{miss},e} + E_{x(y)}^{\text{miss},\gamma} + E_{x(y)}^{\text{miss},\tau} + E_{x(y)}^{\text{miss, jets}} + E_{x(y)}^{\text{miss, SoftTerm}} + E_{x(y)}^{\text{miss},\mu} \quad (4.4)$$

Each term is calculated from the negative sum of calibrated cell energies inside the corresponding objects, where only cells up to $|\eta| < 2.7$ are considered. Objects are added to the calorimeter term in the given order, such that in case of overlapping clusters only the higher priority object is considered. The term $E_{x(y)}^{\text{miss},\mu}$ is only added for non isolated and forward muons, as will be addressed in the next paragraph.

Muon term

The muon term is calculated as the negative sum of the momenta of muon tracks with $|\eta| < 2.7$. In the region $|\eta| < 2.5$, only combined muons are considered as to reduce the contribution of fake muons. In the region $2.5 < |\eta| < 2.7$ standalone tracks are used and in regions with reduced muon spectrometer coverage also segment-tagged muons are taken into account.

Muons lose a small part of their energy in the calorimeter, which should be taken into account in order to avoid double counting of energy. In the region $|\eta| < 2.5$ isolated muons are not considered in the calorimeter term, $E_{x(y)}^{\text{miss},\mu}$, as combined muon tracks are already corrected for the energy loss in the calorimeters. For non-isolated CB muons this approach is not possible, as their energy deposit in the calorimeter cannot be resolved from the energy deposits of nearby particles. Therefore the expected energy of non-isolated muons is taken into account in the $E_{x(y)}^{\text{miss},\mu}$ calorimeter term, and complemented in the muon term with the p_T of the muon track, measured after energy loss. In the region $2.5 < |\eta| < 2.7$ the latter approach is used both for isolated and non-isolated muons, since there is no inner detector track matched to these muons.

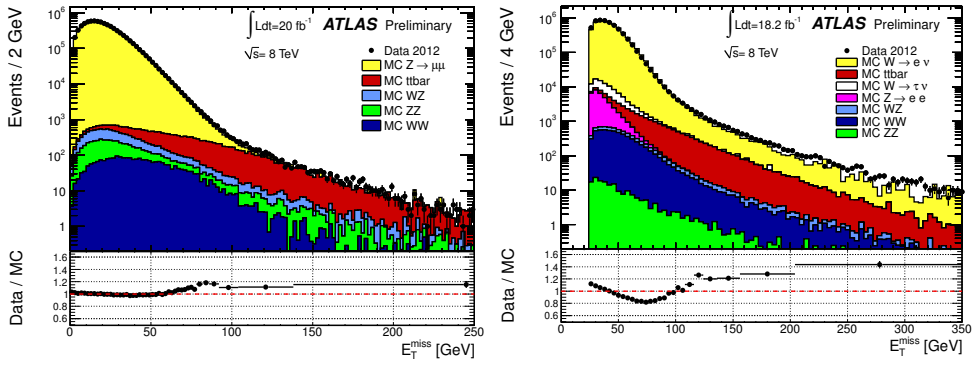

(a) (b)

Figure 4.13: *The distributions of E_T^{miss} in $Z \to \mu\mu$ (a) and $W \to e\nu$ (b) events, comparing the 2012 dataset with MC simulations. The MC samples are superimposed. The lower panels indicate the ratio of data and MC events [85].*

Performance

The E_T^{miss} performance has primarily been studied using $Z \to \ell\ell$ and $W \to \ell\nu$ events. While in the latter process the neutrino in the final state is a source of real E_T^{miss}, the final state of the former does not include E_T^{miss}, allowing to study the resolution of the E_T^{miss} variable. Figure 4.13 shows the distributions of E_T^{miss} for data and MC simulations for $Z \to \mu\mu$ and $W \to e\nu$ events. Similar distributions are obtained for other final state flavour combinations. The data resemble the full 2012 dataset. The MC distributions, including signal and backgrounds, are superimposed, where each MC sample is weighted with its corresponding cross section and the total MC expectation is normalised to the number of events in data. Good agreement between data and MC is observed for $Z \to \ell\ell$, while $W \to \ell\nu$ has a small data-MC discrepancy at low E_T^{miss} values. This may partly be caused by the fact that the QCD background, which predominantly populates the region of low E_T^{miss}, is not included in the MC expectations [86].

The E_T^{miss} resolution decreases with increasing pile-up, because especially the Soft-Term is negatively affected by the increase of activity. To reduce this effect, various methods have been developed [86]. The soft term vertex fraction (STVF) method is applied in the analysis described in this thesis. In this method the $E_{x(y)}^{\text{miss, SoftTerm}}$

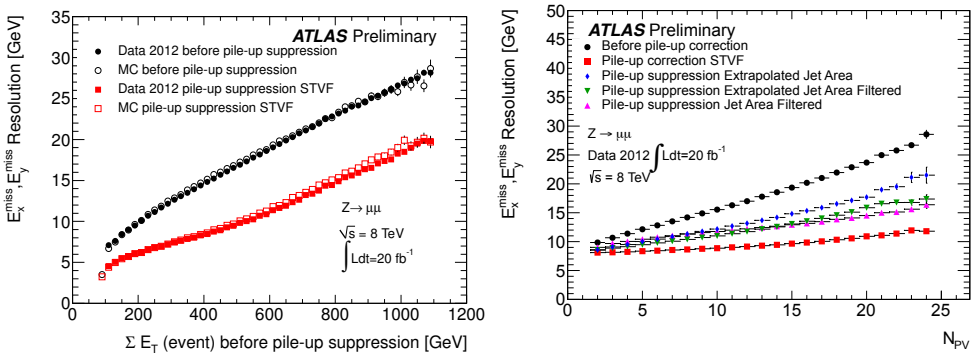

(a) (b)

Figure 4.14: *The $E_{x(y)}^{miss}$ resolution determined for $Z \to \mu\mu$ events, before and after pile-up suppression. (a) As a function of the total E_T in the event, compared for data and MC [85]. (b) As a function of the number of primary vertices in the event, determined for various pile-up suppression methods [86].*

term is scaled with the fraction of the momenta of soft tracks that are associated with the primary vertex.

Figure 4.14a shows the E_T^{miss} resolution, as a function of the total transverse energy in the event, compared for data and MC for $Z \to \mu\mu$ events, with and without applying the STVF method. Here, it has been assumed that the true values of $E_{x(y)}^{\text{miss}}$ are equal to zero, allowing to determine the resolution from the width of the combined distribution of E_x^{miss} and E_y^{miss}. Good agreement between the 2012 dataset and MC simulations is observed. The E_T^{miss} resolution clearly improves by applying the STVF method.

Figure 4.14b shows the resolution of $E_{x(y)}^{\text{miss}}$ as a function of the number of primary vertices in the event, being an indicator of the amount of pile-up. The resolution is determined for the 2012 dataset, with and without pile-up suppression, and shown for various methods. Again, significant improvement is observed with the STVF correction. Moreover, the resolution depends less on the number of primary vertices. If only events with muons with $p_T > 20$ GeV and a jet veto are considered, the pile-up dependence becomes almost negligible after application of the STVF method.

4.4.5 Jets

Quarks and gluons produced in the pp collisions are colour charged and therefore radiate off new quarks and gluons, resulting in a shower of new particles, as described in section 4.1.1. Such a shower is called a jet. Although the original parton that was produced in the initial interaction cannot be resolved, its energy can be estimated from the energies of the particles that constitute the jet. The challenge here is to determine which particles belong to the jet, and which emanated from other showers or pile-up events. Jet clustering algorithms are developed to this end.

Jets are reconstructed from energy deposits in the calorimeters. First, a topological clustering algorithm is used to cluster groups of cells with energy deposits [87]. These clusters serve as input for the jet clustering algorithm. The algorithm used in the analysis presented in this thesis is the anti-k_t jet algorithm [88]. This algorithm is preferred since it is both infrared and collinear safe, meaning that emission of soft or collinear gluons by the initial parton does not affect the outcome of the jet reconstruction.

The anti-k_t algorithm uses a procedure based on the sequential combination of clusters, based on their distance and momentum. For this, two distances are defined: the distance, d_{ij}, between objects i and j, and the distance, d_{iB}, between object i and the beam (B). The clustering then proceeds by identifying which of these two distances is smallest. If it is d_{ij}, the objects i and j are combined, while if it is d_{iB} i is defined as a jet and removed from the list of to be scanned objects. Then the distances are recalculated and the procedure is repeated until no objects are left.

More specifically, the two distances used in the anti-k_t algorithm are defined as:

$$d_{ij} = \min(1/p_{T,i}^2, 1/p_{T,j}^2)\frac{\Delta R_{ij}^2}{R^2} \tag{4.5}$$

$$d_{iB} = 1/p_{T,i}^2 \tag{4.6}$$

where $\Delta R_{ij}^2 = \Delta\phi_{ij}^2 + \Delta\eta_{ij}^2$, and R is a fixed resolution parameter chosen to be $R = 0.4$ for jets used in this thesis. The distances are defined such that low-p_T particles will cluster with hard objects, long before they cluster among themselves. If there are two

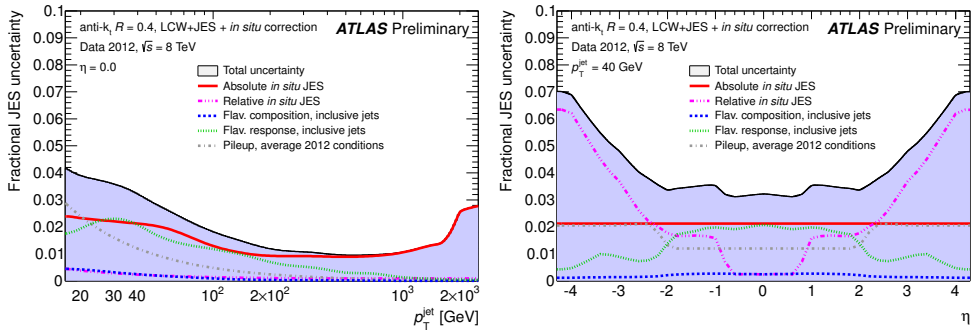

(a) (b)

Figure 4.15: *The systematic uncertainty on the jet energy scale (JES), as a function of p_T (a) and η (b). The total uncertainty is shown as the filled blue region. Average 2012 pile-up conditions were used. [90]*

hard objects within a distance of 2R, but with $\Delta R > R$, then two jets are formed. If $\Delta R < R$, the two hard particles will cluster within one jet.

The energy deposited in the calorimeter is not equal to the true energy of the jet. The main reason for this is the fact that the calorimeters are sampling devices and as such most energy is deposited in the absorber material. Hence, it is on the basis of the fraction of the energy deposited in the active medium that the true deposited energy has to be determined. Furthermore, also the limited calorimeter acceptance and pile-up induce differences between the true energy and measured energy. A jet energy calibration scheme is applied to relate the calorimeter response directly to the true jet energy. In the analysis presented in this thesis the EM+JES calibration scheme is used [89]. The calibration starts from the measured calorimeter energy at the electromagnetic (EM) energy scale, since the calorimeters have initially been calibrated on the basis of electromagnetic showers. Since hadronic showers have a lower energy density and hence a lower calorimeter response, corrections are applied in the calibration scheme to hadronic clusters. Then further corrections, that are mostly derived from MC studies of the calorimeter response to true jets, are applied. The calibration according to these corrections is referred to as the jet energy scale (JES). The uncertainty on the JES depends on the uncertainties of the various methods used to estimate the JES. These uncertainties as well as the total uncertainty on the JES are given in figure 4.15 as a function of the jet p_T and η.

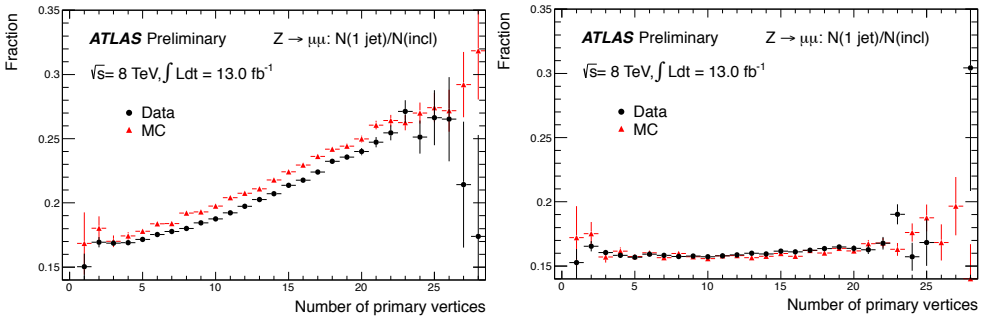

Figure 4.16: *Fraction of $Z \to \mu\mu$ + 1 jet events to all $Z \to \mu\mu$ candidates as a function of the number of primary vertices in the event, without (a) and with (b) the $|JVF| > 0.5$ requirement applied. Only statistical uncertainties are included [91].*

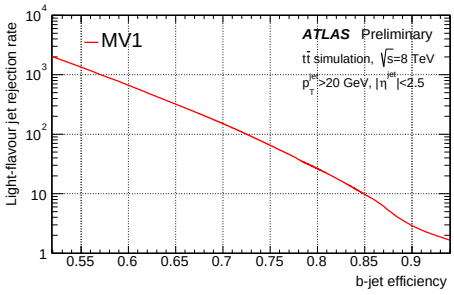

Figure 4.17: *The efficiency of tagging a b-jet as a function of the light jet rejection for a 8 TeV MC sample of $t\bar{t}$ events, obtained for the MV1 b-tagging algorithm [94].*

The reconstruction of jets is negatively affected by the additional jets that are produced with increasing pile-up. To correct for this, the jet vertex fraction (JVF) algorithm is used [89]. The value of the JVF defines which fraction of the transverse momentum of the tracks associated to a jet must be associated to the primary vertex. As such JVF=0 implies that all tracks associated to the jet are originating from pile-up events, while JVF=1 implies that the jet has no contributions of pile-up. Figure 4.16 shows the ratio of $Z \to \mu\mu$ + 1 jet events to $Z \to \mu\mu$ inclusive events, as a function of the number of reconstructed primary vertices, with (b) and without (a) JVF requirement. Clearly, the application of the JVF results in robustness against pile-up. In the analysis presented in this thesis, the JVF is required to be larger than 0.5.

Special attention is given to jets emanating from b-quarks. For this purpose b-tagging algorithm are developed [92]. With these algorithms can be determined if a jet stems from a b-quark, because B-mesons have a decay time of 1.5 ps, allowing to distinguish its decay vertex from the primary vertex. As top quarks mostly decay into b-quarks, the b-tagging enables identification of $t\bar{t}$ and single top events, which are backgrounds to the Higgs signal studied in this thesis. Several b-tagging algorithms are available. In this thesis the MV1 algorithm is used, which is a neural network that uses the output weights of other b-tag algorithms as input [93]. According to this algorithm, jets are assigned a weight that indicates if the jet is more probable to be a light jet or a b-jet. A cut on this weight is chosen depending on the preferred working point: a higher b-tagging efficiency or higher purity. Figure 4.17 shows the b-tag efficiency as a function of the light jet rejection, for a 8 TeV MC sample of $t\bar{t}$ events, with jets selected according to $p_T^{jet} > 20$ GeV and $|\eta^{jet}| < 2.5$. The figure shows that a higher efficiency comes at the cost of more light jet contamination. In the analysis presented in this thesis, the chosen operation point of the algorithm has a b-tagging efficiency of 85%, and a light flavour rejection of 10%.

This concludes the discussion of the reconstruction of the events that will be used in the analysis. The reconstructed physics objects can be used to reconstruct the rest frame of the Higgs boson. The algorithm that is developed for this purpose, is presented in the next chapter.

Chapter 5

Higgs rest frame reconstruction

5.1 Introduction

To distinguish different physics processes emanating from pp collisions the kinematical and topological properties of final state particles are used. These properties are exploited in the form of variables that can be employed in a data analysis, for example, to obtain an optimal signal-background ratio of events or to discriminate between processes according to the shapes of variables.

Typically, variables are defined in the frame of reference in which the final state particles are detected, called the laboratory (lab) frame. This is however not the frame in which the physics underlying an event is most apparent, because events are often subjected to a substantial Lorentz boost. These boosted events distort the shapes of the distributions of lab frame variables that as a result do not optimally reflect the physical characteristics of the studied process. Realising that physics is Lorentz invariant, it is possible to reconstruct events in a frame that does give an optimal account of the physics underlying events. This would be the rest frame of the parent particle(s).

In this chapter a method to reconstruct the Higgs rest frame of the $H \to WW \to \ell\nu\ell\nu$ decay is presented. Later on, the reconstructed rest frame can be used to reconstruct rest frame variables. The reconstruction of the rest frame for this particular decay is not a straightforward procedure, since it involves reconstruction of an unconstrained system due to the undetectable neutrinos in the final state. Hence, to allow for calculation of the Lorentz boost of the Higgs boson, first the momentum of the dineutrino system should be determined. This is the primary challenge in the development of the reconstruction method.

Before the discovery of the Higgs-like boson, the mass of the Higgs boson was an additional unknown parameter of the system. Various methods to constrain the system, and reconstruct the rest frame, were practiced, but were limited in precision. The discovery, however, gave rise to a measurement of the mass of the Higgs-like boson that could be used to constrain the system with higher precision. This makes the reconstruction method and resultant rest frame variables interesting to use in the analysis of the spin and parity of the Higgs-like boson. Thus, the reconstruction algorithm presented in this chapter is optimised for the spin and parity analysis of the Higgs-like boson.

The ultimate goal is to obtain rest frame variables that discriminate between the SM Higgs boson decay and decays of Higgs-like bosons with alternative J^{CP} hypotheses.

The algorithm is optimised for the reconstruction of the rest frame of the SM Higgs boson. Nevertheless, the alternative signal hypotheses can be evaluated using the same reconstruction algorithm. In sections 5.3 and 5.4 the reconstruction algorithm is formulated. Subsequently, the performance of the algorithm, both for the SM signal and the alternative hypotheses is discussed. Sections 5.5.1, 5.5.2 and 5.5.3 are devoted to the performance for reconstruction of the SM Higgs boson. In section 5.5.4 the physics constraints used in the algorithm are reassessed for the alternative hypotheses and the performance of the algorithm for these specific models is evaluated. Finally, section 5.5.5 gives a preview of the spin and parity sensitivity of the rest frame variables.

The figures and numbers presented throughout this chapter are extracted from the MC signal samples that are listed in section 6.3. The used samples are referred to as:

- Standard analysis sample: $ggH \rightarrow WW \rightarrow e\nu\mu\nu$ process generated for a 125 GeV SM Higgs boson. The sample includes object and event selections as presented in section 6.4;
- VBF analysis sample: same as the standard analysis sample, but with the Higgs boson produced through VBF instead of ggF;
- J^{CP} analysis samples: same as the standard analysis sample, but for Higgs-like bosons with alternative J^{CP} configurations;
- Generator sample: same process as the process of the standard analysis sample, but without selections, detector modelling and object reconstruction. Particles correspond to the MC truth objects.

Whenever distributions with different numbers of events are compared within one figure, the distributions are scaled to the same number of events.

5.2 Motivation for the rest frame reconstruction

Only if the average Lorentz boost of the Higgs boson is not negligible, the development of a reconstruction method for the Higgs rest frame is worthwhile. The impact of the boost can be studied by means of the momentum of the Higgs boson in the lab frame, decomposed in a component in the z-direction, p_z^H, and a component in the transverse plane, p_T^H. If these momenta are on average small, then the Lorentz boost is negligible. Figure 5.1 shows the momentum distributions of the Higgs boson, evaluated in the lab frame, in the transverse plane (a) and in the z-direction (b) for the standard analysis sample, in the 0-jet and 1-jet channels.

In the z-direction the mean value of the momentum of the Higgs boson is in the order of 150 GeV. Clearly, a non negligible value. There are various processes that constitute the longitudinal boost and as such explain the substantial value of p_z^H. The major contribution comes from the net momentum of the two colliding partons. To produce a heavy particle like the Higgs boson, one parton will generally carry a much larger momentum fraction than the other. This results in an excess of momentum in either the positive or negative z-direction that is passed onto the produced Higgs

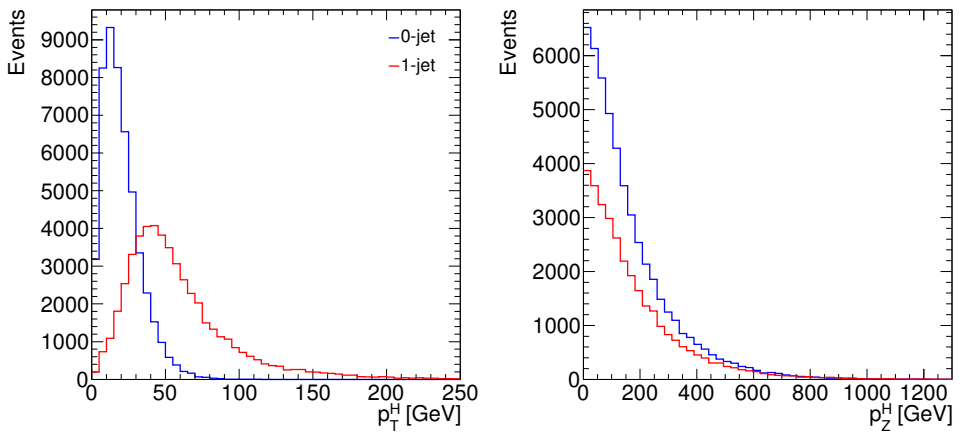

(a) (b)

Figure 5.1: *Transverse (a) and longitudinal (b) momentum of a simulated SM Higgs boson of* 125 *GeV, shown for the 0-jet and 1-jet channels separately.*

boson. Other contributions to the longitudinal boost come from initial state radiation and the Higgs production mechanism.

In the transverse plane, the boost emanates also from net transverse momentum of the colliding partons, initial state radiation and jets originating from the Higgs production mechanism, but in different proportions, than for the longitudinal boost. The magnitude of the transverse boost varies widely with the number of jets present in the final state. In the 0-jet channel the transverse boost results in an average transverse momentum of the Higgs boson in the order of 20 GeV, while this increases to 60 GeV in the 1-jet channel.

As will be detailed in due course, only the transverse boost in the 0-jet channel can be neglected as it does not seriously affect the spin and parity sensitivity of lab frame variables. The transverse boost in the 1-jet channel as well as the longitudinal boost in the 0-jet and 1-jet channels affect the event topology to such an extend that the performance of intrinsically sensitive variables is significantly reduced.

Thus, introduction of rest frame variables into the spin and parity analysis is beneficial. Not only because the sensitivity of the 1-jet channel may be increased, but also

because variables with a component in the z-direction can be reconstructed, increasing the number of spin sensitive variables. Furthermore, given that the rest frame variables are independent of the Lorentz boost, they are less sensitive to uncertainties in the modelling of ISR and the Higgs P_T spectrum. These arguments will be further developed in section 5.5. Concerning a possible properties analysis in the VBF channel, rest frame variables may also be interesting to use, since the jets emanating from the production mechanism induce a large boost. This is not further exploited in this thesis.

5.3 Reconstruction of the dineutrino system

Reconstruction of the Higgs rest frame corresponds to expressing the four-momenta of the final state particles in the Higgs rest frame. Given the energy and momentum of a final state particle in the lab frame $(E, \vec{p})$, the corresponding energy and momentum in the rest frame $(E^*, \vec{p}^*)$ are obtained by application of the Lorentz transformations to $(E, \vec{p})$. The velocity, $\vec{\beta}$, used in the Lorentz transformations is taken as the velocity of the lab frame with respect to the Higgs rest frame: $\vec{\beta} = \vec{p}_H/E_H$, where $\vec{p}_H \equiv (p_x^H, p_y^H, p_z^H)$. Additionally, the Lorentz factor is used in the transformations and defined as: $\gamma = 1/\sqrt{1-\beta^2}$, with $\beta^2 = |\vec{\beta}|^2$. The Lorentz transformations that convert four-momenta from lab frame to rest frame read:

$$\begin{bmatrix} E^* \\ \vec{p}^* \end{bmatrix} = \begin{bmatrix} \gamma & -\gamma\vec{\beta}^T \\ -\gamma\vec{\beta} & \vec{I} + (\gamma-1)\vec{\beta}\vec{\beta}^T/\beta^2 \end{bmatrix}^{-1} \begin{bmatrix} E \\ \vec{p} \end{bmatrix} \tag{5.1}$$

where $\vec{\beta}$ corresponds to the column vector and $\vec{\beta}^T$ to its transpose, i.e. the row vector, and $\vec{I}$ is the [3x3] identity matrix. Considering that $\vec{\beta}$ depends on $\vec{p}_H$, the Lorentz transformations imply that the four-momentum of the Higgs boson in the lab frame, p_H, should be known in order to perform the boost. p_H can be derived from the four-momenta of the final state particles, where it suffices to know the energy and momentum of the pairs of leptons and neutrinos:

$$p_H^2 \equiv M_H^2 = (E_{\ell\ell} + E_{\nu\nu})^2 - (\vec{p}_{\ell\ell} + \vec{p}_{\nu\nu})^2 \tag{5.2}$$

The energy and momentum of the leptons are known, since the leptons are fully reconstructed. However, the four-momentum of the neutrinos is not established. The only available information about the neutrinos consists of the transverse momentum of the dineutrino system that is given by the missing transverse energy variable, $E_T^{\text{miss}} = \sqrt{(E_x^{\text{miss}})^2 + (E_y^{\text{miss}})^2}$, that is described in section 4.4.4. The momentum of the dineutrino system in the z-direction, $p_z^{\nu\nu}$, and consequently its invariant mass, $M_{\nu\nu}$, and energy, $E_{\nu\nu}$, are not determined. Thus, p_x^H and p_y^H can be calculated straightaway, but in order to determine p_z^H and consequently p_H, $p_z^{\nu\nu}$ should be estimated. The remainder of this section is devoted to this.

Firstly, Eq 5.2 is rewritten to:

$$M_H^2 = 2E_{\ell\ell}E_{\nu\nu} - 2\vec{p}_{\ell\ell} \cdot \vec{p}_{\nu\nu} + M_{\ell\ell}^2 + M_{\nu\nu}^2 \tag{5.3}$$

Using $E_{\nu\nu} = \sqrt{M_{\nu\nu}^2 + (E_T^{\text{miss}})^2 + (p_z^{\nu\nu})^2}$ and additionally writing out the momenta in components, shows that $p_z^{\nu\nu}$ is left as the only unknown if and only if constraints are imposed on both M_H and $M_{\nu\nu}$:

$$M_H^2 = 2E_{\ell\ell}\sqrt{M_{\nu\nu}^2 + (E_T^{\text{miss}})^2 + (p_z^{\nu\nu})^2} - 2p_x^{\ell\ell}E_x^{\text{miss}} - 2p_y^{\ell\ell}E_y^{\text{miss}} - 2p_z^{\ell\ell}p_z^{\nu\nu} + M_{\ell\ell}^2 + M_{\nu\nu}^2 \tag{5.4}$$

Since the primary objective of the rest frame reconstruction is to study the discovered Higgs-like boson, M_H can be fixed to the measured mass of the Higgs-like boson: $M_H \equiv 125$ GeV.

Figure 5.2 shows the truth distribution of $M_{\nu\nu}$ that is obtained from the standard analysis sample including the 0-jet and 1-jet channels. In order to acquire a single solution for $p_z^{\nu\nu}$ one value for $M_{\nu\nu}$ must be chosen. It is not possible to include the distribution of $M_{\nu\nu}$ itself in the algorithm as no assumptions about the shape of the distribution of $M_{\nu\nu}$ should be made, in order to allow the use of the algorithm for the reconstruction of the alternative hypotheses. Therefore, the only valid choice is to fix $M_{\nu\nu}$ to the mean value of the distribution: $M_{\nu\nu} \equiv 30$ GeV. This introduces a small bias in the reconstruction, but does not gives preference for specific solutions.

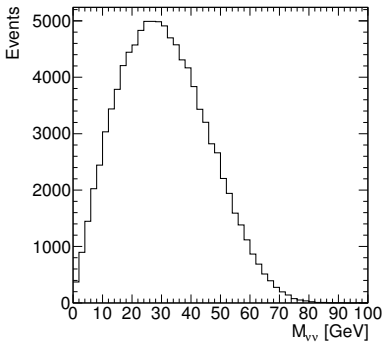

Figure 5.2: *The simulated invariant mass distribution of the dineutrino system, obtained from the standard analysis sample.*

Thus, the two estimates used to constrain the system yield: $M_H \equiv 125$ GeV and $M_{\nu\nu} \equiv 30$ GeV.

All knowns in Eq 5.4 can be gathered into one expression, M^2_{fix}:

$$M^2_{fix} = M^2_H - M^2_{\ell\ell} - M^2_{\nu\nu} + 2p^{\ell\ell}_x E^{\text{miss}}_x + 2p^{\ell\ell}_y E^{\text{miss}}_y \tag{5.5}$$

Substitution of M^2_{fix} into Eq 5.4 reveals that M^2_H is quadratic in $p^{\nu\nu}_z$. The following quadratic equation is derived:

$$0 = \underbrace{((p^{\ell\ell}_z)^2 - E^2_{\ell\ell})}_{\text{a}}(p^{\nu\nu}_z)^2 + \underbrace{M^2_{fix}p^{\ell\ell}_z}_{\text{b}}p^{\nu\nu}_z + \underbrace{\frac{1}{4}M^4_{fix} - E^2_{\ell\ell}((E^{\text{miss}}_T)^2 + M^2_{\nu\nu})}_{\text{c}} \tag{5.6}$$

This equation has two solutions that in terms of the quadratic coefficients, a, b, c, are defined as: $(-b \pm \sqrt{\Delta})/(2a)$, with determinant $\Delta \equiv b^2 - 4ac$. The two solutions can be both real, both imaginary or coincide, corresponding to $\Delta > 0$, $\Delta < 0$ and $\Delta = 0$ respectively. Each situation requires a different approach to obtain a value for $p^{\nu\nu}_z$.

In the exceptional case that the two solutions coincide, there is one solution for $p^{\nu\nu}_z$ that automatically fits into the phase space of the constrained event, and no further

action is required. The other two situations do not lead to a trivial solution and additional procedures are formulated in order to obtain a unique value for $p_z^{\nu\nu}$.

5.3.1 Negative determinant: obtaining a real solution

A negative determinant gives rise to two solutions that are both imaginary, which indicates that no valid solution for $p_z^{\nu\nu}$ can be established within the constrained phase space. This occurs whenever input parameters of the reconstruction algorithm deviate from their true values to such an extend that the phase space of the event cannot accommodate this. There are three input parameters that can induce a negative determinant: $M_{\nu\nu}$, M_H and E_T^{miss}.

$M_{\nu\nu}$ and M_H can cause a negative determinant, because they both have a fixed value for all events and as such diverge significantly from their actual values for part of the events. The E_T^{miss} variable is reconstructed per event, but has a limited resolution that causes differences between true and reconstructed values that are in the order of 20 GeV, for events with a negative determinant. The latter is not an effect of the reconstruction algorithm itself, but nonetheless accounts for two thirds of the events with a negative determinant. The total number of events with an initial negative determinant is 32% for the standard analysis sample, including the 0-jet and 1-jet channels.

Since the E_T^{miss} smearing cannot be precluded, the reconstruction of events with an initial negative determinant can only be effectuated by adjusting the constraints that are imposed on $M_{\nu\nu}$ and M_H. If E_T^{miss} smearing is temporarily disregarded by means of insertion of the true value of $p_T^{\nu\nu}$ into the algorithm, it appears that for events with a negative determinant the actual mean value of $M_{\nu\nu}$ is only 17 GeV instead of 30 GeV. Therefore, the first iteration of the algorithm for events with a negative determinant is to adjust the constraint on the invariant mass of the neutrinos to $M_{\nu\nu} \equiv 0$. This enables reconstruction of events with $0 < M_{\nu\nu} < 30$ GeV, and additionally allows for reconstruction of part of the events with excessive E_T^{miss}. Implementation of this iteration into the reconstruction algorithm leads to a decrease of events with a negative determinant from 32% to 19%.

Events that acquire a positive determinant after the first iteration can be handled according to the procedure described in the next section. The other events remain yet unreconstructed due to excessive reconstructed E_T^{miss}, or, but this concerns less than 1% of the events, because they sit in an exceptional corner of phase space where both $M_{\nu\nu} \ll 30$ GeV and $M_H > 125$ GeV.

To permit reconstruction of the remaining events a second iteration is included: the constraint on M_H is abandoned and instead a value for $p_z^{\nu\nu}$ is calculated by minimising the derivative of the Higgs four-momentum with respect to $p_z^{\nu\nu}$: $\frac{\partial M_H^2}{\partial p_z^{\nu\nu}} = 0$, where M_H is given by Eq 5.4. This leads to the following expression for $p_z^{\nu\nu}$:

$$p_z^{\nu\nu} = p_z^{\ell\ell} \frac{\sqrt{(E_T^{\text{miss}})^2 + M_{\nu\nu}^2}}{\sqrt{E_{\ell\ell}^2 - (p_z^{\ell\ell})^2}} \tag{5.7}$$

$M_{\nu\nu}$ remains fixed to zero in order to ensure continuity between the kinematic regions that are covered with the different iterations. Inclusion of the second iteration in the reconstruction algorithm leads to reconstruction of all events with an initially negative determinant.

Compared to the reconstruction of $p_z^{\nu\nu}$ for events with an initially positive determinant, the reconstruction for events with an initially negative determinant is slightly less accurate. However, these events cannot be disregarded, as they cover specific corners in the phase space of the Higgs signal under study and rejection of this set of events would induce a bias.

5.3.2 Positive determinant: selection of the best solution

A positive determinant for Eq 5.6 results in two distinct real solutions for $p_z^{\nu\nu}$ that both fit the topology of the event. This necessitates a procedure that selects one of the solutions.

There are various adequate methods to select one of the two solutions. To decide which is the best method in the view of the spin and parity analysis, the performance of the resulting rest frame variables has been evaluated for various selection methods. In this section, first, the most basic selection method is presented as a reference

method and its performance is evaluated. Subsequently, the selection method that is eventually incorporated in the reconstruction algorithm is discussed.

Minimal $|p_z^{\nu\nu}|$ selection method

A good reference selection method is one that results in the best resolutions of the rest frame variables. This is achieved with a method that most often selects the solution closest to the true value of $p_z^{\nu\nu}$. It turns out that simply selecting the smallest of the two solutions results in the highest efficiency, where the efficiency is defined as the fraction of events for which the solution closest to the true value is selected. In Appendix A is summarised how this selection method has been established. It has an efficiency of $\sim 60\%$ and is particularly limited by the impact of E_T^{miss} smearing, considering that the efficiency would increase to $\sim 80\%$ if smearing would be absent.

The performance of the reference method is studied regarding the shapes of the resulting rest frame variables. Especially the modelling of the lepton observables is of importance, since these are most sensitive to the spin and parity of the Higgs-like boson. The distributions of these observables have first been evaluated at generator level, since this allows to study the plain effect of the reconstruction algorithm - and thus of the selection method - on the modelling, without contributions of e.g. E_T^{miss} smearing.

The only lepton observable with some deformations with respect to the truth is $\psi^*_{\ell 0}$: the angle of the leading momentum lepton with respect to the z-axis. The asterisk, *, denotes that the variable is reconstructed in the Higgs rest frame. Figure 5.3a shows $\psi^*_{\ell 0}$ for the generator sample. The truth distribution is given in red and the distribution of reconstructed values that is obtained with the reference method is shown in green.

Two features can be observed: the reconstructed distribution is slightly broader, and has a dip around $\frac{1}{2}\pi$. This implies that especially leptons close to the transverse plane are reconstructed in a more forward or backward direction. Figure 5.3a also shows the distribution for simulations including a fictive selection method with an efficiency of 100%, shown in black. The same behaviour is observed for this ideal selection method. This indicates that the deformations in the shape of the reconstructed distribution are

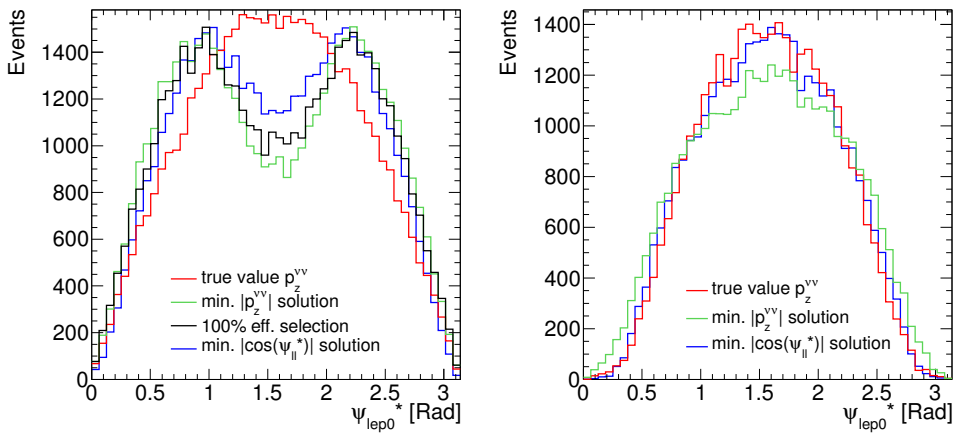

(a) *Generator sample* (b) *Standard analysis sample, 0-jet and 1-jet.*

Figure 5.3: *The opening angle of the leading lepton with respect to the z-axis, reconstructed in the Higgs rest frame for various selection methods.*

primarily not induced by the selection method, but probably a result of the constraints used in the reconstruction algorithm. The constraints can however not be modified for the purpose of improving the shape of this variable.

The overall modelling of the rest frame variables is already good, seeing that only $\psi^*_{\ell 0}$ shows some deformations, nevertheless it is worthwhile to see if the modelling can still be improved by using another selection method.

Minimal $|\cos\psi^*_{\ell\ell}|$ selection method

The modelling could improve if not the smallest $|p_z^{\nu\nu}|$ solution, but the solution that pushes the leptons more towards the transverse plane is selected. This is the solution closest to $\psi = \frac{1}{2}\pi$. Selection of these solutions is effectuated with a method that selects the solution that leads to the smallest value of $|\cos\psi^*_{\ell\ell}|$. Here, it is chosen to use $\psi^*_{\ell\ell}$, being the opening angle of the dilepton system with the z-axis, as to not induce asymmetry between the leading and sub-leading lepton. The distribution acquired with this selection method is also shown in figure 5.3a in blue. A clear improvement with respect to the reference selection method is observed.

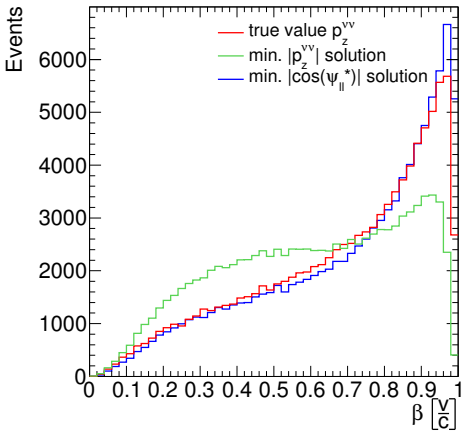

Figure 5.4: *The velocity parameter, $\beta = p_H/E_H$, that is used in the Lorentz transformations. Distributions are acquired from the standard analysis sample, 0-jet and 1-jet.*

Ultimately, the distributions need to be well modelled, also when detector modelling and reconstruction resolutions are taken into account, as this reflects the circumstances in which the actual analysis is performed. Figure 5.3b shows the distribution of $\psi^*_{\ell 0}$ for the truth and the two selection methods at analysis level, acquired from the standard analysis sample including the 0-jet and 1-jet channels. The distribution obtained with the minimal $|\cos\psi^*_{\ell\ell}|$ selection method shows good agreement with the truth distribution.

It has been verified that the $|\cos\psi^*_{\ell\ell}|$ selection procedure does not negatively affect the modelling of other rest frame variables. Indeed, most shapes even improve, owing to the method resulting in more accurate reconstruction of the Lorentz boost itself. Figure 5.4 shows the distribution of $\beta = p_H/E_H$, the input parameter of the Lorentz transformations, for the truth and the two selection methods, acquired from the standard analysis sample. A good agreement with the truth is observed for the minimal $|\cos\psi^*_{\ell\ell}|$ selection procedure.

Unavoidably, the modelling has been improved on the cost of some efficiency in selecting the solution closest to the truth. The efficiency drops from $\sim 60\%$ for the reference method to $\sim 50\%$ for this method. From this can be deduced that, although the overall shapes of the observables improve, the difference between true and

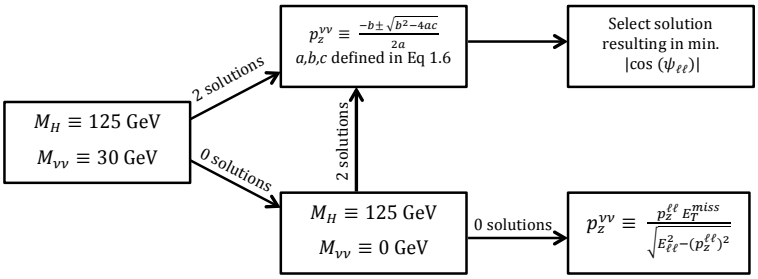

Figure 5.5: *Schematic representation of the decision making in the reconstruction algorithm to obtain a value for* $p_z^{\nu\nu}$.

reconstructed values increases on a per-event basis. Consequently, the resolutions of the rest frame variables decrease on average with $\sim 5\%$ with respect to the reference method. Nevertheless, this is acceptable since the resolutions remain high, as will be discussed in section 5.5.2. No other studied selection method has shown to have a better balance between the resolutions and modelling of the rest frame variables. Therefore it has been chosen to incorporate the minimal $|\cos\psi^*_{\ell\ell}|$ selection method in the reconstruction algorithm.

5.3.3 Summary

To reconstruct final state particles in the Higgs rest frame, the Lorentz boost has to be determined. This comes down to estimation of $p_z^{\nu\nu}$. Fixing the values of M_H and $M_{\nu\nu}$ in Eq 5.4 leads to a constraint system that is quadratic in $p_z^{\nu\nu}$. Thus, either none or two solutions are obtained for $p_z^{\nu\nu}$. Figure 5.5 schematically depicts the approach used in the reconstruction algorithm to obtain a valid solution for $p_z^{\nu\nu}$.

With a method at hand to define for any event a value for $p_z^{\nu\nu}$, the final state particles can be reconstructed in the Higgs rest frame and rest frame variables may be defined. As such the reconstruction algorithm is ready. Yet, the algorithm is extended with a method to approximate separate neutrino momenta.

5.4 Reconstruction of separate neutrino momenta

For the reconstruct of the Higgs rest frame it is not necessary to have information about the individual neutrinos. However, estimates of the momenta of the individual neutrinos in the rest frame can be used to construct spin and parity sensitive rest frame variables. With the introduction of two assumptions, the separate neutrino four-momenta can roughly be approximated.

Firstly, the neutrinos are assumed to be collinear. This is a reasonable assumption for a SM Higgs boson, because helicity conservation tends to focus the two neutrinos in the same direction, as explained in section 1.3. The collinear approximation allows to write the individual neutrino momenta as: $\vec{p}_{\nu 0} = \alpha^2 \vec{p}_{\nu\nu}$ and $\vec{p}_{\nu 1} = (1 - \alpha^2)\vec{p}_{\nu\nu}$. This ensures that the momentum balance of the event is not affected. The scaling factor, α^2, is taken to be squared to ensure that it cannot be negative, as this would contradict the collinear approximation. The collinear approximation also implies that $M_{\nu\nu} = 0$, which is however not in agreement with the constraint previously imposed on $M_{\nu\nu}$. This will be addressed later.

Secondly, a constraint is imposed on the mass of one of the two intermediate W-bosons. Since the mass of the Higgs-like boson is smaller than two times the W-boson mass of $M_W \simeq 80$ GeV, only one W-boson is produced on-shell. The other W-boson is produced off-shell and has a mass smaller than 80 GeV[1]. This permits to constrain one neutrino-lepton pair to an invariant mass of 80 GeV. To establish which of the two leptons fits best in this 'on-shell pair' the invariant mass is consecutively calculated for the dineutrino system with each of the leptons. The lepton that leads to the largest invariant mass of the dineutrino-lepton system is selected.

Now the scaling factor, α^2, can be determined by means of imposing the W-boson mass constraint on the on-shell pair:

[1] Given the Breit-Wigner shape of the W-boson resonance, the configuration in which the W-bosons are both a bit off-shell is unlikely, compared to the assumed configuration.

$$\begin{aligned} M_W^2 &= E_W^2 - |\vec{p}_W|^2 \\ &= (\alpha^2 E_{\nu\nu} + E_\ell)^2 - (\alpha^2 \vec{p}_{\nu\nu} + \vec{p}_\ell)^2 \\ &= 2\alpha^2 E_\ell E_{\nu\nu} - 2\alpha^2 \vec{p}_\ell \cdot \vec{p}_{\nu\nu} \end{aligned} \tag{5.8}$$

Rewriting leads to an expression for α^2:

$$\alpha^2 = \frac{M_W^2}{2(E_\ell E_{\nu\nu} - \vec{p}_\ell \cdot \vec{p}_{\nu\nu})} \tag{5.9}$$

Note that in Eqs 5.8 and 5.9: $E_{\nu\nu} = \sqrt{M_{\nu 0}^2 + |\vec{p}_{\nu\nu}|^2}$, with $M_{\nu 0} = 0$.

In 7% of the cases the topology of the event is affected by the Lorentz boost such that $\alpha^2 > 1$. For these events $\alpha^2 = 1$ is taken, since $\alpha^2 > 1$ would lead to the reconstruction of two neutrinos that are (slightly) back to back and this is not in agreement with the collinear approximation nor with the topology of the event.

To overcome the contradiction between the collinear approximation yielding $M_{\nu\nu} = 0$ and the constraint of $M_{\nu\nu} \equiv 30$ GeV used to reconstruct most events, a fictive mass is assigned to the neutrino allocated to the off-shell W-boson. This is merely a mathematical method to acquire an opening angle between the neutrinos, while the momenta are reconstructed as if there is no opening angle. The value of the fictive mass is chosen such that the adopted constraint for $M_{\nu\nu}$, being either $M_{\nu\nu} \equiv 0$ or $M_{\nu\nu} \equiv 30$ GeV, is preserved. Hence, only for events reconstructed with the latter constraint the fictive mass is non zero.

The fictive mass is assigned to the neutrino that is allocated to the off-shell W-boson, because assigning a mass to the neutrino of the on-shell W-boson would interfere with the assumption of $M_W \simeq 80$ GeV for the on-shell pair. The fictive mass, $M_{\nu f}$, can be derived from the sum of the individual neutrino energies:

$$E_{\nu\nu} = E_{\nu 0} + E_{\nu 1} = \alpha^2 |\vec{p}_{\nu\nu}| + \sqrt{(1-\alpha^2)^2 |\vec{p}_{\nu\nu}|^2 + M_{\nu f}^2} \tag{5.10}$$

Rewriting leads to an equation for the fictive neutrino mass:

$$M_{\nu f} = \sqrt{(E_{\nu\nu} - \alpha^2|\vec{p}_{\nu\nu}|)^2 - (1-\alpha^2)^2|\vec{p}_{\nu\nu}|^2} \tag{5.11}$$

where $E_{\nu\nu} = \sqrt{M_{\nu\nu}^2 + |\vec{p}_{\nu\nu}|^2}$.

The individual neutrino four-momenta can now be defined as:

$$p_\nu^{\text{on}} = (\alpha^2 E_x^{\text{miss}}, \alpha^2 E_y^{\text{miss}}, \alpha^2 p_z^{\nu\nu}, 0) \tag{5.12}$$

$$p_\nu^{\text{off}} = ((1-\alpha^2) E_x^{\text{miss}}, (1-\alpha^2) E_y^{\text{miss}}, (1-\alpha^2) p_z^{\nu\nu}, M_{\nu f}) \tag{5.13}$$

where p_ν^{on} indicates the neutrino assigned to the on-shell W-boson and p_ν^{off} the one assigned to the off-shell W-boson, and α^2 is given by Eq 5.9.

The four-momenta are subsequently converted into their rest frame equivalents by applying the Lorentz transformations, and the momenta of the neutrinos can be used in the construction of rest frame variables. Angular neutrino variables should not be used, since no angular information was used to reconstruct the individual neutrino four-momenta. The precision of the neutrino momenta will be evaluated in the next section as part of the discussion of the performance of the algorithm.

5.5 Performance of the reconstruction algorithm

The performance of the reconstruction algorithm is assessed, regarding two aspects. The modelling of the rest frame variables is examined to see if and to which extend the constraints used in the algorithm induce biases, and the resolutions are evaluated since these provide a quantitative measure of the performance.

The algorithm has been optimised for one specific SM Higgs process that in the following is referred to as the reference process: $ggH \to WW \to e\nu\mu\nu + 0$ jets. The 1-jet channel is however also considered in the spin and parity analysis. Moreover, there are other Higgs processes with an $\ell\nu\ell\nu$ final state that are interesting to reconstruct with the algorithm as well. Furthermore, the algorithm will also be used to reconstruct the rest frames of the alternative signal hypotheses. Therefore, the performance of

the reconstruction algorithm is first discussed for the SM Higgs reference process in sections 5.5.1 and 5.5.2, and subsequently evaluated for other $H \to WW$ processes in section 5.5.3, as well as for the alternative hypotheses in section 5.5.4. A preview of the spin and parity sensitivity of the rest frame variables is given in section 5.5.5.

Rest frame variables

Any variable can in principle be reconstructed in the Higgs rest frame. The discussion in this section is restricted to the observables of the leptons, and rest frame variables that are used in the analysis presented in this thesis. Concerning the notation of the variables: the leptons as well as the neutrinos are ordered according to their total momentum, hence, ℓ_0 (ν_0) denotes the lepton (neutrino) with the highest momentum and $\ell 1$ ($\nu 1$) the lepton (neutrino) with sub-leading momentum. The asterisk, *, indicates that the variables are reconstructed in the Higgs rest frame. The rest frame variables include:

- $p^*_{\ell 0}$, $p^*_{\ell 1}$, $p^*_{\nu 0}$, $p^*_{\nu 1}$: the magnitudes of the three-momenta of the leptons and neutrinos;
- $\psi^*_{\ell 0}$, $\psi^*_{\ell 1}$, $\psi^*_{\ell\ell}$: the opening angles of the leptons and the dilepton system with respect to the z-axis;
- $\Delta\phi^*_{\ell\ell}$, $\Delta\psi^*_{\ell\ell}$: the angle between the leptons in the transverse plane (ϕ) and the $(r-z)$ plane (ψ);
- E^*_{dif}: the difference in energy (magnitude of the three-momenta) between the two leptons, defined as: $E^*_{\text{dif}} = p^*_{\ell 0} - p^*_{\ell 1}$;
- E^*_{sum}: empirical variable used in the analysis, defined as: $E^*_{\text{sum}} = p^*_{\ell 0} + p^*_{\nu 1} - \frac{1}{2} p^*_{\ell 1}$.

5.5.1 Modelling

To study the impact of the constraints used in the reconstruction algorithm on the modelling of the rest frame variables, the reconstructed values are compared with the

truth information of the same MC samples. In figures 5.6 and 5.7, two-dimensional distributions with the reconstructed values on the x-axis and the truth values on the y-axis are shown. The distributions are given for all rest frame variables and are obtained from the standard analysis sample that is described in the introduction of this chapter. The distributions are combined for the 0-jet and 1-jet channel.

If reconstruction perfectly matches the truth, a narrow linear distribution, yielding $y = x$, is expected. Differences with respect to this ideal situation give insight in the modelling and performance of the variables. The following differences are observed:

Smearing There is a limit to the accuracy of the reconstruction and as such true and reconstructed values will differ, where small differences are more frequent than larger ones. This results in a broadened distribution around the diagonal that gradually depletes. Specific contributions to the smearing come from the resolution of the E_T^{miss} variable and from events with a positive determinant for which the solution that is furthest from the truth is selected. Smearing does not indicate that there are biases due to the algorithm.

Structures Structures of events that cannot be accommodated as part of the smeared diagonal distribution reflect a systematic difference and may point to a problem in the modelling. Such differences may arise as a result of the constraints imposed on $M_{\nu\nu}$ and M_H, the selection method for events with a positive determinant and the reconstruction method for events with a negative determinant. Small biases are inevitable, yet harmless, as they are mostly not retrieved in the reconstructed one-dimensional distributions of the variables due to the much larger impact of E_T^{miss} smearing. Larger systematic differences do not necessarily affect the shape of the one-dimensional distributions either, but ask for individual evaluation.

Asymmetry Also due to the imposed constraints, the reconstruction of a variable may be structurally lower or higher than the truth. This is however not manifested as a structure but rather as a shift, c, of the diagonal distribution: $y = x + c$.

For each rest frame variable a primary diagonal distribution is observed, this indicates that the reconstruction follows the truth. Note that also for the reconstructed

neutrino momenta diagonal distributions are visible, which implies that the W-boson mass constraint and the collinear approximation of the neutrinos provided sufficient information to approximate separate neutrino momenta.

As expected, all distributions exhibit a certain degree of smearing. Various studies that have been performed indicate that the structures that are visible for $\psi^*_{\ell 0}$ and $p^*_{\ell 0}$ are caused by the constraints on $M_{\nu\nu}$ and M_H. Consequently, rest frame variables that are composed of these observables may also exhibit biases. The structure observed for $\psi^*_{\ell\ell}$ consists of events with a negative determinant. Since for every variable the bulk of the events is distributed around the diagonal, none of the divergences severely affects the shapes of the reconstructed distributions of the variables. Other measures of the modelling that have been evaluated neither disclosed problems. The 2D distributions have also been evaluated for the generator sample. Both the structures and diagonals appeared more distinct as a result of the elimination of the E_T^{miss} smearing, but no other structures or effects were observed. These distributions are included in Appendix B Thus, concerning the modelling of the variables there are no drawbacks for their use in the spin and parity analysis.

5.5.2 Resolutions

The resolutions are a quantitative measure of the extend to which true and reconstructed values differ. In the following two measures of the resolution are used: the RMS and the core resolution. Both can be extracted from 'resolution distributions' filled with the difference between reconstructed and true values of the respective rest frame variable. The core resolution is defined as the RMS of the narrow gauss of a double gauss fit that is applied to the resolution distributions. The fit is set such that the narrow gauss includes at least 60% of the events and has an absolute mean value smaller than 1.5 GeV or 0.05 Rad. Thus, while the RMS takes into account all events, including the fraction of events that constitutes the tails, the core resolution reflects the resolution of the bulk of the events that is situated in the peak of the distribution.

Figure 5.8 shows the resolution distributions for the momenta and opening angles of the leptons, as well as for the momenta of the neutrinos. Each variable is distributed both at analysis level and at generator level. The generator distributions show a

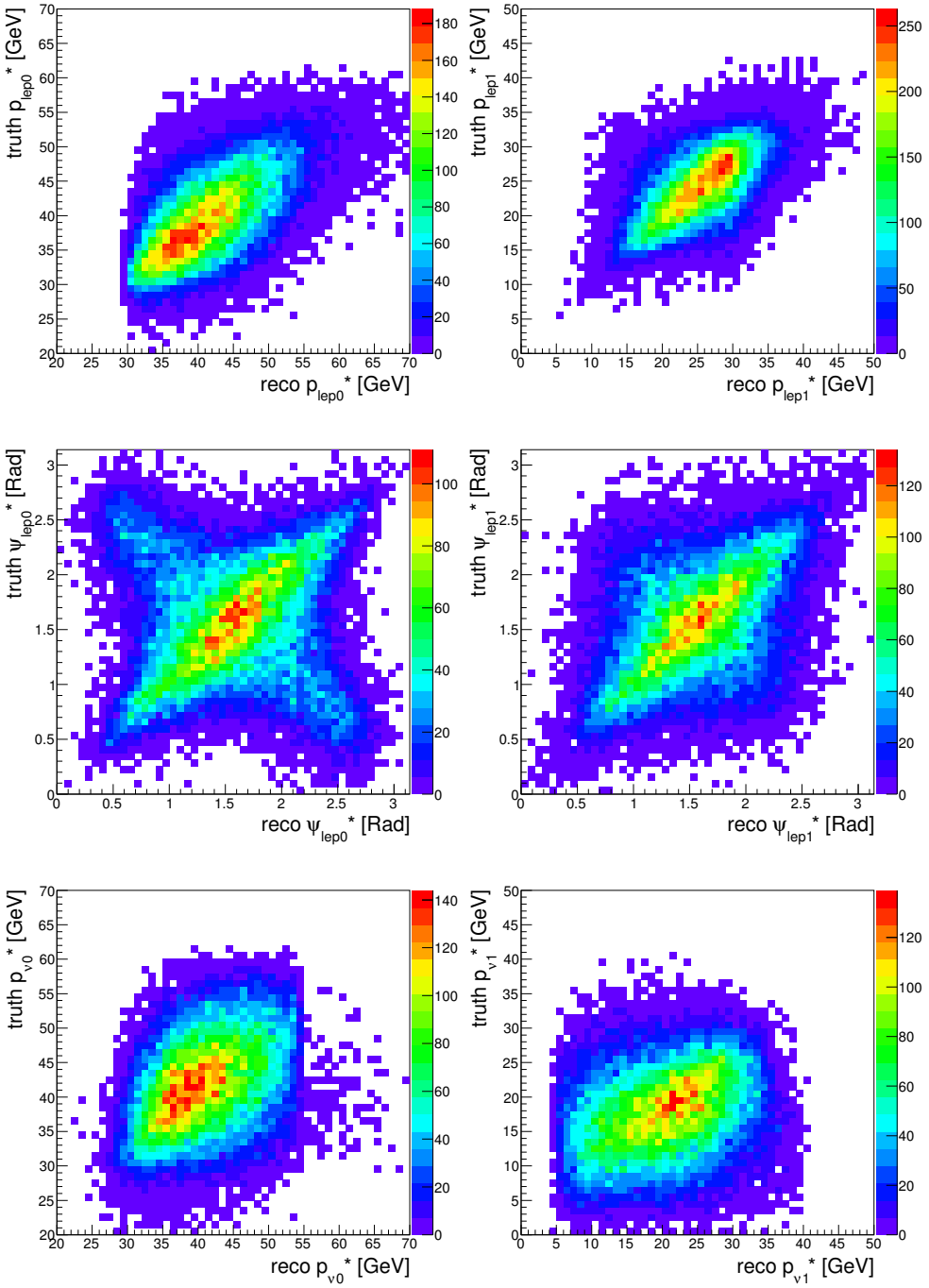

Figure 5.6: *The reconstructed values on the x-axis versus the true values on the y-axis for the lepton observables and neutrino momenta, reconstructed in the Higgs rest frame. Distributions are obtained from the standard analysis sample, including the 0-jet and 1-jet channels.*

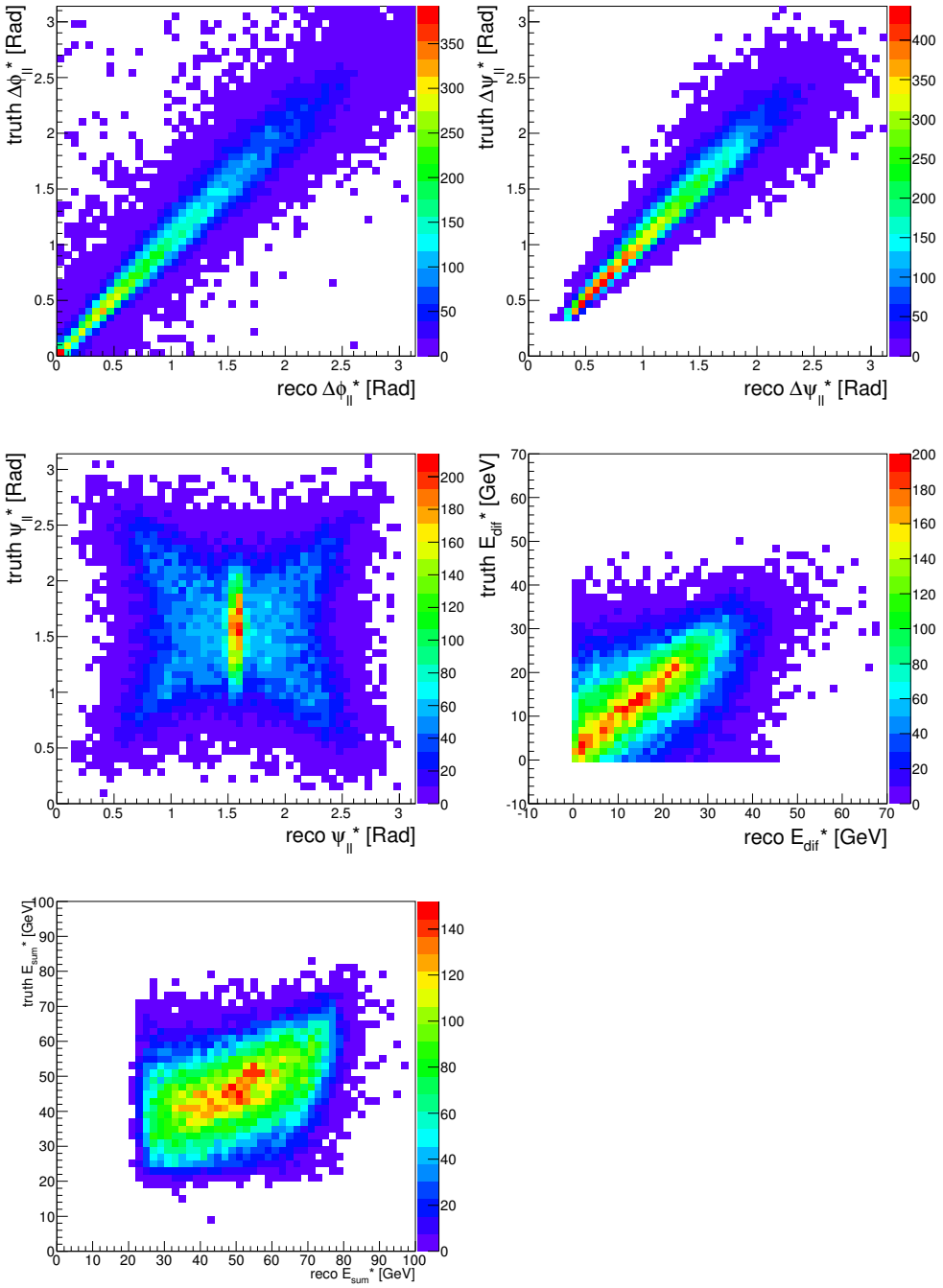

Figure 5.7: *The reconstructed values on the x-axis versus the true values on the y-axis for the composite rest frame variables. Distributions are obtained from the standard analysis sample, including the 0-jet and 1-jet channels.*

Variable	Unit	RMS	Core reso	Fraction	Mean of variable	Mean of (reco-truth)
$p^*_{\ell 0}$	[GeV]	5.66 ± 0.02	4.21 ± 0.03	0.6	42.31 ± 0.04	2.13 ± 0.03
$p^*_{\ell 1}$	[GeV]	4.99 ± 0.02	3.42 ± 0.03	0.6	25.33 ± 0.03	1.08 ± 0.03
$\psi^*_{\ell 0}$	[rad]	0.776 ± 0.003	0.501 ± 0.002	0.6	1.575 ± 0.003	0.002 ± 0.004
$\psi^*_{\ell 1}$	[rad]	0.529 ± 0.002	0.510 ± 0.002	0.6	1.570 ± 0.003	-0.002 ± 0.003
$p^*_{\nu 0}$	[GeV]	7.28 ± 0.03	6.50 ± 0.03	0.92	41.38 ± 0.03	-0.62 ± 0.04
$p^*_{\nu 1}$	[GeV]	8.41 ± 0.03	6.79 ± 0.06	0.6	20.47 ± 0.04	2.69 ± 0.05
$\Delta\phi^*_{\ell\ell}$	[rad]	0.207 ± 0.001	0.130 ± 0.001	0.6	1.175 ± 0.004	-0.042 ± 0.001
$\Delta\psi^*_{\ell\ell}$	[rad]	0.154 ± 0.001	0.090 ± 0.001	0.71	1.272 ± 0.003	-0.065 ± 0.001
$\psi^*_{\ell\ell}$	[rad]	0.758 ± 0.003	0.459 ± 0.004	0.6	1.573 ± 0.003	0.001 ± 0.004
E^*_{dif}	[GeV]	9.52 ± 0.03	6.15 ± 0.06	0.6	17.01 ± 0.06	1.06 ± 0.05
E^*_{sum}	[GeV]	13.90 ± 0.05	11.99 ± 0.09	0.6	50.15 ± 0.08	4.29 ± 0.07

Table 5.1: *The RMS, core resolution, fraction of events in the narrow gauss, mean value of the reconstructed variable and the mean value of the resolution distributions, given for the rest frame variables. The results are obtained from the standard analysis samples, including the 0-jet and 1-jet channels.*

narrower peak as there is no smearing due to limited reconstruction resolution. From this can be deduced that the precision of the rest frame variables that will be used in the analysis is largely affected by smearing effects and does not solely depends on the precision of the reconstruction algorithm. Finally, the bottom two distributions in figure 5.8 indicate that, despite the limited information available to reconstruct the separate neutrinos, the reconstructed and true values match reasonably well.

In table 5.1 the RMS and core resolution, as well as various supporting parameters, are listed for all rest frame variables. The numbers are extracted from the standard analysis sample, including the 0-jet and 1-jet channels. Note that this includes smearing and detector effects. The RMS and core resolutions of the momentum variables are easier to interpret with respect to the mean values of the respective variables, which are listed in the second last column. The fractions of events used to measure the core resolution are also listed in the table. The core resolution is slightly conservative as the fit does not extend up to the top most events in the peak. No anomalous resolutions are observed.

The last column in the table lists the mean values of the resolution distributions. These mean values provide a measure of the overall offset of the reconstructed variables with respect to the truth. This has also been addressed in the previous section as 'asymmetry' in the two-dimensional distributions. Offsets are correlated among

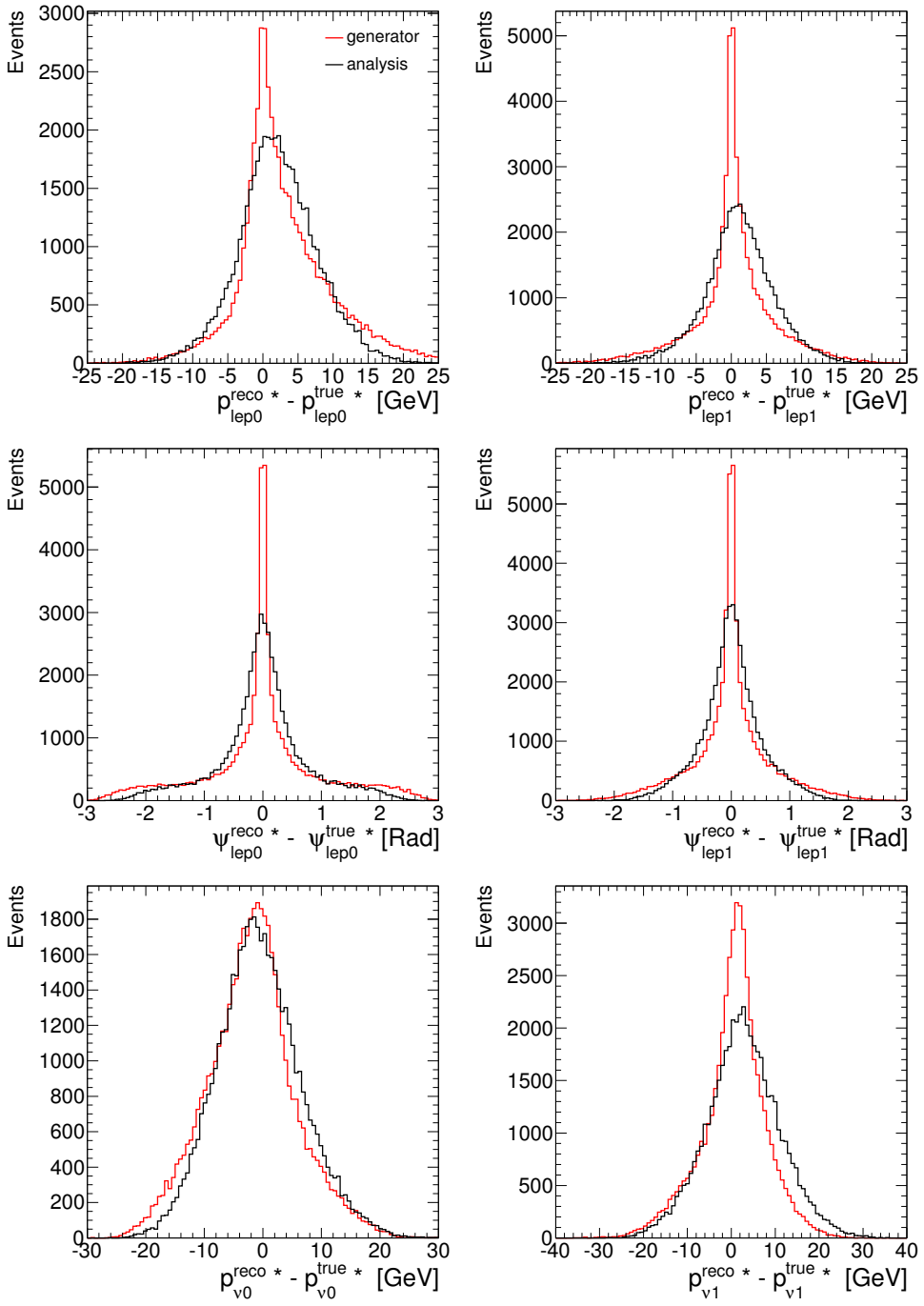

Figure 5.8: *The difference between the reconstructed values and the true values are shown for the lepton observables and neutrino momenta, reconstructed in the Higgs rest frame. Distributions are obtained at generator level with no cuts applied, and at analysis level including the 0-jet and 1-jet channels with event selections.*

the different rest frame variables as an effect of the reconstruction algorithm. A considerable contribution to the offsets comes from the reconstruction of events with a negative determinant. Comparison of the offsets with the mean values of the variables, that are listed in the penultimate column, shows that all shifts are acceptable.

5.5.3 Performance for other SM subprocesses

Other processes that contribute to the $H \to WW$ channel, differ from the reference process with respect to the flavour of the final state leptons, the number of jets in the final state and the production mechanism of the Higgs boson. In this section is explained why these different features do not require adjustments of the reconstruction algorithm and the performance of the algorithm is presented for these subprocesses.

Flavour of the final state particles

The final state of the reference process involves one muon and one electron. Final states containing two electrons or two muons however also occur in the the SM Higgs signal. The algorithm is equally well applicable to these flavour combinations as electrons and muons have the same quantum numbers, do not decay, and their masses can be neglected. The W-bosons also decay into τ-leptons, however, these do decay and are therefore not observed as final state particles. The Higgs decays involving τ-leptons are already taken into account in the MC simulations of the reference process and did not lead to complications. Thus, the other flavour combinations do not require adjustments of the algorithm.

Number of jets in the final state

The final states generally taken into account include up to two jets. Figure 5.9 shows the distributions of two prominent rest frame variables used in the spin and parity analysis, $\Delta\psi^*_{\ell\ell}$ and E^*_{sum}, obtained from the standard analysis sample and distributed separately for the 0-jet, 1-jet and 2-jet channels. Only small differences in the shapes are observed among the different channels. The little impact of the presence of jets on the shapes of the variables can be explained, realising that the decay under study

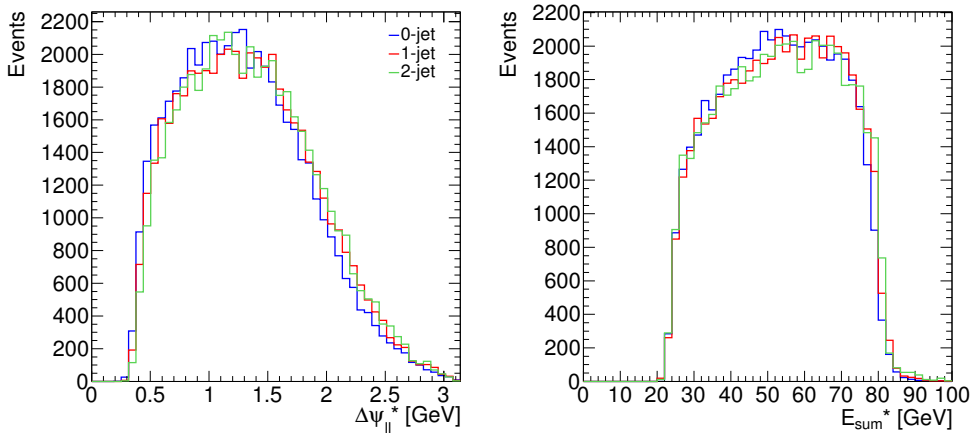

(a) (b)

Figure 5.9: *The distributions of $\Delta\psi^*_{\ell\ell}$ (a) and E^*_{sum} (b), acquired from the standard analysis sample and shown separately for the 0-jet, 1-jet and 2-jet channels.*

is electroweak: jets present in the final state do not emanate from the decay particles of the Higgs boson, but rather from ISR and the Higgs production mechanism. Thus, production of these jets precedes the decay of the Higgs boson. As such the jets do not carry part of the momentum of the Higgs boson and therefore, the algorithm can be applied without adjustments. The differences that are observed in figure 5.9 are induced by different event selections and E_T^{miss} smearing among the jet channels. Figure 5.9 additionally implies that the rest frame variables are virtually independent of uncertainties in the modelling of ISR and the Higgs p_T spectrum.

Higgs production mechanism

According to the same explanation as given for additional jets, the algorithm is also applicable to processes in which the Higgs boson is produced through other production mechanisms. This is the case, since the production obviously precedes the decay of the Higgs boson. In figure 5.10 the distributions of $\Delta\psi^*_{\ell\ell}$ and E^*_{sum} are shown for production through ggF and VBF. The distributions are acquired from the standard analysis sample and the VBF analysis sample, without application of event selections.

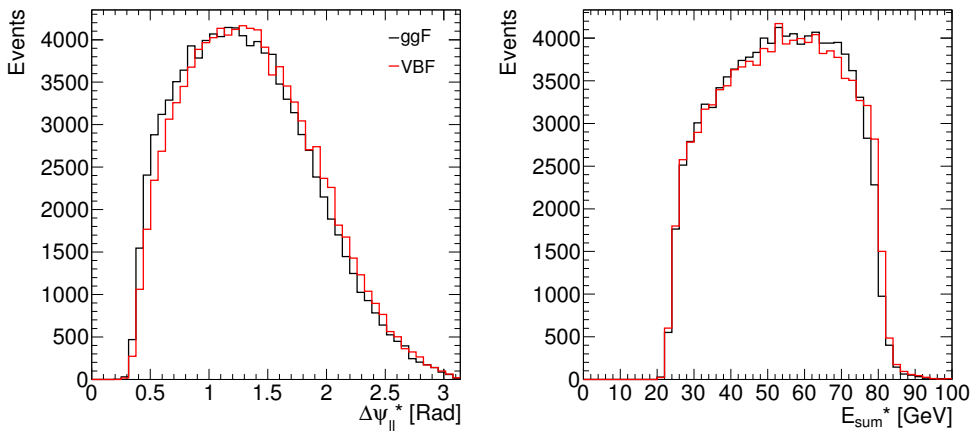

(a) (b)

Figure 5.10: *The distributions of $\Delta\psi_{\ell\ell}^{*}$ (a) and E_{sum}^{*} (b), shown for Higgs production through ggF and VBF and acquired from the standard analysis sample and the VBF analysis sample respectively. No event selections are applied.*

As expected, the effect of the production mechanism on the modelling of the distributions is small. This indicates that the reconstruction algorithm is also applicable to SM subprocesses that involve other Higgs production mechanisms.[2] Consequently, it can be concluded that the impact of the production mechanism on the angular momentum of the Higgs boson and thus on the configuration of the final state particles is negligible regarding the modelling of the variables.

In table 5.2 the RMS values are listed for the reference process and the relevant subprocesses of the SM Higgs signal. The 2-jet channel is not included as there is not yet a dedicated spin and parity analysis for VBF production and the 2-jet channel in general. The migration of VBF production into the 1-jet channel, however, is taken into account. Other production mechanisms have even lower cross sections and are therefore not yet taken into account in the analysis.

[2]Production mechanisms like associated production may give rise to additional leptons or substantial missing momentum in the final state. This might affect the performance of the algorithm, since extraction of the final state particles emanating from the Higgs boson is more complicated. However, this difficulty is inherent to the overall analysis of these Higgs processes and not to the reconstruction mechanism specifically.

Variable	Unit	reference	ggF 0-jet	ggF 1-jet	VBF 1-jet
$p^*_{\ell 0}$	[GeV]	5.66 ± 0.02	5.55 ± 0.03	5.85 ± 0.04	5.83 ± 0.05
$p^*_{\ell 1}$	[GeV]	4.99 ± 0.02	4.92 ± 0.02	5.11 ± 0.03	5.07 ± 0.04
$\psi^*_{\ell 0}$	[rad]	0.776 ± 0.003	0.781 ± 0.004	0.767 ± 0.005	0.77 ± 0.01
$\psi^*_{\ell 1}$	[rad]	0.529 ± 0.002	0.522 ± 0.002	0.541 ± 0.003	0.565 ± 0.004
$p^*_{\nu 0}$	[GeV]	7.28 ± 0.03	7.21 ± 0.03	7.41 ± 0.05	7.48 ± 0.06
$p^*_{\nu 1}$	[GeV]	8.41 ± 0.03	8.37 ± 0.04	8.47 ± 0.05	8.32 ± 0.07
$\Delta\phi^*_{\ell\ell}$	[rad]	0.207 ± 0.001	0.195 ± 0.001	0.228 ± 0.001	0.238 ± 0.002
$\Delta\psi^*_{\ell\ell}$	[rad]	0.154 ± 0.001	0.150 ± 0.001	0.161 ± 0.001	0.165 ± 0.001
$\psi^*_{\ell\ell}$	[rad]	0.758 ± 0.003	0.770 ± 0.004	0.735 ± 0.005	0.75 ± 0.01
E^*_{dif}	[GeV]	9.52 ± 0.03	9.41 ± 0.04	9.72 ± 0.06	9.66 ± 0.08
E^*_{sum}	[GeV]	13.90 ± 0.05	13.77 ± 0.06	14.14 ± 0.09	13.9 ± 0.1

Table 5.2: *The RMS values for the reference process (ggF 0-jet plus 1-jet), ggF 0-jet channel, ggF 1-jet channel and VBF 1-jet channel. Numbers are extracted from the relevant analysis samples.*

The resolutions substantiate the conclusions deduced from figures 5.9 and 5.10: the algorithm is suitable to reconstruct any of the processes that constitute the SM Higgs signal.

5.5.4 Alternative spin and parity hypotheses

The alternative hypotheses that are evaluated in the analysis include bosons with different spin and parity combinations: $J^{CP} = 0^-, 1^+, 1^-, 2^+$. These alternative hypotheses for the Higgs-like boson result in decays that are intrinsically different from the SM Higgs decay. Therefore the accuracy of the constraints and assumptions used in the reconstruction method is reassessed for the alternative hypotheses. The simulations of the alternative models are performed assuming that the Higgs-like boson has a mass of 125 GeV, is produced through similar production mechanisms, decays into two W-bosons and results in the same set of final states as the SM Higgs boson.

Since the same mass of the Higgs-like boson is assumed, the constraints imposed on the Higgs boson mass and the W-boson mass are equally well applicable in the reconstruction of the rest frame of the alternative bosons. Also the collinear approximation of the neutrinos is still applicable, since the approximation is considered in the lab

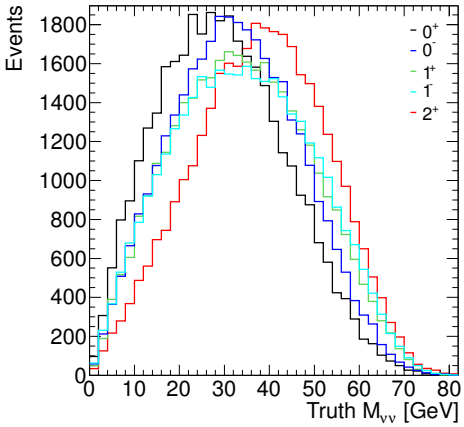

Figure 5.11: *Truth distributions of $M_{\nu\nu}$ shown for the SM Higgs signal and the alternative J^{CP} hypotheses. Distributions are acquired from the standard analysis sample, including the 0-jet and 1-jet channels.*

frame and therefore the boost will generally focus the neutrinos in the same direction, even when this is not initiated by helicity conservation.

The constraint value of $M_{\nu\nu}$ is the only value that significantly depends on the spin of the Higgs-like boson. Figure 5.11 shows the truth distributions of $M_{\nu\nu}$ for the different hypotheses. The assumption $M_{\nu\nu} \equiv 30$ GeV is most different for the 2^+ model which has a mean value of $M_{\nu\nu} \simeq 40$ GeV. Nevertheless, all distributions cover a kinematical region comparable to that of the SM signal hypothesis. Thus, $M_{\nu\nu} = 30$ GeV is a probable value for any of the hypotheses. Therefore, it is not beneficial to make the constraint on $M_{\nu\nu}$ hypothesis dependent, as this would complicate the analysis considerably. Moreover, it has been verified that using $M_{\nu\nu} \equiv 30$ GeV does not decrease the sensitivity of the rest frame variables for any of the hypotheses, while using a higher value, like the average mean value of all hypothesis, does lead to implications.

Figure 5.11 additionally provides information about the validity of the assumption $M_{\nu\nu} \equiv 0$ that is used both to reconstruct events with a negative determinant and to reconstruct separate neutrino momenta. The figure shows that $M_{\nu\nu} = 0$ takes up a similar position with respect to the mean value of the $M_{\nu\nu}$ distribution, for the SM Higgs signal as well as for any of the alternative hypotheses. Therefore this

Var.	Unit	standard 0^+	0^-	1^+	1^-	2^+
$p^*_{\ell 0}$	[GeV]	5.66 ± 0.02	5.70 ± 0.02	5.86 ± 0.02	6.17 ± 0.02	6.04 ± 0.02
$p^*_{\ell 1}$	[GeV]	4.99 ± 0.02	5.29 ± 0.01	4.84 ± 0.02	5.15 ± 0.02	5.24 ± 0.02
$\psi^*_{\ell 0}$	[rad]	0.776 ± 0.003	0.809 ± 0.002	0.715 ± 0.002	0.804 ± 0.003	0.814 ± 0.003
$\psi^*_{\ell 1}$	[rad]	0.529 ± 0.002	0.552 ± 0.002	0.502 ± 0.002	0.548 ± 0.002	0.533 ± 0.002
$p^*_{\nu 0}$	[GeV]	7.28 ± 0.03	7.51 ± 0.02	7.27 ± 0.02	7.72 ± 0.03	7.26 ± 0.02
$p^*_{\nu 1}$	[GeV]	8.41 ± 0.03	8.97 ± 0.03	7.79 ± 0.03	7.93 ± 0.03	8.36 ± 0.03
$\Delta\phi^*_{\ell\ell}$	[rad]	0.207 ± 0.001	0.220 ± 0.001	0.202 ± 0.001	0.217 ± 0.001	0.241 ± 0.001
$\Delta\psi^*_{\ell\ell}$	[rad]	0.154 ± 0.001	0.170 ± 0.001	0.175 ± 0.001	0.185 ± 0.001	0.211 ± 0.001
$\psi^*_{\ell\ell}$	[rad]	0.758 ± 0.003	0.782 ± 0.002	0.736 ± 0.002	0.836 ± 0.003	0.790 ± 0.002
E^*_{dif}	[GeV]	9.52 ± 0.03	9.88 ± 0.03	9.66 ± 0.03	10.34 ± 0.03	10.21 ± 0.03
E^*_{sum}	[GeV]	13.90 ± 0.05	14.52 ± 0.04	13.66 ± 0.04	14.17 ± 0.05	14.07 ± 0.04

Table 5.3: *The RMS values of the reference process (ggF 0-jet plus 1-jet), complemented with the RMS values of the alternative signal hypotheses. Numbers are extracted from the relevant J^{CP} analysis samples.*

assumption is equally well applicable in the reconstruction of the rest frame of the alternative bosons.

The performance of the reconstruction algorithm has been studied just as extensively for the alternative models, as for the SM Higgs process. This led to the conclusion that no significant mismodelling of variables for the alternative hypotheses is induced by any of the assumptions applied in the reconstruction algorithm. In Appendix C the two-dimensional distributions of the reconstructed values versus the truth values of the rest frame variables are presented for the $J^{CP} = 2^+$ process. No deviations other than the ones that were also observed for the SM process in figures 5.6 and 5.7 have been discovered.

In table 5.3 the RMS values are listed for the reference process as well as for the alternative hypotheses. The resolutions vary slightly due to the distinct kinematics of the different models. The resolutions confirm that the imposed constraints do not severely affect the performance of the reconstruction algorithm. Hence, the reconstruction algorithm is also suitable to reconstruct the rest frame of Higgs-like bosons with other spin and parity combinations.

5.5.5 Rest frame variables

Rest frame variables are only of use in the spin and parity analysis if the shapes of their distributions are different for the SM signal and the alternative signal hypotheses. To demonstrate that the precision of the reconstruction algorithm is such that rest frame variables exhibit this sensitivity and to show their added value in the spin and parity analysis, the discrimination between the SM process and the $J^{CP} = 2^+$ process is concisely evaluated.

The most powerful *lab* frame variable used in the spin and parity analysis is $\Delta\phi_{\ell\ell}$. In figure 5.12a $\Delta\phi_{\ell\ell}$ is shown for the SM process and the 2^+ process in the 0-jet channel. Indeed distinct shapes are observed. Figure 5.12b shows equivalent distributions for the 1-jet channel. Clearly, the discriminating power of $\Delta\phi_{\ell\ell}$ is limited for the 1-jet channel due to the boost that is produced by the jet recoiling. This results in an overall reduced spin and parity sensitivity for the 1-jet channel. If the same variable is instead reconstructed in the Higgs rest frame its sensitivity is preserved, as shown in figures 5.12c and 5.12d, in which $\Delta\phi^*_{\ell\ell}$ is distributed for the 0-jet and 1-jet channels respectively. Thus, introduction of this rest frame variable into the analysis will increase the sensitivity of the 1-jet channel.

Eventually spin sensitive variables, both reconstructed in the lab frame and in the rest frame, are combined to acquire maximal spin and parity sensitivity for every signal hypothesis. This will be detailed in chapters 6 and 7.

5.6 Discussion and conclusions

An algorithm to reconstruct the rest frame of a Higgs-like boson that decays into two leptons and two neutrinos has been developed with the aim to apply it in the analysis of the spin and parity of the observed Higgs-like boson.

It has been verified that the reconstruction algorithm is applicable regardless of the Higgs production mechanism and the number of jets in the final state. Additionally, it has been established that the method can be employed to reconstruct the rest frames of both the SM Higgs boson and alternative signal hypotheses. This enables the use

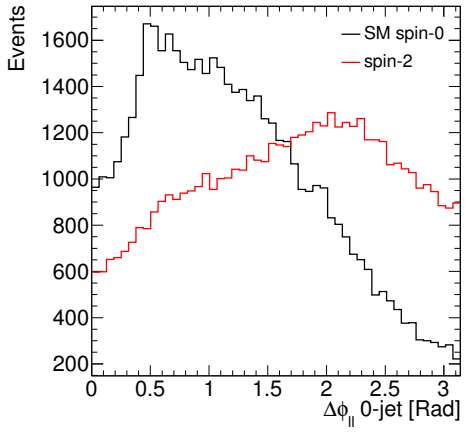

(a) *Lab frame:* $\Delta\phi_{\ell\ell}$*, 0-jet channel*

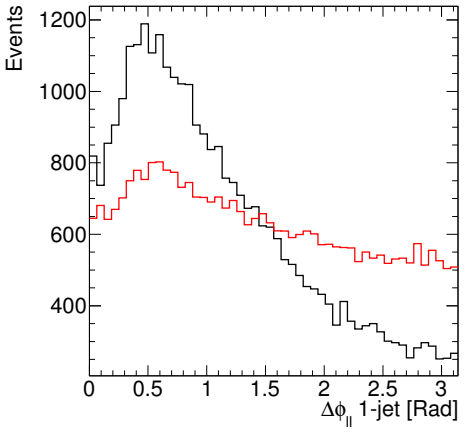

(b) *Lab frame:* $\Delta\phi_{\ell\ell}$*, 1-jet channel*

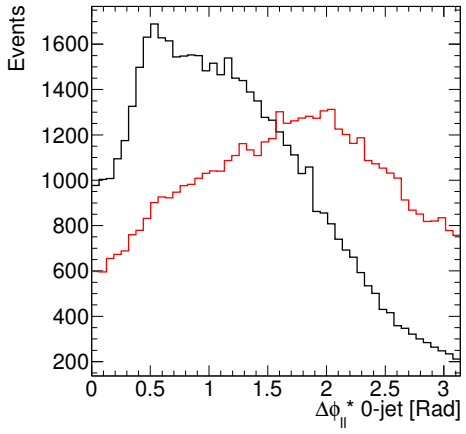

(c) *Rest frame:* $\Delta\phi^*_{\ell\ell}$*, 0-jet channel*

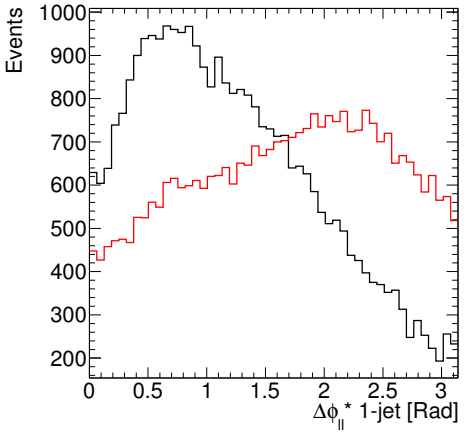

(d) *Rest frame:* $\Delta\phi^*_{\ell\ell}$*, 1-jet channel*

Figure 5.12: *The distributions are compared for the SM process and the* $J^{CP} = 2^+$ *process, and obtained from the respective analysis samples.*

of rest frame variables in the spin and parity analysis of the discovered Higgs-like boson.

The performance of the reconstruction algorithm has been extensively studied by means of the modelling and resolutions of the rest frame variables and proves to be satisfactory. The necessary assumptions and constraints used in the algorithm do not lead to problems in the modelling of the variables. The performance of the reconstruction algorithm is most affected by the resolution of the reconstructed E_T^{miss} variable.

The previous section shows in practice that the performance of the reconstruction algorithm is such that rest frame variables exhibit significant spin and parity sensitivity. Therewith the goal of the development of a reconstruction algorithm for the Higgs rest frame is accomplished. It is time to apply it to the data.

In the next chapters the spin and properties analysis is presented: first the preparations needed for the spin and parity measurement are described, and subsequently the measurement itself is discussed. The rest frame variables will play an important role for the measurement.

Chapter 6

Preparations for the Spin and parity measurement

6.1 Introduction

One of the three decay modes in which the Higgs-like boson has initially been discovered is the $H \to WW \to \ell\nu\ell\nu$ final state. The observed signal corresponds to that of the SM Higgs boson in terms of its production rate and its charge, and due to its decay into a pair of vector bosons it can be identified as a boson. However, it cannot be excluded yet that the observed signal comes from a more exotic Higgs-like boson with slightly different properties than predicted by the Standard Model.

Two quantum numbers that are important in the characterisation of the discovered boson, and which can be studied with the 2012 LHC dataset, are the spin and parity, or CP. The SM Higgs boson is predicted to have spin-0 and even parity, i.e. $J^{CP} = 0^+$, while other possible spin and parity combinations for the observed signal include: $J^{CP} = 0^-, 1^+, 1^-, 2^+$, where the plus sign denotes even parity and the minus sign odd parity. Other spin and CP combinations are unlikely and therefore disregarded. The hypothesis that the observed signal comes from a mixture of two bosons, e.g. a CP-even and a CP-odd boson, belongs to the possibilities as well, but will not be

studied in this thesis. To test the different hypotheses, the observed signal is compared both to the SM prediction and to the four fixed alternatives for the signal. In section 1.4, the characterisation of these alternative hypotheses has been discussed.

Since the cross sections of the alternative hypotheses are unknown, the analysis has to be performed on the basis of the shapes of distributions of kinematical variables that are sensitive to the spin and parity of the Higgs-like boson. Event yields cannot be used. The relatively large signal yield of the $H \to WW$ decay mode allows for such a shape analysis. However, the channel also suffers from a large background that makes it difficult to obtain a spin sensitive analysis. Hence, the first part of the analysis, which is described in this chapter, is devoted to obtain an analysis with sufficient sensitivity to do a spin and parity measurement. The relevant background processes are listed in section 6.2. Monte Carlo (MC) simulations are used to model the background processes, as well as the different hypotheses for the observed signal, which will be discussed in section 6.3. Since it is not possible to perfectly model the backgrounds with only MC simulations, additional methods are used as will be explained in section 6.5. To reduce the background, while preserving the sensitivity of variables that are discriminating between the different signal hypotheses, dedicated selections are applied, as will be discussed in section 6.4. After these steps, it is possible to construct spin sensitive variables and perform the statistical analysis, with which the results are obtained. This will be discussed in the next chapter.

The analysis is performed on the full 2012 dataset which yields 20.7 fb^{-1} of $\sqrt{s} = 8$ TeV proton-proton collision data. Only final states with one electron, one muon, missing transverse energy and up to one jet are considered. Final states including ee or $\mu\mu$ pairs are not included in the analysis as these final states suffer from backgrounds, especially $Z \to e^+e^-/\mu^+\mu^-$, that cannot be rejected without reducing the spin sensitivity. Furthermore, only Higgs production through gluon gluon fusion is considered, since other production mechanisms do not add much sensitivity in the 0-jet and 1-jet channel, while complicating the analysis.

6.2 Background processes

The final state of the studied Higgs signal comprises of an electron, a muon, missing transverse energy and up to one jet. SM processes with the same final state contaminate the signal region and are therefore treated as backgrounds in this analysis. Knowing the signatures of the background processes, these can partially be removed from the data sample using dedicated rejection cuts. The background processes with non negligible contributions in the signal regions of the 0-jet and 1-jet channels are the following:

- **WW** This background is largely irreducible, since the final state products also come from the decay of two W-bosons. The differences in the helicity configuration and the mass of the WW system in the SM production and Higgs decay may however lead to differences in the kinematics of the final state particles, which can be used to reduce this background;
- **Top quarks** including production of top quarks in pairs ($t\bar{t}$), and in association with a W-boson (Wt) or quark(s) (single-t). Given that the top quark decays into a W-boson and a b-quark these processes result in final states with two leptons, E_T^{miss} and either one (Wt) or two ($t\bar{t}$) b-jets. In the case of single-t, only one lepton emerges from a W-boson decay, the other lepton is then assumed to be a jet misidentified as a lepton;
- **W+jets** The final state of this process consists of one lepton and E_T^{miss}, due to the decay of the W-boson, and a second lepton coming from misidentification of a jet. The QCD multijet background, having a final state that consists of two jets that are misidentified as leptons, is evaluated jointly with the W+jets background;
- **Drell-Yan (DY)** which is the decay of either a Z-boson or a virtual photon into two leptons. The largest contribution to this background is $Z/\gamma^* \to \tau\tau$, where the τ-leptons decay leptonically, resulting in a final state with two leptons and E_T^{miss}. A smaller contribution comes from the decay into a pair of electrons or muons, where one electron is misidentified as a muon or vice versa;
- **W$\gamma^{(*)}$** where conversion of the photon gives rise to a second lepton in the final state;

- **WZ$^{(*)}$ and ZZ$^{(*)}$** In the case of two Z-bosons the final state has to include fake E_T^{miss} in order to mimic the Higgs signal.

There are a few other backgrounds to the analysis, such as $Z\gamma$ production and WW pairs produced in double parton interactions, but these have such small cross sections that, after applying the event selection, their contributions are negligible. These backgrounds are not further discussed, but nonetheless treated in the analysis. The modelling of the listed backgrounds will be discussed in the next section 6.3.

6.3 Data and Monte Carlo samples

The SM Higgs signal, alternative hypotheses and background processes are simulated using event generators. This is a vital part of the analysis, since the samples are used to compare the experimental data with the SM predictions, as well as with the alternative hypotheses. Given the complexity of a physics process, its modelling is only possible by dividing the process in several parts: the hard scatter, hadronisation, parton showering and the underlying event. There are various MC generators that are dedicated to the modelling of the specific parts of the physics process. The details of event generation as well as an overview of the available MC generators have already been given in section 4.3. In this section the modelling of the physics processes relevant for the analysis, as well as the specifics of the data sample are discussed.

6.3.1 Data sample

The data used for this analysis were collected during the 2012 LHC run by the ATLAS experiment and consist of pp collisions at $\sqrt{s} = 8$ TeV. From the recorded data, only events that were triggered by single or dilepton event filter triggers are used. The p_T threshold of the single lepton trigger is, both for muons and electrons, 24 GeV. The dilepton trigger requires a muon with $p_T > 8$ GeV and an electron with $p_T > 12$ GeV. Furthermore, data quality requirements are applied to the recorded data, such that events taken in periods when the relevant detector components were not efficiently operating are rejected. The resulting total integrated luminosity of the used data sample is 20.3 fb^{-1}.

6.3.2 MC background samples

Even after all event selections, which are used to improve the ratio of signal and background events, are applied, the data sample still consists for approximately 95% of background processes. Thus, to be able to identify a signal, it is important that the backgrounds are precisely modelled. After extensive studies of the best way to model the different backgrounds, a MC sample is generated for every background process, except for the W+jets and multijet backgrounds, since these can be better estimated using a fully data-driven method, as will be explained in section 6.5.5.

The MC samples generated for the various background processes are listed in table 6.1, together with the used generators, applied cuts, derived cross sections times branching fraction (σ·BR), and the order at which the cross section is determined. The cross sections and branching fractions are derived at $\sqrt{s} = 8$ TeV, and include the decays $t \to Wb$, $W \to \ell\nu$ and $Z \to \ell\ell$, where ℓ refers to e, μ or τ. The neutral current process is denoted either as Z or γ^*, depending on the mass of the produced lepton pair. The effects of pile-up are simulated separately with PYTHIA8, assuming no interference with the hard scatter, and are subsequently incorporated in the background samples. Further explanations about the content of the table are given below.

To model the momentum fractions of the partons in the events, Parton Distribution Functions (PDF) are used, as explained in section 4.1.2. Various PDF sets are available and it depends on the generator and process which set is used. For the samples listed in table 6.1 that are generated with POWHEG, GG2VV, MC@NLO and SHERPA the CT10 PDF set [104] has been used, while ALPGEN, HERWIG, MADGRAPH, PYTHIA8 and ACERMC samples are generated, using cteq6L1 [105]. The Z/γ^* background forms an exception as it is generated with SHERPA, while using the MRST PDF set [106]. The GG2VV generator [107] is used to model the small contribution from quark box diagrams in the WW background, which is not included in POWHEG.

The MC generators that are optimal to model a certain process may not give the most precise value of the cross section, for example, because the process is modelled at LO, while the cross section can be calculated including NLO corrections. Therefore, the cross sections are sometimes determined using a specific program, as is indicated in the table along with the order at which the cross section is calculated.

Some processes are generated with a filter that consists of cuts that select the specific final state that forms the background for the WW Higgs decay mode. Additionally, some processes are split into different subprocesses or mass ranges, that are generated separately, in order to optimise the modelling of the different phase spaces of the process. If different (sub)processes overlap, then overlapping events are removed from one of the samples.

6.3.3 MC signal samples

The SM Higgs signal is modelled with POWHEG, interfaced with PYTHIA8 for the parton showering. The used PDF set is CT10. Only the gluon gluon fusion production mechanism is taken into account, according to the physics arguments explained before, and the modelling is performed for $M_H = 125$ GeV. The total cross section is computed with NNLO accuracy, using the $m_t \to \infty$ approximation [111], and NNLL QCD corrections and NLO EW corrections are applied. The MC is normalised to these calculations. The cross section times branching fraction of the SM Higgs boson signal under study is calculated to be 0.435 pb.

The Higgs p_T spectrum is reweighted such that it corresponds to the prediction of the NNLO+NNLL calculation which is given by the hres2.1 program [112,113], since this leads to a more precise description of the p_T spectrum than the one obtained with POWHEG.

The MC samples of the alternative hypotheses are generated according to the Higgs characterisation model that has been discussed in section 1.4. Several MC generators have been considered for the modelling of the alternative hypotheses. Both JHU [114, 115] and MADGRAPH5 [116] gave good results, but since also the 1-jet channel is included, MADGRAPH5 is preferred as it is capable of generating multiple additional partons in the final state. Moreover, in MADGRAPH5 the AMC@NLO package is integrated, such that NLO corrections can be included. The showering is simulated with PYTHIA6 and the used PDF set is CTEQ6L1. The samples, including up to two partons in the final state, are generated with NLO accuracy. Since there are no clear predictions for the cross sections of the alternative bosons, the cross sections are normalised to the SM Higgs boson cross section. A total of eight samples are generated with MADGRAPH5_AMC@NLO+PYTHIA6: a 0^- sample with the settings

Process	**MC generator**	**Filter**	$\sigma\times$ **BR [pb]**	**Normalisation**
WW				
$q\bar{q} \to WW$, $qg \to WW$	POWHEG+PYTHIA6		5.68	NLO (MCFM)
$gg \to WW$	GG2VV+HERWIG		0.196	LO (GG2VV)
Top quarks				
$t\bar{t}$	POWHEG+PYTHIA6		26.6	NNLO+NNLL (TOP++2.0)
Wt	POWHEG+PYTHIA6		2.35	NNLL ([108–110])
$tq\bar{b}$	ACERMC+PYTHIA6		28.4	" "
$t\bar{b}$	POWHEG+PYTHIA6		1.82	" "
Other dibosons (VV)				
$W\gamma$	ALPGEN+HERWIG	$p_T^\gamma > 8$ GeV, $\Delta R(\gamma, \ell) > 0.25$	369	NLO (MCFM)
$W\gamma^*$	SHERPA	$m_{\ell\ell} \leq 7$ GeV, $N_{lep} = 2$, $p_T^\ell > 5$ GeV, $\lvert\eta_\ell\rvert < 3$	12.2	ratio of MCFM NLO and SHERPA LO
WZ	POWHEG+PYTHIA8	$m_{\ell\ell} > 7$ GeV	12.7	NLO (POWHEG)
$Z\gamma$	SHERPA	$p_T^\gamma > 8$ GeV, $\Delta R(\gamma, \ell) > 0.1$, $M_\ell > 10$ GeV	163	NLO (MCFM)
$Z\gamma^*$	SHERPA	$m_{\ell\ell 1} \leq 4$ GeV, $m_{\ell\ell 1} > 4$ GeV	7.31	ratio of MCFM NLO and SHERPA LO
ZZ	POWHEG+PYTHIA8	$m_{\ell\ell} \leq 4$ GeV	0.733	LO (SHERPA)
$ZZ \to \ell\ell\nu\nu$	POWHEG+PYTHIA8	$m_{\ell\ell} \leq 4$ GeV	0.504	" "
Drell-Yan				
Z	ALPGEN+HERWIG	$m_{\ell\ell} > 10$ GeV	16500	NNLO (DYNNLO)

Table 6.1: *The event generators, filters, cross section times branching fraction, and cross section normalisation, used to model the background processes. If no filter is given, no specific cuts are applied. [9]*

listed in 1.1, a 1^+ sample and a 1^- sample, with the settings listed in 1.2 and five 2^+ samples, of which the different settings are given in table 1.3.

6.4 Object and event selections

The total cross section of pp interactions in the LHC at $\sqrt{s} = 8$ TeV is in the order of 100 millibarn, while the cross section of Higgs events decaying into the $\ell\nu\ell\nu$ final state is only in the order of 500 femtobarn. A difference of twelve orders of magnitude. Besides the background processes that occur in collisions, also non-collision activity such as cosmic rays and detector noise form a background to the Higgs signal. The trigger system already improves the signal over background ratio, but to allow for the study of the observed Higgs signal, selection criteria are needed in order to further reduce the number of background events, while preserving the signal as much as possible. Firstly, an object selection is applied to reduce the contribution of physics objects that do not come from the hard scatter, as will be discussed in section 6.4.1. Subsequently, an event selection is applied. The event selection criteria are focussed on increasing the spin sensitivity of the analysis, as well as on obtaining a good signal over background ratio. This makes the spin and parity analysis substantially different from the rate analysis that focusses on the measurement of the SM Higgs signal, and therefore uses spin sensitive variables to reduce backgrounds. The event selection is discussed in section 6.4.2. The object and event selections are defined and optimised using the MC signal and background samples and eventually applied to both the MC samples and the data sample.

6.4.1 Object selection

A selection of physics objects is defined to select the final state of the studied Higgs decay and suppress backgrounds. The objects present in the final state include electrons, muons, missing transverse energy (E_T^{miss}) and jets, therefore the selections for these objects are discussed. The reconstruction of the objects has already been addressed in section 4.4. In case that two close by leptons or jets are selected, an overlap removal procedure is applied, as will be discussed in section 6.4.1.4.

6.4.1.1 Leptons

Electron and muon candidates can be selected according to various sets of predefined ATLAS identification criteria that range from tight to loose, where the tighter criteria give a higher purity of the selected leptons at the price of a lower identification efficiency. In this analysis electrons with $p_T < 25$ GeV are selected according to the very tight likelihood requirements, while electrons with $p_T > 25$ GeV are selected according to the so-called *medium++* selection criteria. Both sets of identification criteria are defined from various calorimeter, track and combined variables and detailed in Ref. [117]. Concerning the muons, only combined muons that are reconstructed with the chain I algorithm, as explained in section 4.4.2, are used in the analysis. On top of these identification criteria, additional analysis specific cuts are applied. Both electrons and muons are required to have a p_T above 15 GeV, and to have a pseudorapidity of $|\eta| < 2.5$. Electrons in the transition region ($1.37 < |\eta| < 1.52$) are excluded.

To ensure that leptons are originating from the primary vertex, i.e. from the hard scatter, cuts are applied on the impact parameters. The longitudinal impact parameter, z_0, is defined as the distance in z with respect to the primary vertex. The actual cut is applied on $|z_0 \sin\theta|$, in order to take into account that more forward tracks have a longer projection on the z-axis and as such a larger uncertainty. The transverse impact parameter, d_0, is defined as the distance in the transverse plane with respect to the primary vertex. The cut is applied on d_0 divided by its estimated uncertainty, σ_{d_0}. The required values of these parameters differ for electrons and muons and are listed in table 6.2 and 6.3 respectively.

Additionally, track and calorimeter isolation criteria are applied to reduce the contribution from fake leptons and leptons in jets coming from heavy quark decays. These criteria concern the activity in close proximity of a lepton, since leptons coming from the W-boson decay are mostly well isolated. The track isolation is based on the scalar sum of the transverse momenta of all tracks, $\sum p_T$, within a specified cone in $\eta - \phi$ space around the lepton, excluding the p_T of the lepton track itself. Tracks used in this sum are required to come from the primary vertex, and only tracks with $p_T > 1$ GeV for muons and tracks with $p_T > 400$ MeV for electrons are taken into account. The cone size used in the selection of both electrons and muons is $\Delta R = 0.3$. The

$\mathbf{p_T}$ (GeV)	Calo isolation	Track isolation	$\mathbf{z_0}$	$\mathbf{d_0}$
$15-20$	$\sum E_T^{\text{cells}}/p_T < 0.24$	$\sum p_T^{\text{trks}}/p_T < 0.08$	$\lvert z_0 \sin\theta\rvert < 0.4$ mm	$d_0/\sigma_{d_0} < 3.0$
> 20	$\sum E_T^{\text{cells}}/p_T < 0.28$	$\sum p_T^{\text{trks}}/p_T < 0.10$		

Table 6.2: *The isolation and impact parameter requirements for electrons used in the analysis.*

$\mathbf{p_T}$ (GeV)	Calo isolation	Track isolation	$\mathbf{z_0}$	$\mathbf{d_0}$
$15-20$	$\sum E_T^{\text{cells}}/p_T < 0.12$	$\sum p_T^{\text{trks}}/p_T < 0.08$	$\lvert z_0 \sin\theta\rvert < 1.0$ mm	$d_0/\sigma_{d_0} < 3.0$
$20-25$	$\sum E_T^{\text{cells}}/p_T < 0.18$	$\sum p_T^{\text{trks}}/p_T < 0.12$		
> 25	$\sum E_T^{\text{cells}}/p_T < 0.30$			

Table 6.3: *The isolation and impact parameter requirements for muons used in the analysis.*

actual cut is applied on the scalar sum divided by the transverse lepton energy. The calorimeter isolation is defined in a similar way, namely as the sum of the transverse cluster energies, $\sum E_T$, of energy deposits in the electromagnetic and hadronic calorimeters inside a cone of $\Delta R = 0.3$ around the candidate electron cluster or muon candidate, divided by the transverse lepton energy. Concerning electrons, cells within 0.125×0.175 in $\eta \times \phi$ around the electron cluster barycentre are excluded from the sum, while for muons all cells within $\Delta R < 0.05$ are excluded. The isolation requirements depend on the p_T of the lepton and are listed in table 6.2 for electrons and in table 6.3 for muons.

6.4.1.2 Jets

Jets are reconstructed using the anti-k_t algorithm, as described in section 4.4.5. The jets that are present in the final state of the Higgs signal are selected using the so called looser jet cleaning, which is detailed in Ref. [118]. This looser selection has an efficiency of more than 99.8%. Only jets with $p_T > 25$ GeV and $|\eta| < 4.5$ are considered. The jet p_T threshold is increased to 30 GeV in the forward region ($2.4 < |\eta| < 4.5$) to reduce the contribution from jets produced in pile-up. To also reduce the pile-up contamination in the central region ($|\eta| < 2.4$) a requirement is imposed on the jet vertex fraction (JVF), which has been addressed in section 4.4.5. For jets with $p_T < 50$ GeV, it is required that $|JVF| > 0.5$.

One of the largest background in the analysis is top production. This background is characterised by jets coming from b-quarks, the so called b-jets. To identify these b-jets specific selections are defined. For the identification of b-jets, all jets with $p_T > 20$ GeV and $|\eta| < 2.4$ are taken into account. The b-jets are identified with the MV1 algorithm, which has been discussed in section 4.4.5. An operating point that is 85% efficient in identifying b-jets is adopted. At this operating point the probability of misidentifying a light jet as a b-jet is 10.3% [119].

6.4.1.3 Missing transverse energy

The missing transverse energy (E_T^{miss}) is the only way to identify neutrinos in an event. Since many analyses are dealing with processes with neutrinos in the final state, a lot of effort has been put in constructing various kinds of E_T^{miss} variables, each with specific features. The E_T^{miss} does not require a further object selections, because this is already incorporated in its reconstruction. In this analysis three different E_T^{miss} definitions are used. To construct the rest frame variables and the transverse momentum of the Higgs boson, the E_T^{miss} as defined in section 4.4.4 is used. This variables is officially called $E_{\text{T,RefFinal}}^{\text{miss}}$. A detailed description of its reconstruction algorithm, and the specific selections applied to the objects used in the reconstruction, are given in Ref. [84]. The E_T^{miss} variable used in the event selections is denoted as $E_T^{\text{miss, J-TRK}}$. Instead of using calorimeter information and muon tracks to construct the missing E_T, this variable is reconstructed using both muon and inner detector tracks, and only calorimeter information for the jets. The third variable used in the analysis is the relative missing E_T, $E_{\text{T,rel}}^{\text{miss}}$, which is the component of the $E_{\text{T,RefFinal}}^{\text{miss}}$ in the direction of the closest reconstructed object. This variable can be used to reject events with significant fake E_T^{miss} that arises due to the mismeasurement of objects. More information on this variable can be found in e.g. Ref. [119]. In the analysis, the $E_{\text{T,rel}}^{\text{miss}}$ is used in the construction of a combined variable that separates signal from background in the 0-jet channel.

6.4.1.4 Overlapping leptons and jets

If after the object selections, two leptons or jets within an event are in high proximity in $\eta \times \phi$, they are assumed to be two reconstructions of the same physics object. In

this case the lepton or jet candidate that is most probable to be the actual physics object is kept, while the other is removed from the event. The overlap removal takes into account jets, muons and electrons, and is applied in the following order:

- If a muon and an electron overlap within $\Delta R < 0.1$, the electron is removed;
- If two electrons overlap within $\Delta R < 0.1$, the lower p_T electron is removed;
- If an electron and a jet overlap within $\Delta R < 0.3$, the jet is removed;
- If a muon and a jet overlap within $\Delta R < 0.3$, the muon is removed.

6.4.2 Event selection

The event selection is motivated by the requirement to improve the ratio of signal over background events, however, the selection criteria should not substantially reduce the spin sensitivity. These requirements are rather conflicting, since the variables that are especially powerful to reject background events, while preserving the SM Higgs signal are sensitive to the spin and parity. Applying cuts on these variables introduces a dependence on the spin and parity. Thus, while in an analysis, like the measurement of the SM Higgs signal, such variables are perfect to apply tight cuts upon in order to cut away background, in the spin and CP analysis one wants to preserve the shape of these variables and cannot exploit them to achieve an optimal signal over background ratio. A balance between reducing the background and preserving spin sensitivity has to be found.

In table 6.4 all selection criteria, which will be motivated in the following sections, are summarised. Since the signatures of the alternative signal hypotheses differ from one another, it has also been tested if separate selections for each hypothesis are useful, but no significant gain in sensitivity has been observed. The event selection consists of two parts. First a pre-selection is applied to all events, as discussed in section 6.4.2.1 and then jet channel specific selections are applied, as the background composition differs with the number of jets in the final state. These selections will be discussed in sections 6.4.2.2 and 6.4.2.2 for the 0-jet and 1-jet channels respectively. The selection criteria are discussed in the order in which they are applied to evaluate the event yields, however, to obtain the final results, the order of the selections is irrelevant.

Variable	Spin/CP analysis	Rate analysis
	Pre-selection	
$N_{leptons}$	2, $e\mu$, opposite sign	2, $e\mu$, opposite sign
p_T^{lead}	> 22 GeV	> 22 GeV
$p_T^{sub-lead}$	> 15 GeV	> 10 GeV
$M_{\ell\ell}$	> 10 GeV	> 10 GeV
E_T^{miss}	> 20 GeV	> 20 GeV
	0-jet Selection	
N_{jets}	0	0
$\Delta\phi_{\ell\ell,E_T^{\text{miss}}}$	-	$> \pi/2$
$p_T^{\ell\ell}$	> 20 GeV	> 30 GeV
$M_{\ell\ell}$	< 80 GeV	< 55 GeV
$\Delta\phi_{\ell\ell}$	< 2.8	< 1.8
M_T	$62.5 < M_T < 150$ GeV	-
	1-jet Selection	
N_{jets}	1	1
b-veto	no b-jets with $p_T > 20$ GeV	no b-jets with $p_T > 20$ GeV
max M_T^{ℓ}	> 50 GeV	> 50 GeV
$M_{\tau\tau}$	$< (m_Z - 25)$ GeV	$< (m_Z - 25)$ GeV
$M_{\ell\ell}$	< 80 GeV	< 55 GeV
$\Delta\phi_{\ell\ell}$	< 2.8	< 1.8
M_T	< 150 GeV	-

Table 6.4: *List of the selection cuts that define the 0-jet and 1-jet signal regions, the pre-selection is in common for both jet bins. The cuts that are applied in the spin and CP analysis are shown on the left. The cuts applied in the rate analysis are given for comparison (right).*

To illustrate the effect of the selection criteria, in the following many plots will be shown. The ones that show both MC and data all have the same layout: the MC samples of the various background processes are shown in different colours, which are specified in the legend, and stacked. On top of the backgrounds, the simulated SM Higgs signal is shown in red. The statistical and experimental uncertainties on the total background are shown as a shaded area. The data are shown in black, where the error bars include statistical and systematical uncertainties. Most plots are accompanied with a plot showing the ratio between data and the expectation from MC for the background plus signal, where a yellow band includes both the statistical and systematical uncertainties.

6.4.2.1 Pre-selection

The effect of each cut in the event selection on the expected signal, the different background processes and the observed events in data is shown in table 6.5. The table shows a clear excess in data after all selections, which can be attributed to the Higgs boson signal. In the following the selection criteria are discussed.

First events are selected according to the leptons present in the final state: exactly one electron and one muon of opposite charge that both meet the object selections that have been described in the previous section are required. No other leptons are allowed in the event.

Different p_T thresholds have been tested for the leptons, since this is a good handle, especially in the spin and CP analysis, to remove background events. In the case of the rate measurement leptons with a sub-leading p_T as low as 10 GeV can be included, however, in the spin and CP analysis the optimal thresholds are: $p_T > 22$ GeV for the leading lepton and $p_T > 15$ GeV for the sub-leading lepton.

To suppress low mass DY events, the invariant mass of the two leptons, $M_{\ell\ell}$ is required to be above 10 GeV. Furthermore, as the DY and W+jets backgrounds tend to have lower E_T^{miss} than the SM Higgs signal, a cut on the E_T^{miss} is applied: $E_T^{\text{miss}} > 20$ GeV. In the optimisation of this cut it has been taken into account that some of the alternative hypotheses, especially the spin-2 boson, have also lower E_T^{miss} than the SM Higgs signal.

After the pre-selections, the background compositions of the 0-jet and 1-jet channel differ significantly, as clarified by figure 6.1, which shows the distribution of the jet multiplicity after the pre-selections. Therefore, the pre-selection is followed by separate selections for the 0-jet and 1-jet channel.

6.4.2.2 0-jet channel event selection

The 0-jet channel is dominated by the WW and Drell-Yan backgrounds. To reduce these and the other backgrounds, four more cuts are applied in the 0-jet channel. The variables that are very efficient in reducing the background, especially WW and DY, are the transverse momentum of the dilepton system, $p_T^{\ell\ell}$, the invariant mass of

	ggF [125 GeV]	WW	$WZ/ZZ/W\gamma$	$t\bar{t}$	Single Top	$Z \to \ell\ell + \gamma$/jets	$Z \to \tau\tau + \gamma$/jets	W+jets	Total Bkg.	Observed
quality cuts	536.2 ± 0.8	10033.6 ± 13.6	3782.2 ± 19.3	59515.1 ± 28.8	5683.8 ± 7.2	1145.8 ± 59.5	17787.4 ± 53.2	18714.0 ± 46.8	116661.7 ± 99.9	111442
lepton p_{T}	426.4 ± 0.7	9368.1 ± 13.2	2769.2 ± 16.1	55849.4 ± 27.9	5320.6 ± 6.8	349.1 ± 23.6	11523.9 ± 42.6	7218.4 ± 27.7	92398.7 ± 66.3	94686
Opposite sign leptons	425.9 ± 0.7	9335.5 ± 13.2	1385.0 ± 11.5	58306.8 ± 29.2	5524.5 ± 6.8	226.8 ± 23.0	11479.2 ± 42.5	4288.6 ± 21.6	90546.4 ± 63.3	90893
$m_{\ell\ell} > 10$ GeV	425.9 ± 0.7	9335.5 ± 13.2	1385.0 ± 11.5	58306.8 ± 29.2	5524.5 ± 6.8	226.8 ± 23.0	11479.2 ± 42.5	4267.0 ± 21.5	90524.8 ± 63.3	90893
$E_{\mathrm{T,RefFinal}}^{\mathrm{miss}} > 20$ GeV	372.0 ± 0.7	8553.9 ± 12.6	1074.4 ± 10.1	35366.8 ± 22.7	4078.4 ± 5.9	146.5 ± 19.7	7704.1 ± 35.7	1937.8 ± 13.2	58861.9 ± 51.4	60037
0j: jet veto	228.8 ± 0.5	6439.7 ± 11.9	518.0 ± 7.3	769.1 ± 3.4	379.8 ± 1.9	84.3 ± 14.4	2843.9 ± 22.2	937.9 ± 8.0	11972.6 ± 31.2	12133
0j: $p_{\mathrm{T},\ell\ell} > 20$ GeV	223.5 ± 0.5	6158.5 ± 11.7	492.7 ± 7.1	737.1 ± 3.3	366.7 ± 1.9	65.5 ± 10.8	1566.3 ± 16.4	802.4 ± 7.0	10189.1 ± 25.2	10338
0j: $m_{\ell\ell} < 80$ GeV	222.4 ± 0.5	2860.9 ± 7.9	323.8 ± 5.9	240.4 ± 1.9	137.3 ± 1.3	45.4 ± 7.8	1402.3 ± 15.5	437.0 ± 5.6	5447.1 ± 20.9	5781
0j: $\Delta\phi_{\ell\ell} < 2.8$	218.2 ± 0.5	2796.1 ± 7.8	311.4 ± 5.8	235.4 ± 1.9	134.9 ± 1.2	31.7 ± 4.8	514.8 ± 9.1	365.6 ± 4.9	4389.8 ± 15.1	4730
0j: $0.5 \cdot m_{\mathrm{H}} < m_{\mathrm{T}} \leq 1.2 \cdot m_{\mathrm{H}}$	216.0 ± 0.5	2324.4 ± 7.1	294.7 ± 5.7	142.1 ± 1.5	81.8 ± 1.0	30.9 ± 4.8	513.7 ± 9.1	355.6 ± 4.8	3743.2 ± 14.6	4052
0j: $Z \to \tau\tau$ control region	6.1 ± 0.1	86.2 ± 1.3	18.2 ± 1.3	8.9 ± 0.4	4.0 ± 0.3	15.7 ± 6.2	1921.2 ± 18.5	128.2 ± 4.1	2182.4 ± 20.0	2198
0j: WW control region	1.1 ± 0.0	2183.6 ± 7.0	116.5 ± 3.3	286.0 ± 2.1	143.1 ± 1.2	14.0 ± 5.9	140.5 ± 4.9	277.8 ± 3.7	3161.5 ± 11.8	3170
1j: one jet	108.3 ± 0.3	2645.4 ± 7.2	425.6 ± 6.1	7672.5 ± 10.5	2106.3 ± 4.2	59.1 ± 13.4	4207.4 ± 24.7	720.5 ± 8.4	17836.8 ± 32.8	17888
1j: b-jet veto	94.4 ± 0.3	2310.5 ± 6.7	360.6 ± 5.6	1473.5 ± 4.6	504.2 ± 2.2	49.6 ± 12.4	3664.8 ± 22.9	580.6 ± 7.3	8943.7 ± 28.9	8947
1j: max $m_T^{\ell} > 50$ GeV	85.6 ± 0.3	2183.5 ± 6.5	318.3 ± 5.3	1414.2 ± 4.5	484.6 ± 2.2	39.1 ± 11.1	1556.5 ± 15.2	393.3 ± 5.5	6389.5 ± 21.9	6467
1j: $Z \to \tau\tau$ veto	80.6 ± 0.3	1597.4 ± 5.6	233.7 ± 4.6	1005.0 ± 3.8	353.8 ± 1.8	18.8 ± 5.3	548.5 ± 9.5	236.6 ± 4.1	3993.8 ± 14.3	4067
1j: $m_{\ell\ell} < 80$ GeV	80.3 ± 0.3	805.1 ± 4.0	152.2 ± 3.8	465.5 ± 2.6	174.9 ± 1.4	12.1 ± 3.6	526.0 ± 9.2	145.5 ± 3.5	2281.3 ± 12.2	2370
1j: $\Delta\phi_{\ell\ell} < 2.8$	78.3 ± 0.3	768.0 ± 3.9	145.0 ± 3.7	451.2 ± 2.5	169.3 ± 1.3	6.2 ± 1.1	228.0 ± 6.0	127.9 ± 3.2	1895.5 ± 9.1	2014
1j: $m_{\mathrm{T}} \leq 1.2 \cdot m_{\mathrm{H}}$	76.6 ± 0.3	554.8 ± 3.3	131.4 ± 3.6	267.2 ± 1.9	103.4 ± 1.1	5.8 ± 1.0	227.7 ± 6.0	122.9 ± 3.1	1413.2 ± 8.6	1569
1j: $Z \to \tau\tau$ control region	4.8 ± 0.1	85.4 ± 1.3	20.7 ± 1.3	47.6 ± 0.8	15.6 ± 0.5	5.4 ± 3.3	940.9 ± 11.6	54.1 ± 2.7	1169.8 ± 12.5	1184
1j: WW control region	0.4 ± 0.0	1170.5 ± 4.8	130.4 ± 3.2	808.3 ± 3.4	262.0 ± 1.5	16.6 ± 8.7	81.2 ± 3.5	171.9 ± 3.0	2640.9 ± 12.0	2647
1j: Top control region	12.2 ± 0.1	292.0 ± 2.5	54.0 ± 2.2	5451.7 ± 8.9	1399.4 ± 3.3	3.9 ± 1.9	150.4 ± 5.2	88.1 ± 3.3	7439.6 ± 11.9	7422

Table 6.5: *The event yields for expected SM Higgs signal, expected background processes and observed data, for all stages in the pre-selection, 0-jet selection and 1-jet selection. The event yields in the different control regions are also given. The quoted uncertainties are statistical only.*

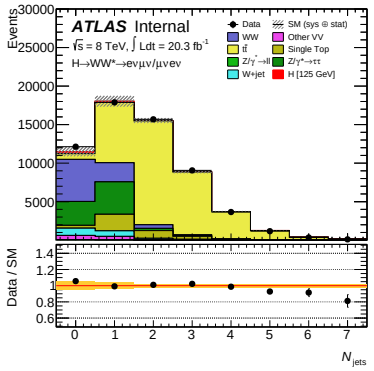

Figure 6.1: *Jet multiplicity after the cut on the E_T^{miss}. The various background processes are shown, as well as the SM Higgs signal.*

the leptons, $M_{\ell\ell}$, and the transverse angle between the leptons, $\Delta\phi_{\ell\ell}$, however, these variables are also sensitive to the spin. If the cuts on these variables would be set in accordance with the rate analysis, the sensitivity to spin and hence the separation power between the SM Higgs signal and the alternative hypotheses would be lost. This is illustrated in figures 6.2a, 6.2b and 6.2c for $p_T^{\ell\ell}$, $M_{\ell\ell}$ and $\Delta\phi_{\ell\ell}$ respectively, where in blue the distribution of the SM Higgs signal is shown and in red the spin-2 signal, being the most different from the SM signal. The distributions are shown after the pre-selection cuts, plus the jet veto and a cut on a variable called M_T that is discussed below. The black arrow shows the cut that would lead to the best signal over background ratio, i.e. the cut that is applied in the rate measurement. Clearly, cutting at these values would remove most separating power of these variables with respect to the different signal hypotheses. Therefore the cuts are loosened, as indicated in the figures with an orange arrow. The cuts are set to: $p_T^{\ell\ell} > 20$ GeV, $M_{\ell\ell} < 80$ GeV and $\Delta\phi_{\ell\ell} < 2.8$, where the cuts on $p_T^{\ell\ell}$ and $\Delta\phi_{\ell\ell}$ are especially useful to reduce the DY background. The cut on $M_{\ell\ell}$ is efficient in reducing the WW background, since the SM WW system is characterised by larger $M_{\ell\ell}$ values.

Figures 6.3a, 6.3b and 6.3c show again the distributions for $p_T^{\ell\ell}$, $M_{\ell\ell}$ and $\Delta\phi_{\ell\ell}$, but now for the SM Higgs signal, the backgrounds and the data, after the pre-selection and jet veto are applied. Again the optimal background rejection cut and the chosen spin preserving cut are indicated in respectively black and orange. Clearly, loosening the cuts, comes at a cost of an increased background rate, especially of DY and WW.

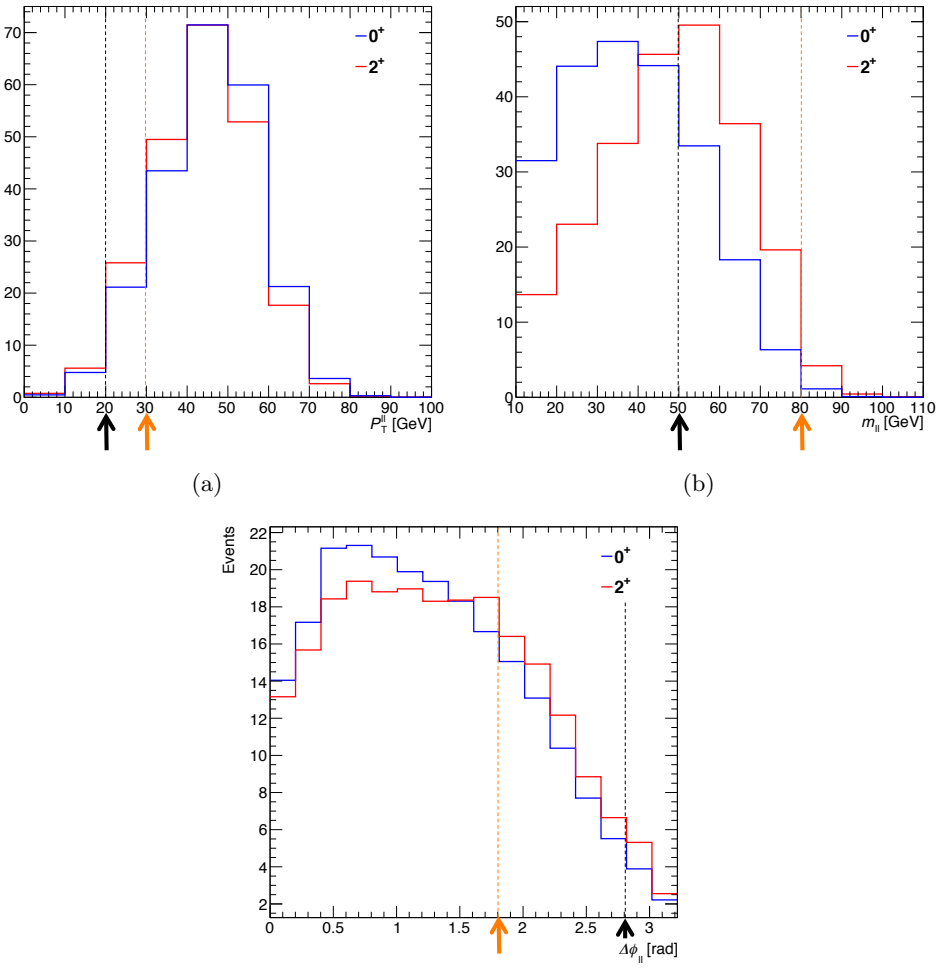

Figure 6.2: *The distributions of the SM Higgs signal and the spin-2 signal for three spin sensitive variables: $p_T^{\ell\ell}$ (a), $M_{\ell\ell}$ (b) and $\Delta\phi_{\ell\ell}$ (c). The black arrow indicates the optimal cut to reject background events and the orange arrow shows the cut used in order to preserve the spin and CP sensitivity.*

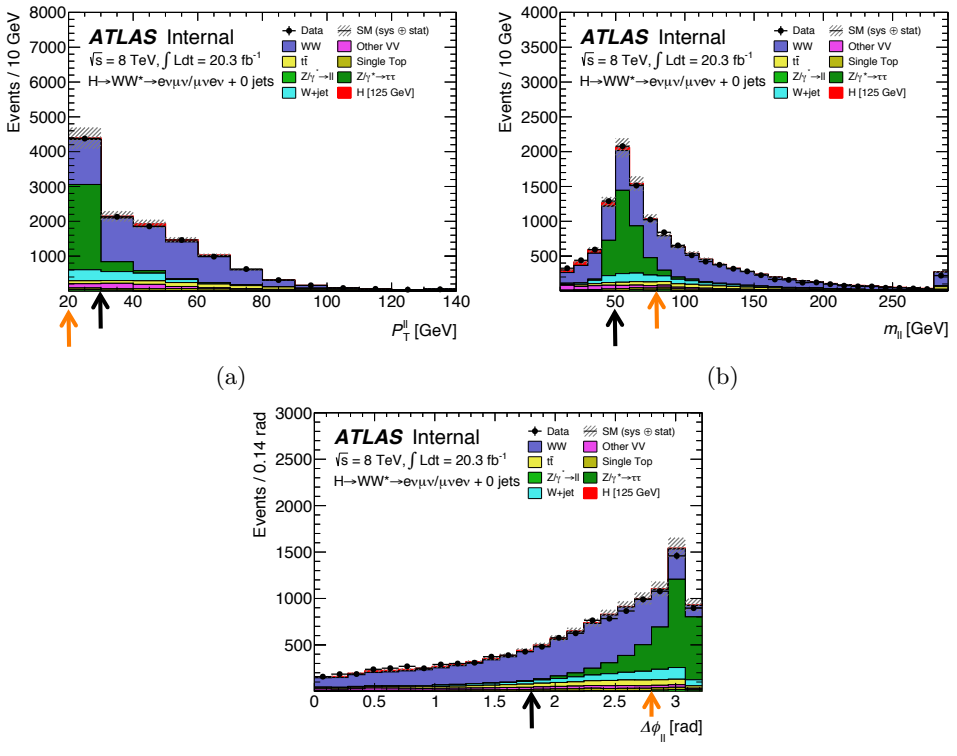

Figure 6.3: *The distributions of $p_T^{\ell\ell}$ (a), $M_{\ell\ell}$ (b) and $\Delta\phi_{\ell\ell}$ (c) for the expected SM Higgs signal and backgrounds, as well as data. The distributions are obtained after the pre-selection plus the jet veto. The black arrows indicate the cuts that are optimal to reject background, while the orange arrows indicate the cuts that are used in the analysis, such that the spin sensitivity is preserved.*

To compensate for this, a final cut on the so called transverse mass, M_T, of the Higgs boson is introduced [120]. This variable is developed to be used as an indicator of the Higgs boson mass, as its endpoint points approximately to the Higgs mass. Nevertheless, this variable turns out to also be very efficient to reject background events, while preserving the spin sensitivity. The transverse mass is defined as:

$$M_T = \sqrt{(E_T^{\ell\ell} + E_T^{\text{miss}})^2 - |\vec{p}_T^{\,\ell\ell} + \vec{E}_T^{\text{miss}}|^2} \tag{6.1}$$

with $E_T^{\ell\ell} = \sqrt{|\vec{p}_T^{\,\ell\ell}|^2 + M_{\ell\ell}^2}$ and $\vec{p}_T^{\,\ell\ell} = \vec{p}_T^{\,\ell 1} + \vec{p}_T^{\,\ell 2}$. The definition of $E_T^{\ell\ell}$ shows that also

	ggF 0^+	$J^{CP} = 0^-$	$J^{CP} = 1^+$	$J^{CP} = 1^-$	$J^{CP} = 2^+$
quality cuts	536.2 ± 0.8	565.5 ± 2.8	455.4 ± 2.6	497.7 ± 3.0	650.0 ± 3.3
lepton p_{T}	426.4 ± 0.7	448.8 ± 2.5	344.8 ± 2.2	375.6 ± 2.6	513.7 ± 2.9
Opposite sign leptons	425.9 ± 0.7	448.2 ± 2.5	344.2 ± 2.2	375.0 ± 2.6	513.1 ± 2.9
$m_{\ell\ell} > 10$ GeV	425.9 ± 0.7	448.2 ± 2.5	344.2 ± 2.2	375.0 ± 2.6	513.1 ± 2.9
$E^{miss}_{\mathrm{T,RefFinal}} > 20$ GeV	372.0 ± 0.7	388.9 ± 2.3	319.4 ± 2.1	341.2 ± 2.5	423.2 ± 2.7
0j: jet veto	228.8 ± 0.5	231.0 ± 1.8	243.0 ± 1.9	252.6 ± 2.1	249.8 ± 2.0
0j: $p^{\ell\ell}_{\mathrm{T}} > 20$ GeV	223.5 ± 0.5	224.6 ± 1.8	236.0 ± 1.8	242.0 ± 2.1	235.3 ± 2.0
0j: $m_{\ell\ell} < 80$ GeV	222.4 ± 0.5	223.7 ± 1.8	231.3 ± 1.8	235.9 ± 2.0	230.7 ± 2.0
0j: $\Delta\phi_{\ell\ell} < 2.8$	218.2 ± 0.5	218.0 ± 1.7	216.5 ± 1.8	216.5 ± 2.0	217.7 ± 1.9
0j: $0.5 \cdot m_{\mathrm{H}} < m_{\mathrm{T}} \leq 1.2 \cdot m_{\mathrm{H}}$	216.0 ± 0.5	216.0 ± 1.7	216.0 ± 1.8	216.0 ± 2.0	216.0 ± 1.9

Table 6.6: *The event yields for the expected SM Higgs signal, and the four alternative hypotheses for the observed signal. The event yields of the alternative hypotheses are normalised to the event yield of the SM Higgs signal after all cuts are applied.*

the z-component of the dilepton system is used. This results in a better resolution of the M_T variable compared to an older definition in which only the transverse component of the dilepton system was used. The missing E_T variable used in the definition is the $E^{\mathrm{miss}}_{\mathrm{T,RefFinal}}$. The requirement applied on the M_T in the 0-jet channel is: $62.5 < M_T < 150$ GeV. The effect of the 0-jet event selection is also shown in table 6.5, where the expected signal, background and data events are given after each selection criterium in the 0-jet channel. The expected background events are corrected with normalisation factors that are applied to normalise the backgrounds to the data. This will be discussed in section 6.5. It can be observed that the WW background remains the dominant background.

Table 6.6 shows the expected event yields for the five different signal hypotheses at all stages in the pre-selection and 0-jet selection. Since the cross sections of the alternative hypotheses are unknown, the event yields are normalised to the event yield of the SM Higgs signal after all selections, such that similar event yields are obtained after the M_T cut. This normalisation is only relevant for the evaluation of the event yields and the spin sensitivity of kinematical variables. The signal normalisation is left as a free parameter in the fit with which the final results will be obtained.

The events that are left in the data and MC samples after all selections, form the input for the shape analysis with which the spin sensitivity of the analysis is optimised, therefore, it is important that no mismodelling is observed in the spin sensitive distributions. Figures 6.4a to 6.4d show the distributions of $\Delta\psi^*_{\ell\ell}$, E^*_{sum}, E^*_{dif} and $M_{\ell\ell}$

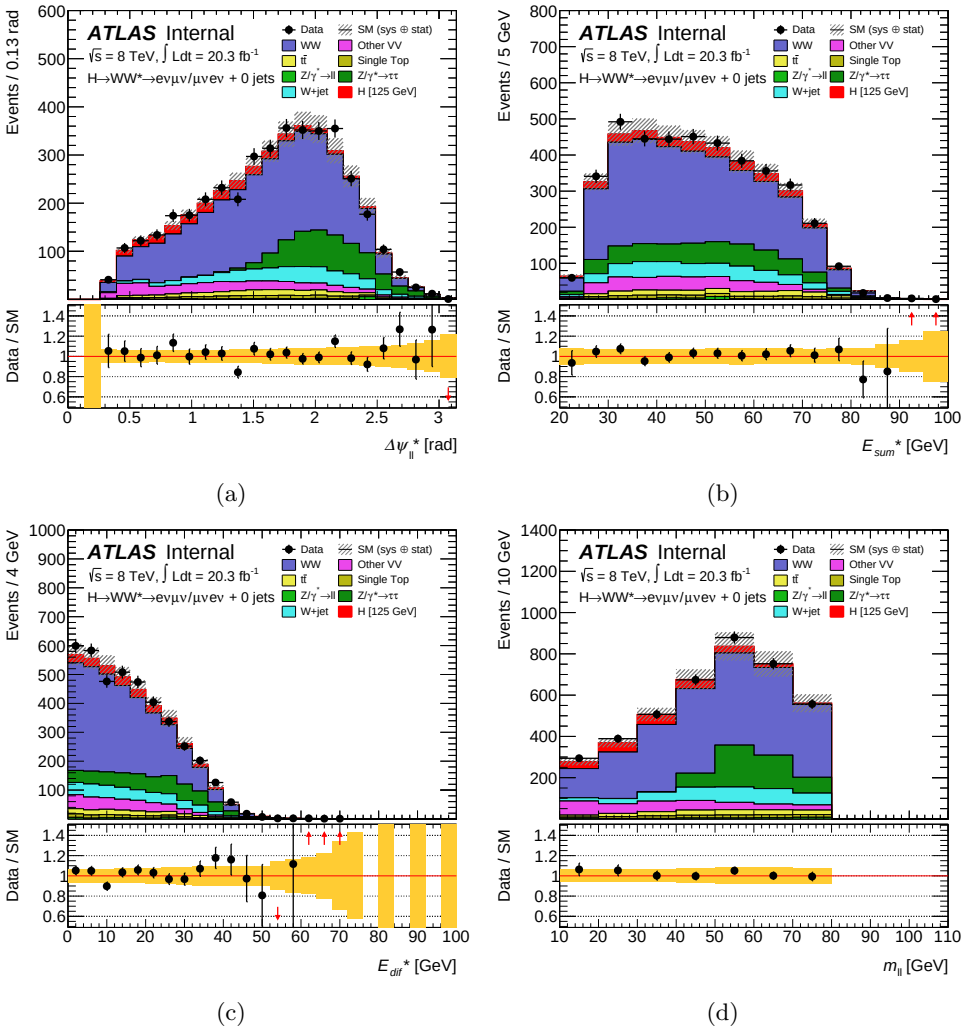

Figure 6.4: *The distributions of $\Delta\psi^*_{\ell\ell}$ (a), E^*_{sum} (b), E^*_{dif} (c) and $M_{\ell\ell}$ (d) after the 0-jet selection.*

after all selections. The first three variables are rest frame variables and defined in section 5.5. The distributions show good agreement between data and MC. Also the other distributions that will be used in the shape analysis show no mismodelling.

6.4.2.3 1-jet channel event selection

In the 1-jet channel the top background, especially $t\bar{t}$ production, dominates the total background. Since a top quark decays into a W-boson and a b-quark, the $t\bar{t}$, Wt and the single-t backgrounds can be reduced by applying a veto on b-jets, where the b-jets are defined as discussed in section 6.4.1.2. This is the first cut applied after the requirement of having exactly one jet in the event.

The DY background is the second largest background and mainly concerns decays into τ-quarks: $Z/\gamma^* \to \tau\tau$. Therefore, this background can be reduced by applying a cut on the invariant mass of the τ-leptons, $m_{\tau\tau}$. To reconstruct $m_{\tau\tau}$, a collinear approximation [121] is used: assuming that the visible decay products from the τ decays have the same direction as the corresponding τ-lepton, and that the neutrinos from the τ decays are the only source of missing energy, the τ momenta can be reconstructed. Then, if the energy fractions $x_{\tau 1}$ and $x_{\tau 2}$ carried by the visible decay products are positive and if $m_{\tau\tau} < (m_Z - 25GeV)$ the event is rejected.

To reduce the DY and W+jets backgrounds, a requirement is applied to the transverse lepton mass, which is defined as:

$$M_T^{\ell_i} = \sqrt{2p_T^{\ell_i} \cdot E_T^{\text{miss}} \cdot (1 - \cos(\Delta\phi_{\ell, E_T^{\text{miss}}}))} \tag{6.2}$$

where $\Delta\phi_{\ell, E_T^{\text{miss}}}$ is the angle between the lepton and the transverse momentum, $\vec{E}_T^{\text{miss}}$, and the missing E_T is defined as $E_{\text{T,RefFinal}}^{\text{miss}}$. The M_T^{ℓ} tends to have smaller values for the DY and W+jets backgrounds, compared to the signal. The transverse mass is determined for both leptons, and then it is required that the larger value of M_T^{ℓ} is required to be above 50 GeV. Furthermore, the same cuts on $M_{\ell\ell}$ and $\Delta\phi_{\ell\ell}$ as in the 0-jet channel are applied. Again, to compensate for the increased background rate, due to the loosened cuts on $M_{\ell\ell}$ and $\Delta\phi_{\ell\ell}$, a cut is applied on the transverse mass of the Higgs boson: $M_T < 150$ GeV.

Table 6.5 shows also the event yields for the expected signal, background and observed events at every stage in the 1-jet event selection. Again, normalisation factors are applied. Table 6.7 shows the expected event yields for the five different signal hypotheses at all stages in the pre-selection and 1-jet selection. The event yields of

	ggF 0^+	$J^{CP} = 0^-$	$J^{CP} = 1^+$	$J^{CP} = 1^-$	$J^{CP} = 2^+$
quality cuts	536.2 ± 0.8	539.0 ± 2.7	859.1 ± 4.8	920.9 ± 5.5	694.2 ± 3.5
lepton p_{T}	426.4 ± 0.7	427.7 ± 2.4	650.5 ± 4.2	695.0 ± 4.8	548.6 ± 3.1
Opposite sign leptons	425.9 ± 0.7	427.2 ± 2.4	649.3 ± 4.2	693.9 ± 4.8	547.9 ± 3.1
$m_{\ell\ell} > 10$ GeV	425.9 ± 0.7	427.2 ± 2.4	649.3 ± 4.2	693.9 ± 4.8	547.9 ± 3.1
$E_{\mathrm{T,RefFinal}}^{\mathrm{miss}} > 20$ GeV	372.0 ± 0.7	370.7 ± 2.2	602.6 ± 4.0	631.4 ± 4.5	452.0 ± 2.8
1j: one jet	108.3 ± 0.3	115.3 ± 1.2	123.0 ± 1.8	137.8 ± 2.1	140.0 ± 1.6
1j: b-jet veto	94.4 ± 0.3	99.9 ± 1.1	106.7 ± 1.7	120.3 ± 2.0	121.3 ± 1.5
1j: max $m_T^{\ell} > 50$ GeV	85.6 ± 0.3	87.4 ± 1.1	95.1 ± 1.6	103.2 ± 1.8	101.0 ± 1.3
1j: $Z \to \tau\tau$ veto	80.6 ± 0.3	80.4 ± 1.0	82.1 ± 1.5	84.9 ± 1.7	83.7 ± 1.2
1j: $m_{\ell\ell} < 80$ GeV	80.3 ± 0.3	80.3 ± 1.0	81.2 ± 1.5	83.2 ± 1.6	82.7 ± 1.2
1j: $\Delta\phi_{\ell\ell} < 2.8$	78.3 ± 0.3	77.9 ± 1.0	77.6 ± 1.4	77.7 ± 1.6	77.6 ± 1.2
1j: $m_{\mathrm{T}} \leq 1.2 \cdot m_{\mathrm{H}}$	76.6 ± 0.3	76.6 ± 1.0	76.6 ± 1.4	76.6 ± 1.6	76.6 ± 1.2

Table 6.7: *The event yields for expected SM Higgs signal, and the alternative hypotheses for the observed signal. The event yields of the alternative hypotheses are normalised to the event yield of the SM Higgs signal after all cuts are applied.*

the alternative hypotheses are normalised to the event yield of the expected SM Higgs signal after the 1-jet selection. Because of the different normalisations applied to the events in 0-jet and 1-jet channel, the yields in the pre-selections of the 0-jet and 1-jet channel differ for the alternative hypotheses.

Figures 6.5a to 6.5d show the distributions of $\Delta\psi_{\ell\ell}^{*}$, E_{sum}^{*}, E_{dif} and $M_{\ell\ell}$ after the 1-jet event selection. Good agreement between data and MC is observed.

6.5 Background estimation

The cross sections of the background processes that are simulated with MC generators may suffer from uncertainties, since the generators have as only input the theoretical predictions of the physics processes. To improve the modelling of some of the backgrounds their yields are normalised to the observed yields in data. The associated normalisation factor is determined in control regions (CR) that are defined for each background process separately, such that they are dominated by the relevant background. The general definition of a CR is explained in section 6.5.1. This procedure is used to normalise the WW, top and DY backgrounds, as will be addressed in sections 6.5.2, 6.5.3 and 6.5.4. The event yields in data of the non-WW diboson backgrounds are too small to use for normalisation of these background. Instead, the estimates

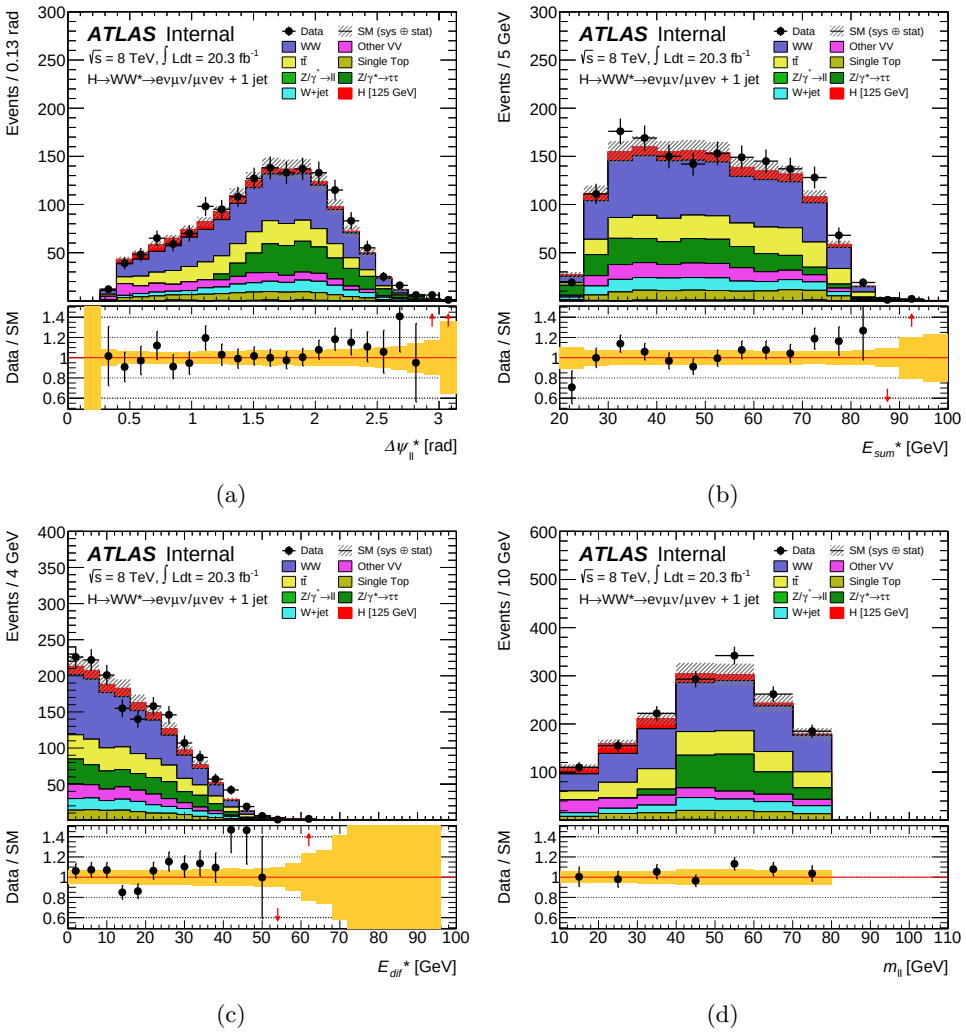

Figure 6.5: *The distributions of $\Delta\psi^*_{\ell\ell}$ (a), E^*_{sum} (b), E^*_{dif} (c) and $M_{\ell\ell}$ (d) after the 1-jet selection.*

acquired from MC for these backgrounds are checked in a validation region, as will be discussed in section 6.5.6. Finally, the W+jets and multijet backgrounds are evaluated jointly, and estimated using only data, since fake leptons are better estimated with a data-driven method than with a MC generator. The data-driven method is explained in section 6.5.5.

6.5.1 Definition of a control region

The construction of a control region (CR) is similar for the various backgrounds. The set of cuts with which a CR is defined is ideally orthogonal to the event selection in the SR, in order to minimise the number of signal events in the CR. The cuts are defined such that the CR is dominant in the relevant background. Since the normalisation factor is determined in the CR, but applied to the events in the SR, the CR event selection should be kept close to the SR event selection, as to minimise the extrapolation uncertainties from the CR to the SR. The CR selection criteria depend on the background that has to be extracted and are discussed in the relevant sections.

The normalisation factor, β, is defined as the ratio of the yields of the observed (data) and expected (MC) events of the background under study in the CR. The observed yield in the CR is obtained by subtracting the expected other background contributions and signal from the data yield. The best estimate in the SR for the yield of the background process under consideration, B_{SR}^{est}, is defined as:

$$B_{SR}^{\text{est}} = B_{SR} \cdot \underbrace{N_{CR}/B_{CR}}_{\text{normalisation } \beta} = N_{CR} \cdot \underbrace{B_{SR}/B_{CR}}_{\text{extrapolation } \alpha} \tag{6.3}$$

where N_{CR} is the observed yield in the CR, B_{CR} the MC estimate in the CR and B_{SR} the MC estimate in the signal region, where the latter is the theoretical prediction that needs to be corrected. The parameter α defines the extrapolation factor from the CR to the SR and is determined from the MC expectations. The normalisation factors will be simultaneously determined for all relevant backgrounds in the fit with which the final results are obtained. However, to evaluate the background yields, the normalisation factors are also calculated at an earlier stage.

In the following sections the background estimation is discussed separately for each background and illustrated with distributions of $\Delta\psi^*_{\ell\ell}$ and E^*_{sum}, two variables that are important in the spin and CP analysis.

6.5.2 WW background

The 0-jet WW CR is defined by applying all SR cuts up till the $p_T^{\ell\ell}$ cut and adjusting the cut on $M_{\ell\ell}$ to $80 < M_{\ell\ell} < 150$ GeV, since the SM WW process is characterised by larger $M_{\ell\ell}$ values than the SM Higgs signal. The cuts on $\Delta\phi_{\ell\ell}$ and M_T are not applied. The 1-jet WW CR is defined by all SR cuts up till the M_T^{ℓ} cut and additionally requiring that $M_{\ell\ell} > 80$ GeV, the remaining SR cuts are not applied. These CRs are orthogonal to the SRs and have a purity of respectively 69% and 43% for the 0-jet and 1-jet channel. The background composition of the two CRs is given in table 6.5.

Figures 6.6a to 6.6d show the distributions for $\Delta\psi^*_{\ell\ell}$ and E^*_{sum} in the 0-jet and 1-jet CRs. A good agreement between data and MC is observed. The resulting normalisation factors for the WW backgrounds in the 0-jet and 1-jet channel are 1.18 ± 0.03 and 1.04 ± 0.05 respectively.

6.5.3 Top quark background

The top quark CRs are used to jointly normalise the $t\bar{t}$, Wt and single-t backgrounds. Since the cross section of top production is so large and jets are not always identified, the top quark background contributes also to the 0-jet channel. Therefore, both a 0-jet and 1-jet top CR are constructed.

In the 0-jet channel, the top CR is defined by all pre-selection cuts and the requirement that $\Delta\phi_{\ell\ell} < 2.8$. As such, the CR is inclusive in the number of jets and since there is no cut that makes the CR orthogonal to the SR, there is a small overlap between the SR and the CR. Nevertheless, the signal contamination in the CR is less than 1%. The purity of the 0-jet CR is 74%. The normalisation factor is 1.08 ± 0.02.

In the 1-jet channel, the CR is defined by all pre-selection cuts, the requirement of one jet in the final state and requiring that at least one jet is a b-jet and applying a

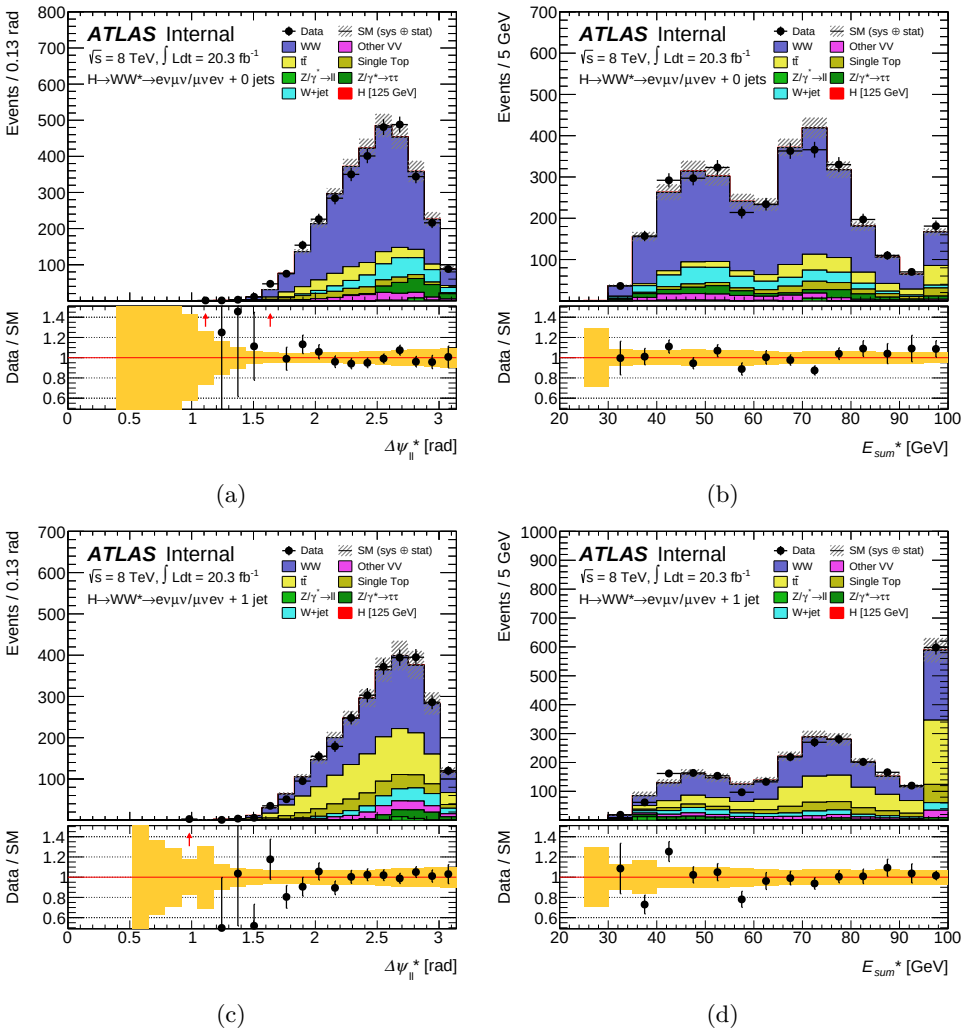

Figure 6.6: *The distributions of $\Delta\psi^*_{\ell\ell}$ and E^*_{sum} in the 0-jet (a,b) and 1-jet (c,d) WW control regions.*

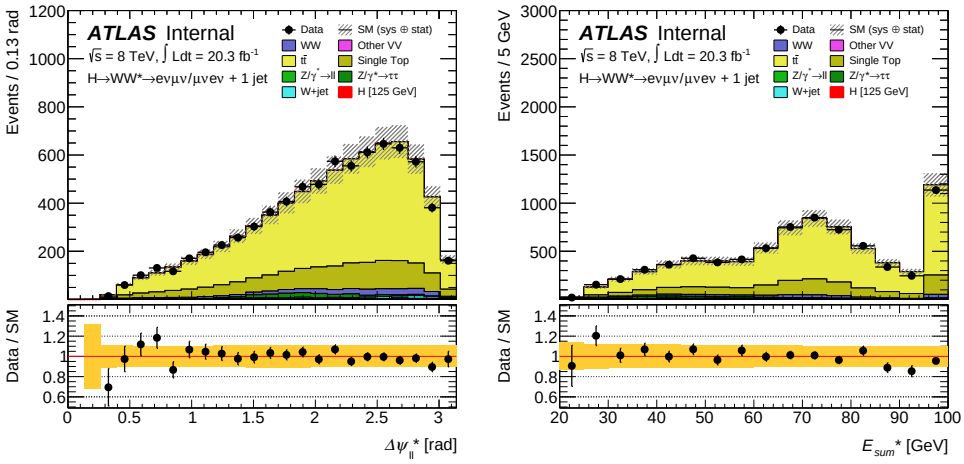

(a) (b)

Figure 6.7: *The distributions of $\Delta\psi^*_{\ell\ell}$ (a) and E^*_{sum} (b) in the 1-jet top control region.*

veto on additional b-jets with $20 < p_T < 25$ GeV. Furthermore, the cuts on M_T^ℓ and $M_{\tau\tau}$ are applied to reduce the contamination of other backgrounds. The purity of the 1-jet CR is 73%. Figures 6.7a and 6.7b show the distributions for $\Delta\psi^*_{\ell\ell}$ and E^*_{sum} in the 1-jet CR. A good agreement between data and MC is observed, as also shown in table 6.5. The normalisation factor is calculated to be 1.03 ± 0.01.

Since the top quark background substantially contaminates the 1-jet WW CR - around 40% of the CR consists of top quark events - an extrapolation factor from the 1-jet top CR to the 1-jet WW CR is also included in the analysis.

6.5.4 Drell-Yan background

The 0-jet CR is defined by all pre-selection cuts, the jet veto, the cut $M_{\ell\ell} < 80$ GeV and additionally requiring that $\Delta\phi_{\ell\ell} > 2.8$, since DY production is characterised with a larger opening angle than the SM Higgs signal. The resulting CR has a purity of 90%, and its composition is shown in table 6.5. The normalisation factor is 1.01 ± 0.03.

In the 0-jet DY CR a mismodelling of the transverse mass of the Z-boson, reconstructed as $p_T^{\ell\ell}$, is observed. This is due to the fact that the ALPGEN+HERWIG MC

generation does not lead to adequate modelling of the parton showering of soft jets, which should balance the $p_T^{\ell\ell}$ in events without jets in the final state. To correct for this, weights derived from a data to MC comparison in the Z mass peak, are applied to MC events in bins of $p_T^{\ell\ell}$ in the 0-jet category. Figures 6.8a and 6.8b show the distributions of $\Delta\psi_{\ell\ell}^*$ and E_{sum}^* in the 0-jet CR after correction for this mismodelling. A good agreement between data and MC is observed.

The 1-jet CR is defined by all selection cuts up to $M_T^\ell > 50$ GeV and in addition requiring that $|m_{\tau\tau} - m_Z| < 25$ GeV, which is the inverted $Z\tau\tau$ veto. The 1-jet CR has a purity of 80%. The normalisation factor is estimated to be 1.05 ± 0.04. Figures 6.8c and 6.8d show the distributions of $\Delta\psi_{\ell\ell}^*$ and E_{sum}^* in the 1-jet CR, again good agreement between data and MC is observed.

Both in the 0-jet and 1-jet channel, the DY background contaminates the WW CR, with around 5%. Therefore, for each jet channel, an extrapolation factors from the DY CR to the WW CR is defined.

6.5.5 W+jets and multijet backgrounds

The W+jets background is estimated with a fully data-driven method, since this gives better results than normalising the MC sample of this background. In the estimation of the W+jets background, the multijet background is included, because this background also has misidentified leptons in the final state. Since the multijet background is very small compared to the W+jets background and the uncertainty on W+jets is large, it is allowed to ignore the small differences between the two backgrounds.

To estimate this background, a control sample is defined from data by requiring that one of the two lepton candidates satisfies the identification and isolation criteria that are described in section 6.4.1, while the other lepton must explicitly fail these criteria, but satisfy a looser selection. This latter lepton is referred to as anti-identified. The events should furthermore satisfy the full event selection. The resulting control sample consists for 85% to 90% of W+jets events, where one jet gives rise to an object that is reconstructed as a lepton. This lepton may either be the decay of a heavy quark or a jet misidentified as a lepton.

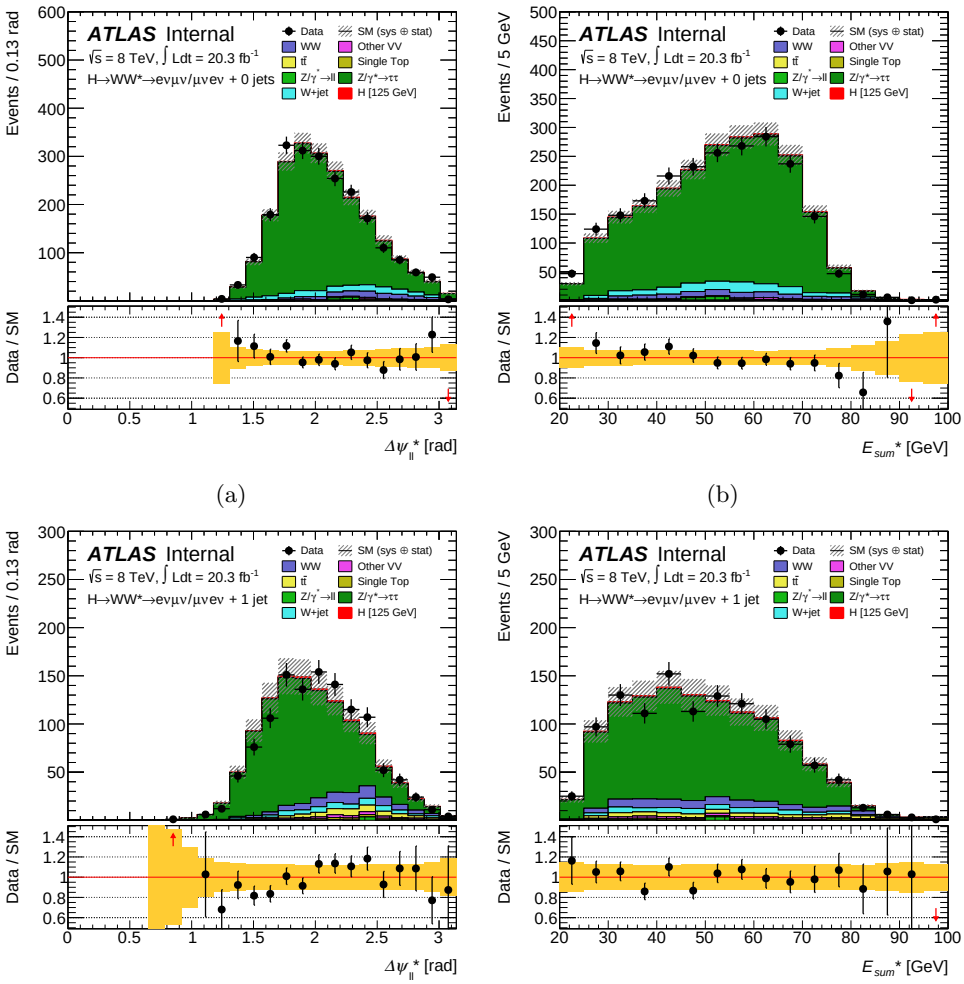

Figure 6.8: *The distributions of $\Delta\psi^*_{\ell\ell}$ and E^*_{sum} in the 0-jet (a,b) and 1-jet (c,d) DY control regions.*

The number of W+jets events in the SR is estimated by scaling the number of events in the control sample by an extrapolation factor. The extrapolation factor is estimated from data, using a sample of events with jets produced in association with a Z-boson. This sample is referred to as Z+jets and is used since it has a large cross section and a good selection efficiency. Then, to obtain for the Z+jets events a final state similar to that of W+jets, one identified lepton is removed, while a fake lepton is required. The extrapolation factor is defined as the ratio of the number of identified lepton candidates in the Z+jets sample that pass all lepton selection criteria to the number of anti-identified leptons in the sample. The factor is measured in bins of the anti-identified lepton p_T and η. The extrapolation factors are corrected for the presence of processes other than Z+jets in the data sample.

Furthermore, a correction is applied to the extrapolation factor for the fact that the contributions of heavy-flavour and light-flavour jets in the Z+jets and W+jets samples are different. MC simulations are used to determine the correction factor that is applied to the extrapolation factors. Finally, the W+jets background modelling is checked in a validation region, which is defined in the next section.

6.5.6 Same sign validation region

The modelling of the W+jets and non-WW diboson backgrounds is checked in a so called validation region (VR). This VR is used to evaluate the agreement between the MC and data in a region that is dominated by these backgrounds. The VR is defined by all SR cuts, but with the requirement of two oppositely charged leptons is inverted. In this way a sample of same sign (SS) leptons that is orthogonal to the SR is obtained. The 0-jet SS VR consists for 35% of W+jets background and for 58% of non-WW diboson backgrounds, and the 1-jet VR for 33% of W+jets and 61% of non-WW diboson backgrounds.

Figures 6.9a to 6.9d show the distributions of $\Delta\psi^*_{\ell\ell}$ and E^*_{sum} after al VR selection cuts in the 0-jet and 1-jet channel. Given the limited statistics of the data sample in the VR, the agreement between data and MC is good.

All preparations for the spin and parity measurement have now been made: MC samples that will be used to compare the data with the theoretical predictions have

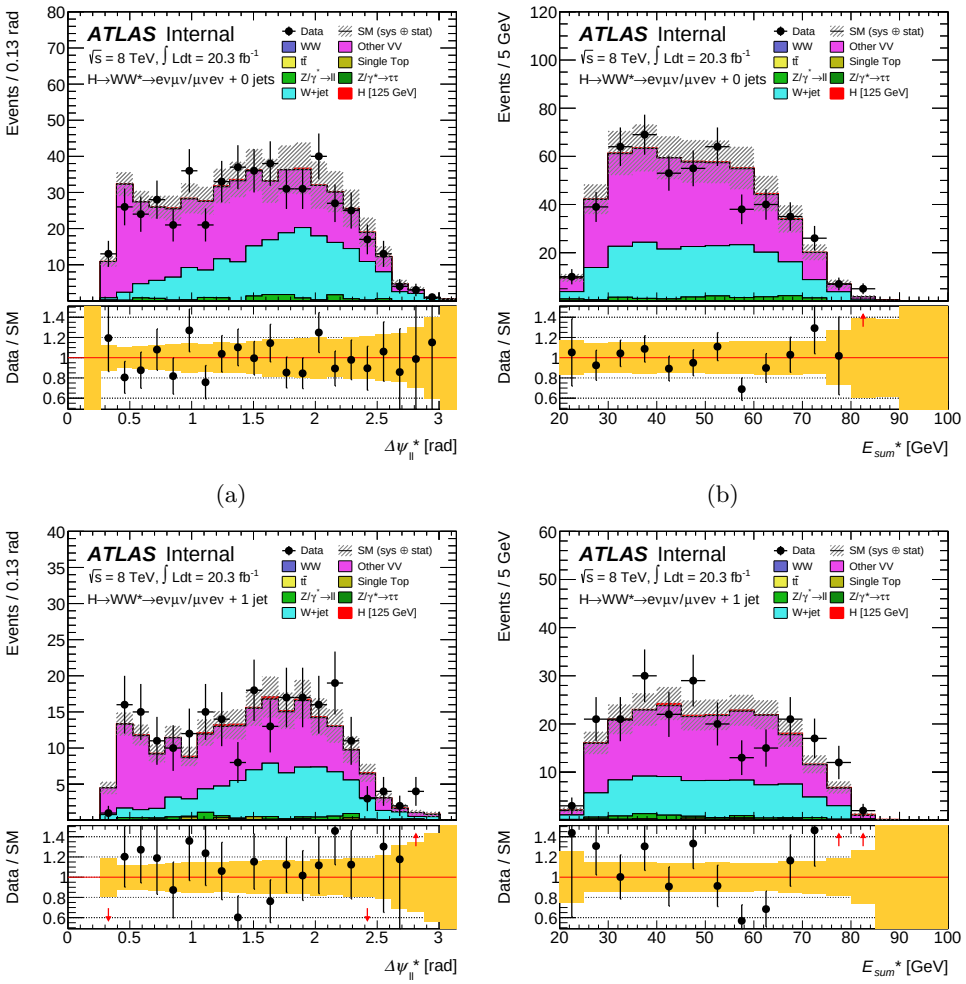

Figure 6.9: *The distributions of $\Delta\psi^*_{\ell\ell}$ and E^*_{sum} in the 0-jet (a,b) and 1-jet (c,d) channels in the same sign validation region.*

been validated, selections to reduce the backgrounds and enhance the spin and parity sensitivity of the signal have been formulated, and the backgrounds are precisely estimated. In the next chapter the optimisation of the spin sensitivity of the analysis will be discussed, and the measurement and its results will be presented.

Chapter 7

Spin and parity measurement

7.1 Introduction

The preparations described in the previous chapter result in an analysis with sufficient sensitivity to measure the spin and parity of the observed signal. The second part of the analysis focuses on constructing spin and parity sensitive variables that are discriminating between the SM Higgs signal and the alternative hypotheses, on top of the irreducible background. This is done for each hypothesis by analytically combining sensitive lab frame and rest frame variables into a new variable that exhibits the highest possible spin and parity sensitivity. The construction of these variables is explained in section 7.2. In the following the spin and parity sensitivity will be referred to as spin sensitivity.

The final combined variables are the input for the statistical analysis. In the statistical analysis, for each hypothesis, a likelihood is determined for the SM Higgs signal and for the alternative hypothesis. The likelihoods are determined in a fit in which all backgrounds, uncertainties, normalisation factors and other parameters are simultaneously fitted. The resulting likelihoods are used to build a so called test statistic with which the observed signal in data can be compared with the signal hypotheses. In this way the probabilities that the observed signal is that of the SM Higgs boson or of the alternative hypothesis can be calculated. The statistical analysis will be

explained in section 7.4. The final results are given in section 7.5. The systematic uncertainties, which have to be taken into account in the likelihood fit, are discussed in section 7.3.

7.2 The construction of spin sensitive variables

Now that the event selections and background estimation have been performed, the obtained MC and data samples are ready for the construction of the final spin sensitive variables. A total of eight of these variables is needed, namely one for each of the four hypotheses, 0^-, 2^+, 1^+ and 1^-, in both the 0-jet and 1-jet channel. The construction of the final variables is divided into two parts. First variables that optimally separate the SM Higgs signal from the alternative signal hypotheses are constructed. Additionally, for each jet channel, a variable is constructed that separates the SM Higgs signal from the total background. The procedure used to construct these spin and background separating variables is explained in section 7.2.1. Subsequently, the spin and background separating variables are combined to obtain the eight final variables that can be used to distinguish the signal hypotheses on top of the total remaining background. This will be discussed in section 7.2.2.

7.2.1 Combining spin sensitive variables

There are various ways to combine sensitive variables into one combined variable, one example is to use a multivariate analysis program that systematically combines variables. This is the type of analysis performed to obtain the official ATLAS results [9]. For the analysis in this thesis it has been chosen to make an analytical combination of variables, such that each step in the process can be tested and evaluated. This is useful since the measurement of the properties of the Higgs-like boson is a new kind of analysis. To ensure that the spin sensitivity of the variables is maximally exploited and that correlations between variables are taken into account, the following procedure is employed.

Firstly, the spin sensitivities of the various variables are consecutively evaluated, starting with the variable with most sensitivity. Of this first variable the spin sensitivity

is parametrised. Then, the parametrised sensitivity of the first variable is removed from the next variable, after which the additional spin sensitivity of this variable is parametrised. This procedure continues until no uncorrelated spin sensitivity is found in the remaining variables. The final spin separating variable is then constructed as the product of the parametrisations. To provide a better insight in the procedure, it will now be explained, step by step, for the case of obtaining a combined spin sensitive variable that distinguishes the SM Higgs signal, 0^+, from the 2^+ hypothesis, in the 0-jet channel. The same procedure is adopted to obtain the combined variables for the 0^-, 1^+ and 1^- hypotheses as well as for the combined variables that separate SM Higgs signal from background.

The variable that is most discriminating between the 0^+ and 2^+ hypotheses is $\Delta\psi^*_{\ell\ell}$. The spin sensitivity of $\Delta\psi^*_{\ell\ell}$ is determined as follows: the distributions of $\Delta\psi^*_{\ell\ell}$ for the 0^+ and 2^+ MC samples are normalised to the same number of events. Then, the spin sensitivity of $\Delta\psi^*_{\ell\ell}$ is extracted by parametrising the ratio distribution:

$$R_x(\Delta\psi^*_{\ell\ell}) = \frac{N(\Delta\psi^*_{\ell\ell})^{2^+}}{N(\Delta\psi^*_{\ell\ell})^{0^+}} \tag{7.1}$$

The fact that the ratio is defined as the alternative hypothesis divided by the SM hypothesis, is an arbitrary choice and could as well be turned around. The next step is to parametrise the ratio distribution with a fit function. This function is required to have good behaviour at low and high values of the fitted variable, as well as in parts with low statistics. Figure 7.1a shows the fit of $R_x(\Delta\psi^*_{\ell\ell})$. The parametrisation of the spin sensitivity of $\Delta\psi^*_{\ell\ell}$ is given by the fit function:

$$R_x(x) = p_0 \cdot e^{p_1 \cdot x} + p_2 \cdot e^{p_3 \cdot x} \tag{7.2}$$

with $x = \Delta\psi^*_{\ell\ell}$ and the determined fit parameters p_0 to p_3 inserted. The parametrisation, $R_x(x)$, has the same spin sensitivity as $\Delta\psi^*_{\ell\ell}$ and is the first term of the final spin separating variable for the 2^+ hypothesis, in the 0-jet channel.

The subsequent step is to remove the spin sensitivity of $\Delta\psi^*_{\ell\ell}$ from the second best spin sensitive variable and parametrise its remaining uncorrelated spin sensitivity. In this case the second best variable is E^*_{sum}. Its uncorrelated spin sensitivity is

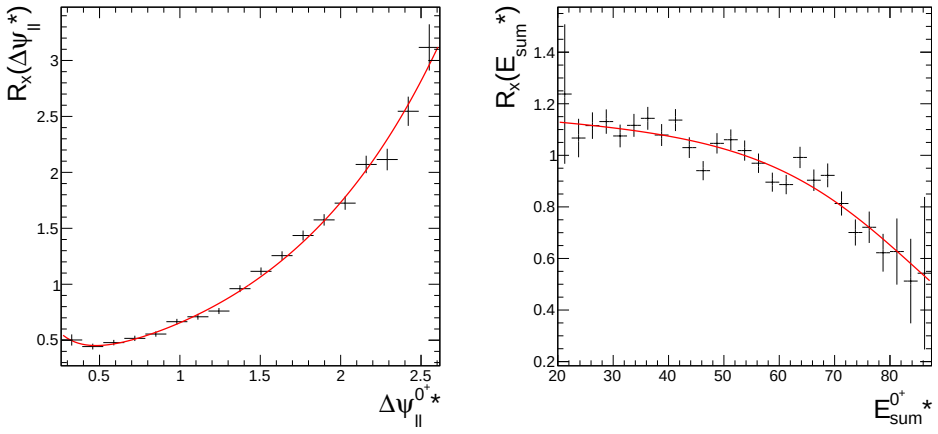

(a) (b)

Figure 7.1: *(a) Fit of the ratio distribution $R_x(\Delta\psi^*_{\ell\ell})$, which is defined in Eq. 7.1. (b) Fit of the ratio distribution $R_y(E^*_{sum})$, which is defined in Eq. 7.3.*

determined by again evaluating a ratio distribution of 2^+ and 0^+ samples, but now *after reweighting* the distribution for the 0^+ sample with $R_x(x)$:

$$R_y(E^*_{\text{sum}}) = \frac{N(E^*_{\text{sum}})^{2^+}}{N(E^*_{\text{sum}})^{0^+}_{\text{reweighted}}} \tag{7.3}$$

The reweighted distribution for the 0^+ sample is obtained by multiplying the weight of each event with the corresponding value of $R_x(x)$ in the event. In this way, the ratio distribution is flat, would E^*_{sum} have no additional uncorrelated spin sensitivity. Hence, if this step is carried out for $\Delta\psi^*_{\ell\ell}$ instead of E^*_{sum}, a flat distribution should be obtained, making it a good test to check if the spin sensitivity has been well parametrised.

The fact that E^*_{sum} has most uncorrelated spin sensitivity has been established by evaluating the reweighted ratio distribution for every possibly interesting variable. Figure 7.1b shows $R_y(E^*_{\text{sum}})$, where the distribution is parametrised with the fit function:

$$R_y(y) = \frac{p_0 \cdot e^{p_1 \cdot y}}{1 + e^{p_2 \cdot (y - p_3)}} \tag{7.4}$$

with $y = E^*_{\text{sum}}$. From the y-axis of the histogram in figure 7.1b can be read that the fit extends from 0.6 to 1.1. Figure 7.1a shows that the fit of $\Delta\psi^*_{\ell\ell}$ ranges from 0.5 to 3.0. This indicates that the additional spin sensitivity of E^*_{sum} is less than the spin sensitivity of $\Delta\psi^*_{\ell\ell}$, yet, it is certainly not negligible. If however this procedure is repeated for a third variable, no significant additional spin sensitivity is found: the reweighted ratio distributions of possible third variables are almost flat, where the reweighted ratio distributions are obtained by reweighting the 0^+ sample with $R_x(x)\cdot R_y(y)$. The fact that this reweighting may be performed with the multiplication of the two parametrisations is clarified below.

Thus, the total spin sensitivity is extracted with two parametrisations, $R_x(x)$ and $R_y(y)$. To check that factorisation of these parametrised spin sensitivities to obtain the final spin sensitive variable, does not lead to a loss of spin sensitivity, a test is performed. It is by construction that $R_x(\Delta\psi^*_{\ell\ell})$, plotted as a function of $R_x(x)$, gives a linear distribution that goes through the point (1,1), as shown in figure 7.2a. This is the case because the parametrisation is constructed in such a way that it has a value of one, when there is no separation between the 0^+ and 2^+ distributions. If factorisation is indeed a valid method to combine the two parametrisations without loss of sensitivity, then $R_x(\Delta\psi^*_{\ell\ell}) \cdot R_y(E^*_{\text{sum}})$, plotted as a function of $R_x(x) \cdot R_y(y)$, should also give a linear relation. Figure 7.2b shows that this is indeed the case.

Thus, the final spin separating variable for the 2^+ hypothesis in the 0-jet channel is given by:

$$W^{2^+}_{\text{spin}} = R_x(x) \cdot R_y(y) \tag{7.5}$$

The upper left distribution in figure 7.3 shows the final spin separating variable for the 2^+ hypothesis in the 0-jet channel, distributed for the SM Higgs signal in blue and the 2^+ signal in red. Good separation between the two hypotheses is observed.

The procedure is repeated to obtain the spin separating variables for the other hypotheses. Figure 7.3 shows the resulting combined variables distributed for the SM Higgs signal and the relevant alternative signal. All variables have been obtained by the factorisation of two parametrisations. Adding a third variable did not significantly increase the spin sensitivity for any of the hypotheses. The variables that are

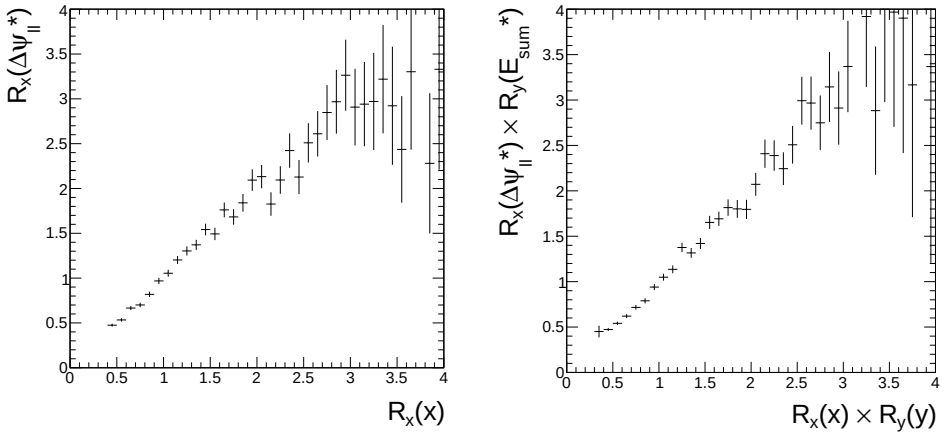

(a) (b)

Figure 7.2: *(a) $R_x(\Delta\psi^*_{\ell\ell})$, plotted as a function of $R_x(x)$, (b) $R_x(\Delta\psi^*_{\ell\ell}) \cdot R_y(E^*_{sum})$, plotted as a function of $R_x(x) \cdot R_y(y)$.*

Hypothesis	**Parametrised variables**			
	0-jet			
2^+	$\Delta\psi^*_{\ell\ell}$	E^*_{sum}		
0^-	E^*_{dif}	$M_{\ell\ell}$		
1^+	$M_{\ell\ell}$	$\Delta\psi^*_{\ell\ell}$		
1^-	$M_{\ell\ell}$	$Y_{\ell\ell}$		
bkg	M_T	$E^{\text{miss}}_{\text{T,rel}}$	$p_T^{\text{sub-lead}}$	$\Delta\psi^*_{\ell\ell}$
	1-jet			
2^+	$\Delta\psi^*_{\ell\ell}$	E^*_{sum}		
0^-	E^*_{dif}	$E_\nu^{\text{sub-lead}}$		
1^+	$\Delta\phi^*_{\ell\ell}$	$p_T^{\ell\ell}$		
1^-	$M_{\ell\ell}$	$\Delta\phi^*_{\ell\ell}$		
bkg	M_T	$M_{\ell\ell}$	$p_T^{\ell\ell}$	

Table 7.1: *The variables that are parametrised, in given order, to obtain maximal spin or background separation for the different spin hypotheses in the two jet channels.*

parametrised to obtain the spin separating variables for the different hypotheses are listed in table 7.1.

The background separating variables are obtained with the same procedure, but with the ratios defined as $\frac{N(\text{var})^{0^+}}{N(\text{var})^{\text{bkg}}}$. The 0-jet combined background separating variable

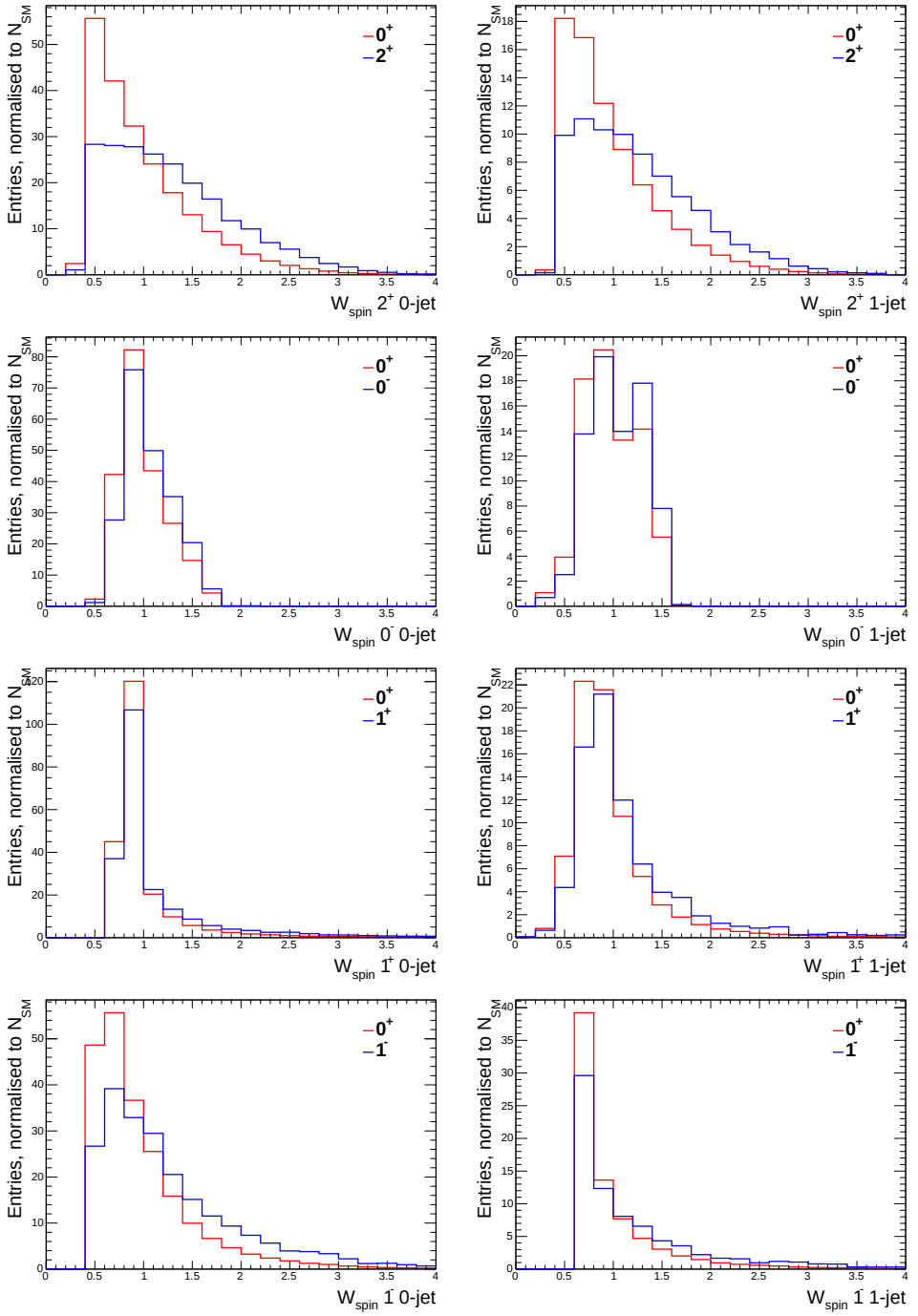

Figure 7.3: *The combined spin separating variables for the four alternative hypothesis in the 0-jet and 1-jet channel, distributed for the SM Higgs signal and the alternative hypothesis.*

is obtained with four parametrisations and the 1-jet variable with three parametrisations, as also listed in table 7.1. For both background separating variables it has been verified that a linear relation is obtained after multiplication of the three or four parametrisations.

7.2.2 Constructing the final variables

Every combined spin sensitive variables shown in figure 7.3 yields good separation between the two signal hypotheses. The effect of the irreducible background on the separation power is however not shown, since the distributions are plotted for signal only. To preserve as much of the spin sensitivity of the variables as possible, for each hypothesis, the spin separating variable is combined with the background separating variable. The highest sensitivity is obtained by combining W_{spin} and W_{bkg} in a two-dimensional histogram that can subsequently be used to construct a final variable that separates the two signal hypotheses, while also discriminating between signal and background. This final variables is obtained, following the subsequent procedure.

Firstly, the 2D histogram is used to define a cut on W_{bkg} that results in two distributions of W_{spin} with a maximal total sensitivity, where one distribution is filled for the events below the cut and one is filled for the events above the cut. This can be seen as binning W_{bkg} into two bins with a specifically chosen bin border and subsequent mapping to a 1D histogram. The optimal cut is determined on the basis of the total significance. The significance is determined from the 2D histograms filled for the SM Higgs signal, the alternative signal and the total background, where a 40×40 binning is used. The total significance is consecutively determined for each of the forty possible values of the cut (bin border), where the total significance is defined as the sum of the significances below the cut and above the cut:

$$\text{Significance} \equiv \sqrt{\left|\frac{(N_{\text{up}}^{\text{SM}})^2 - (N_{\text{up}}^{\text{alt}})^2}{N_{\text{up}}^{\text{bkg}})}\right| + \left|\frac{(N_{\text{low}}^{\text{SM}})^2 - (N_{\text{low}}^{\text{alt}})^2}{N_{\text{low}}^{\text{bkg}})}\right|} \tag{7.6}$$

In the definition of the significance both signal hypotheses are taken into account, and therefore the optimal cut has to be determined for every hypothesis separately.

Hypothesis	0-jet	1-jet
2^+	1.25	1.55
1^+	0.85	1.35
1^-	0.95	1.15
0^-	1.85	2.65

Table 7.2: *The cuts on W_{bkg} that divide the events in two optimal sets for which W_{spin} can be distributed. W_{bkg} ranges from 0 to 4.*

The obtained values are given in table 7.2 for each hypothesis, where W_{bkg} runs from 0 to 4.

The two resulting distributions for W_{spin} have a different composition. Considering that the background separating variable is constructed as a ratio of signal over background, the distribution constructed for the events below the cut is background enriched, while the distribution obtained for the events above the cut is signal enriched. Figure 7.5 shows the signal enriched distributions for the four hypotheses in the 0-jet channel, both for the SM Higgs signal and the relevant alternative hypothesis. Figure 7.6 shows the same distributions but for the 1-jet channel. The distributions show a clear signal on top of the background, and good agreement between data and MC.

The background enriched distributions of W_{spin} for the different hypotheses, both in the 0-jet and 1-jet channel, are shown in figure 7.7. Only the SM Higgs signal is included. A good agreement between data and MC is observed.

The final step is to combine the signal and background enriched distributions for each hypothesis. This is achieved by simply plotting the signal enriched distribution in a range from 0 to 2, and the background enriched distribution, from 2 to 6. Entries that fall outside these ranges are added to the last bin of the relevant distribution. A total of sixty bins is initially used. To make the final distributions suitable as input for the statistical analysis and likelihood fit, bins with a low number of background events ($N_b < 10$) are merged. In this way continuous distributions are obtained. A finer binning for the distributions has been tested but did not lead to an increased sensitivity. Furthermore, the use of more than two bins for W_{bkg} has been evaluated, by dividing the events for which W_{spin} is distributed according to more optimised cuts on W_{bkg}. However, the total significance increases with approximately 23% when going from one bin in W_{bkg} to two bins, but going from two to four bins leads

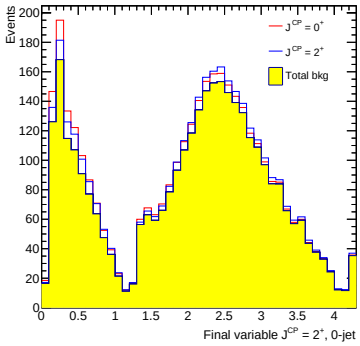

Figure 7.4: *The final spin sensitive variable for the* 2^+ *hypothesis in the 0-jet channel,* $W^{2^+}_{spin}$*, distributed in two optimised bins of* W^{0jet}_{bkg}*. The distribution is shown for the total background and the two signal hypothesis stacked on top of the background.*

only to an additional increase in significance of 4%, and going from four to eight bins only results in an additional increase of $< 1\%$, on the cost of a substantial more complicated and less stable analysis. Thus, the final spin sensitive variables are obtained by constructing W_{spin} in two optimised bins of W_{bkg} and combining the two resulting distributions by plotting one after the other. Figure 7.4 shows the final distribution for the 2^+ hypothesis in the 0-jet channel, for the total background and the two signal hypotheses stacked on top of the background. Separation between the two hypotheses on top of the background is visible.

7.3 Systematic uncertainties

There are several sources of uncertainties that influence the final measurement of the analysis, because they have an effect on the estimation of the signal, the backgrounds or both. The sources can be divided in three categories. There are theoretical uncertainties, which include the uncertainties on the QCD scale, the parton density functions (PDFs) and the MC modelling. Additionally, there are experimental uncertainties that arise from the finite precision of the object reconstruction, and detector and collider performance. Finally, there is a statistical uncertainty due to the limited MC statistics, which is treated as an experimental uncertainty in the following. A

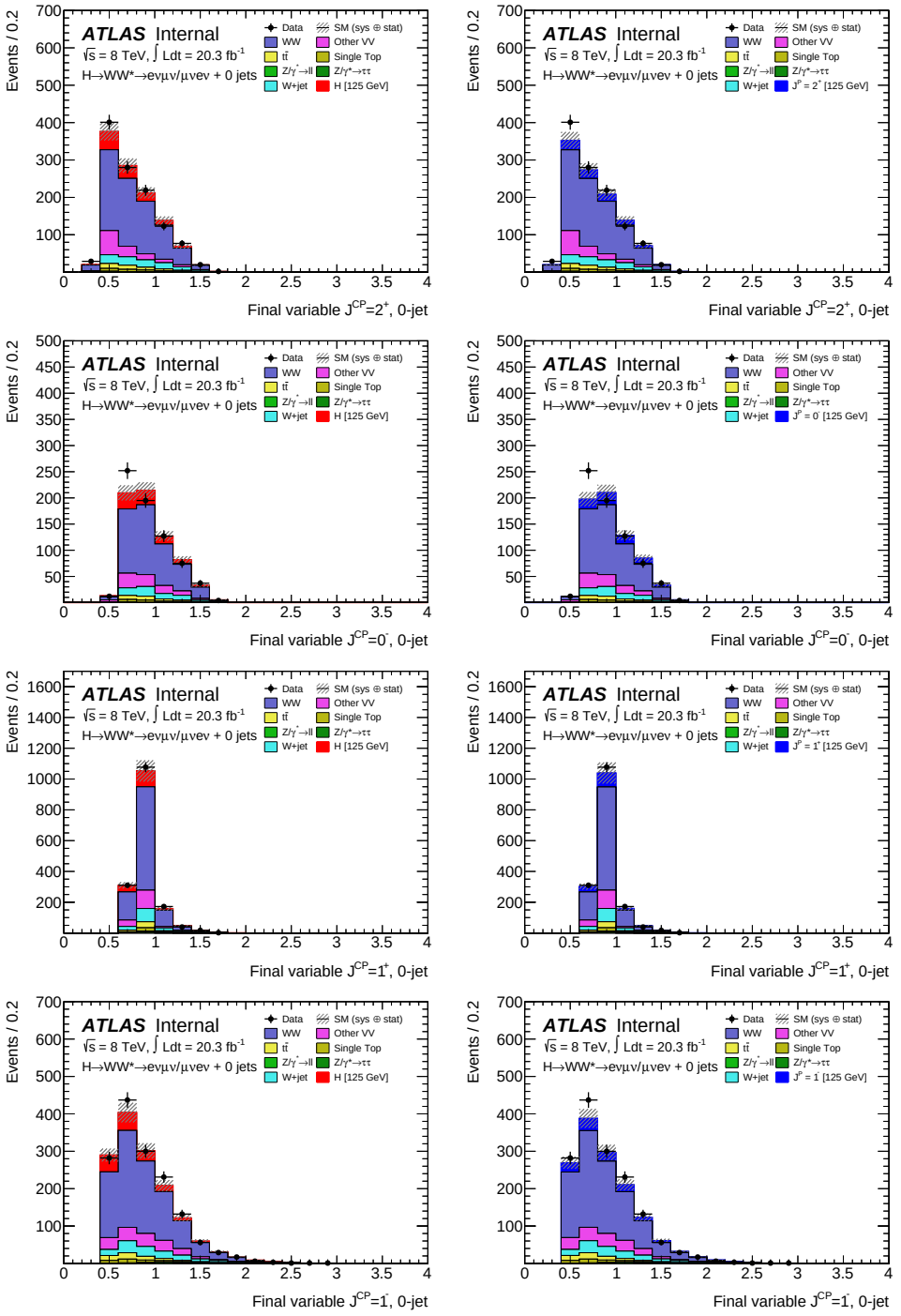

Figure 7.5: *The signal enriched distributions of the four final spin sensitive variables in the 0-jet channel, shown on the left for the SM Higgs signal, and on the right for the relevant alternative hypothesis.*

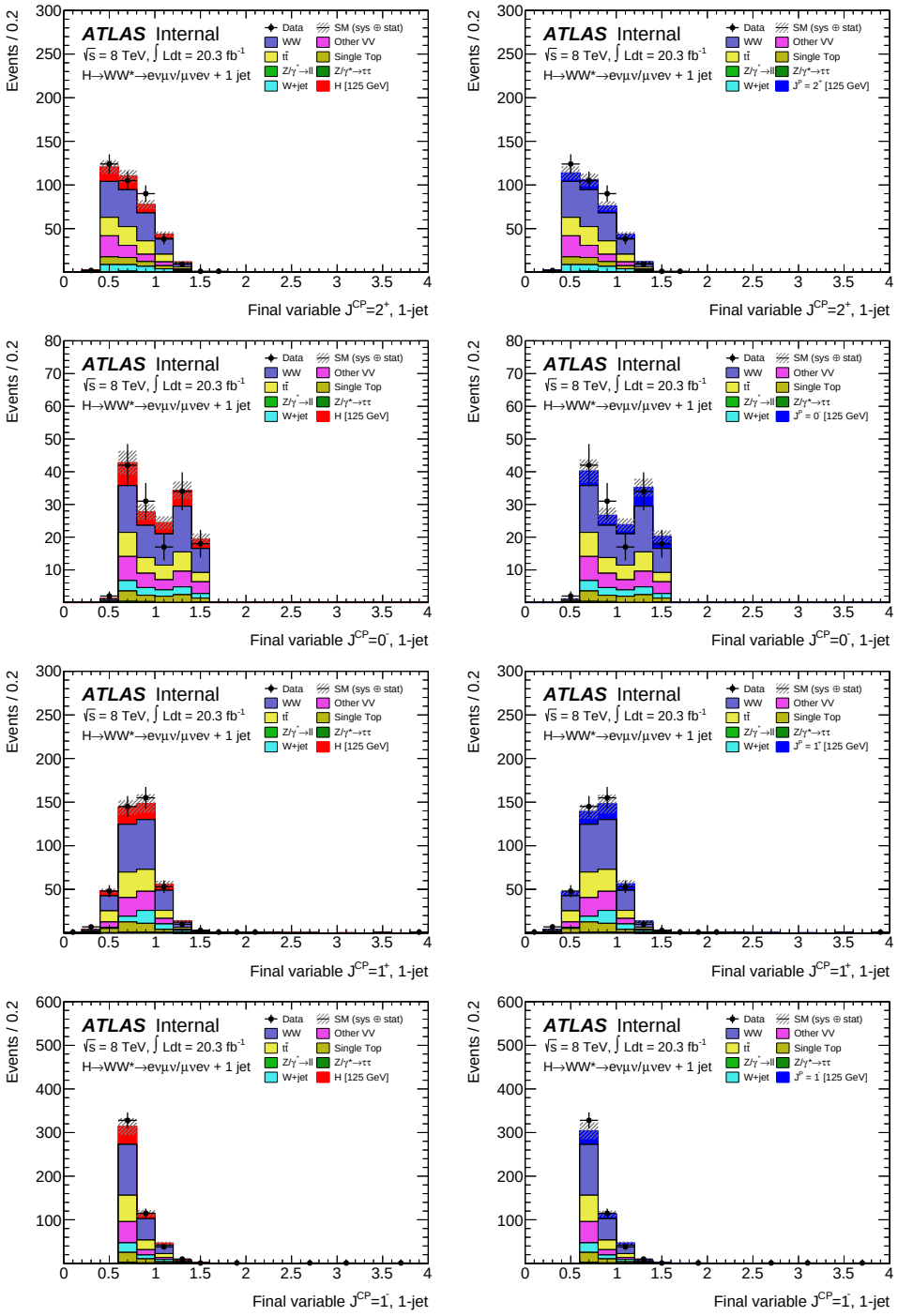

Figure 7.6: *The signal enriched distributions of the four final spin sensitive variables in the 1-jet channel, shown on the left for the SM Higgs signal, and on the right for the relevant alternative hypothesis.*

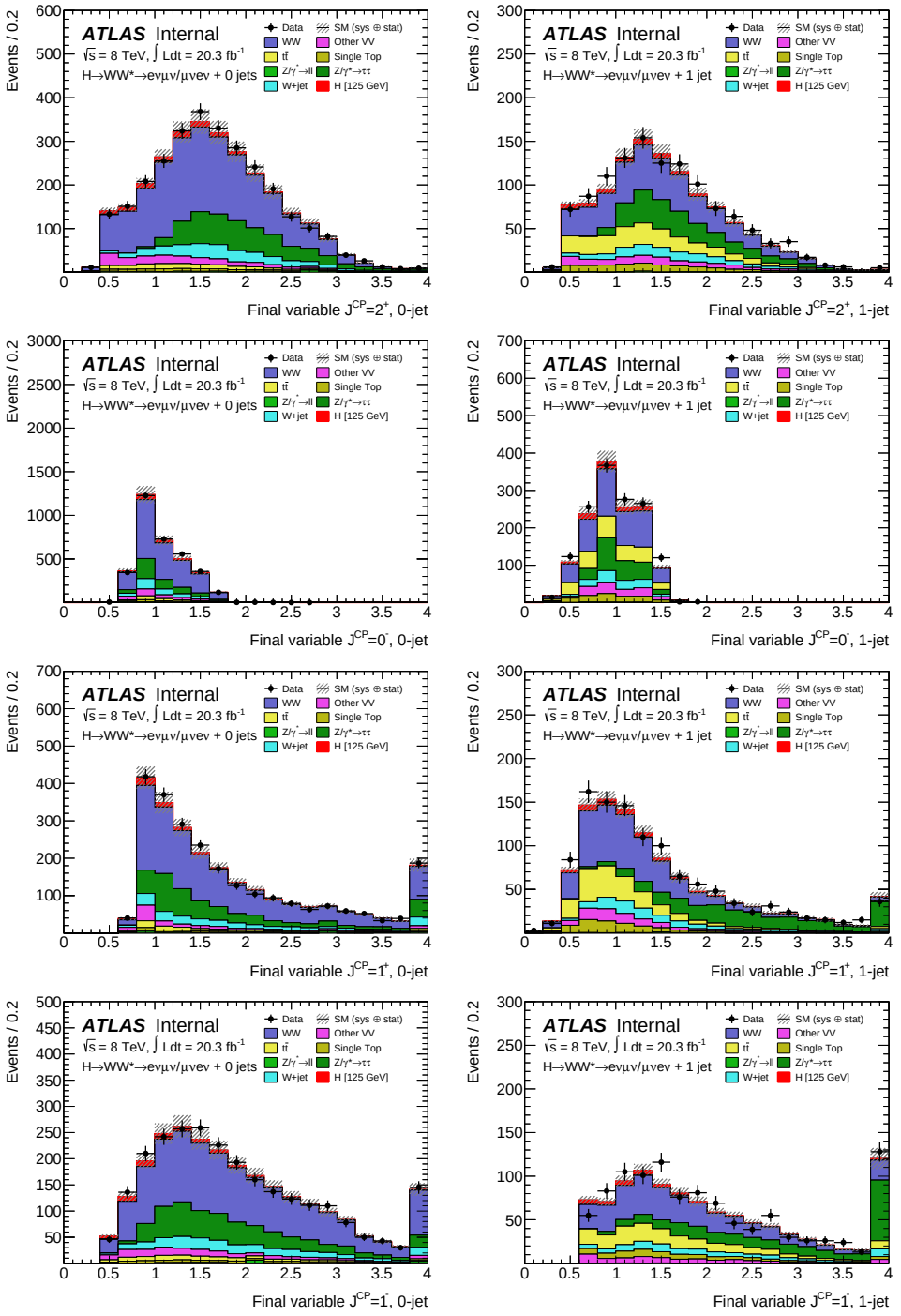

Figure 7.7: *The background enriched distributions of the eight final spin sensitive variables, with the distributions for the 0-jet channel on the left and for the 1-jet channel on the right.*

systematic uncertainty can have an effect on the normalisation and on the shape of the final spin sensitive variables.

The effect of the systematic uncertainties on the measurement are taken into account by including each non-negligible uncertainty as a nuisance parameters in the likelihood fit with which the final results are obtained, as will be explained in section 7.4. Each nuisance parameter is constraint according to its uncertainty, with a probability density function, where the exact form of this function depends on the nature of the systematic uncertainty in question, i.e. if it is a shape or a normalisation uncertainty. Furthermore, in the likelihood, the nuisance parameters are factorised, which requires that a correlation factor is included in the fit for correlated uncertainties. In this section the various sources of systematic uncertainties, possible correlations and their estimation is briefly discussed. A more detailed explanation of the systematics is given in Ref. [119].

7.3.1 Theoretical uncertainties

The uncertainty on the QCD scale affects both the normalisations and shapes of kinematical variables. Its effect is determined by varying the renormalisation and factorisation scales up and down, independently, by a factor of two around their nominal value. The resulting maximum deviations from the nominal value are taken as the $\pm 1\sigma$ uncertainties. This uncertainty is assumed to be uncorrelated among the signal and background processes, as well as among the jet channels, allowing for factorisation of these uncertainties.

The uncertainty on the used PDFs affects the cross sections of the physics processes that are considered in the analysis and consequently the normalisation and shapes of the final separating variables. These uncertainties are determined for the relevant signal and background processes, following the procedures that are described in Refs. [122, 123]. These uncertainties are taken to be correlated between processes with similar production modes, and are therefore grouped into the three possible categories: gg, gq and $q\bar{q}$.

The choice of MC generator for the modelling of the underlying event (UE) and parton showering (PS) has an effect on the shapes of the final variables. The associated

uncertainty is evaluated by comparing different MC generators. The largest variations from the average are taken as the $\pm 1\sigma$ uncertainties. This so called UEPS uncertainty is calculated for all signal and background processes, but is only significant for the SM WW background.

The theoretical uncertainties on the modelling of the ggF Higgs signal, are already accounted for when reweighting the Higgs p_T spectrum, as explained in section 6.3.3. No additional uncertainties on the cross section are taken into account, since the theoretical prediction is given at NNLL+NNLO, and considering that the spin analysis is a shape analysis, further normalisation uncertainties on the cross section may be neglected. The 0^- signal hypothesis is reweighted according to the same p_T spectrum as the SM Higgs signal and no further systematic uncertainties need to be assumed. Concerning the $1^\pm$ and 2^+ hypotheses, the theoretical uncertainties are negligible compared to the large approximations and uncertainties present in these models, and are therefore not included.

Concerning the background processes, for the backgrounds that are normalised using only MC, the theoretical uncertainties on the absolute expected yields are important, while for the backgrounds that are normalised using data, the uncertainties on the extrapolation parameters from the control to the signal regions are important. In the following the theoretical uncertainties for the SM WW background, being the dominant background in the analysis, are discussed.

The SM WW production cross section is estimated by extrapolating the number of events in a background enriched CR to the SR, as explained in section 6.5. Therefore the theoretical uncertainties on the extrapolation factors need to be considered. The relevant uncertainties on the extrapolation parameters in the 0-jet and 1-jet channel are summarised in table 7.3. The QCD scale uncertainty is determined as explained above. The UEPS uncertainty is determined by comparing the predictions from POWHEG+PYTHIA8, POWHEG+PYTHIA6 and POWHEG+HERWIG. An additional uncertainty that accounts for the dependence on the choice of MC generator for the modelling of the hard scatter is taken into account. To determine this uncertainty the extrapolation parameters have been evaluated and compared for the MCNLO, POWHEG and MCFM generators. Furthermore, an uncertainty due to the not included higher order QCD radiative corrections is considered as well. This uncertainty is evaluated by comparison of the nominal extrapolation factors to those derived after reweighting

Channel	QCD scale	UEPS	MC modelling	EW corr	PDFs	Total
SR 0-jet	0.9	-4.1	6.9	-0.8	3.8	8.2
SR 1-jet	1.8	-4.4	1.8	-2.3	1.5	5.7

Table 7.3: *Theoretical uncertainties on the extrapolation parameters from the WW CRs to the SRs of the 0-jet and 1-jet channel, given in %. The sign of the uncertainties indicates if it results in an increase or decrease of the WW signal yield [9].*

to account for kinematic effects of higher order electroweak corrections. Finally, the PDF uncertainty is evaluated by comparing the CT10 PDF error set with the ones of MSTW2008 and NNPDF2.3 [124]. The total uncertainties on the 0-jet and 1-jet extrapolation parameters are 8.2% and 5.7% respectively. The effect of the QCD scale and PDF uncertainties on the shapes of the final separating variables are negligible and therefore included in the likelihood fit as overall normalisations. The UEPS and generator uncertainties were found to have an effect on the shapes and are therefore included in the fit as bin-by-bin uncertainties.

7.3.2 Experimental uncertainties

Experimental uncertainties that need to be considered include the uncertainties on the reconstruction, identification and trigger efficiencies, as well as on the momentum or energy scales and resolutions of the physics objects used in the analysis. Additionally, the uncertainty on the luminosity is included as an experimental uncertainty. The jet energy scale (JES) and resolution (JER), and the b-tagging efficiency are the dominant sources of experimental uncertainties. The experimental uncertainties that are taken into account in the analysis are listed in table 7.4.

In the likelihood fit, the experimental uncertainties are taken as correlated between the signal and background processes. The uncertainty on each experimental source is estimated by varying it with $\pm 1\sigma$ around its nominal value and calculating the effect on the expected rates. Shape uncertainties are taken into account if they are larger than 5%, which is larger than the statistical uncertainty. Normalisation uncertainties are considered if the are larger than 0.1%.

Source of uncertainty	Treatment in the analysis and magnitude
Jet Energy Scale (JES)	1 – 7% in total as a function of jet η and p_T
Jet Energy Resolution (JER)	5 – 20% as a function of jet η and p_T Relative uncertainty on the resolution is 2 – 40%
b-tagging	b-jet identification: 1 – 8% decomposed in p_T bins Light-quark jet misidentification: 9 – 19% as a function of η and p_T c-quark jet misidentification: 6 – 14% as a function of p_T
Leptons	Reconstruction, identification, isolation, trigger efficiency: below 1% except for electron identification: 0.2 – 2.7% depending on η and p_T Momentum scale and resolution: $< 1\%$
Missing Transverse Momentum	Propagated jet-energy and lepton-momentum scale uncertainties Resolution (1.5 – 3.3 GeV) and scale variation (0.3 – 1.4 GeV)
Pile-up	The amount of pile-up events is varied by 10%
Luminosity	2.8% [125]

Table 7.4: *Sources of experimental uncertainties considered in the analysis. The magnitude of the source and treatment in the analysis are indicated [9].*

7.4 Statistical analysis

To allow for a quantitative statement about the spin and parity of the observed signal a statistical analysis is performed. The statistical analysis is performed on the basis of the event yields that are obtained with the previously described part of the analysis, and the final separating variables that are discussed in section 7.2.2 serve as input. The statistical analysis is explained on the basis of a simple example that is extended to match with the method used in the spin and CP analysis to obtain the final sensitivities.

Likelihood functions form the basis of any statistical analysis [126]. The simplest example yields a single bin counting experiment, with expected signal rate S, expected background rate B and observed events N. A single parameter of interest, which is the parameter one wishes to make a statement about, μ, normalises S such that $\mu = 1$ corresponds the nominal signal hypothesis, while $\mu = 0$ corresponds to the background-only hypothesis. Given that S, B and N are simple constants, the

likelihood is a function of μ only, and can be identified with a Poisson probability of the observed and expected events:

$$\mathcal{L}(\mu) = P(N|\mu S + B) = \frac{e^{-\lambda}\lambda^N}{N!} \tag{7.7}$$

with $\lambda = \mu S + B$ the number of expected events. This function can be interpreted as the probability of observing N event, given λ expected events. To provide insight in the treatment of systematical uncertainties, the example can be extended by assuming that B is normalised with normalisation factor θ, using a control region (CR), which has observed events N_{CR} and expected background B_{CR}:

$$\mathcal{L}(\mu, \theta) = P(N|\mu S + \theta B)\, P(N_{CR}|\theta B_{CR}) \tag{7.8}$$

In this specific example θ is a normalisation factor, however, in general θ denotes the nuisance parameter of the specific systematic uncertainty. The second Poisson probability in Eq. 7.8 is the auxiliary constraint that constraints θ, and N_{CR} is the auxiliary measurement, also referred to as central value, which is denoted as $\tilde{\theta}$ in the following.

The spin and parity analysis has many systematic uncertainties, as addressed in the previous section. All non negligible systematics are included in the likelihood by introducing a nuisance parameter θ. Each nuisance parameter is constraint with a probability density function, where the exact form of this function depends on the systematic uncertainty in question. As can be seen from Eq 7.8, the background expectation is a function of the nuisance parameter. Generalising this to the likelihood used in the analysis, both the signal and background expectations are functions of the relevant nuisance parameters. These functions are parametrised such that the response of S and B to each θ is factorised from the nominal value of the expected rates. More information about the technical treatment of systematics in the likelihood is given in Ref. [126].

The likelihood function given in Eq. 7.8 can be used to distinguish the hypothesis to have a Higgs signal in the data from the alternate hypothesis of having no signal and thus only background. In the case of the spin and CP analysis, however, there are two

signal hypotheses, the SM Higgs hypothesis and the alternative signal hypothesis. To take this into account, the number of expected events is defined as:

$$\lambda = \mu\epsilon S_{\mathrm{SM}} + \mu(1-\epsilon)S_{\mathrm{alt}} + B \tag{7.9}$$

where S_{SM} is the number of expected SM Higgs boson events and S_{alt} the number of expected events from the alternative hypothesis. In this case the parameter of interest is ϵ, which is the fraction of SM Higgs events with respect to the expected signal yield and can only assume discrete values: $\epsilon = 0$ for the alternative hypothesis and $\epsilon = 1$ for the SM hypothesis. The signal normalisation, μ, is not treated as a parameter of interest, but as a free nuisance parameter, because the cross section of the alternative signal hypotheses are unknown. The likelihood used in the spin and parity analysis can then be written as:

$$\mathcal{L}(\epsilon,\mu,\theta) = \prod_{i}^{N_{\mathrm{bins}}} P(N_i|(\mu(\epsilon S_{\mathrm{SM},i}(\theta) + (1-\epsilon)S_{\mathrm{alt},i}(\theta)) + B_i(\theta))) \times \prod_{j}^{N_{\mathrm{sys}}} A(\tilde{\theta_j}|\theta_j) \tag{7.10}$$

where the last term represents the factorisation over the auxiliary measurements for the nuisance parameters. The first term is factorised over the number of bins of the relevant final variable as will be explained below.

The next step is to determine the likelihood both for the SM hypothesis ($\epsilon = 1$) and the alternative hypothesis ($\epsilon = 0$), such that these likelihoods can be used to determine the level of agreement of data with the two hypotheses. The likelihoods are determined on the basis of two binned template histograms. These template histograms represent the final separating variables. One template histogram is filled for the alternative signal hypothesis plus background rate and another for the SM signal hypothesis plus background. Subsequently, the likelihood is determined, separately for the two hypotheses, by fitting the nuisance parameters and signal normalisation. This is done bin by bin for the relevant template histogram, by calculating the Poisson probability, and setting the nuisance parameters and signal normalisation to the values that maximise the likelihood. In this way the binned likelihoods for the SM and alternative hypothesis are obtained.

To put the obtained likelihoods in perspective, the values obtained for $\epsilon = 1$ and $\epsilon = 0$ are compared using a so called test statistic. A test statistic, q, distinguishes between two hypotheses, given the same set of data. The test statistic used in this analysis is defined as:

$$q = \ln \frac{\mathcal{L}(\epsilon = 1, \hat{\mu}_{\epsilon=1}, \hat{\theta}_{j,\epsilon=1})}{\mathcal{L}(\epsilon = 0, \hat{\mu}_{\epsilon=0}, \hat{\theta}_{j,\epsilon=0})} \tag{7.11}$$

where $\hat{\mu}$ and $\hat{\theta}_j$ are the maximum likelihood estimators obtained by maximising the two likelihoods independently from one another.

The test statistic for the data sample, q_{obs}, can be obtained by simply calculating its value. Concerning the test statistics for the signal hypotheses, the expected values need to be extracted from MC samples of the backgrounds plus relevant signal. Also, to interpret the compatibility of q_{obs} with the two hypotheses, MC distributions of the test statistic are needed. To obtain sufficient statistics, a toy Monte Carlo generator is used to generate 5000 toy experiments per hypothesis. In this way probability density distributions of the test statistic for each of the signal plus background hypotheses are obtained.

Figure 7.8a shows two example probability density distributions of the test statistic, one for the SM hypothesis (red) and one for the alternative hypothesis (blue). Also the observed value, q_{obs}, for the test statistic is indicated. To quantify the consistency of the two hypotheses with the data, a probability, called the p-value, can be calculated. The p-value, p, is a frequentist statement about the probability of q under repeated measurements assuming that only one of the hypotheses is true. There are two interesting p-values. The first one concerns the SM hypothesis and yields the probability to obtain a value for q smaller than q_{obs}, under the assumption that the SM hypothesis is true. This value is obtained from integrating the probability density distribution of the test statistics, $f(q|\epsilon = 1)$, downwards: $p_{\text{SM}} = \int_{-\infty}^{q^{\text{obs}}} f(q|\epsilon = 1)\, dq$, as is indicated as the red area in the figure. The other interesting p-value concerns the alternative assumption, p_{alt}, and yields the probability to obtain a value for q larger than q_{obs}, under the assumption that the alternative hypothesis is true. It is obtained from integrating the distribution, $f(q|\epsilon = 0)$, upwards: $p_{\text{alt}} = \int_{q_{\text{obs}}}^{\infty} f(q|\epsilon = 0)\, dq$, and is indicated as the blue area in the figure. The expected p-values are obtained by

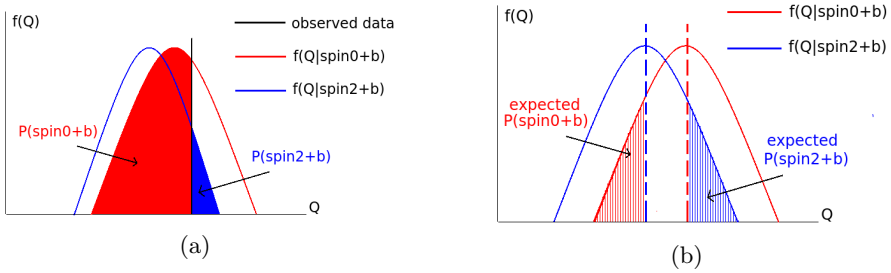

Figure 7.8: *Example probability density distributions of the test statistics. (a) indicates the determination of the observed p-values for the two hypothesis and (b) indicates the determination of the expected p-values. The red areas indicate the expected and observed p-values for the SM hypotheses, and the blue areas for the alternative hypothesis [9].*

integrating from the relevant expected median values, instead of q_{obs}. The expected p-value for the SM hypothesis is obtained by integrating the SM distribution downwards from the median of the distribution of the alternative hypothesis, and vice versa for the expected p-value of the alternative hypothesis, as is shown in figure 7.8b.

To avoid the exclusion of one of the hypotheses, while the analysis has actually no sensitivity for this, which could happen for example when the two probability density distributions of the test statistic are very similar, a quantity called the confidence level is used in addition to the p-value. The confidence level for excluding the alternative signal hypothesis in favour of the SM hypothesis is quantified as:

$$\text{CL}_\text{s} = \frac{p^{\text{alt}}_{\text{obs}}}{1 - p^{\text{SM}}_{\text{obs}}} \tag{7.12}$$

Since the CL_s indicates the probability of rejecting the alternative hypotheses, while it is actually the true hypothesis, the quantity $1 - \text{CL}_\text{s}$ gives the probability of correctly rejecting the alternative hypothesis. Both the p-values and the CL_s will be used in the next section to evaluate the compatibility of the data with the different spin and parity hypotheses.

7.5 Results

The results of the analysis of the spin and parity of the observed Higgs signal are presented in this section. The considered alternative hypotheses for the signal are $J^{CP} = 0^-$, 1^+, 1^- and 2^+, where the 2^+ hypothesis is evaluated according to the five different models that have been described in section 1.4.3. To obtain the results, the statistical procedure that is explained in the previous section is applied for every hypothesis, using the corresponding separating final variable. The data and MC samples that are used to obtain the final results are prepared according to the selections and background estimations discussed in sections 6.4 and 6.5. Since the reliability of the final results depends on the fit to the data that determines the binned likelihood, first the fit results will be evaluated. Subsequently, the distributions for the test statistic, the sensitivities and confidence levels are discussed.

7.5.1 The likelihood fit

The fit of the likelihood is performed to constrain all nuisance parameters and obtain the likelihood values for the SM hypothesis and the alternative hypothesis. Figure 7.9a shows the final variable of the 2^+ hypothesis after the fit, assuming the SM hypothesis ($\epsilon = 1$), distributed for the SM Higgs signal in blue and for the data as black dots. Figure 7.9b shows the residuals of the fit, which is the difference between the expected number of events from the template and the observed numbers in data. Finally, figure 7.9c shows the pulls, which are defined as the residuals divided by the corresponding uncertainties on the observed number of events. The figures indicate that the fit has been successful, no obvious structure or significant divergences are visible in the distributions. Figures 7.9d, 7.9e and 7.9f show the same distributions, but for the 0^- hypothesis, again assuming $\epsilon = 1$ and with the blue curve showing the distribution of the final variable after the fit, for the SM Higgs signal sample. Also the distributions for the fit assuming $\epsilon = 0$, for the 1-jet channel, and for the other hypotheses indicate no problems in the fits.

To evaluate how the nuisance parameters are treated in the fit, the pulls of the nuisance parameters are determined, where the pull is defined as the difference between

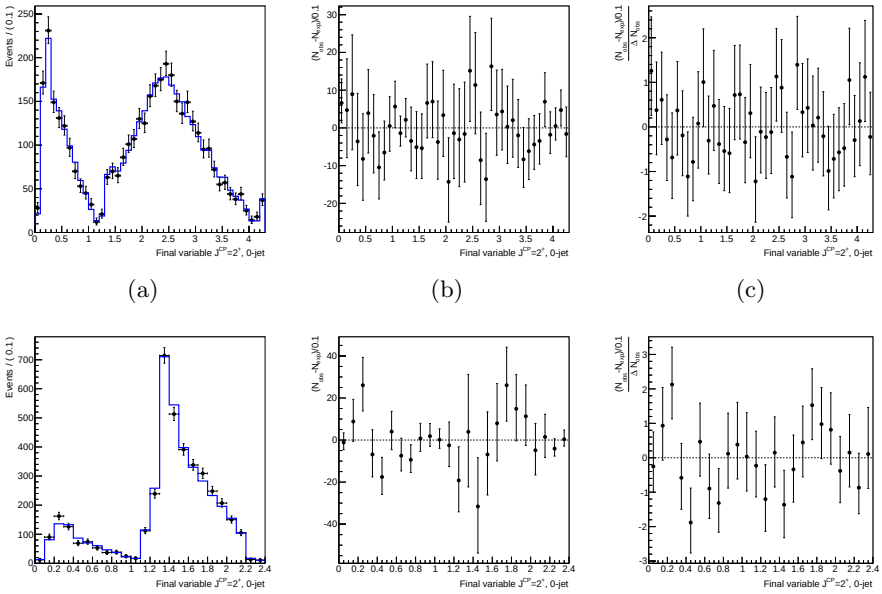

Figure 7.9: *Evaluation of the binned likelihood in the 0-jet channel for the final variable constructed for the 2^+ universal couplings model (a,b,c) and the 0^- model (d,e,f). The results are shown for the SM hypothesis ($\epsilon = 1$). The black dots are data points. (a,d) show the final variable after the fit for data and for the SM Higgs signal sample (blue curve), (b,e) the residuals of the fit and (c,f) the pulls of the fit.*

the central value of the nuisance parameter and the fitted value, divided by the expected error on the central value. Additionally the expected error on the central values of the nuisance parameters are compared to the corresponding errors that result from the fit, where the errors are normalised such that the expected errors correspond to 1σ. A fitted error that is significantly smaller than the expected error, may indicate that correlations between systematics are not correctly treated in the fit, resulting in an overconstraint of the associated nuisance parameters. Figure 7.10 shows the pulls and errors for all nuisance parameters for the fit of the 2^+ universal couplings model, with the two jet channels combined. The scale is given at the lower x-axis. No significant pulls or overconstraints are observed, indicating that all nuisance parameters are correctly treated in the fit.

To study the impact of the nuisance parameters on the spin sensitivity of the analysis,

the fit has also been performed leaving ϵ as a free parameter that can take values between -5 and +5, instead of constraining it to the SM or alternative hypothesis (ϵ = 1 or 0). Then the impact can be defined as the change of ϵ, which is indicated on the upper x-axis in figure 7.10, where in this case the fitted value of ϵ is 0.999. The nuisance parameters are ranked according to their impact, and both the pre-fit and post-fit impact are indicated. It can be seen that the systematic uncertainty on the WW modelling influences the sensitivity most, being in the order of $\Delta\hat{\epsilon} \simeq 0.25$, followed by the UEPS uncertainty on the WW background that is in the order of $\Delta\hat{\epsilon} \simeq 0.20$. The statistical error on ϵ is 0.76. Adding the systematic uncertainties in quadrature and comparing this to the statistical error shows that the measurement for the 2^+ hypothesis is statistics dominated.

Figure 7.11 shows again the pulls and impact of the nuisance parameters but now for the 0^- hypothesis. Also for this hypothesis the nuisance parameters are well constraint in the fit. The impact and ranking of the nuisance parameters is slightly different with respect to the 2^+ hypothesis. The WW modelling has still the largest impact and is in the order of $\Delta\hat{\epsilon} \simeq 0.20$. The impact of the other uncertainties falls off more steeply than is the case for the 2^+ hypothesis. This may be caused by the fact that the systematic uncertainties are mostly uncertainties on the backgrounds, and the 0^- hypothesis is more signal-like than the 2^+ hypothesis. As such the uncertainties have less impact on the 0^- hypothesis. The statistical error on ϵ is in this case 0.75. Thus, the measurement for the 0^- hypothesis is also statistics dominated. The pulls have also been evaluated for the other alternative hypotheses and no significant pulls or overconstraints have been observed. The impact and ranking of the nuisance parameters differs only slightly between the different hypotheses, and all measurements are statistics dominated.

Thus, the evaluation of the fits shows that backgrounds, signal and uncertainties are considered in a proper way in the statistical analysis and that the resulting sensitivities for the spin and parity of the observed signal are reliable.

7.5.2 Overview of the results

Figure 7.12 shows the probability density distributions of the test statistic for the different hypotheses, combined for the 0-jet and 1-jet channels, with the distribution

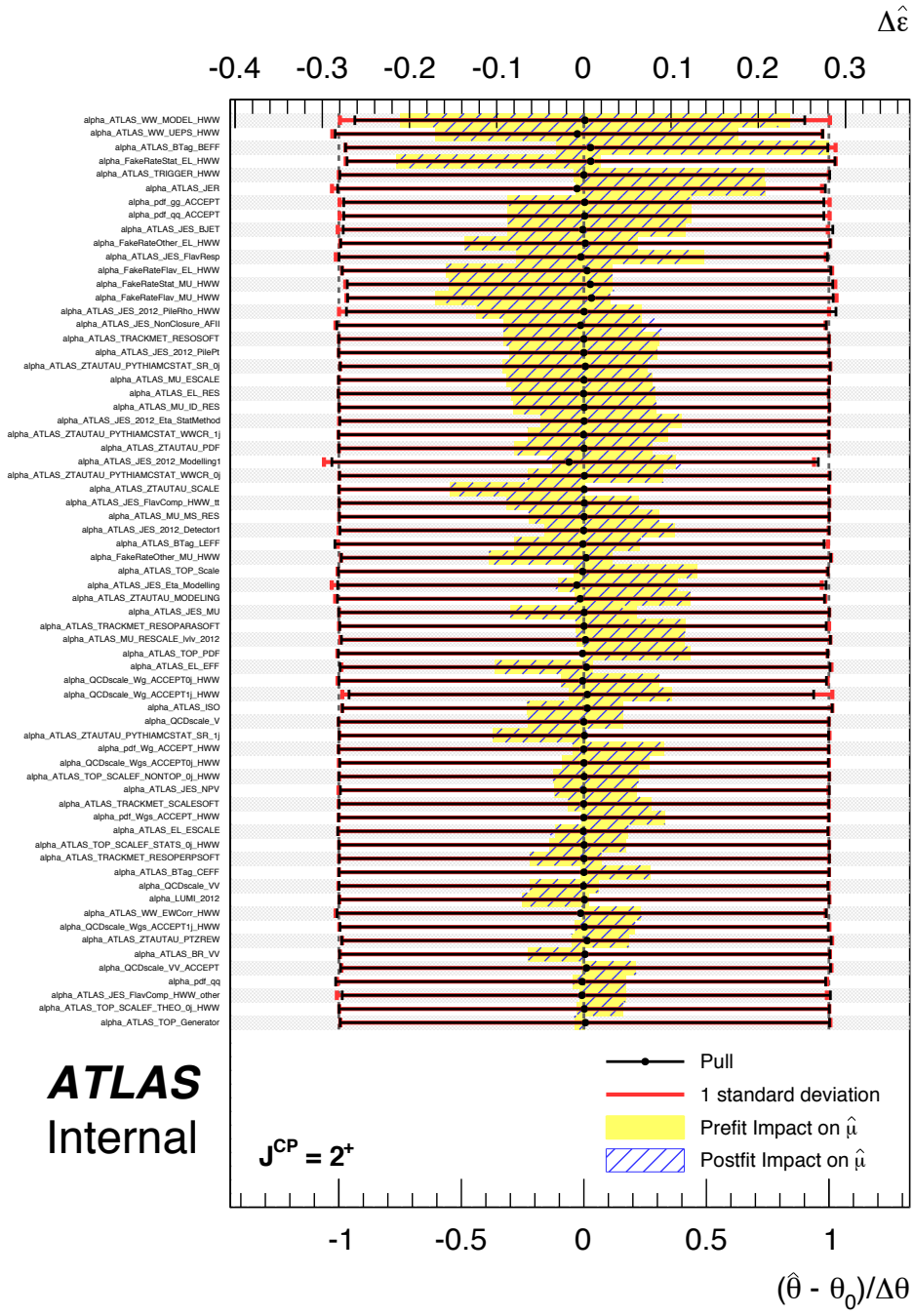

Figure 7.10: *The pulls and associated errors of the nuisance parameters (scale on the lower x-axis) and their relative impact on the spin sensitivity (scale on the upper x-axis), shown for the spin-2 universal couplings model, combined for the 0-jet and 1-jet channel. The nuisance parameters are ordered according to decreasing impact on the spin sensitivity.*

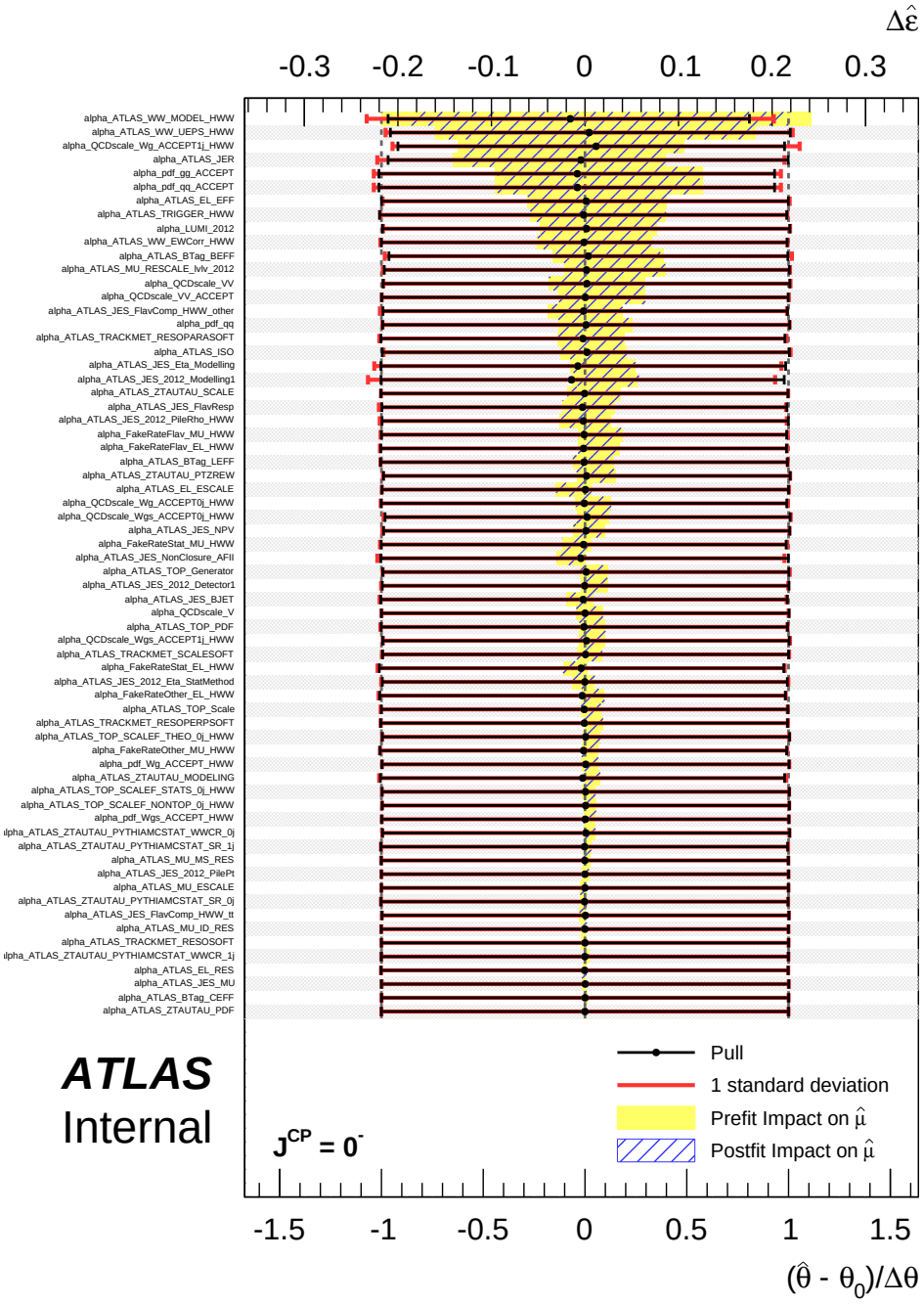

Figure 7.11: *The pulls and associated errors of the nuisance parameters (scale on the lower x-axis) and their relative impact on the spin sensitivity (scale on the upper x-axis), shown for the 0^- hypothesis, combined for the 0-jet and 1-jet channel. The nuisance parameters are ordered according to decreasing impact on the spin sensitivity.*

Hypothesis	$p_{\text{exp}}^{\text{SM}}$	$p_{\text{exp}}^{\text{alt}}$	$p_{\text{obs}}^{\text{SM}}$	$p_{\text{obs}}^{\text{alt}}$	$1 - \text{CL}_\text{s}$
0^-	0.852	0.115	0.178	0.015	98.2%
2^+, $\kappa_g = 1$, $\kappa_q = 1$	0.804	0.091	0.176	0.012	98.5%
2^+, $\kappa_g = 0.5$, $\kappa_q = 1$, $p_T^H < 125$ GeV	0.766	0.073	0.239	0.009	98.8%
2^+, $\kappa_g = 0.5$, $\kappa_q = 1$, $p_T^H < 300$ GeV	0.762	0.078	0.315	0.021	96.9%
2^+, $\kappa_g = 1$, $\kappa_q = 0$, $p_T^H < 125$ GeV	0.775	0.080	0.278	0.022	97.0%
2^+, $\kappa_g = 1$, $\kappa_q = 0$, $p_T^H < 300$ GeV	0.769	0.075	0.332	0.023	96.6%
1^+	0.746	0.170	0.168	0.018	97.8%
1^-	0.812	0.068	0.436	0.044	92.2%

Table 7.5: *The expected and observed p-values and the observed $1 - CL_s$ for the alternative hypotheses compared to the SM Higgs boson hypothesis. The results are combined for the 0-jet and 1-jet channel.*

for the SM hypothesis in red and the distribution for the alternative hypothesis in blue. The observed value for the test statistic is shown as a black line. By eye it can already be seen that the observed value for the test statistic is more compatible with the SM Higgs signal than with any of the other alternative hypotheses. The separation between the two probability density distributions and hence the expected sensitivity of the analysis, differs for the different hypotheses. This is primarily due to the fact that the final state signatures of some hypotheses are more alike the SM Higgs signal than others. From the distributions the expected and observed p-values and confidence levels are determined, which are listed in table 7.5. Since the value of the test statistic depends on the probability distributions of both the SM and the alternative hypothesis, the sensitivities for the SM Higgs hypothesis are different for the different alternative hypotheses.

The expected sensitivities to exclude the alternative hypotheses, range from 1.0σ for the 1^+ hypothesis to 1.5σ for the 1^- hypothesis, and indicate that the analysis exhibits sufficient sensitivity to make a statement about the compatibility of the data with the alternative hypotheses. The sensitivity is driven by the 0-jet channel, since the 1-jet channels adds roughly 10% to the sensitivity.

The SM hypothesis is favoured in all tests. The alternative models for the 2^+ hypothesis are excluded with confidence levels ranging from 96.6% to 98.8%. The 1^+ and 1^- hypotheses are excluded with 97.8% and 92.2% confidence levels respectively, and

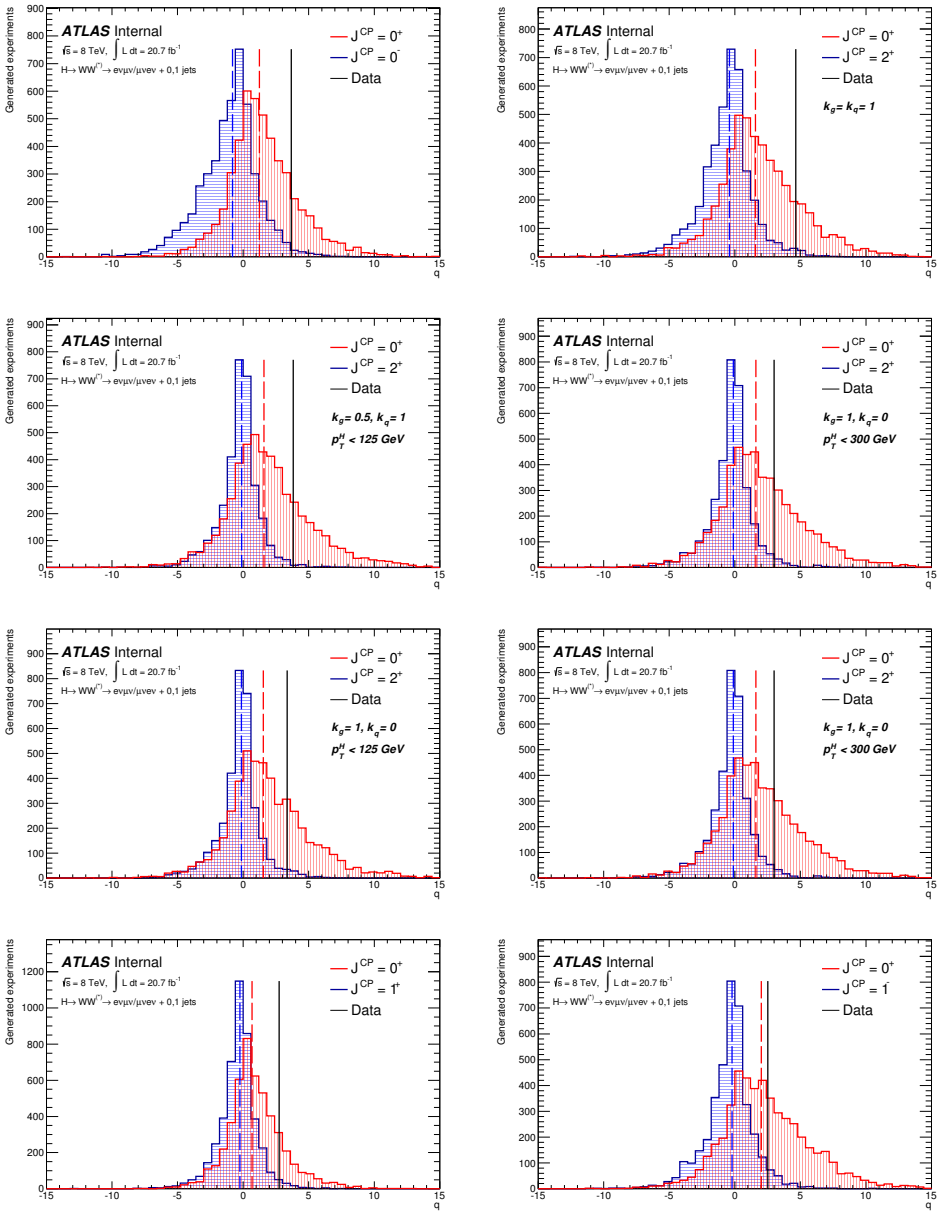

Figure 7.12: *The probability density distributions of the test statistic for the different hypotheses, combined for the 0-jet and 1-jet channel. The SM Higgs hypothesis is shown in red and the alternative hypotheses in blue. The observed value for the test statistic is shown as a black line.*

the 0^- hypothesis is excluded with a confidence level of 98.2%. The results are compatible with the results obtained with the official ATLAS analysis that is described in Ref. [9]. In the next section, the conclusions that can be drawn from these results will be given.

Conclusions and outlook

In this thesis a measurement of the spin and parity of the discovered Higgs-like boson in the $H \to W^+W^- \to \ell^+\nu\ell^-\bar{\nu} + 0,1$ jets decay mode has been presented. For the measurement 20.3 fb^{-1} of pp collision data, accumulated by the ATLAS experiment at the LHC at $\sqrt{s} = 8$ TeV have been used. The goal of the measurement was to make a statement about the compatibility of the observed signal with the Standard Model hypothesis of a spin-0 Higgs boson with even parity: $J^{CP} = 0^+$. To allow for the measurement, four alternative hypotheses for the observed signal were formulated, in terms of different spin and parity combinations: $J^{CP} = 0^-$, 2^+, 1^+ and 1^-, where the 2^+ hypothesis has been tested according to five different models. For each hypothesis, its compatibility with the data is compared to the SM hypothesis. An analytical method has been used to achieve maximal spin and parity sensitivity for the different hypotheses. The choice for a fully analytical method was made to allow for step by step evaluation and insight in the measurement. To add sensitivity to the analysis, a method has been developed to reconstruct the rest frame of the Higgs boson, in which spin sensitive kinematical variables can be reconstructed. The analysis has been performed in parallel to the official ATLAS multivariate analysis.

At the time of the discovery of the Higgs-like boson in 2012 it did not seem feasible to measure the spin and parity in the $H \to WW^*$ decay channel. To measure subtle shape differences, while the final state cannot be completely reconstructed. This analysis proves the opposite: it is possible to use small differences in the shapes of kinematical variables to make a statement about the properties of the Higgs-like boson in the WW decay channel.

The expected sensitivities to exclude the alternative hypotheses in favour of the SM Higgs boson allow to set an exclusion limit on the alternative hypotheses. The data favour the SM hypothesis for the spin and parity in all cases. The spin-2 hypothesis is excluded with confidence levels ranging from 96.6% to 98.8%, depending on the model. The CP-even and CP-odd spin-1 hypotheses are excluded at 97.8% CL and 92.2% CL respectively. The CP-odd spin-0 hypothesis is excluded at 98.2% CL.

The observed exclusions are compatible with the results obtained with the ATLAS multivariate analysis [9, 127]. The expected exclusions of the multivariate analysis are slightly better, because the boosted decision tree method that has been used, is capable of extracting spin sensitivity from more variables. Additionally, more rounds of optimisations have already been performed for this analysis. The spin and parity measurement has also been performed for other decay channels. Both the official ATLAS $H \to ZZ^*$ [127, 128] and $H \to \gamma\gamma$ [127] analyses exclude the alternative hypotheses in favour of the SM Higgs boson. The CMS collaboration has also carried out the spin and parity measurements for the various channels and draws the same conclusion: the data favour the SM Higgs boson [129–132].

The developed Higgs rest frame reconstruction algorithm that has been presented in this thesis has proven to be a valuable tool. The resulting rest frame variables have a good resolution, and information in the z-component of the event can be used, while this is not possible with standard lab frame variables. In the analysis presented in this thesis, the use of rest frame variables resulted in an improved spin sensitivity.

The results presented in this thesis are not conclusive yet. In order to set a firmer limit on the exclusion of the alternative hypotheses the expected sensitivities should be higher than 99.5%. There are various ways to improve the sensitivity. First of all, analysis of more data will result in an increased sensitivity, since the measurement is still statistically limited. In May 2015 the LHC will start delivering new data at $\sqrt{s} = 13$ TeV, allowing to update the analysis with more statistics. Furthermore, a firmer statement can be made, when the results are combined for different decay channels. There are also improvements for the analysis method itself that may result in a higher sensitivity. The rest frame variables suffer from the limited resolution of the E_T^{miss} variable, because this variable is used in the reconstruction of the Higgs rest frame. A better resolution of the E_T^{miss} will automatically increase the resolution of the rest frame variables and therefore the sensitivity of the analysis. Another improvement

would be to introduce a more precise parametrisation of the spin sensitivity. Now the fits with which the spin sensitivity of the variables is parametrised are quite coarse, allowing only to extract spin sensitivity from a total of two sensitive variables. A more precise parametrisation of the spin sensitivity could allow for the extraction of sensitivity from more variables, leading to an increase of the total sensitivity.

The analysis presented in this thesis resulted in a first measurement of the spin and parity of the observed Higgs-like boson. The next generation of analyses will include more complex models in addition to the four discrete models tested in this analysis. It is possible to formulate effective field theories in which the couplings can be varied in a continuous scan, allowing to test the compatibility of the observed signal with a whole range of models. One important test will be that of the CP mixing of the Higgs boson in an extended Higgs sector of the Standard Model. Ultimately, all the properties of the observed signal should be measured, both in decays into bosons and into fermions, to conclude if the observed signal is of the Standard Model Higgs boson or if the discovered particle reveals new physics. The analysis presented in this thesis is a first step in the characterisation of the new Higgs-like boson.

Summary

Have you ever wondered why the things around you have mass? If so, you are not the only one. For many years many physicists have pondered on this exact question. Finding the smallest building blocks of the universe is one thing; to understand how these building blocks acquire a mass, and experimentally proof this, is something else.

The elementary, indivisible, particles that form matter are gathered in the Standard Model of Particle Physics, which is shown in figure 7.20. It is a mathematical model that describes the elementary particles and their interactions. In the past century, the existence of each of these particles has experimentally been proven. But there is one more particle predicted by the Standard Model: the Higgs boson. Experimental proof for this particle would result in a fully experimentally verified Standard Model, however, it turns out to be very hard to detect.

Initially, the Standard Model describes the elementary particles as massless particles. From experiments and everyday life we know however that the particles do have a mass. This discrepancy can be explained with the Higgs mechanism that has been developed in 1964 by Peter Higgs and other physicists. The Higgs mechanism predicts that elementary particles acquire a mass through interaction with an omnipresent Higgs field. The Higgs field cannot be observed alike e.g. the gravitational force, but can be imagined as a sticky substance that fills the universe, and the more a particle sticks to this substance the heavier it is, while particles that do not stick are massless. Since the Higgs mechanism fits perfectly into the Standard Model, both to describe massive particles, and to answer a number of other essential questions, it is assumed to describe nature in the correct way and regarded as an integral part of the Standard Model.

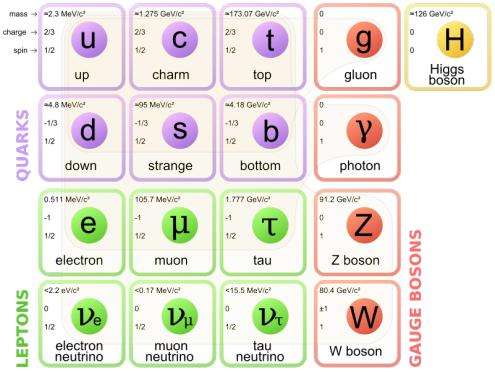

Figure 7.13: *The elementary particles, gathered in the Standard Model of Particle Physics [17]. The quarks and leptons are referred to as matter particles. The gauge bosons are the propagators of three fundamental forces: the strong, electromagnetic and weak force. The Higgs boson is responsible for the masses of the elementary particles.*

Nevertheless, to *prove* that the Higgs mechanism indeed gives a correct description of particle physics, it needs experimental verification. This can be achieved by detection of a manifestation of the Higgs field: the Higgs boson.

The search for the Higgs boson has been one of the primary motivations to build the Large Hadron Collider (LHC) at CERN, the European Organisation for Nuclear Research. The LHC is a circular particle accelerator that collides particles (protons) with record breaking energies of up to 8 TeV in 2012, which are energies sufficient to produce a Higgs boson, if it exists. In the collisions of the protons heavy new particles - possibly Higgs bosons - are created that almost immediately decay into the known elementary particles. The Higgs boson itself can therefore not be observed, but it can be recognised by the observable decay particles. At the four points along the LHC where the proton beams are collided, detectors are positioned to measure the traces that are left by the decay particles. By evaluation of these traces, which are electrical signals that are effectuated by the traversing particles, the original particles can be identified. Two of the detectors, ATLAS and CMS, have the objective to discover the Higgs boson; both succeeded in doing so.

On the 4th of July 2012 - almost fifty years after the first notion of the Higgs mechanism - the discovery of a Higgs-like boson was announced. Both the ATLAS and CMS experiments claimed the discovery of a new particle with a mass of around 125

GeV and properties that are in agreement with the predictions for a Higgs boson. To allow for this discovery each experiment analysed approximately a quadrillion (10^{15}) proton-proton collisions. The observed excess of collision events in which presumably a Higgs boson has been produced was reported to have a significance of 5σ. This means that the probability for the observed excess to be a statistical fluctuation instead of the result of a Higgs-like boson, is one in 3.5 million. A firm statement that a new particle was found.

One could naively think of this discovery as the completion of the Standard Model (SM) and that no more research on this topic has to be done. However, more research is required, namely to characterise the discovered boson. We do not yet know if the observed particle is really the Higgs boson as it is predicted by the Standard Model. The discovered particle is consistent with a Higgs boson, in the sense that its roughly measured properties match with these predicted by the Standard Model: its mass falls in the allowed range, its production rate in the various different sets of decay particles is as expected, and the particle can be identified as an electrically neutral particle with an integer spin value; the latter indicating that it is a boson. However, this does not yet prove that the particle is the SM Higgs boson. There are many more properties that have to be determined and only when all of these are measured and found to agree with the predictions of the Standard Model, it can be excluded that the observed signal is not that of a Higgs boson 'look-alike' with slightly different properties. Thus, the experimental research currently focusses on analysing the properties of the Higgs-like boson.

Two of the properties of the Higgs boson that can be measured with the current amount of data are its spin and parity. Spin and parity are quantum mechanical properties. Classically, spin can be seen as the rotation of a particle around its axis, but quantum mechanically it has no intuitive explanation. Every particle has a fixed spin value. It can be an integer value (0,1,2,...) or half-integer ($\frac{1}{2}$, $\frac{3}{2}$, $\frac{5}{2}$, ...). All elementary particles have a non-zero spin, but the Higgs boson is the only particle that is predicted to have zero spin. This property is inherent to a field that generates mass for elementary particles. Consequently, if the Higgs-like boson turns out to have a non-zero spin it cannot be a manifestation of the Higgs field. Parity can be understood as a symmetry property. Are the properties of a particle the same or opposite if you would measure it via a mirror? If the properties are the same, the

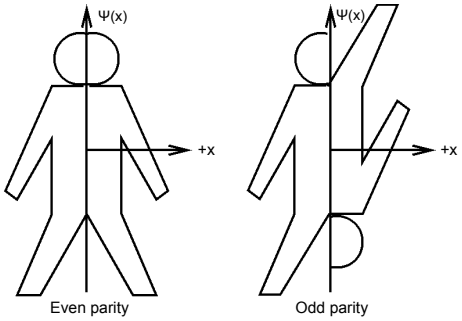

Figure 7.14: *Illustration of even and odd parity.*

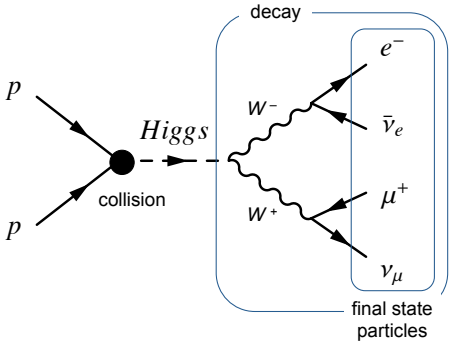

Figure 7.15: *Schematic overview of the studied Higgs production and decay.*

particle has even parity, if the properties are exactly the opposite the parity is odd, as is depicted in figure 7.21. The SM Higgs boson is predicted to have even parity. There are however theoretical extensions of the Standard Model that predict more than one Higgs boson, where one of the additional Higgs bosons has odd parity. Thus, the measurement of the spin and parity of the Higgs-like boson will already give a clear indication of its nature.

In the analysis presented in this thesis, the spin and parity of the Higgs-like boson are measured, using the data of the ATLAS detector. To do this measurement alternative hypotheses for the observed boson are formulated. The SM hypothesis corresponds to a Higgs boson with spin-0 and even parity, denoted as: $J^P = 0^+$. The studied alternative hypotheses include: $J^P = 0^-, 2^+, 1^+$ and 1^-. The total dataset of collision data that are collected in 2012 is compared to the SM hypothesis and each of the alternative hypotheses. In this way a statement can be made about the spin and parity of the observed Higgs-like boson. Are the data more compatible with the SM hypothesis or one of the alternatives? Is it possible to exclude the other spin and parity hypotheses?

To evaluate the spin and parity of the Higgs-like boson, the particles into which the Higgs boson decays, referred to as final state particles, are studied. The Higgs boson can decay into different sets of final state particles. The specific decay that has been studied in this thesis, the so-called WW channel, is shown in figure 7.22. The final state consists of an electron (e), a muon (μ) and two neutrinos (ν); which are

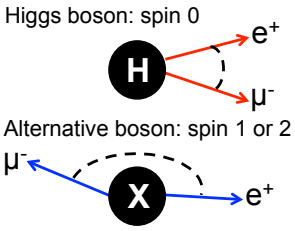

Figure 7.16: *Illustration of the effect of the spin of the original particle on the angle between the muon and electron.*

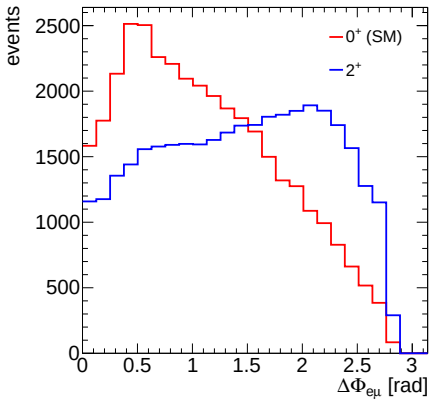

Figure 7.17: *Distributions of the angle between the electron and the muon ($\Delta\phi_{e\mu}$), simulated for a SM Higgs boson in red and a hypothetical spin-2 boson in blue.*

elementary stable particles. The properties of these particles give information about the spin and parity of the original particle. Hence, by studying the properties of the final state particles, the spin and parity of the original particle can be determined.

One property of the final state that is particularly sensitive to the spin and parity of the Higgs-like boson is the angle between the electron and the muon, denoted as $\Delta\phi_{e\mu}$. If the Higgs-like boson is indeed a spin-0 particle, this angle will be small, while the angle will be much larger if the Higgs-like boson has spin-1 or spin-2, which is schematically depicted in figure 7.23. This angle can also be calculated for simulations of collision events in which either a 0^+ or a 2^+ boson is produced. Figure 7.24 shows distributions of $\Delta\phi_{e\mu}$ for the simulated SM Higgs boson in red and a hypothetical 2^+ boson in blue. Clearly, the distributions are different for the two hypotheses. This makes it possible to compare the collision data with the two simulated hypotheses and determine which hypothesis fits best with the data.

In figure 7.24 only simulations of the signal hypotheses, i.e. a SM Higgs boson or a 2^+ boson, are taken into account. However, the collision data consist mostly of background events. These are events in which no Higgs boson is produced. Only one in ten billion collisions a Higgs boson is produced. Thus, to allow for a sensitive comparison between data and the simulated hypotheses, the number of background

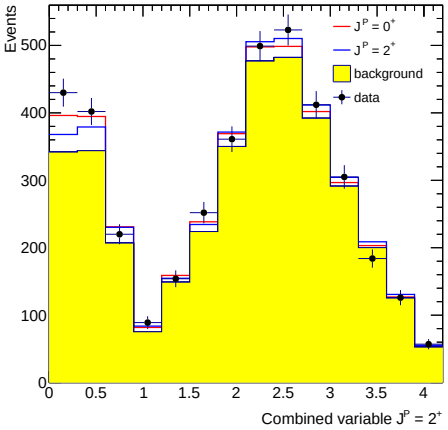

Figure 7.18: *The simulated separating distributions for a SM Higgs boson in red and a hypothetical spin-2 boson in blue, on top of the irreducible background (yellow). The data are indicated as black dots.*

events in the dataset has to be reduced. This is done by applying selections to the dataset that remove as much background as possible, while preserving most of the signal, i.e. Higgs events. After these selections we are left with approximately 200 signal events and 4000 background events.

The background cannot be further reduced without substantially reducing the signal. Therefore the different hypotheses have to be distinguished on top of this irreducible background. Consequently, only using $\Delta\phi_{e\mu}$ to separate the different hypotheses is not sufficient. More final state properties that are sensitive to the spin and parity of the Higgs-like boson need to be utilised in order to obtain the required separation power between the hypotheses. This is done by analytically combining the sensitive properties into an ultimately separating variable. For each alternative hypothesis such a combined variable is made. Figure 7.25 shows the combined variable - after background rejecting selections - for the simulations of the SM Hypothesis in red and the 2^+ hypothesis in blue, on top of the simulated irreducible background that is indicated in yellow. In this combined variable also the momenta of the final state particles are exploited. The separation between the two hypotheses is small but large enough to evaluate if the data are more compatible with one or the other hypothesis. The black dots show the actual collision data after applying the background

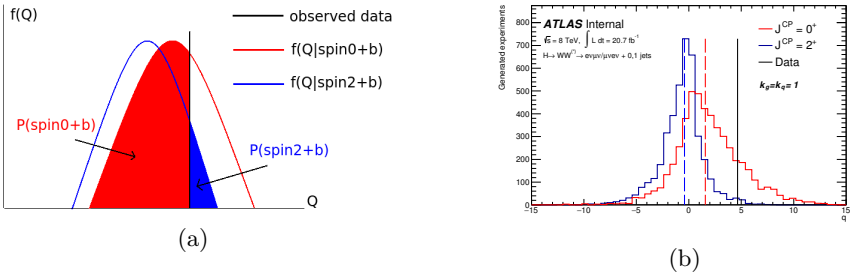

Figure 7.19: *Example (a) and real result (b) for the probability distributions used to quantify the compatibility of the data (indicated as a black vertical line) with the two hypotheses: the SM Higgs boson (red) and the 2^+ boson (blue). The shaded red area in (a) represents the compatibility of the SM hypothesis with the data, while the blue area indicates the compatibility with the alternative hypothesis.*

rejecting selections. By eye it is hard to see with which hypothesis the data are more compatible, therefore the compatibility is quantified using a *statistical analysis*.

In the statistical analysis the combined variable is fitted such that the compatibility of the data with the different hypotheses can be quantified with a variable q. Figure 7.26a shows a fictive example of the q distributions. The red distribution is made of the sum of the simulated SM hypothesis events and irreducible background and the blue distribution of the simulated 2^+ hypothesis plus background. The black vertical line represents the actual data. The red area indicates the compatibility of the data with the SM hypothesis, and the blue area with the 2^+ hypothesis. The larger the area, the more compatible the data with the corresponding hypothesis. Figure 7.26b shows the real result for the comparison of the data with the SM and 2^+ hypotheses. Clearly, the data are more compatible with the SM hypothesis. From this figure can be extracted that the probability that the 2^+ hypothesis is correctly rejected in favour of the SM Higgs boson is 98.5%. These distributions have also been evaluated for the other alternative hypotheses, $J^P = 0^-, 1^+$ and 1^-, and show that the data favour the SM Higgs boson and that the probability that the alternative hypothesis is correctly rejected in favour of the SM Higgs boson is more than 92.2% for any of the hypotheses.

This measurement is one of the early stage properties analyses of the discovered Higgs-like boson and contributes to the characterisation of the new boson. It shows that it is possible to perform a spin and parity measurement for the WW Higgs decay,

something that did not seem feasible at the time of the discovery in 2012. The results are however not conclusive yet. Although the alternative hypotheses seem unlikely, one cannot yet be sure that the spin of the observed boson is zero and the parity even. In order to be able to make a firmer statement about the spin and parity of the observed boson, the analysis should become more sensitive. To improve the sensitivity, various optimisations of the analysis are possible, which requires further research. One example is to make a more precise combination of the spin sensitive properties of the final state particles. Furthermore, analysis of more data will result in an increased sensitivity. In May 2015 the LHC will start delivering new data, allowing to update the measurement with more statistics.

The next generation of spin and parity analyses of the Higgs-like boson will include more complex hypotheses that allow for a more precise measurement. Ultimately, all the properties of the new boson have to be measured and compared to the Standard Model prediction. Only then can be concluded if the observed Higgs-like boson is the Standard Model Higgs boson, or if the discovered particle does not belong to the Standard Model and reveals new physics. The analysis that has been presented in this thesis is a first step in the characterisation of the new Higgs-like boson and suggests that the discovered boson is the Standard Model Higgs boson.

Samenvatting

Als u zich ooit heeft afgevraagd waarom de materie om ons heen massa heeft, dan bent u niet de enige. Jarenlang hebben natuurkundigen zich over dit vraagstuk gebogen. De bouwstenen van de natuur, de elementaire deeltjes, zijn beschreven in een wiskundig model, genaamd het Standaardmodel (SM) van de deeltjesfysica, dat is weergegeven in figuur 7.20. De elementaire deeltjes zijn opgedeeld in fermionen - deze staan weergegeven aan de linkerkant - en vectorbosonen die aan de rechterkant weergegeven zijn. De fermionen worden ook wel materiedeeltjes genoemd, omdat de lichtste fermionen de atomen vormen waaruit materie is opgebouwd. De vectorbosonen zijn de krachtdeeltjes en verantwoordelijk voor het overdragen van de sterke, zwakke en elektromagnetische kracht. In de afgelopen eeuw is voor het bestaan van elk van de fermionen en vectorbosonen experimenteel bewijs gevonden. Er is echter nog een ander deeltje voorspeld: het higgsdeeltje. Dit deeltje complementeert het Standaard Model maar was tot juli 2012 nog niet ontdekt.

In eerste instantie beschreef het Standaardmodel de elementaire deeltjes als massaloos. Maar we weten uit het dagelijks leven en experimenten dat de deeltjes wel degelijk massa hebben. Deze tegenstrijdigheid is te verklaren met het *higgsmechanisme* dat in 1964 door Peter Higgs en andere wetenschappers werd bedacht. Deze wiskundige uitbreiding van het Standaardmodel voorspelt dat de elementaire deeltjes massa krijgen doordat ze een wisselwerking aangaan met een overal aanwezig higgsveld. U kunt zich dit voorstellen als een universum gevuld met een soort onzichtbare 'stroop', het higgsveld. Hoe meer een deeltje aan deze stroop blijft plakken hoe zwaarder het is. Deeltjes die zich helemaal niet hechten zijn daarentegen massaloos. Het higgsmechanisme past perfect in het Standaardmodel; het beschrijft massieve deeltjes en lost

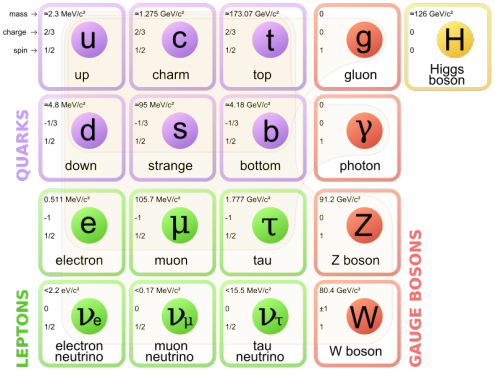

Figuur 7.20: *De elementaire deeltjes, verzameld in het Standaardmodel van de deeltjesfysica [17].*

een aantal cruciale problemen van het SM op. Daarom is het aannemelijk dat het higgsmechanisme de juiste manier is om de natuur te beschrijven.

Om te *bewijzen* dat het higgsmechanisme de deeltjesfysica op de juiste wijze beschrijft is er ook experimenteel bewijs nodig. Het higgsveld zelf kan niet worden gedetecteerd, maar het deeltje dat hier onlosmakelijk mee verbonden is wel. Daarom zijn wetenschappers al jaren op zoek naar het higgsdeeltje.

Om deze zoektocht mogelijk te maken is op CERN - het grootste natuurkundelaboratorium ter wereld - een deeltjesversneller, genaamd de Large Hadron Collider (LHC), gebouwd. De LHC botst met gigantische energie deeltjes (protonen) op elkaar. In deze botsingen ontstaan nieuwe deeltjes, wellicht higgsdeeltjes. Een higgsdeeltje heeft, net als andere zware deeltjes, echter een hele korte levensduur en valt bijna meteen uiteen in de bekende elementaire deeltjes, de 'vervalsdeeltjes'. Dus het higgsdeeltje bestaat steeds maar even en kan niet worden gedetecteerd. Het higgsdeeltje kan echter wel worden herkent aan de hand van de waarneembare vervalsdeeltjes. Op de vier plekken in de LHC waar de botsingen plaatsvinden zijn detectoren gebouwd die de 'sporen' van de stabiele vervalsdeeltjes vastleggen. Deze sporen zijn gebaseerd op de elektrische signalen die in de detector worden gemeten als een deeltje door dat specifieke detectoronderdeel is heengegaan. Door de sporen te onderzoeken kan worden vastgesteld welk deeltje in de botsing is gemaakt. Twee detectoren, genaamd ATLAS en CMS, hebben als doel om het higgsdeeltje op te sporen en beide zijn daarin geslaagd.

Op 4 juli 2012, 48 jaar na de ontwikkeling van het higgsmechanisme, werd de ontdekking van een higgsachtig deeltje bekend gemaakt. Zowel ATLAS als CMS verkondigden dat ze een nieuw deeltje hadden gevonden met een massa van ongeveer 125 GeV en eigenschappen die ongeveer overeenkomen met de voorspellingen voor een higgsdeeltje. Om tot deze ontdekking te komen analyseerden ATLAS en CMS elk ongeveer een quadriljoen (1 000 000 000 000 000) botsingen.

Met het experimentele bewijs voor het bestaan van een higgsachtig deeltje zijn we er echter nog niet. Voordat kan worden gezegd of dit hét SM higgsdeeltje is, moet worden onderzocht wat zijn exacte eigenschappen zijn en of deze overeenkomen met wat de Standaardmodeltheorie voorspelt. Als er eigenschappen zijn die niet overeen blijken te komen, dan is er een fantastische ontdekking gedaan van een nieuw exotisch deeltje, maar niet van het SM higgsdeeltje.

Twee belangrijke eigenschappen die momenteel worden onderzocht zijn de spin en pariteit van het higgsdeeltje. Dit zijn kwantummechanische kenmerken die niet eenvoudig kunnen worden voorgesteld. Allereerst de spin van het deeltje. Dit kan worden gezien als de rotatie van het deeltje om zijn as. Alle elementaire deeltjes hebben een spinwaarde van ofwel 1 ofwel $\frac{1}{2}$. Het higgsdeeltje is het enige deeltje waarvoor is voorspeld dat het spin-0 heeft. Deze waarde voor de spin is essentieel voor een veld dat massa genereert voor de elementaire deeltjes. Als blijkt dat het higgsdeeltje wel spin zou hebben dan kan het geen manifestatie zijn van het higgsveld en is het higgsmechanisme niet experimenteel bevestigd. De pariteit is de tweede onderzochte eigenschap en uitgelegd in figuur 7.21. Pariteit kan worden voorgesteld als de manier waarop de eigenschappen van een deeltje veranderen als het zou worden geobserveerd via een spiegel. Als een deeltje even pariteit heeft veranderen zijn eigenschappen niet, maar als het deeltje oneven pariteit heeft, dan zijn de meeste eigenschappen precies tegenovergesteld. Het SM higgsdeeltje heeft even pariteit. Er zijn echter theoretische uitbreidingen van het Standaardmodel die meerdere higgsdeeltjes voorspellen, waaronder een higgsdeeltje met oneven pariteit. Dus we moeten wel zeker weten of het gevonden deeltje niet net dat deeltje is met oneven pariteit. Dus door de spin en pariteit te meten komen we al veel verder in het vaststellen van de aard van het gevonden higgsachtige deeltje.

In dit proefschrift is de analyse van de spin en pariteit van het higgsachtige deeltje beschreven. Voor de analyse is gebruik gemaakt van de data (botsingen) die in 2012

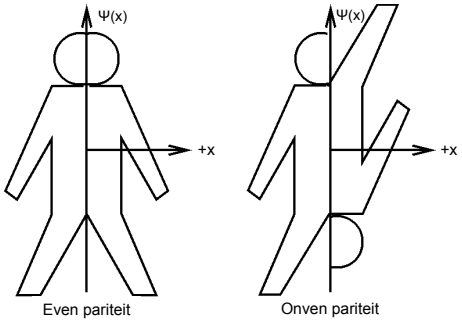

Figuur 7.21: *Illustratie van even en oneven pariteit.*

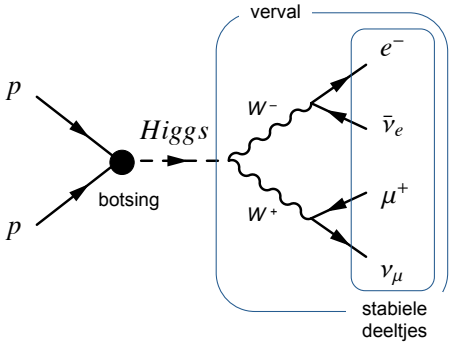

Figuur 7.22: *Schematische weergave van de productie en het verval van het higgsdeeltje in het WW vervalskanaal. Het proces verloopt van links naar rechts. De hoeken tussen de deeltjes reflecteren niet de werkelijke hoeken.*

met de ATLAS detector zijn gemeten. Om de spin en pariteit te bepalen, worden de sporen van de elementaire deeltjes waarin het higgsdeeltje uiteenvalt (vervalt) onderzocht. Het higgsdeeltje kan vervallen in verschillende sets van elementaire deeltjes. Het specifieke verval waarnaar ik onderzoek heb gedaan is schematisch weergegeven in figuur 7.22 en heet het WW vervalskanaal. De eindtoestand van het verval bestaat uit een elektron (e), een muon (μ) en twee neutrino's (ν). De energie en richting van de vervalsdeeltjes reflecteren de spin en pariteit van het originele deeltje. Zo zal de hoek tussen het elektron en muon, aangeduid als $\Delta\phi_{e\mu}$, klein zijn als het originele deeltje spinloos is, maar groot voor een hypothetisch deeltje dat bijvoorbeeld een spinwaarde van 1 of 2 heeft. Dit is schematisch weergegeven in figuur 7.23. Dus door de eigenschappen van de vervalsdeeltjes te bestuderen kunnen we de spin en pariteit van het higgsachtige deeltje onderzoeken.

Om dit onderzoek te doen zijn verschillende hypotheses voor de spin en pariteit geformuleerd. De Standaardmodel hypothese correspondeert met een higgsdeeltje met spin-0 en even pariteit, aangeduid als: $J^P = 0^+$. De alternatieve hypotheses bestaan uit: $J^P = 0^-, 2^+, 1^+$ en 1^-. Voor elk van de hypotheses zijn botsingen *gesimuleerd* waarin het betreffende hypothetische deeltje wordt geproduceerd en in dezelfde deeltjes als het SM Higgsdeeltje uiteenvalt. Vervolgens kunnen de echte botsingsdata

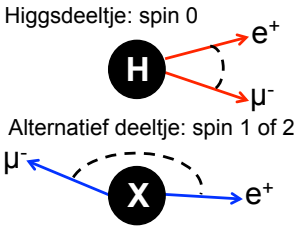

Figuur 7.23: *Illustratie van het effect van de spin van het originele deeltje op de hoek tussen het muon en elektron.*

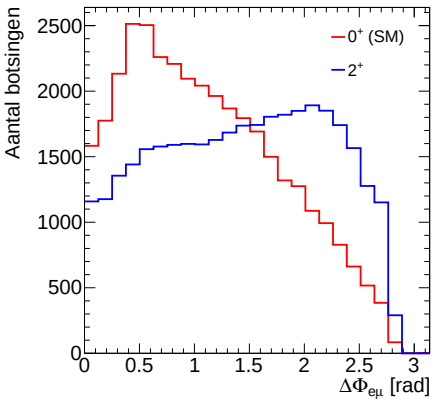

Figuur 7.24: *Distributies van de hoek tussen het elektron en muon ($\Delta\phi_{e\mu}$), weergegeven voor gesimuleerde botsingen waarin het SM higgsdeeltje is geproduceerd (rood) en het hypothetische 2^+ deeltje (blauw).*

worden vergeleken met de simulaties en kan worden bekeken hoe groot de overeenkomst is van de data met elk van de hypotheses. Op deze manier kijken we of we de alternatieve hypotheses kunnen uitsluiten en of de data overeenkomen met de SM hypothese.

De volgende stap is om de eigenschappen van de vervalsdeeltjes die gevoelig zijn voor de spin en pariteit van het higgsachtige deeltje te evalueren voor de verschillende hypotheses. Als voorbeeld kijken we nogmaals naar de hoek tussen het muon en elektron, $\Delta\phi_{e\mu}$, en we doen dit voor de SM hypothese en de hypothese dat het deeltje spin-2 heeft en even pariteit (2^+). De hoek kan worden uitgerekend voor de simulaties van beide hypotheses. Het resultaat is weergegeven in figuur 7.24, waar in rood de distributie voor de SM hypothese is weergegeven en in blauw de distributie voor de 2^+ hypothese. De twee distributies verschillen duidelijk van elkaar. Dit maakt het mogelijk om $\Delta\phi_{e\mu}$ ook voor de echte botsingsdata uit te rekenen en vervolgens met de twee hypotheses te vergelijken om zo te bepalen welke hypothese het best met de data overeenkomt.

Nu is het zo dat in de botsingen bijna nooit een higgsdeeltje wordt gemaakt: maar in 1 op de 10 miljard botsingen wordt er een vermoedelijk higgsdeeltje gemaakt.

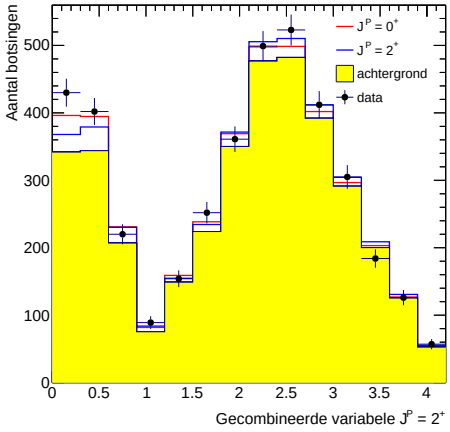

Figuur 7.25: *Distributie van de gecombineerde eigenschappen van de vervalsdeeltjes. De achtergrond is weergegeven in geel en daar bovenop zijn de gesimuleerde botsingen voor de SM hypothese (rood) en de 2^+ hypothese (blauw) weergegeven. De data zijn voorgesteld als de zwarte punten.*

De andere botsingen worden 'achtergrond' genoemd. Dus om de botsingsdata met de simulaties voor de verschillende hypotheses te kunnen vergelijken moet de grote hoeveelheid achtergrond in acht worden genomen. Gedeeltelijk kan de achtergrond worden onderdrukt door een gedeelte van de botsingen weg te gooien met behulp van slimme selecties. Hierdoor houden we een uiteindelijke dataset over met ongeveer 200 signaalbotsingen en 4000 achtergrondbotsingen.

Door ook nog eens verschillende spingevoelige eigenschappen van de vervalsdeeltjes te combineren, en dus niet alleen $\Delta\phi_{e\mu}$ te gebruiken, kunnen de SM hypothese en de 2^+ hypothese worden onderscheden en vergeleken met de echte botsingsdata, ondanks de aanwezige achtergrond. Figuur 7.25 laat het resultaat zien. Het gele vlak duidt de overgebleven gesimuleerde achtergrond aan. Bovenop de achtergrond zien we in rood de SM hypothese en in blauw de 2^+ hypothese. Het verschil in vorm tussen de twee hypotheses is klein, maar groot genoeg om na te gaan met welke hypothese de botsingsdata het best overeenkomen. De zwarte punten representeren de botsingsdata. Het is moeilijk om met het oog vast te stellen welke hypothese het beste met de data overeenkomt. Daarom wordt er een *statistische analyse* gedaan om de mate van overeenkomst vast te stellen.

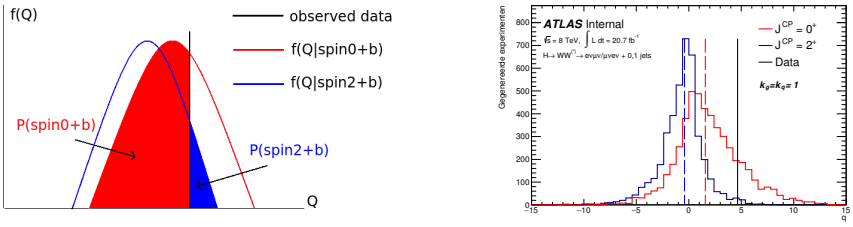

(a) (b)

Figuur 7.26: *Voorbeeld (a) en echte resultaat (b) voor de q distributies die zijn gebruikt om de overeenkomst van de data (weergegeven als de zwarte verticale lijn) met de twee hypotheses te kwantificeren: het SM higgsdeeltje (rood) en een hypothetisch 2^+ deeltje (blauw). Het rode oppervlak in (a) representeert de compatibiliteit van de SM hypothese met de data en het blauwe oppervlak die met de alternatieve hypothese.*

In de statische analyse gebruiken we weer de combinatie van spin- en pariteitsgevoelige eigenschappen van de vervalsdeeltjes, deze combinatie duiden we aan als q. Vervolgens wordt q geanalyseerd voor de twee hypotheses en de data. Figuur 7.26a laat een fictief voorbeeld zien van de statistische analyse. De rode distributie (lijn) representeert de SM hypothese en de blauwe distributie de 2^+ hypothese. De zwarte verticale lijn geeft de data weer. Het rood ingekleurde oppervlak laat de overeenkomst van de SM hypothese met de data zien en het blauwe oppervlak de overeenkomst van de data met de 2^+ hypothese. Hoe groter het gekleurde oppervlak hoe beter de overeenkomst. In dit voorbeeld is de overeenkomst met de SM hypothese dus veel beter. Het werkelijke resultaat is weergegeven in figuur 7.26b. De zwarte verticale lijn ligt middenin de distributie voor de SM hypothese. De data komen dus beter overeen met het SM higgsdeeltje en bijna niet met de 2^+ hypothese. Kwantitatief vertelt figuur 7.26b dat de kans dat de 2^+ hypothese correct wordt verworpen (ten gunste van de SM hypothese) 98.5% is. Oftewel de data zijn in overeenstemming met de SM hypothese en niet met de 2^+ hypothese. Deze analyse is ook uitgevoerd voor de eerder genoemde andere alternatieve hypotheses ($J^P = 0^-, 1^+$ en 1^-) en hieruit blijkt dat ook deze hypotheses onwaarschijnlijk zijn en de data overeenkomen met de SM hypothese.

Deze spin en pariteitsmeting is een van de eerste generatie analyses van de eigenschappen van het ontdekte higgsachtige deeltje en draagt bij aan het in kaart brengen van het nieuwe deeltje. De analyse laat zien dat het mogelijk is om een spin en pariteitsmeting te doen in het WW vervalskanaal. Iets wat niet plausibel leek ten tijde

van de ontdekking in 2012. Het resultaat is echter nog niet sluitend. De alternatieve hypotheses zijn onwaarschijnlijk, maar men kan er nog niet zeker van zijn dat de spin van het nieuwe deeltje nul is en de pariteit even. Voor een stelligere uitspraak is een gevoeligere analyse nodig. De gevoeligheid van de analyse kan op verschillende manieren worden geoptimaliseerd, maar dat vereist meer onderzoek. Een voorbeeld van een verbetering is het preciezer combineren van de spingevoelige eigenschappen van de vervalsdeeltjes. Wat ook zal zorgen voor een gevoeligere meting is de analyse van meer botsingsdata. Na een 'shutdown' van twee jaar waarin de versneller en detectoren zijn verbeterd, start de LHC dit jaar (2015) weer met het leveren van nieuwe data. Dit maakt een update van de analyse met meer data mogelijk.

De volgende generatie van spin en pariteit analyses van het higgsachtige deeltje zal complexere hypotheses bestuderen en een preciezere meting doen. Uiteindelijk zullen niet alleen de spin en pariteit, maar alle eigenschappen van het nieuwe deeltje gemeten moeten worden en vergeleken met de voorspellingen van het Standaardmodel. Alleen dan kan met zekerheid worden vastgesteld of het ontdekte deeltje echt het voorspelde SM higgsdeeltje is, of dat het deeltje niet tot het Standaardmodel behoort en nieuwe fysica blootlegt. De analyse die in dit proefschrift is opgetekend is een eerste stap in de typering van het higgsachtige deeltje en duidt erop dat het ontdekte deeltje het SM higgsdeeltje is.

Appendix A

Higgs rest frame: selection method for the neutrino z-component

When the estimation of the z-component of the momentum of the dineutrino system, $p_z^{\nu\nu}$, yields two valid solutions, one of these should be chosen. Several methods to do so are developed. Here, the development of the maximal efficiency method is discussed, where the efficiency is defined as the fraction of events for which the solution closest to the true value is selected.

To assure that the method with maximal efficiency will be acquired, all information that is available in the z-direction needs to be investigated. This entails three uncorrelated parameters: the two solutions themselves, denoted as $(p_z^{\nu\nu})^0$ and $(p_z^{\nu\nu})^1$, and the reconstructed momentum of the dilepton system in the z-direction, $p_z^{\ell\ell}$. Using these three parameters, two distances are defined. The first distance is used to select the smallest solution:

$$D_A = |(p_z^{\nu\nu})^0|^2 - |(p_z^{\nu\nu})^1|^2 \tag{A.1}$$

When D_A is negative $(p_z^{\nu\nu})^0$ is selected and when D_A is positive $(p_z^{\nu\nu})^1$ is selected. The second distance is used to select the solution closest to the dilepton system:

$$\begin{aligned} D_B &= |(p_z^{\nu\nu})^0 - p_z^{\ell\ell}|^2 - |(p_z^{\nu\nu})^1 - p_z^{\ell\ell}|^2 \\ &= |(p_z^{\nu\nu})^0|^2 - |(p_z^{\nu\nu})^1|^2 - 2((p_z^{\nu\nu})^0 - (p_z^{\nu\nu})^1)p_z^{\ell\ell} \end{aligned} \tag{A.2}$$

Again, when D_B is negative $(p_z^{\nu\nu})^0$ is selected and otherwise $(p_z^{\nu\nu})^1$ is picked. To define the optimal combination of the three input parameters, D_A and D_B are combined into a composite distance:

$$D_C = |(p_z^{\nu\nu})^0|^2 - |(p_z^{\nu\nu})^1|^2 - 2\alpha((p_z^{\nu\nu})^0 - (p_z^{\nu\nu})^1)p_z^{\ell\ell} \tag{A.3}$$

The dimensionless parameter α is introduced to scan all possible combinations of the two selection criteria. α runs from 0 to 1, where $\alpha = 0$ corresponds to $D_C = D_A$ and $\alpha = 1$ to $D_C = D_B$. Again, when the distance is negative $(p_z^{\nu\nu})^0$ is taken and vice versa.

A scan over α is performed counting the events for which the solution closest to the simulated true value of $p_z^{\nu\nu}$ is selected. The result of the scan is shown in figure A.1a for the standard analysis sample including the 0-jet and the 1-jet channels. The distribution is almost flat up till $\alpha \simeq 0.3$, which indicates that these values yield similar efficiencies. To establish a single value for α, an additional measure is studied.

Not only the efficiency contributes to a reconstructed value of $p_z^{\nu\nu}$ that has a high resolution, the average difference between the true value and the selected 'wrong' solutions does so as well. If two values of α yield similar efficiencies, the one for which the selected wrong solutions are on average closer to the truth will entail more accurate results.

To define the optimal value of α an additional scan is performed: in figure A.1b the square of the difference between the two solutions, being $((p_z^{\nu\nu})^0 - (p_z^{\nu\nu})^1)^2 =$

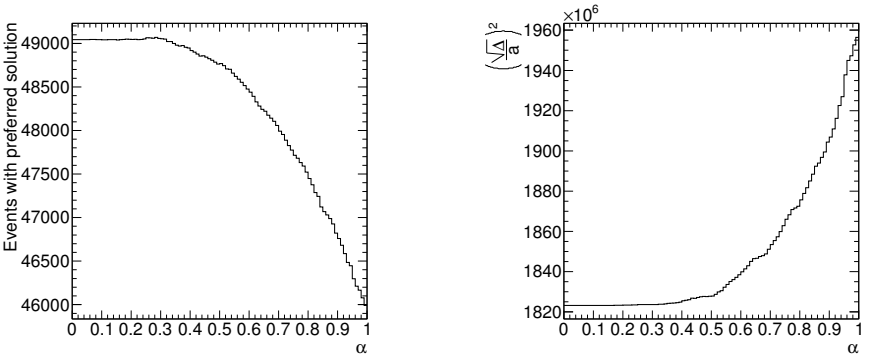

(a) (b)

Figure A.1: *Tests to determine which value of α leads to the highest resolutions. (a) α is distributed as a function of the events for which the solution closest to the truth is selected. (b) α is distributed for the set of wrongly selected solutions as a function of the squared difference between the two solutions.*

$(\sqrt{\Delta}/a)^2$, is plotted as a function of α for the set of wrongly selected solutions. The distribution shows that α is again optimal for the range $0 < \alpha < 0.3$, with no specific value preferred. Hence, any value in this range can be chosen and will yield maximal resolutions. The least complicated choice is $\alpha \equiv 0$, as then only the two solutions themselves are used in the selection method and $p_z^{\ell\ell}$ can be disregarded.

In conclusion, there is not a unique selection method that leads to maximal efficiency. Therefore the least complex procedure is chosen, which entails the selection of the smallest of the two solutions.

Appendix B

Performance of the reconstruction algorithm on generator level

The following plots are auxiliary material for the performance study of the Higgs rest frame reconstruction algorithm that is presented in chapter 5. The plots show the two-dimensional distributions of the reconstructed values versus the truth values of various rest frame variables. The distributions are obtained for the SM Higgs signal simulated at generator level. Hence, detector modelling and reconstruction resolutions are disregarded. A discussion of the distributions is given in section 5.5.1.

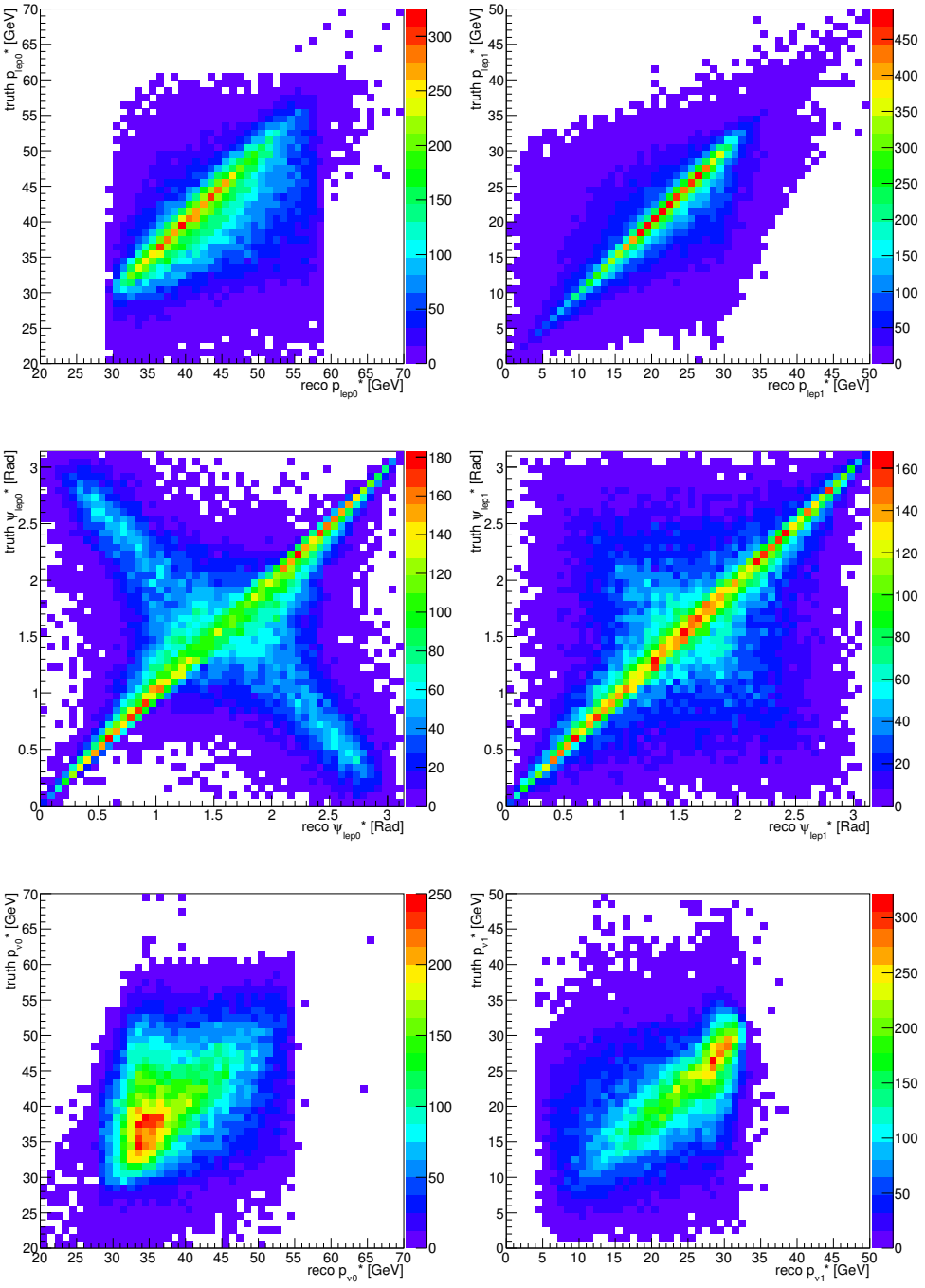

Figure B.1: *The reconstructed values on the x-axis versus the true values on the y-axis for the lepton observables and neutrino momenta, reconstructed in the Higgs rest frame. Distributions are obtained for the SM Higgs boson simulated at generator level.*

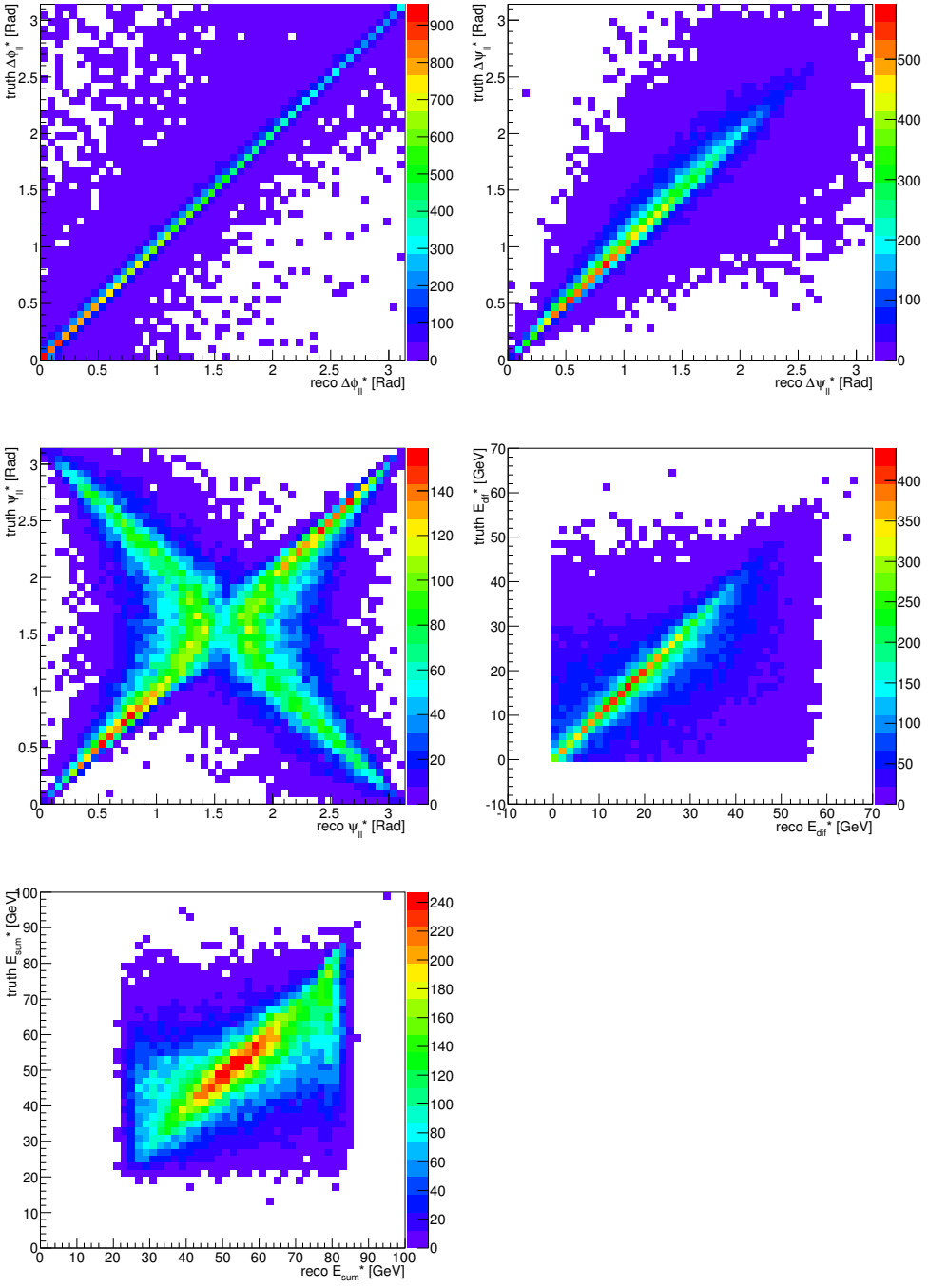

Figure B.2: *The reconstructed values on the x-axis versus the true values on the y-axis for the composite rest frame variables. Distributions are obtained for the SM Higgs boson simulated at generator level.*

Appendix C

Performance of the reconstruction algorithm for a spin-2 boson

The following plots are auxiliary material for the performance study of the Higgs rest frame reconstruction algorithm that is presented in chapter 5. The plots show the two-dimensional distributions of the reconstructed values versus the truth values of various rest frame variables. Results are shown for a Higgs-like boson with $J^{CP} = 2^+$. The distributions are obtained from the $J^{CP} = 2^+$ analysis sample that is described in section 5.1. A discussion of the distributions is given in section 5.5.4.

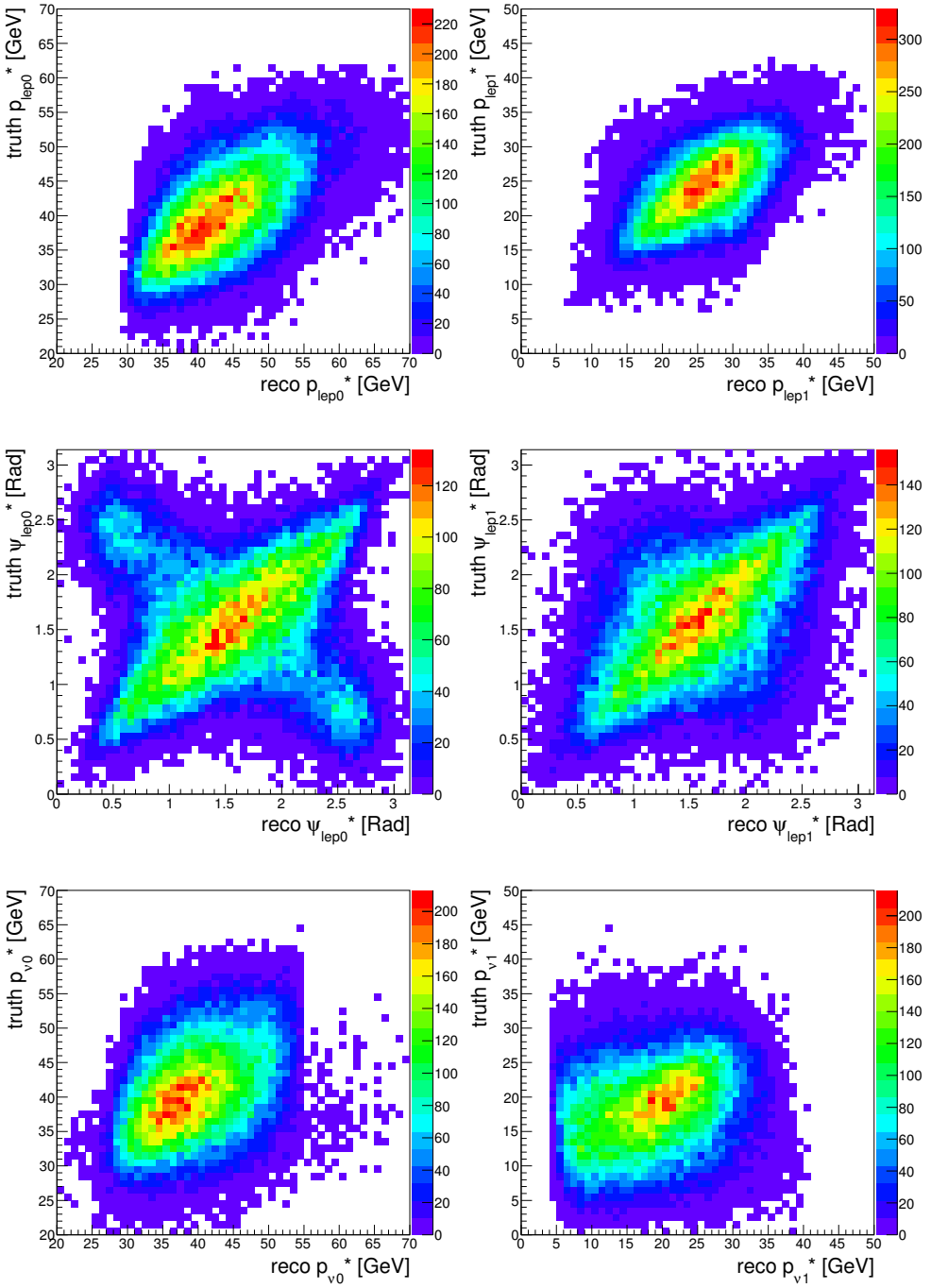

Figure C.1: *The reconstructed values on the x-axis versus the true values on the y-axis for the lepton observables and neutrino momenta, reconstructed in the Higgs rest frame. Distributions are shown for a Higgs-like boson with* $J^{CP} = 2^+$.

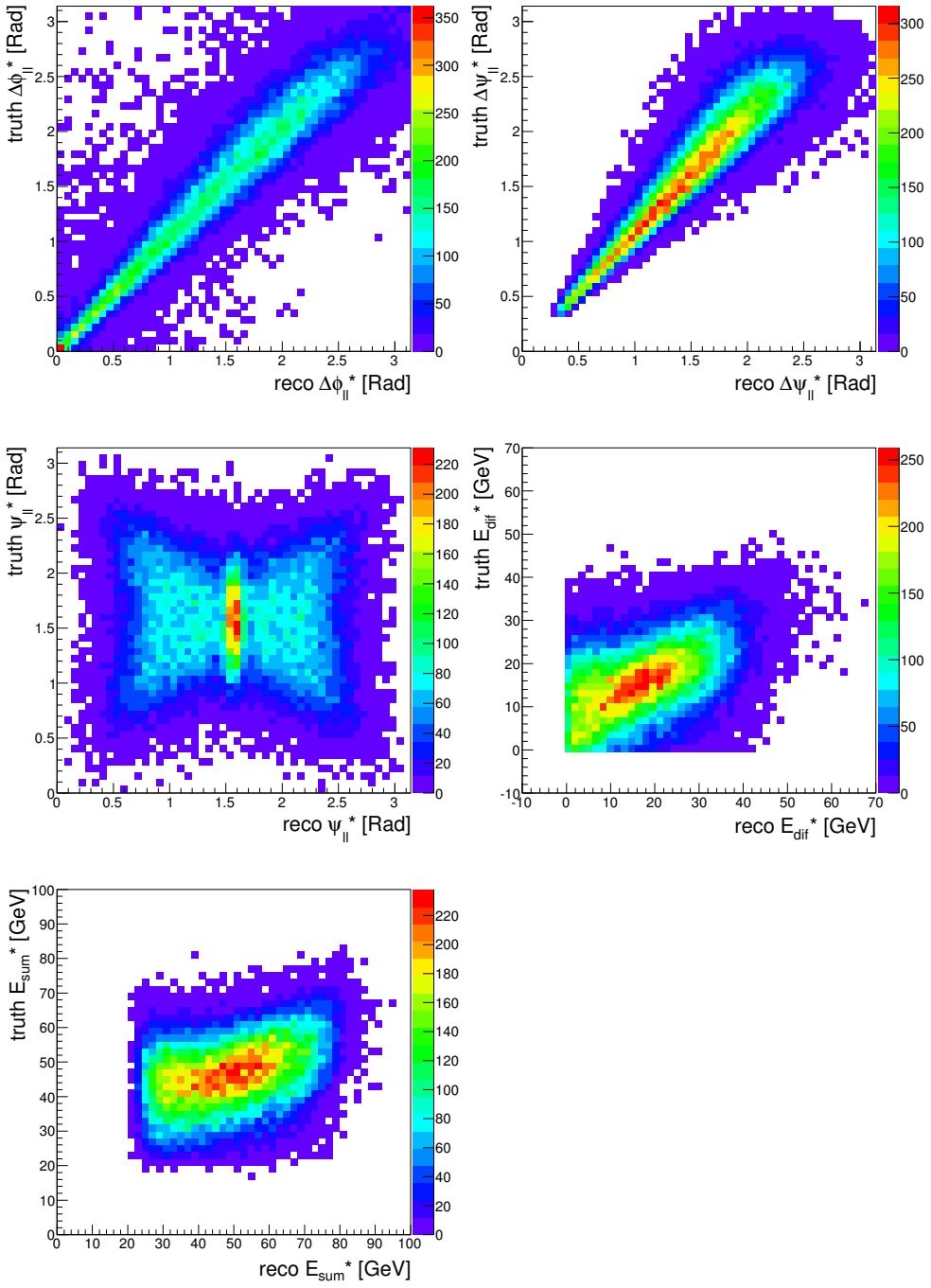

Figure C.2: *The reconstructed values on the x-axis versus the true values on the y-axis for the composite rest frame variables. Distributions are shown for a Higgs-like boson with* $J^{CP} = 2^+$.

Bibliography

[1] P. W. Higgs, Broken symmetries, massless particles and gauge fields, Phys. Lett. 12 132 (1964).

[2] P. W. Higgs, Broken Symmetries and the Masses of Gauge Bosons, Phys. Rev. Lett. 13 508 (1964).

[3] F. Englert and R. Brout, Broken Symmetry and the Mass of Gauge Vector Mesons, Phys. Rev. Lett. 13 321 (1964).

[4] G. Guralnik, C. Hagen and T. Kibble, Global conservation laws and massless particles, Phys. Rev. Lett. 13 585 (1964).

[5] P. W. Higgs, Spontaneous symmetry breakdown without massless bosons, Phys. Rev. 145 1156 (1966).

[6] T. Kibble, Symmetry breaking in non-Abelian gauge theories, Phys.Rev. 155 1554 (1967).

[7] ATLAS Collaboration, Observation of a new particle in the search for the Standard Model Higgs boson with the ATLAS detector at the LHC, Phys.Lett. B716 1 (2012).

[8] CMS Collaboration, Observation of a new boson at a mass of 125 GeV with the CMS experiment at the LHC, Phys. Lett. B716 30 (2012).

[9] ATLAS Collaboration, Determination of the spin and parity properties of the Higgs boson in the $WW^{(*)} \to \ell\nu\ell\nu$ decay channel, arXiv:1503.03643 [hep-ex] (2015).

[10] D. Griffiths, Introduction to Elementary Particles, second, revised edition, Wiley-VCH (2008).

[11] T. Plehn, Lectures on LHC Physics, arXiv:0910.4182v6 [hep-ph] (2014).

[12] W. Hollik, Quantum field theory and the Standard Model, CERN Yellow Report CERN-2010-002, arXiv:1012.3883 [hep-ph] (2010).

[13] I. van Vulpen, The Standard Model Higgs Boson. Part of the Lecture Particle Physics II, Universiteit van Amsterdam, (2013).

[14] C. Quigg, Gauge Theories of the Strong, Weak, and Electromagnetic Interactions, Westview Press (1997).

[15] A. Pich, The Standard Model of Electroweak Interactions, arXiv:0705.4264v1 [hep-ph] (2007).

[16] M. Bustamante, L. Cieri and J. Ellis, Beyond the Standard Model for Montaneros, arXiv:0911.4409v2 [hep-ph] (2010).

[17] MissMJ, PBS NOVA, Fermilab, Office of Science, Particle Data Group, Licensed under CC BY 3.0.

[18] Particle Data Group, K. Nakamura et al., J. Beringer et al., PR D86, 010001 (2012).

[19] Super-Kamiokande Collaboration, Y. Fukuda et al., Evidence for Oscillation of Atmospheric Neutrinos, Phys.Rev.Lett. 81, 1562 (1998).

[20] H. Murayama, The origin of neutrino mass, Physics World (2002).

[21] S. A. Bludman, Nuovo Cimento 9, 443 (1958).

[22] S. L. Glashow, Partial Symmetries of Weak Interactions, Nucl. Phys. 22, 579 (1961).

[23] S. Weinberg, A Model of Leptons, Phys. Rev. Lett. 19, 1264 (1967).

[24] A. Salam, Weak and Electromagnetic Interactions, Svartholm: Elementary Particle Theory, proceedings of the Nobel symposium (1968).

[25] G. 't Hooft, Renormalization of massless Yang-Mills fields, Nucl. Phys. B33, 173 (1971).

[26] G. 't Hooft, Renormalizable Lagrangians for massive Yang-Mills fields, Nucl. Phys. B35, 167 (1971).

[27] C. Wu et al., Experimental Test of Parity Conservation in Beta Decay, Phys. Rev. 105, 1413 (1957).

[28] J. Goldstone, A. Salam and S. Weinberg, Broken Symmetries, Phys. Rev. 127, 965 (1962).

[29] G. C. Branco et al., Theory and phenomenology of two-Higgs-doublet models, arXiv:1106.0034v3 [hep-ph] (2011).

[30] E. Schmidt, Search for the Standard Model Higgs boson in the $H \to W^+W^- \to \ell^+\nu\ell^-\bar{\nu}$ decay mode in proton-proton collisions at $\sqrt{s} = 7$ TeV and $\sqrt{s} = 8$ TeV with the ATLAS experiment, Ph.D. thesis, Albert-Ludwigs-Universität Freiburg (2013).

[31] L. Evans and P. Bryant, LHC Machine, JINST 3 S08002 (2008).

[32] M. Lamont, Status of the LHC, Journal of Physics: Conference Series 455 012001, 201 (2013).

[33] CERN Document server: http://cds.cern.ch/record/1621894.

[34] S. Myers, The first years of LHC operation, Proceedings of IPAC2012, New Orleans (2012).

[35] ATLAS Luminosity public results: `https://twiki.cern.ch/twiki/bin/view/AtlasPublic/LuminosityPublicResults`.

[36] ATLAS Collaboration, The ATLAS Experiment at the CERN Large Hadron Collider, JINST 3 S08003 (2008).

[37] ATLAS Collaboration, ATLAS: Technical proposal for a general-purpose pp experiment at the Large Hadron Collider at CERN, CERN-LHCC- 94-43 (1994).

[38] ATLAS LARG Unit, Liquid Argon Technical Design Report, CERN/LHCC 96-41 (1996).

[39] ATLAS/Tile Calorimeter Collaboration, Tile Calorimeter Technical Design Report, CERN/LHCC 96-42 (1996).

[40] ATLAS Muon Collaboration, The ATLAS Muon Spectrometer Technical Design Report, CERN/LHCC 97-22 (1997).

[41] ATLAS HLT/DAQ/DCS Group, High-Level Trigger, Data Acquisition and Controls, CERN/LHCC/2003-022 (2003).

[42] ATLAS Collaboration, approved plots for the performance of the ATLAS detector: `https://twiki.cern.ch/twiki/bin/view/AtlasPublic/ApprovedPlotsATLASDetector`.

[43] Y. Arai et al, ATLAS Muon Drift Tubes Electronics, JINST (2008).

[44] S. Ask et al., The ATLAS central level-1 trigger logic and TTC system, ATL-COM-DAQ-2008-006 (2008).

[45] H. Beck et al., The Base-Line DataFlow System of the ATLAS Trigger and DAQ, IEEE Trans.Nucl.Sci. 51 (2004).

[46] S. Zimmerman et al, Detector Control System for the ATLAS Muon Spectrometer and Operational Experience after the First Year of LHC Data Taking, ICALEPCS2011 (2011).

[47] A. Polini, Design and Performance of the ATLAS Muon Detector Control System, J. Phys. Conf. Ser. 331 (2011).

[48] PVSS II: Process visualization and control system, manual on `http://j2eeps.cern.ch/wikis/display/EN/PVSS+Service` (2004).

[49] ATLAS Muon Collaboration, The ATLAS Muon Spectrometer Technical Design Report, CERN/LHCC 97-22 (1997).

[50] R. Hart et al, The ATLAS MDT Control System, ICALEPCS2009 (2009).

[51] S. Aefsky et al, The Optical Alignment System of the ATLAS Muon Spectrometer Endcaps, JINST 3 P11005 (2008).

[52] H. van der Graaf et al, RasNiK, an Alignment System for the ATLAS MDT Barrel Muon Chambers - Technical System Description, NIKHEF ET38110 (2000).

[53] J.C. Barriere et al., The alignment system of the barrel part of the atlas muon spectrometer, ATL-MUON-PUB-2008-007 (2008).

[54] D. Daniels et al, BCAM Calibration, ATL-MUON-2000-026 (2000).

[55] T. Gleisberg et al., Event generation with SHERPA 1.1, JHEP 0902 007, (2009).

[56] M. Gosselink. Radiating Top Quarks, Ph.D. thesis, Nikhef, UvA (2010).

[57] J. M. Campbell, J. W. Huston, and W. J. Stirling, Hard Interactions of Quarks and Gluons: A Primer for LHC Physics, Rept. Prog. Phys. 70 89 (2007).

[58] A. D. Martin, W. J. Stirling, R. S. Thorne, and G. Watt, Parton distributions for the LHC, Eur. Phys. J. C63 189 (2009).

[59] LHC Higgs Cross Section Working Group: `https://twiki.cern.ch/twiki/bin/view/LHCPhysics/CrossSections`

[60] J. Alwall et al., Comparative study of various algorithms for the merging of parton showers and matrix elements in hadronic collisions, Eur. Phys. J. C 53 473 (2008).

[61] T. Sjostrand, S. Mrenna, and P. Z. Skands, PYTHIA 6.4 physics and manual, JHEP 0605 026 (2006).

[62] T. Sjostrand, S. Mrenna, and P. Z. Skands, A Brief Introduction to PYTHIA 8.1, CERN-LCGAPP 04 1 (2007).

[63] G. Corcella et al., HERWIG 6: An event generator for hadron emission reactions with interfering gluons (including super-symmetric processes) , JHEP 0101 010 (2001).

[64] T. Gleisberg et al., Event generation with SHERPA 1.1, JHEP 0902 007 (2009).

[65] M. L. Mangano et al., ALPGEN, a generator for hard multi-parton processes in hadronic collisions, JHEP 0307 001 (2003).

[66] J. Alwall et al., MadGraph/MadEvent v4: The new web generation, JHEP 0709 028 (2007).

[67] J. Alwall et al,, MadGraph 5 : Going Beyond, JHEP 1106 128 (2011).

[68] S. Frixione and B. R. Webber, Matching NLO QCD computations and parton shower simulations, JHEP 0206 029 (2002).

[69] S. Alioli, P. Nason, C. Oleari, and E. Re, A general framework for implementing NLO calculations in shower Monte Carlo programs: the POWHEG BOX, JHEP 1006 043 (2010).

[70] S. Agostinelli et al., GEANT4: A Simulation toolkit. Nucl.Instrum.Meth. A506 (2003).

[71] W. Lukas, Fast Simulation for ATLAS: Atlfast-II and ISF, ATL-SOFT-PROC-2012-065 (2012).

[72] ATLAS Collaboration, Concepts, Design and Implementation of the ATLAS New Tracking (NEWT), ATL-SOFT-PUB-2007-007 (2007).

[73] ATLAS Collaboration, Charged-particle multiplicities in pp interactions measured with the ATLAS detector at the LHC, New J.Phys. 13 (2011).

[74] K. Grimm et al., Reconstruction of primary vertices in high pile-up environment: first control plots, ATL-COM-PHYS-2012-474 (2012).

[75] ATLAS Collaboration, Performance of primary vertex reconstruction in proton-proton collisions at $\sqrt{s} = 7$TeV in the ATLAS experiment, ATLAS-CONF-2010-069 (2010).

[76] ATLAS Collaboration, Measurement of the muon reconstruction performance of the ATLAS detector using 2011 and 2012 LHC proton proton collision data, arXiv:1407.3935v1 [hep-ex] (2014).

[77] T. Lagouri et al., A Muon Identification and Combined Reconstruction Procedure for the ATLAS Detector at the LHC at CERN, IEEE Trans.Nucl.Sci. 51 (2004).

[78] S. Hassani et al., A muon identification and combined reconstruction procedure for the ATLAS detector at the LHC using the (MUONBOY, STACO, MuTag) reconstruction packages, Nucl.Instrum.Meth. A572 (2007).

[79] ATLAS Collaboration, Muon reconstruction efficiency in reprocessed 2010 LHC proton-proton collision data recorded with the ATLAS detector, ATLAS-CONF-2011-063 (2011).

[80] ATLAS Collaboration, Electron reconstruction and identification efficiency measurements with the ATLAS detector using the 2011 LHC proton proton collision data, Eur. Phys. J. C (2014).

[81] ATLAS Collaboration, Improved electron reconstruction in ATLAS using the Gaussian Sum Filter-based model for bremsstrahlung, ATLAS-CONF-2012-047 (2012).

[82] ATLAS Collaboration, Expected performance of the ATLAS experiment: detector, trigger and physics, arXiv:0901.0512 [hep-ex] (2008)

[83] ATLAS Collaboration, Electron efficiency measurements in early 2012 data, ATL-COM-PHYS-2011-783 (2011).

[84] ATLAS Collaboration, Performance of Missing Transverse Momentum Reconstruction in Proton-Proton Collisions at 7 TeV with ATLAS, Eur.Phys.J. C72 (2012).

[85] ATLAS Collaboration, Performance of missing transverse momentum reconstruction in ATLAS studied in proton-proton collisions recorded in 2012 at 8 TeV, Tech. Rep. ATLAS-CONF-2013-082 (2013).

[86] ATLAS Collaboration, Measurement of the $W \to \ell\nu$ and $Z \to \ell\ell$ production cross sections in proton-proton collisions at $\sqrt{s} = 7$ TeV with the ATLAS detector, J. High Energy Phys. 12, 060 (2010).

[87] W. Lampl et al. Calorimeter clustering algorithms: Description and performance, ATL-LARG-PUB-2008-002 (2008).

[88] M. Cacciari, G. P. Salam and G. Soyez, The Anti-k(t) jet clustering algorithm, Journal of High Energy Physics 0804 (2008).

[89] ATLAS Collaboration, Jet energy measurement and its systematic uncertainty in proton proton collisions at $\sqrt{s} = 7$ TeV with the ATLAS detector, arXiv:1406.0076 [hep-ex] (2014).

[90] ATLAS Collaboration, Approved plots for the jet energy scale uncertainty: `https://twiki.cern.ch/twiki/bin/view/AtlasPublic/JetEtmissApproved2013JESUncertainty`.

[91] ATLAS Collaboration, Update of the $H \to WW^{(*)} \to e\nu\mu\nu$ analysis with 13.0 fb^{-1} of $\sqrt{s} = 8$ TeV data collected with the ATLAS detector, ATLAS-CONF-2012-158 (2012).

[92] ATLAS Collaboration, Commissioning of high performance b-tagging algorithms with the ATLAS detector, ATLAS-CONF-2011-102 (2011).

[93] ATLAS Collaboration, Measurement of the b-tag Efficiency in a Sample of Jets Containing Muons with 5 fb^{-1} of Data from the ATLAS Detector, ATLAS-CONF-2012-043 (2012).

[94] ATLAS Collaboration, Calibration of the performance of b-tagging for c and light-flavour jets in the 2012 ATLAS data, ATLAS-CONF-2014-046 (2014).

[95] P. Artoisenet et al., A framework for Higgs characterisation, arXiv:1306.6464v3 [hep-ph] (2014)

[96] Y.Gao et al., Spin determination of single-produced resonances at hadron colliders, Phys. Rev. D 81 (2010).

[97] M. Carena et al., CP-violating MSSM Higgs bosons in the light of LEP 2, Phys. Lett. B495 (2000).

[98] G. Isidori, A. V. Manohar, and M. Trott, Probing the nature of the Higgs-like Boson via $h \to VF$ decays, arXiv:1305.0663 (2013).

[99] B. Grinstein, C. W. Murphy, and D. Pirtskhalava, Searching for New Physics in the Three-Body Decays of the Higgs-like Particle, arXiv:1305.6938 (2013)

[100] C. N. Yang, Selection Rules for the Dematerialization of a Particle into Two Photons, Phys. Rev. 77, 242 (1950).

[101] L. D. Landau, Sov. Phys. Doklady 60, 207 (1948).

[102] L.Randall and R. Sundrum, A large mass hierarchy from a small extra dimension, Phys.Rev.Lett. 83 (1999).

[103] ATLAS Collaboration, Measurements of fiducial and differential cross sections for Higgs boson production in the diphoton decay channel at $\sqrt{s} = 8$ TeV with ATLAS, JHEP09 112 (2014).

[104] H. L. Lai et al., New parton distributions for collider physics, Phys. Rev. D82 (2010).

[105] P. M. Nadolsky et al., Implications of CTEQ global analysis for collider observables, Phys.Rev.D78 (2008).

[106] A. Sherstnev and R. S. Thorne, Parton distributions for LO Generators, Eur. Phys. J C55 (2008).

[107] N. Kauer, Interference effects for $H \to WW/ZZ \to \ell\nu\ell\nu$ searches in gluon fusion at the LHC, JHEP 1312 (2013).

[108] N. Kidonakis, NNLL resummation for s-channel single top quark production, Phys.Lett. D81 (2010).

[109] N. Kidonakis, Next-to-next-to-leading-order collinear and soft gluon corrections for t-channel single top quark production, Phys.Rev. D83 (2011).

[110] N. Kidonakis, Two-loop soft anomalous dimensions for single top quark associated production with a W or H, Phys.Rev. D82 (2010).

[111] C. Anastasiou and K. Melnikov, Higgs boson production at hadron colliders in NNLO QCD, Nucl. Phys. B646, 220 (2002).

[112] D. de Florian et al., Transverse-momentum resummation: Higgs boson production at the Tevatron and the LHC, JHEP 11 (2011).

[113] M. Grazzini and H. Sargsyan., Heavy-quark mass effects in Higgs boson production at the LHC, JHEP 1309 (2013).

[114] Y. Gao et al., Spin determination of single-produced resonances at hadron colliders, Phys. Rev. D 81 (2010).

[115] S. Bolognesi et al., On the spin and parity of a single-produced resonance at the LHC, Phys. Rev. D 86 (2012).

[116] J. Alwall et al., The automated computation of tree-level and next-to-leading order differential cross sections, and their matching to parton shower simulations, JHEP 1407 (2014).

[117] ATLAS Collaboration, Electron efficiency measurements with the ATLAS detector using the 2012 LHC proton-proton collision data, ATLAS-CONF-2014-032 (2014).

[118] ATLAS Collaboration, Selection of jets produced in proton-proton collisions with the ATLAS detector using 2011 data, ATLAS-CONF-2012-020, (2012).

[119] ATLAS Collaboration, Observation and measurement of Higgs boson decays to WW^* with the ATLAS detector, arXiv:1412.2641 [hep-ex] (2014).

[120] A. J. Barr, B. Gripaios, and C. G. Lester, Measuring the Higgs boson mass in dileptonic W-boson decays at hadron colliders, J. High Energy Phys. 07 072 (2009).

[121] S. Asai et al., Prospects for the search for a Standard Model Higgs boson in ATLAS using vector boson fusion, Eur. Phys. J. C 32S2 (2004).

[122] LHC Higgs Cross Section Working Group, S. Dittmaier, C. Mariotti, G. Passarino, and R. Tanaka (Eds.). Handbook of LHC Higgs Cross Sections: 1. Inclusive Observables. CERN-2011-002 (2011).

[123] LHC Higgs Cross Section Working Group, S. Dittmaier, C. Mariotti, G. Passarino, and R. Tanaka (Eds.). Handbook of LHC Higgs Cross Sections: 2. Differential Distributions. CERN-2012-002 (2012).

[124] R. D. Ball et al., Parton distributions with LHC data, arXiv:1207.1303 [hep-ph] (2012).

[125] ATLAS Collaboration, Improved luminosity determination in pp collisions at $\sqrt{s} = 7$ TeV using the ATLAS detector at the LHC, Eur. Phys. J. C 73.8 (2013)

[126] A. J. Armbruster, Discovery of a Higgs Boson with the ATLAS Detector, Ph.D. thesis, University of Michigan (2010).

[127] ATLAS Collaboration, Evidence for the spin-0 nature of the Higgs boson using ATLAS data, Phys. Lett. B 726 120 (2013).

[128] ATLAS Collaboration, Study of the spin and parity of the Higgs boson in the $H \to ZZ^* \to 4\ell$ decay mode with the ATLAS detector, ATL-COM-PHYS-2014-1550 (2015).

[129] CMS Collaboration, Measurement of Higgs boson production and properties in the WW decay channel with leptonic final states, JHEP 01 096 (2014).

[130] CMS Collaboration, Measurement of the properties of a Higgs boson in the four-lepton final state, Phys. Rev. D 89 092007 (2014).

[131] CMS Collaboration, Study of the Mass and Spin-Parity of the Higgs Boson Candidate via Its Decays to Z Boson Pairs, Phys. Rev. Lett. 110 081803 (2013).

[132] CMS Collaboration, Observation of the diphoton decay of the Higgs boson and measurement of its properties, Eur. Phys. J. C 74 3076 (2014).